Alma Mater Studiorum - Università Di Bologna

Dottorato di Ricerca in

CHIMICA

Ciclo XXXI

Settore concorsuale di afferenza: 03/C1

Settore Scientifico Disciplinare: CHIM/06

EPR INVESTIGATION OF SUPRAMOLECULAR ARCHITECTURES

Presentata da: Lorenzo Gualandi

Coordinatore Dottorato:

Prof. Aldo Roda

Supervisore:

Prof. Marco Lucarini

Co- supervisore:

Prof.ssa Elisabetta Mezzina

Esame finale anno 2019

Summary:

Abstract

Since the Nobel prize awarded to Lehn, Cramer and Pedersen in 1987 the interest of the scientific community for the principles of supramolecular chemistry has grown considerably, leading to a second Nobel prize awarded in 2016 to Stoddart, Feringa and Sauvage for their work on Molecular Machines. The always increasing complexity of supramolecular machines requires not only new and efficient synthetic approaches but also the development of analytical methods capable of measuring the molecular scale phenomena exhibited by supramolecular assemblies.

EPR spectroscopy, a magnetic resonance spectroscopic technique, has proven to be a useful tool for the investigation of supramolecular systems because it works in the microsecond timescale range, that matches the timescale of many supramolecular kinetics and dynamics. The exploitation of EPR spectroscopy for the investigation of supramolecular architectures is achieved by the spin probing and spin labelling methods.

My Ph.D. was devoted to the application of these strategies for the investigation of several supramolecular architectures by the means of EPR spectroscopy.

The 2nd chapter will be focused on the investigation of an important non-covalent interaction, analogue of hydrogen bond (HB), called halogen bond (XB). The study of this interactions has been realized by the design and synthesis of a suitable spin probe containing both the benzyl-*tert*-butyl nitroxide (BTBN) motif and the XB donor 4-iodo-2,3,5,6-tetrafluoro phenyl group. The use of these spin probes allowed us to measure the kinetic and thermodynamic parameters for this interaction in solution by performing complexation experiments with XB acceptors

The 3rd chapter will be focused on the synthesis of a derivative of a dibenzo-24-crown-8 ether (DB24C8) containing the BTBN motif for the investigation of its host properties toward guests such as alkali metal cations and organic guests. The EPR analysis enabled the measurement of the degree of complexation and to discriminate the guest from the experimental EPR readout. The formation of a pseudorotaxane with a thread molecule containing both the dialkylammonium and bipyridinium recognition sites, and the switching of the ring between the two stations of the guest was detected directly in solution.

The 4th chapter is devoted to the development and optimization of a mild and high yielding synthetic method for the synthesis of spin labelled [2]-rotaxanes by exploiting the active metal template copper catalysed azide alkyne cycloaddition (AT-CuAAC). The rotaxanes were designed to contain nitronyl nitroxide radicals (NN) as stoppers in the thread shaped molecule. Derivatives of different length and composition were synthesized as well as the corresponding non-interlocked threads. The EPR investigation of these NN labelled rotaxanes provided many useful information on the conformational dynamics in solution. Thanks to variable temperature EPR experiments and the comparison between the [2]-rotaxanes and the corresponding threads we were able to assess the effect of rotaxanation on the conformational dynamics of the threads in solution. Their ability to form complexes with metal cations, and the effect it has on the EPR spectra of the spin labelled rotaxanes and threads was also investigated.

Abbreviations, Acronyms and Symbols

°C degrees Celsius

Å angstroms

ATP adenosine triphosphate

ACN acetonitrile

BIPY2+ 4,4´-bipyridinium

Bu4NCl tetra-n-butylammonium chloride

BTBN benzyl-*tert*butyl nitroxide

c-Hex cyclohexane

CBPQT4+ cyclobis(paraquat-*p*-phenylene); bluebox

CD cyclodextrin

CuAAC copper(I)-catalyzed azide-alkynecycloaddition

DABCO

DB24C8 dibenzo[24]crown-8

DCE 1,2-dichloroethane

DCM dichloromethane

DIPEA diisopropylethylamine

DMF N,N-dimethylformamide

DNP 1,5-dioxynaphthalene

DMSO-d_6 deuterated dimethylsulfoxide

EDTA ethylenediaminetetraacetic acid

EI electron impact ionization

ESI electrospray ionization

EPR electron paramagnetic resonance

EWG electron withdrawing group

EtOAc ethyl acetate

Et_2O diethyl ether

g grams

G Gauss

GSCC ground state co-conformation

Hz Hertz (cycles per second)

HSQC NMR Heteronuclear Single-Quantum Correlation

HMBC NMR heteronuclear multiple bond correlation spectroscopy

DB24C8 *iso*-dibenzo[24]crown-8

J Joules

J MOD NMR J modulation NMR spectroscopy

K degrees Kelvin

K equilibrium constant

k rate constant

kcal kilocalories

kg kilograms

kHz kilohertz

M molar

MCPBA 3-chloroperbenzoic acid

MD molecular dynamics

MeOH methanol

MIM mechanically interlocked molecule

min minutes

mM millimolar

μM micromolar

mol moles

MS mass spectrometry/mass spectrum

MSCC metastable state co-conformation

mV millivolts

N number of molecules

n number

NO nitric oxide

n-BuLi *normal*-butyllithium

nm nanometers

NMR nuclear magnetic resonance

nN nanonewtons

o.n. overnight

P.Et. petroleum ether- 40-60°C fraction

PELDOR pulsed electron double resonance

RT room temperature

s seconds

SAM self-assembled monolayer

SOMO single occupied molecular orbital

T temperature

t time

TEA triethylamine

TEMPO (2,2,6,6-tetramethylpiperidin-1-yl)oxidanyl

TFA trifluoroacetic acid

THF tetrahydrofuran

TLC thin layer chromatography

TMP 2,2,5-trimethylpentane

Ts tosyl

TTF tetrathiafulvalene

UV ultraviolet

V volts

α-CD α-cyclodextrin

β-CD β-cyclodextrin

Δ thermal energy

ΔG change in Gibbs free energy

ΔH change in enthalpy

ΔS change in entropy

δ chemical shift

λ wavelength;

μ micro

μM micromolar

μm micrometers

μmol micromoles

μL microliters

ν frequency

1. Introduction:

1.1 Supramolecular Chemistry

Every living organism is nothing else than an extremely complicated and efficient chemical system, capable to perform highly organized and elaborated functions that keep them alive. Such complexity is needed for a system to be able to create order from disorder by decreasing the local entropy of the system itself. Thus, living systems can be considered dissipative thermodynamic systems.[1] This is possible only thanks to an extremely efficient organization at the molecular level that keeps the system out of thermodynamic equilibria (Figure 1.1) by transforming the chemical energy present in the surrounding environment and using a part of it for the complex and energy expensive metabolic processes.

Our molecular constituents have been extensively screened and selected by nature in the evolution process by their ability to recognize and influence each other like the gears of a clock.

Supramolecular chemistry is a branch of chemistry that investigates the interactions that can be observed between two or more molecules. With the Nobel prize awarded to Donald J. Cram, Jean-Marie Lehn, and Charles J. Pedersen in 1987, this field of chemistry has seen an always growing interest by the scientific community. Its importance was enlightened again with the 2016 Nobel prize to Fraser Stoddart, Ben Feringa and Jeanne-Pierre Sauvage (Figure 1.2).

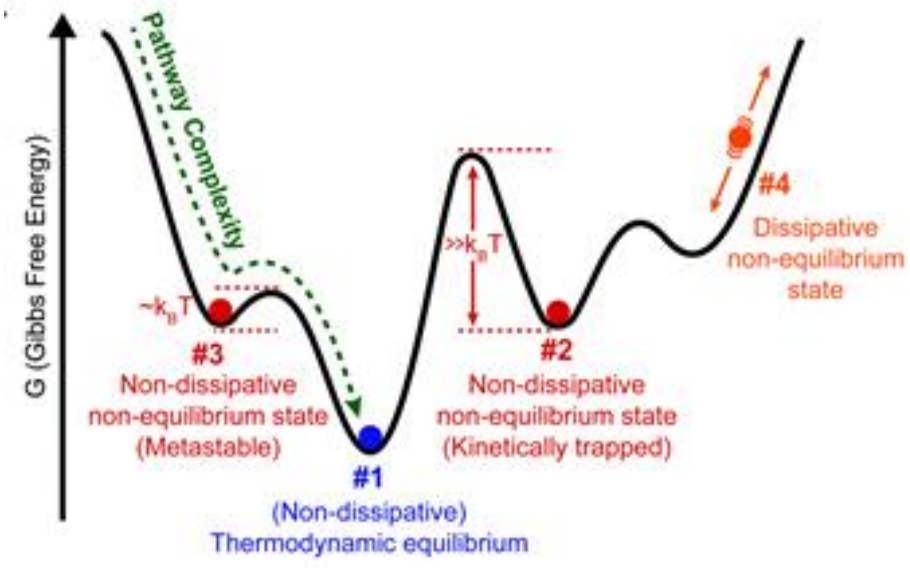

Figure 1.1 *Different thermodynamic states in a supramolecular system* [2]

The core concept of this field of chemistry is that the interactions between two or more molecules can give rise to new "emerging properties" that can be considered more than the sum of the properties of the molecular constituents of the system alone.[3] For this reason, supramolecular chemistry is often referred as the *chemistry beyond the molecules.* The interactions between the molecules mainly considered by

supramolecular chemistry are non-covalent interactions such as ionic interactions, hydrogen bonding (HB), halogen bonding (XB), Van der Waals forces, π-interactions and hydrophobic effects. All these interactions are involved in the recognition processes between molecules and affects the macroscopic properties of the system in which the molecules are comprised. The rationalization of these interactions can be exploited for the design and realization of functional materials with new and unexplored properties.

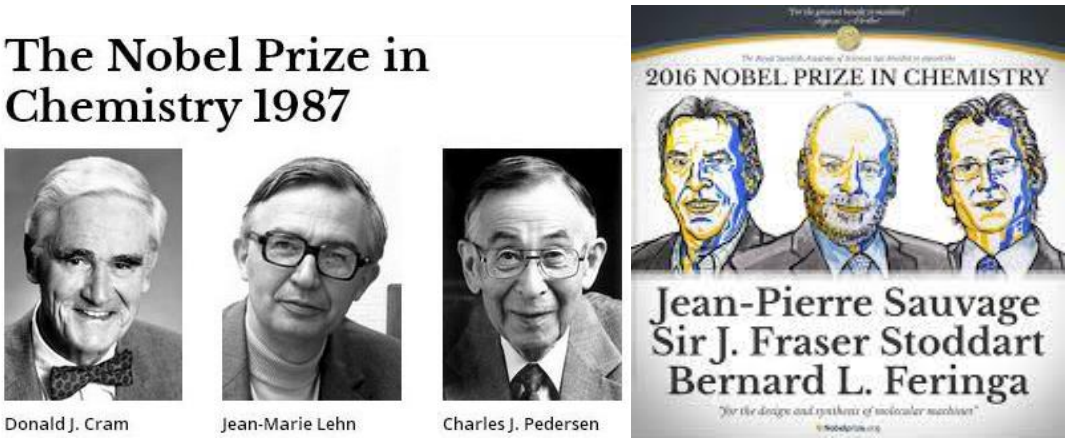

Figure 1.2 *Nobel laureates for the contributions in supramolecular chemistry.*

According to this approach, in the last 20 years a large variety of supramolecular based systems has been synthesized by applying a wide range of interactions that have been exploited for the synthesis of molecular motors, switches and other self-assembled architectures for a wide variety of applications.[4] Like in an enzyme, for example, supramolecular chemistry can be used in fields such as organic and metal catalysis in which the reactivity is selectively directed by non-covalent interactions.[5] It can also be used for the realization of stimuli responsive materials,[6] drug delivery systems[7] and sensors.[8]

1.1.1 Self-assembly.

The most important principle of supramolecular chemistry is the exploitation of interactions between two or more molecules thanks to the self-assembly process, that is generally described as the spontaneous and reversible recognition process between two or more molecules by non-covalent interactions to yield complex structures. This process *i.e.* can be easily observed in nature in the ability of lipids to spontaneously organize themselves in micelles, liposomes and other highly ordered structure when exposed to polar environments without the intervention of external stimuli (Figure 1.3). The recognition between an enzyme and its substrate and the process that realizes muscular contractions are all based on the same principle of self-assembly of the single components in complex hierarchical structures.

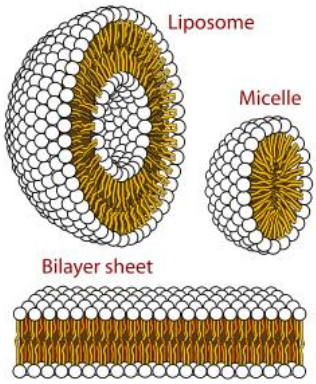

Figure 1.3 *Different kinds of supramolecular architectures formed by phospholipids.*

The stability of the complex between the molecules strongly depends from the strength and the number of the interactions involved, because non-covalent interactions are usually regarded as weak, especially in respect to covalent interactions. These kinds of systems are generally formed by components characterized by many sites of recognition to achieve the selective formation of more stable supramolecular aggregates. These aggregates, if stable enough can be considered by chemists as independent molecular species [9] and the interaction sites can be conceptually regarded as the carriers of a molecular information that is intrinsically encoded in the chemical structure of the molecule.[4a] The selective pairing between the nucleotides of DNA is a clear example of the role of the molecular information in the organization of the single components in a hierarchical and functional structure like the double helix that stores the genetic information. (Fig 1.4)

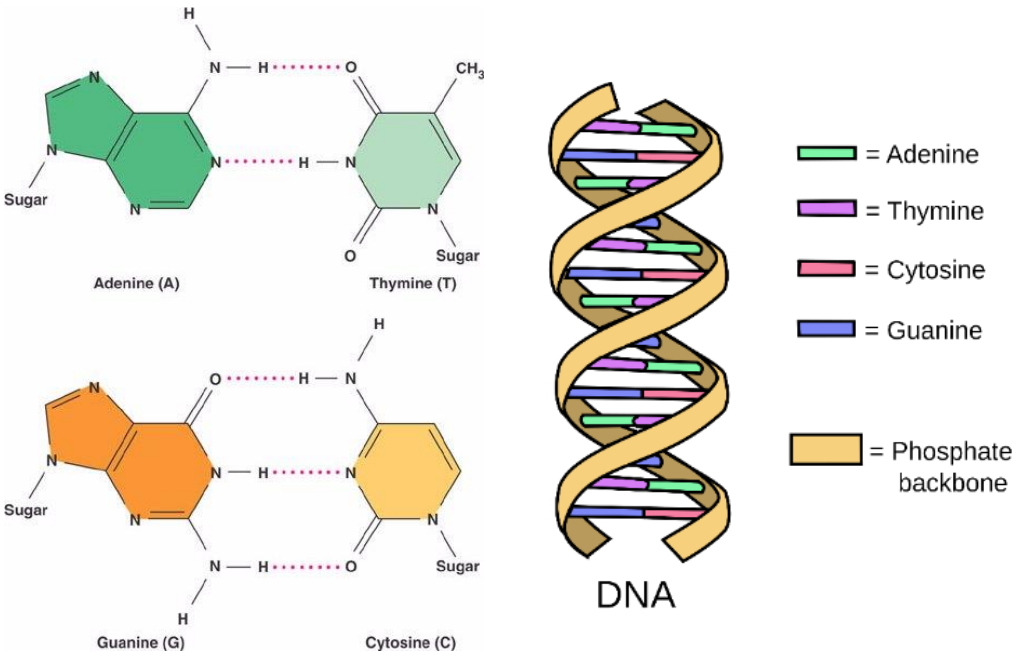

Figure 1.4 *Selective interactions between nucleotides (left) and the resulting double helix structure. (Right)*

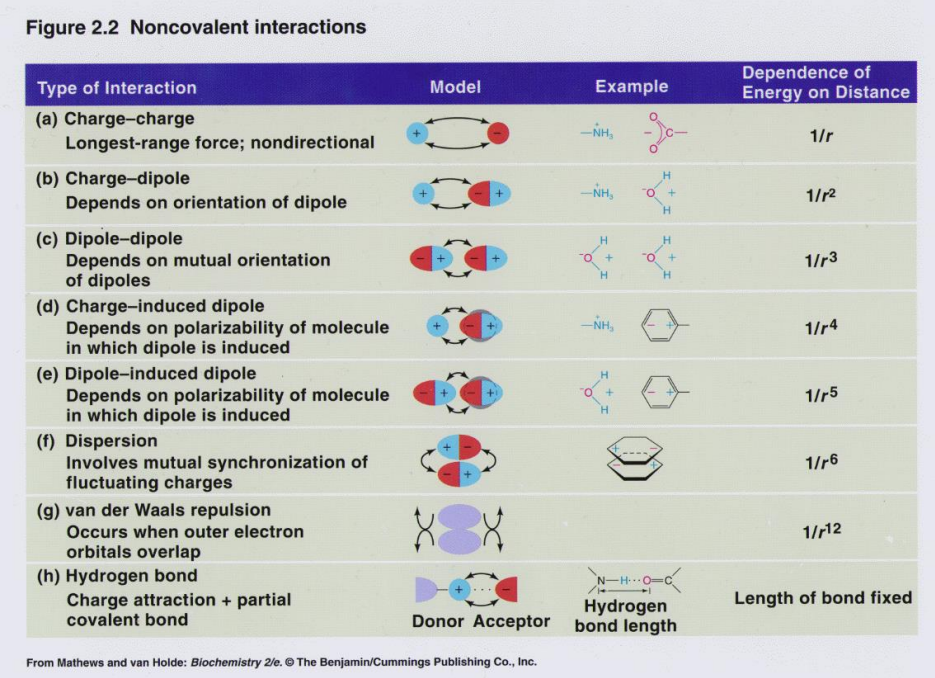

Figure 1.5: *some examples of non-covalent interactions involved in self-assembly.*

From the dawn of supramolecular chemistry, chemists are taking great inspiration from biological systems to design and realize new and synthetic architectures capable of performing complex tasks. To achieve this goal the self-assembling must be directed through the rational design of molecular components, allowing them to spontaneously read the encoded molecular information and organize themselves. There are many kinds of interactions (Figure 1.5) that can be exploited for the realization of the recognition process:

- Electrostatic interactions: involves species with different electronic densities, among them we can find the ionic interaction. Another very important interaction is the hydrogen bond[10] that can be observed between electron rich species (acceptors) and hydrogen atoms (donors) covalently bonded to electron withdrawing groups (EWG). The presence of EWG increases the positive electrostatic potential of the hydrogen atom resulting in a dipole-dipole attraction between the donor and the acceptor. Halogen bond[11] is a similar interaction that takes place between electron rich species and a halogen atom covalently bonded to an electron withdrawing group.
- Van der Waals forces[12]: are forces resulting from the interactions of two or more dipoles that can be permanent or induced by another dipole. These kinds of interactions are generally considered the weakest kind of non-covalent interactions nevertheless plays a crucial role in molecular self-assembly especially when considering multiple interactions. There are different kinds of Van der Waals interaction like the Keesome force (permanent dipole-dipole interactions), the Debye force involving a permanent dipole-induced dipole and the London forces described between induced dipole- induced dipole.

- π - interactions:[13] are interactions caused by the anisotropic distribution of electronic density observed between conjugated or aromatic systems and another molecule. The most important are represented by π -π stacking between two aromatic rings, π-cation interaction, π-metal interaction, π -anion interaction.
- Hydrophobic effects[14]: this term is generally used to describe the tendency of apolar molecules to aggregate in water to minimize the surface in contact with the polar environment of the aqueous media.

All these interactions can give a contribution or can compete with each other in the molecular recognition event.

1.1.2 Host-Guest Chemistry

The natural consequence of the rationalization of the principles of the self-assembly phenomena was the development of a more sophisticated branch of chemistry called Host-Guest chemistry. It mainly focuses on the molecular recognition between molecules with convergent recognition sites (called Hosts) and molecules called Guests, that are characterized by divergent recognition sites. Those two molecules can selectively form inclusion complexes as stated by D.J.Cram in 1960.[15] More in general the term Host-Guest interaction is referred to the peculiar ability of macrocyclic molecules to act with guests in a key-in-the lock[16] fashion with the Guest who is able to occupy the cavity of the macrocyclic partner because of specific non-covalent interactions (Figure 1.6).

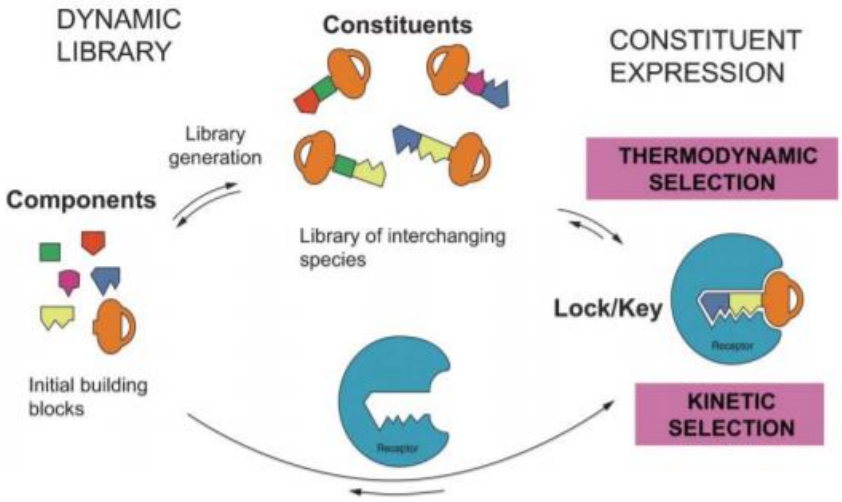

Fig. 1.6 *The key in the lock concept of molecular recognition[16]*

A macrocyclic molecule is a ring-shaped molecule with an inner cavity, and this peculiar geometry allows one to use this cavity as a selective binding site for guests by optimization of the number, strength and distance of interaction. Since the discovery of this kind of compounds, a wide variety of macrocycles have been discovered or synthesised. Among them there are cyclodextrins, cyclic polysaccharidic

molecules composed of 6 or more 1,4-glucopyranoside units, first discovered in 1891 by A. Villers,[17] which are known for their ability to act as host molecules and were extensively studied since the first half of 1900. This behaviour is the result of its 3-D toroidal structure, (Fig 1.7) that is characterized by an outer hydrophilic external surface and a hydrophobic inner cavity that can interact with a wide variety of hydrophobic molecules. The possible guests suitable for this interaction spaces between aliphatic chains, fatty acids, esters, aromatic compounds and many others.

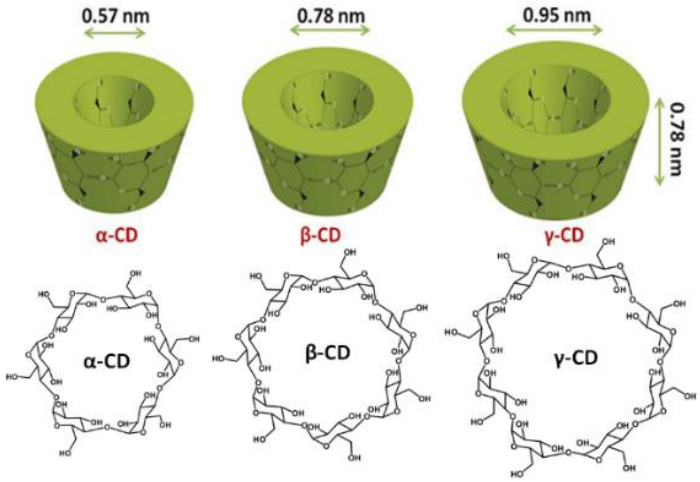

Fig 1.7 *structure of the most common cyclodextrins.*

The formation of the inclusion complex in water is favoured by the decrease in energy of the system due to the release of high enthalpy water molecules present in the cavity of cyclodextrins (CD) when replaced by a more apolar guest. The guest can interact with the inner environment of the macrocycle thanks to lipophilic effects caused by the repulsion between the apolar guest, the cavity, and the polar surrounding aqueous media. By tuning the number of glucopyranoside units it is also possible to control the complexation properties of the cyclodextrins: α-CD (6 glucopyranoside units) shows the ability to host only small hosts like linear aliphatic chains, while γ-CD (8 saccaridic units) can host larger molecules such as steroid molecules. This observation remarks the importance of controlling the relative sizes of the host and guest in order to maximize the interactions between them.[18] Moreover the hydrophilicity of the outer rim can be exploited for the delivery of insoluble molecules in aqueous phase likewise for albumin, a protein present in blood that binds many apolar drugs and carries them in the bloodstream. Moreover, the presence of primary (smaller rim) and secondary (larger rim) hydroxyl groups make this class of molecules especially suitable to chemical modification. These features have already been used in drug delivery applications.[19] In an example reported by Zhao *et al.* γ-CDs were functionalized with linkers in the smaller rim bearing folic acid molecules as pendants. The γ-cyclodextrins were then loaded with Paclitaxel, an antimitotic drug, and p53 gene for a synergic delivery. The folic acid fragment acted as a targeting fragment directed to folate receptors overexpressed by some kinds of cancer cells. Experimental results indicated an increased apoptosis rate in the in vitro tests with cancer cells.[20]

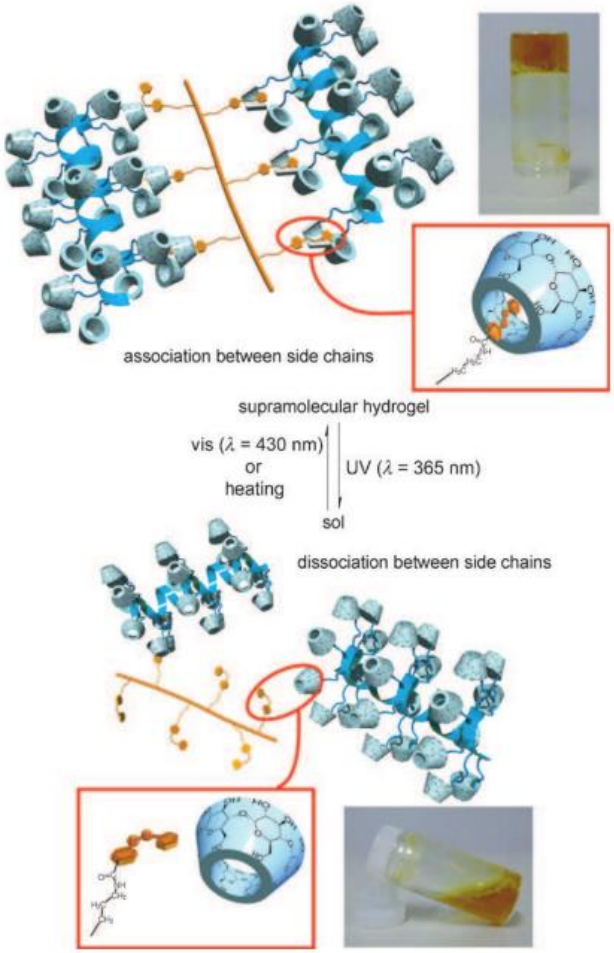

Figure 1.8 *Representation of the molecular events involved in the photo mediated formation/dissociation of the supramolecular hydrogel based on the interactions between CDs and azobenzenes.*[21]

Cyclodextrins were also used for the realization of stimuli responsive materials like in the work reported by Harada et al.[21] in which they covalently bonded *via* click reaction modified α-CDs to 6-azido-curdlan polymer chain (host polymer) and then functionalized poly-(acrylic acid) with light responsive azobenzene moieties (guest polymer). Azobenzene is a well-known photo-switchable molecule that isomerizes from the *trans* to the *cis* isomer upon irradiation with UV light at 365 nm, the process is reversible upon exposure to UV light at 430 nm or to heat. The *trans* isomer can form inclusion complexes with α-cyclodextrin while the *cis* isomer does not bind the CDs cavity. When the two polymers were mixed in a 1:1 ratio a supramolecular hydrogel was formed due to the interactions between the host and the guest polymer that formed non-covalent crosslinks between them. After exposure to UV light at 365 nm the researchers assisted to the dissociation of the polymer chains that resulted in a decrease in the viscosity of the system that led to a solution. After exposure to UV light at 430 nm or by thermal relaxation, the azobenzenes switched back to the trans isomer, reforming the supramolecular crosslinks between the host and the guest polymers to go back to the initial hydrogel

state of the system (Figure 1.8). Thanks to this approach they were able to synthesize a photo-switchable responsive hydrogel that can be interesting for many applications such as drug delivery system and tissue engineering. This work also demonstrates the possibility to choose a guest molecule that can change its affinity towards the host cavity in response to external *stimuli* allowing to control the recognition process between the components of the system thus affecting the macroscopic properties of the system itself. This approach has been widely explored and used to realize other stimuli responsive hydrogels, like redox responsive hydrogel based on the interaction between ferrocene molecules and β-CDs that was used to create a self-healing supramolecular hydrogel.[22]

Many different classes of macrocycles that have been synthesized in the last decades are able to exploit a wide variety of interactions for the recognition of guests. Crown ethers, first discovered in 1967 by Charles Pedersen,[23] are among them one of the most studied class of macrocycles for host guest interactions and are constituted by circular ethylene-oxide oligomers. The presence of many electron rich ethereal oxygen atoms gives to the structure the ability to bind metals cations, electron poor species such as positively charged ammonium groups and many more guests mainly due to the establishment of hydrogen bond interactions as well as electrostatic interactions. These molecules were widely studied as molecular receptors for metal cations in phase transfer catalysis, for the realization of mechanically interlocked molecules, criptands[24] and other supramolecular structures. Many derivatives of this scaffold were realized to finely tune the host properties like dibenzo crown ethers[25] in which the presence of fused phenyl rings also adds the possibility of exploiting π-interactions and azacrown ethers that are derivatives of crown ether in which the oxygens are replaced by nitrogen atoms.

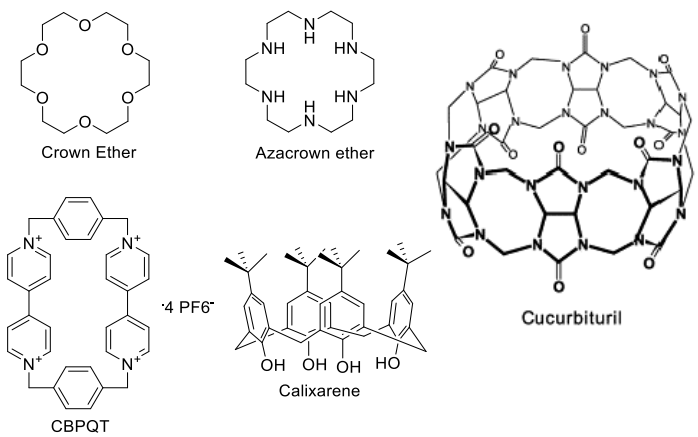

Fig. 1.9 *Some of the most common macrocyclic compounds.*

The use of crown ethers as macrocycles is based on the concept of having an electron rich host and an electron poor guest, this concept has also been reversed by the development of electron poor macrocycles by Stoddart et al.[26] like the cyclobis-(paraquat-*p*-phenylene) ($CBPQT^{4+}$) also known as the Stoddart's blue box. It is characterized by the presence of two electron poor 4-4'-bipyridinium units connected by phenylene bridges. This macrocycle is able to bind electron rich molecules It has been widely studied in many applications, for example it was used for the realization of electrochemically

switchable molecular devices.[27] Other examples of macrocyclic compounds commonly used in host-guest chemistry are calixarenes, pillarenes and cucurbiturils (CBs, Fig 1.9). CBs are pumpkin shaped molecules of cyclic oligomers of glycoluril monomers linked by methylene bridges with very interesting recognition capabilities due to the electron rich portals formed by the carbonyl oxygens of the glycolurilic units that interacts with electron deficient species. The cavity of the macrocycle is characterized by very poor polarizability that is in some case described as "similar to the gas phase" leading to some peculiar effects like the enhancement of fluorescence lifetime of fluorescent molecules included in its cavity.[28] However, the exploitation of its properties, as well as its chemical modification still challenges many research groups mostly because of their poor solubility profile.

1.1.3. Mechanically Interlocked Molecules

The concept of host guest chemistry was then further developed with the idea of kinetically trap guests inside the cavity of macrocyclic molecules. This means that the inclusion complex cannot be separated without breaking any covalent bond while no covalent bond is present between the components, and this can be achieved by mechanically interlocking the molecular components of the inclusion complex by using sterically hindered groups or by exploiting the topology of the complex itself. The two main examples are rotaxanes and catenanes (Figure 1.10). A rotaxane is composed of a macrocyclic molecule with the cavity occupied by a thread shaped molecule with bulky groups present at the extremities, usually called stoppers, that prevents the macrocycle to slip off. A catenane consists of two or more interlocked ring-shaped molecules like in the links of a chain. These kinds of molecules are called Mechanically Interlocked Molecules (MIMs) and were first synthesized by Wasserman[29] and Harrison[30] in 1960 by the cyclization of a long chain diester molecule in presence of a large cycloalkane.

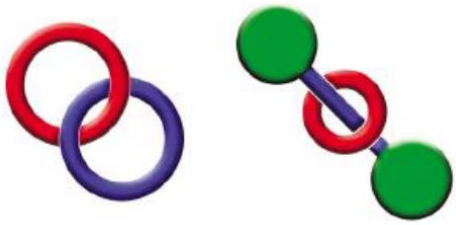

Figure 1.10 *A catenane (left) and a rotaxane (Right).*

The synthesis was however extremely inefficient since it was based on a statistical approach meaning that no or only very poor recognition processes were involved between the components during the formation of the mechanically interlocked assembly. Because of this low yielding and difficult synthetic approach mechanically interlocked molecules were not really considered interesting chemical entities for many years. The situation changed when chemists started to use the principle of the host guest chemistry to direct the formation of the supramolecular complex prior to the interlocking step. The first

example of application of the host guest chemistry to MIMs was reported by Jean-Pierre Sauvage in 1980's when he suggested the use of a metal ion acting as a template by pre-organizing the precursors of the mechanically interlocked molecule in a complex that was then subjected to the interlocking reaction. The first example of this metal template approach regarded the synthesis of a [2]catenane constituted by two diphenolphenantroline molecules and ethylene oxide chains. In this work the ability of the phenanthrolines to form a complex with a 2:1 stoichiometry with copper (I) was exploited. The complex was subsequently reacted in presence of a base, like Cs_2CO_3 with di-iodotetraoxatetradecane chains, in high dilution conditions, necessary to minimize intermolecular reaction and favouring the macrocyclization. With this approach they were able to obtain the target catenane in a remarkable 42% yield, by far the highest yield obtained for interlocked molecules since the discovery of this class of compounds at that time.[31] This first example of template directed synthesis triggered the interest of the scientific community that became more and more interested in the peculiar properties of MIMs. Another important contribution was given to the synthesis of mechanically interlocked molecules by Stoddart and co-workers who described different synthetic approaches based on the threading[32] and stoppering, clipping[33] and slipping[34] concepts (Figure 1.11).

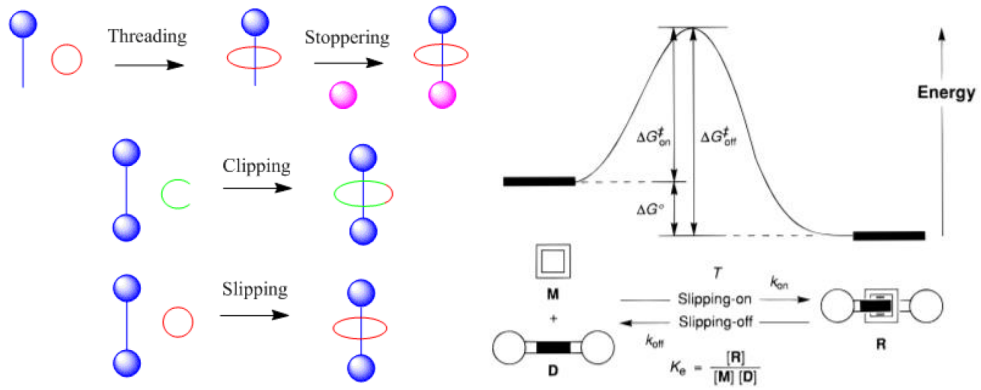

Figure 1.11 *Different synthetic approaches developed by Stoddart et al. (left) and the thermodynamic variations involved in the slipping process.*

Threading and stoppering is realized by mixing the macrocycle and a thread bearing no or only one stopper unit, the two components autonomously assembles in a structure called pseudorotaxane by exploiting host guest interactions between them. The non-stoppered ends of the thread, comprised in the inclusion complex, are then reacted with the stoppers in the appropriate conditions to afford the mechanically interlocked molecule. Clipping on the other hand involves the formation of the rotaxane (or the catenane) by cyclization of a linear precursor of the macrocyclic molecule after the self-assembly with the other components of the MIM. This is one of the most important methods for the synthesis of catenanes, in which the formation of a pseudorotaxane inclusion complex between the linear precursor of the macrocycle and another ring molecule that is then kinetically trapped by the cyclization of the precursor of the ring molecule. Slipping is another approach in which the rotaxane is synthesized starting

from a thread already stoppered at both ends and a macrocycle. If the size of the stoppers and the macrocycle is chosen appropriately, the target rotaxane can be obtained by increasing the thermal energy of the system. Under these conditions a dynamic equilibrium takes place with the macrocycle able to slip over the stoppers. Kinetic trapping is then achieved by cooling and preventing the macrocycle to slip over the stoppers. It's important to remark that the rotaxanes obtained with the slippage approach cannot be formally considered MIMs because they are kinetically stable assemblies only under peculiar conditions and the components can be separated without breaking any covalent bond. [35]

Nowadays many different synthetic approaches have been developed, some of them exceeding 90% yield,[36] making the investigation of this kind of molecules more viable. All of them are still based on supramolecular interactions between the components of the system by using many different recognition patterns. The newly formed structure can be considered an individual chemical entity because the component cannot be separated without breaking one or more covalent bonds. The mechanical interaction between its components can be formally considered a non-covalent interaction commonly called Mechanical Bond.

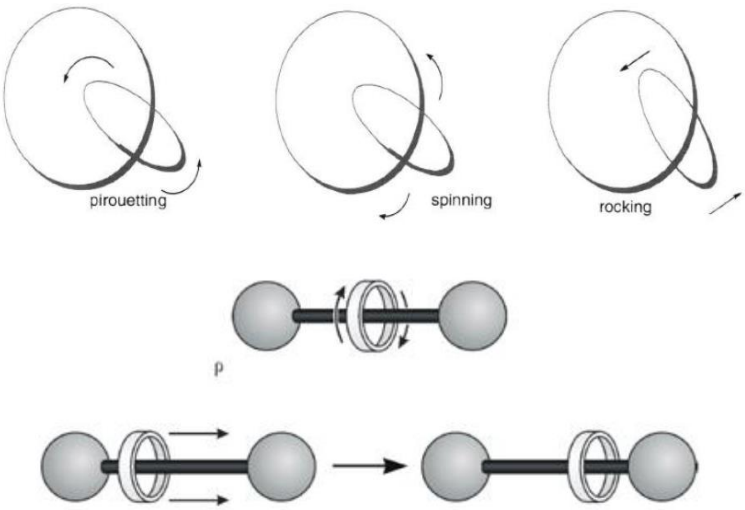

Figure 1.12 *Motions in a catenane (top) and in a rotaxane (bottom).*

The supramolecular complexes held together by this interaction are characterized by properties different from the sum of the properties of the single components: its well known that many properties like solubility, photochemical and optical properties are dramatically affected,[36] mainly due to the topological relationships between the components whose reciprocal movements are restricted by the mechanical interaction. In other words, the properties of these systems depend not only on the nature of the components but also on their relative positions and conformations, called in this context co-conformations. In catenanes the possible motions are: the rotation of one macrocycle on its axis, called *pirouetting*, the translation along the circumference of the other macrocycle, called *circumrotation* (in a homocircuit [2]catenane pirouetting and *circumrotation* are the same movement) and the rocking that consists in the changing of the angles between the planes of the rings. In rotaxanes the possible

movements are the *shuttling*, determined by the movement of the macrocycle from two recognition sites of the thread (if the recognition sites are different this movement is called *switching*) and the *pirouetting* for the rotation of the ring along the axis perpendicular to the plane of the macrocycle (Figure 1.12).
If the components are designed to express a multimodal and tuneable recognition motif, the geometry of the complex, thus the properties of the complex, can be changed by using an external stimulus. This concept is the core of the many examples of molecular machines, motors and switches synthesized in the last 20 years. One of the most famous examples of the application of this concept was reported by Stoddart and co-workers[37] in which they synthesized a [2]catenane constituted by a $CBPQT^{4+}$ and another ring composed of two recognition sites, a dioxynaphtalene (DNP) and a tetrathiafulvalene (TTF) connected by ethylene glycolic chains. The recognition pattern in this system exploits the electrostatic interactions between the electron deficient $CBPQT^{4+}$ and the electron rich DNP-TTF ring, with π-π, charge transfer and dipolar interactions. The TTF has a higher affinity for $CBPQT^{4+}$ compared to DNP and in the ground state co-conformation (GSCC) the CBPQT encircles preferentially the TTF station in a 9:1 ratio. The TTF is a redox active molecule with two reversible oxidation states, to radical cation ($TTF^{+\bullet}$) and to the stable dication (TTF^{2+}), and this electrochemical behaviour allows to modulate the affinity of TTF for $CBPQT^{4+}$. Upon oxidation of TTF to TTF^{2+} the electrostatic repulsion forces the shifting of $CBPQT^{4+}$ to the DNP station that attracts it because of π-π and charge transfer interactions in a push-pull mechanism. This new conformation is characterized by a higher energy compared to the ground state and is called Metastable Co-Conformation (MSCC), that will spontaneously go back to the GSCC after reduction of the TTF unit due to a more favourable free energy of binding (ΔG^{o}) which is 1.6 kcal mol^{-1} lower than of the MSCC state (Figure 1.13). This system has been widely studied for the realization of molecular memory and logic devices for information and communication technologies (ICT).

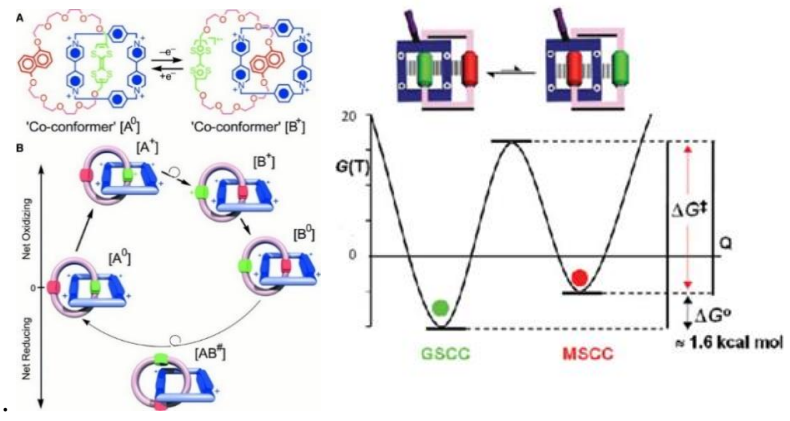

Figure 1.13 *The different Co-conformations of the system (left, A^{0}= GSCC, B^{+}= MSCC) and the energy difference of the two co-conformations (right)*

A very interesting example of altered properties caused by a variation of the relative positions of the components of the supramolecular system was reported by Schalley and co-workers[38] in which the

synthesized a [2]rotaxane based on the crown ether/dialkylammonium recognition motif, in this example they functionalized the crown ether wheel with the redox active TTF unit and a naphthalene unit. The thread was designed to be composed of an anthracene fluorophore unit that also acts as a stopper, the dialkylammonium recognition site next to it and an electron rich secondary station constituted by an isoxazole ring next to the stopper at the opposite end of the anthracene unit. The main interactions in this recognition motif are due to a combination of hydrogen bonding [$O\cdots H_2$-N^+] and π-stacking occurring between the naphthalene unit of the macrocycle and the anthracene stopper. A longer analogue was also synthesized by the insertion of a dodecyl alkyl chain between the ammonium station and the isoxazole (Figure 1.14).

In this system, the proximity of the naphthalene unit present in the wheel act as a quencher of the anthracene's fluorescence that is strongly reduced in the emission spectra of the rotaxane when the crown ether is located on the ammonium station because of energy transfer mechanism taking place between the anthracene stopper and the naphthalene unit of the macrocycle. This effect is due to dipole-dipole interactions between the transition dipoles of the donor and acceptor and the magnitude of this effect strictly depends on the distance between them. The oxidation of the TTF unit to dication (TTF^{2+}) caused the displacement of the wheel from the ammonium station because of electrostatic repulsion between the two positive charged sites to the isoxazole secondary station.

Figure 1.14 *The two rotaxanes described by Schalley et al.,[38] the shorter derivative (left) and the longer derivative (right).*

The displacement of the crown ether was confirmed by ^{1}H-NMR spectroscopy and cyclic voltammetry (CV). However, in the short rotaxane no enhancing of the fluorescence was observed when recording the emission spectra of the oxidized rotaxane because of a still too short distance between the naphthalene unit and the anthracene stopper. In the longer derivative, on the contrary, a dramatic increase in the fluorescent emission peaks of the anthracene was observed, after the oxidation of the TTF unit and the displacement of the macrocycle, confirming therefore the shuttling of the macrocycle to the secondary binding site as shown in Figure 1.15.

These two examples clearly indicate the possibility to modulate the recognition between the components in a MIM in order to change the properties of the system, and this principle was further expanded by the introduction of the concept of molecular machines.

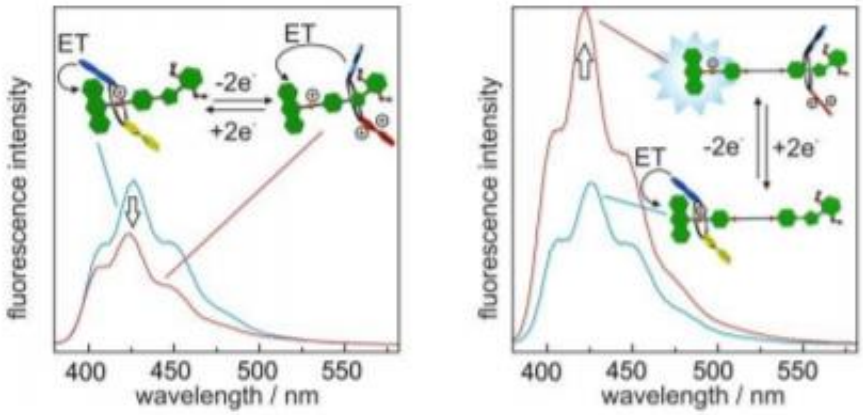

Figure 1.15 *Emission spectra of the rotaxanes in the two electrochemically controlled co-conformations. The shorter derivative (left) and the longer derivative (right).*

1.1.4 Molecular Machines

Right after the understanding and further development of the principles of host guest chemistry and their applications to MIMs systems, it was clear that in principle one could use this approach to mimic the macroscale world at the nanoscale level. By the design and the synthesis of systems capable to act as molecular engines, capable of transforming energy into mechanical work, or molecular machines able to couple the energy transforming abilities of molecular motors to a second mechanism which performs a specific function, it is conceptually possible to create systems that work in analogy with the tools we use in everyday life.

The basic requirements to build molecular machines can be summarized in few components:

- A component capable of harvesting and transforming energy from the surrounding environment, like the plug/wire/transformer assembly in an electrical device and transfer it to the next part of the mechanism.
- The motor, or engine, that absorbs this energy and transforms it into mechanical work.
- The functional unit which uses the mechanical work of the motor for a specific purpose like the wheels of a car.

Of course, the realization of such a complex system at a molecular scale is challenging and the system must meet some specific requirements. Nature of course offers us the possibility to observe such kind of mechanisms and to analyse them, to understand what are the key features that a supramolecular system needs in order to exhibit a functional property. One of the most used analogies between molecular machines and biological systems is the example of the ATP synthase enzyme[39] that exploits a rotational motion of the rotor subunit to catalyse the phosphorylation of adenosine diphosphate (ADP) to give adenosine triphosphate (ATP) which is the chemical energy transporter used for the metabolic processes in living organisms. The ATP is produced by the exploitation of a proton gradient between the two sides of mitochondria's membranes that generates a rotation enabling the uptake of ADP+P_i and

the release of ATP.[40] This ATP can be then used by other systems like the actin-myosin system present in muscle cells and responsible of their contraction.[41] This is a perfect example of how nature has built extremely sophisticated and integrated mechanism to transform energy into other forms of energy, i.e. the electric signals that are generated in the nervous system's cells, caused by the selective opening and closing of metabotropic or ionotropic ion-channel proteins in their membranes, capable to control the electric gradient across it. This gradient results in an electric field that propagates along the nervous system cells until it reaches a functional unit that, triggered by the signal, starts to exhibit its functions. After this event, other proteic ion channels present in the membrane act as pumps to remove the ions from the inside of the cell against a concentration gradient, by ATP consumption, in order to allow the system to return in its initial state.[42] The observation of these systems helped scientists to understand the basic requirements that a functional system must meet:

- The energy source must be readily available to the harvesting unit, and it must be readily transformed and transmitted to the other components of the machine. Energy sources as photons or electrons that causes photochemical and electrochemical reactions respectively, are very good candidates because of their usually fast kinetics. Another important aspect is that electrochemical and photochemical reactions usually generates no side products while chemical fuels, and its degradation products, are usually accumulated in the system. This means that to obtain a functional system also a waste recycling/disposal system must be added to allow continuous cycling. A clear example can be seen in the removal of the CO_2 by the lungs during expiration. Actually, an accumulation of side products can inhibit the system from working.
- The sequential movements of the system must be precisely calibrated in order to avoid energy dispersions that decrease the efficiency of the system. This can be achieved by designing molecules with appropriate patterns of non-covalent interactions. Host guest chemistry has proven to be an extremely useful tool to achieve the spatial and energetic requirements.
- The system must be able to spontaneously go back to the initial state spontaneously of after the application of different stimuli. This is a crucial feature to allow the system to perform multiple cycles.
- The energetic variations of the system and their timescale, expressed in the sequential molecular events of the cycle, must be precisely considered, as a mismatch can lead to an inability of the system to complete a full cycle.
- The possibility to monitor the physical/chemical properties of the system strictly depends on the availability of analytical techniques that are able to detect the involved phenomena and has to operate in a comparable timescale.

Nowadays, we're still quite far away to achieve the complexity and efficiency of biological systems but in literature can be found many examples of application of the above-mentioned concepts.

The exploitation of light as a stimulus for the activation of molecular motors was for example described by Balzani *et al.*[43] in a [2]rotaxane consisting, in this order, of a dumbbell stoppered on one side by a

ruthenium (II) tris (2,2'-bypiridine) ($[Ru(bpy)_3]^{2+}$, P^{2+}), a *p*-terphenyl spacer, a 2,2'-dimethyl-4,4'-(bipyridinium) unit (A_2^{2+}) as secondary station, a 4-4'-bipyridinium unit (A_1^{2+}) as primary station and then another stopper. The A_1^{2+} has a higher binding affinity than A_2^{2+} for the macrocycle which is an electron rich dibenzo-34-crown-10 ether and interacts with the electron poor bipyridinium units of the dumbbell via charge transfer interactions and π-π stacking interactions. The working cycle of this system was described by the authors as they were able to observe four main events involved: A) the absorption in which the P^{2+} unit acts as a photosensitizer, by absorbing the visible light (λ_{max}= 458 nm) to generate a long lived excited state ($*P^{2+}$) with a strong reducing behaviour capable to selectively transfer an electron to the primary station reducing it to radical cation ($A_1^{2+} \rightarrow A_1^{\bullet+}$), B) the displacement of the macrocycle caused by the reduced state of the primary station that has a lower binding affinity for the macrocycle which is forced to move to the A_2^{2+} secondary station, C) a back-electron transfer (BET) between $A_1^{\bullet+}$ and P^{3+} restores the initial oxidation state of the components, D) the ring can shuttle back to its thermodynamically favoured station (Figure 1.16).

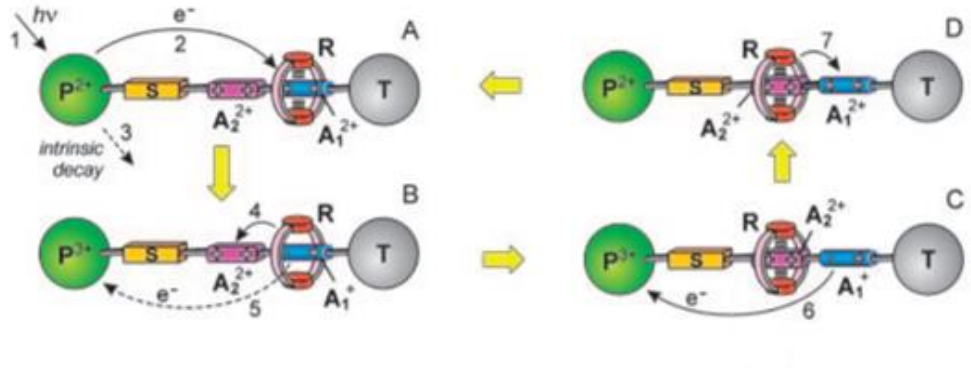

Figure 1.16 *Schematic representation of the steps of the cycle.*[43]

During these events no side product is generated, and this system has proven to be stable for more than 10^3 cycles. However, the kinetic and energetic requirements for the sequential the steps of the cycle allowed to achieve only a quantum yield of 2% in terms of shuttling of the macrocycle. This low yield is imputable to the competition between the BET and the migration of the ring. The authors repeated the same experiments in presence of phenothiazine (ptz) that acted as a negative kinetic modulator by intercepting the P^{3+} generated after the electron transfer and reducing it back to P^{2+} generating ptz^{2+}. The BET is therefore inhibited, and the electronic reset can happen only by reduction of ptz^{2+} by A_1^{+}. The back-electron transfer rate was then reduced by two or three order of magnitude and the yield, in terms of shuttling was increased to 12%. The system was finely tuned to allow the system to complete and repeat full cycles despite the competition of the many other processes involved, like the competition between the photoinduced electron transfer to the A_1^{2+} station, with the spontaneous decay of $*P^{2+}$ and the excitation of the secondary station A_2^{2+}. In Figure 1.17 are summarized the thermodynamic variations involved during the cycle.

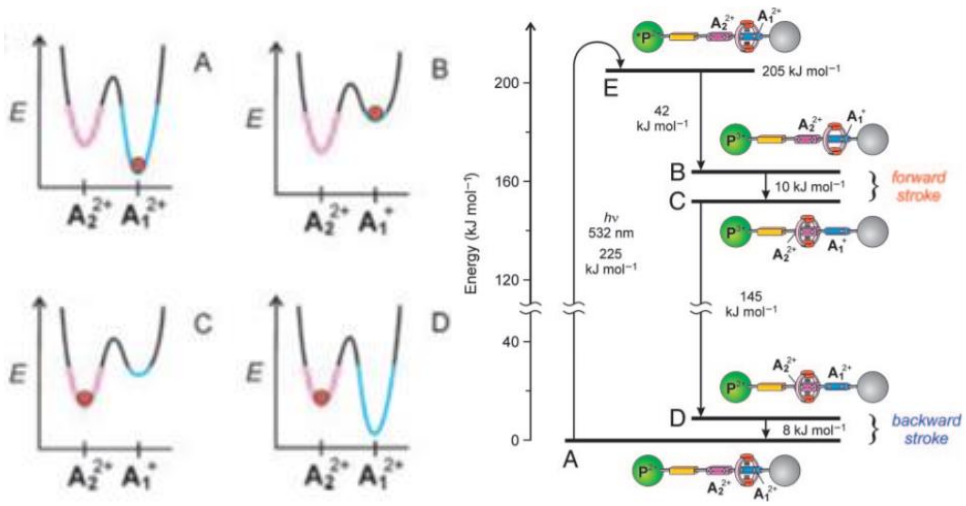

Figure 1.17 *Schematic representation of the energy variation involved in the shuttling (left) and of the energetic variations involved in the complete cycle (right).*[43]

Among the molecular machines operating by chemical fuel, one of the first examples is the [2]-rotaxane developed by Stoddart and co-workers and constituted by a dibenzo-24-crown-8 ether (DB24C8) as macrocycle and a thread composed of a dialkylammonium station (NH_2^+) and a bipyridinium station (Bpy^{2+}) (Figure 1.18).[44] This recognition motif is widely known and exploited since its discovery in 1967 by Pedersen et al.[23] who discovered the ability of this class of macrocycles to form inclusion complexes with metal and organic cations like secondary ammonium groups mainly due to [N^+-H---O] and [C-H---O] hydrogen bonds. These interactions are stronger compared to the ion-dipole interactions involved between the macrocycle and the bipyridinium unit and for this reason in the rotaxane the macrocycle is mainly located on the di-alkylammonium station due to its higher binding affinity.

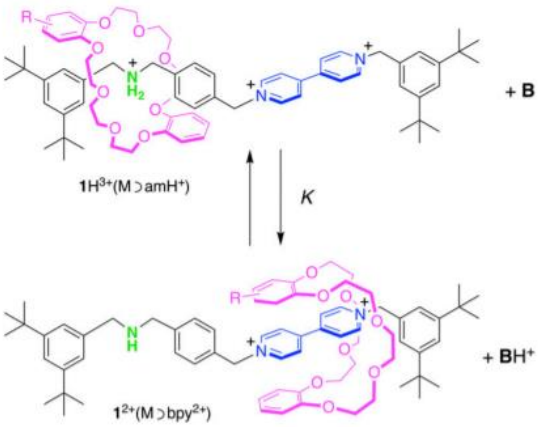

Figure 1.18 *The rotaxane reported by Stoddart et.al.*[44]

When the ammonium station is deprotonated, the electrostatic repulsion between the lone pair of the dialkylamine unit forces the macrocycle to shuttle on the bipyridinium unit. Deprotonation of the encircled dialkylammonium station is not an easy task since the stabilization of the protonated amine by

the non-covalent interactions results in an enhanced basic character of the nitrogen, for this reason excess of base or very strong bases has to be used (i.e. phosphazenes and di-isopropylethylamine). By protonating again the amine unit with trifluoroacetic acid (TFA), the macrocycle shuttles back to its original position. This cycle can be repeated many times but after each cycle the increasing amounts of side products due to the sequential addition of acid and base affects the cycling ability of the system. However, despite the problem linked to the presence of increasing amounts of reactants, a recent investigation of this system by Credi, Lucarini *et. al.* highlighted that the secondary station can be used for the modulation of the basicity of the dialkyl ammonium station. The variation of the oxidation state of the bipyridinium unit, that can be electrochemically reduced to radical cation ($Bpy^{+\bullet}$) or diradical ($Bpy^{\bullet\bullet}$) leads to a decreased affinity for the binding with DB24C8 due to weakening of the charge transfer interactions in this order: $Bpy^{2+} > Bpy^{+\bullet} > Bpy^{\bullet\bullet}$. The ability of the macrocycle to shuttle to the secondary station is therefore affected, with DB24C8 less prone to leave the ammonium site, resulting in a more difficult deprotonation due to a co-conformational allosteric effect, with a 7 units pK_a enhancement of the basicity of the ammonium site of $Bpy^{\bullet\bullet}$ if compared to Bpy^{2+} (Figure 1.19).[45]

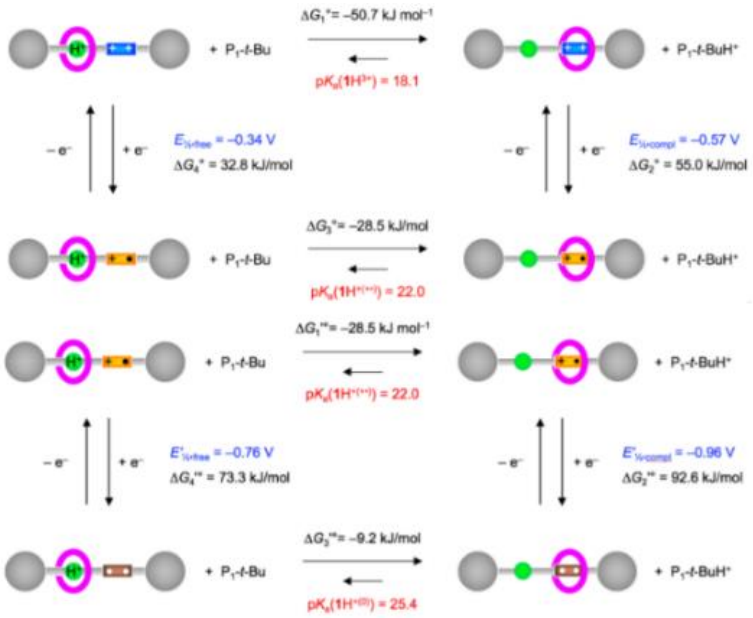

Figure 1.19 *The modulation of the pK_a of the ammonium station by electrochemical variation of the Bpy oxidation states.*[45]

The exploitation of a chemical fuel was further improved by using a molecule that acts both as positive and negative stimuli as reported by Di Stefano and co-workers,[46] in which they synthesized a Sauvage-like [2]catenane bearing a phenanthroline unit on each ring. The catenane, in solution, does not have a precisely defined co-conformation but, if cations are added, it assumes a cross like conformation in which the two phenanthrolines are close together and interacts with the positively charged guest (Figure 1.20). The situation can be reversed by removing the positively charged guest from the cavity generated by the two phenanthrolines.

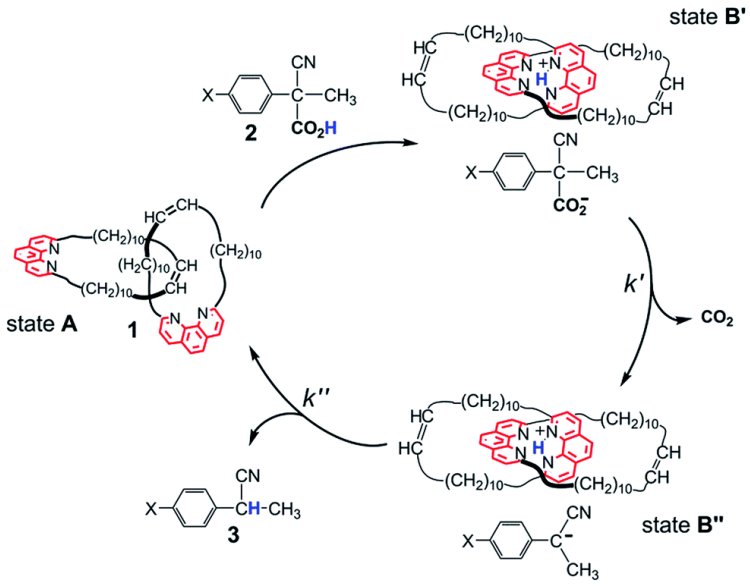

Figure 1.20 *The scheme of the switching cycle in the system developed by Di Stefano et al.*[46]

The use of 2-phenyl-2-cyanopropanoic acid as a source of protons is crucial because of its peculiar behaviour: deprotonation of the carboxylic acid by the phenanthrolines acting as bases, leads to an anion that smoothly undergoes to decarboxylation by releasing CO_2. After decarboxylation, the fuel anion removes the proton from the complex, in a rate determining step that restores the initial state of the catenane with formation of 2-phenyl-propanonitrile as side product (Figure 1.20).

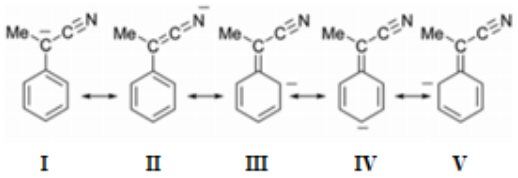

Figure 1.21 *The resonance structures of 1-cyano-1-phenyl ethanide.*[46]

By variation of the substituents present in the phenyl ring of the 2-phenyl-2-cyanopropanoic acid they were able to modulate the rate of switching between the two co-conformers and the time required to complete a full cycle. The efficiency of the fuels in terms of catenane rate motions are as follow: Cl > H > CH_3 > OCH_3. The electron withdrawing chlorine substituent enhanced the basicity of the anionic component by increasing the weight of the resonance structure I of the anion (Figure 1.21) in which the negative charges are located on the benzylic carbon, leading to a faster proton transfer between the protonated catenane and the anion and a shorter time to complete the cycle. The opposite effect is shown by electron donating groups like the methoxy group, in this case the negative charge is mainly located on the nitrogen of the cyano group (resonance structure II) and the rate of proton transfer is slower. The methoxy group required 2 days to complete a cycle while with chlorine cycle lasted few minutes.

Unfortunately, if an excess of the fuel is added to the system, such excess fuel is wasted since the anionic intermediate will take back the proton from this species that is a stronger acid than the protonated catenane. The latter will remain in the protonated state until the excess fuel is present.

To overcome this limitation, they also reported the exploitation of a protecting group for carboxylic acids, the 3,5'-dimethoxy benzoin (DMB), used to preserve the fuel molecule as a pre-fuel. DMB group can be cleaved photochemically with irradiation of UV light at 335 nm. With this process they were able to add an excess of the pre-fuel (10 eq.) respect to the [2]catenane, to control the release of the fuel upon photoirradiation intervals, and to achieve multiple cycles. The efficiency of the fuel, in terms of percentage of catenane molecules adopting the protonated conformation, strictly depended on the irradiation time, with yields comprised between 25% for 60 s, 42% for 120s and 60% for 180 s for the first cycle. The yield of the following cycles was however reduced proportionally to the irradiation time, i.e. a sample irradiated for 300s had a first cycle yield of 70% but the second cycle was characterized by a drop to 35% yield, limiting therefore the number of cycles. Despite this drawback this is a proof of concept of the exploitation of a photochemically controlled chemical fuel able to operate alternatively as positive and negative stimuli whose reactivity can be controlled by functionalization in para position.[46]

Thanks to these advancements and a deeper understanding of the principles governing the chemistry of molecular machines, the grade of complexity and efficiency that characterize these systems is growing at an unprecedented rate, also thanks to the increasing interest in this field expressed by the scientific community. Nevertheless, one of the biggest challenges of this research field is still intriguing scientists regards the transfer of the nanoscale properties expressed by molecular machines to the macroscopic level. One of the main examples was shown by the work of Stoddart et al. based on the [3]rotaxane version (Figure 1.22, left) of the [2]catenane depicted in Figure 1.13. It is composed by two $CBPQT^{4+}$ electron acceptor macrocycles and an electron donor palindromic dumbbell with two TTF stations near the stoppers and two internal DNP stations linked by ethylene glycolic chains, these two fragments were linked by a rigid spacer. Like in the catenane described above, in the GSCC the $CBPQT^{4+}$ encircles the TTF stations, and the distance between them has been reported to be about 4.2 nm (extended conformation) while upon chemical oxidation of the TTF unit to TTF^{2+} and switching to the MSCC, the distance of the two macrocycles encircling the DNP unit was about 1.4 nm (contracted conformation). The subsequent injection of ascorbic acid in the system restored the initial state by reduction of the TTF units followed by migration of the macrocycle on this station because of its higher affinity compared to the DNP station.

The synchronous motion of the two rings resembles the motion of the sarcomere structure that allows muscular contraction even if it happens on a shorter distance. On the basis of this similarity they functionalized the two $CBPQT^{4+}$ with chains containing a disulphide groups at the extremities. This chemical modification allowed the grafting of the rotaxanes on the gold surface of the beams of an array of microcantilevers. The obtained self-assembled monolayer (SAM) consisted of about 6 billion

molecules oriented randomly. By chemical oxidation with an aqueous solution of $Fe(ClO_4)_3$, the switching to the contracted conformations of the rotaxanes of the monolayer resulted in the vertical bending of the edges of the beams of about 35 nm and the reduction with ascorbic acid restored the initial state (Figure 1.22). They were also able to switch the system electrochemically and to perform up to 25 cycles but with a decreasing trend in the amplitude of the sequential bending movements attributable to a chemical or physical degradation of the SAM.[47] The evidence of the cooperation of single molecules, even in a disordered SAM, represented a crucial step in the development of Molecular Machines.

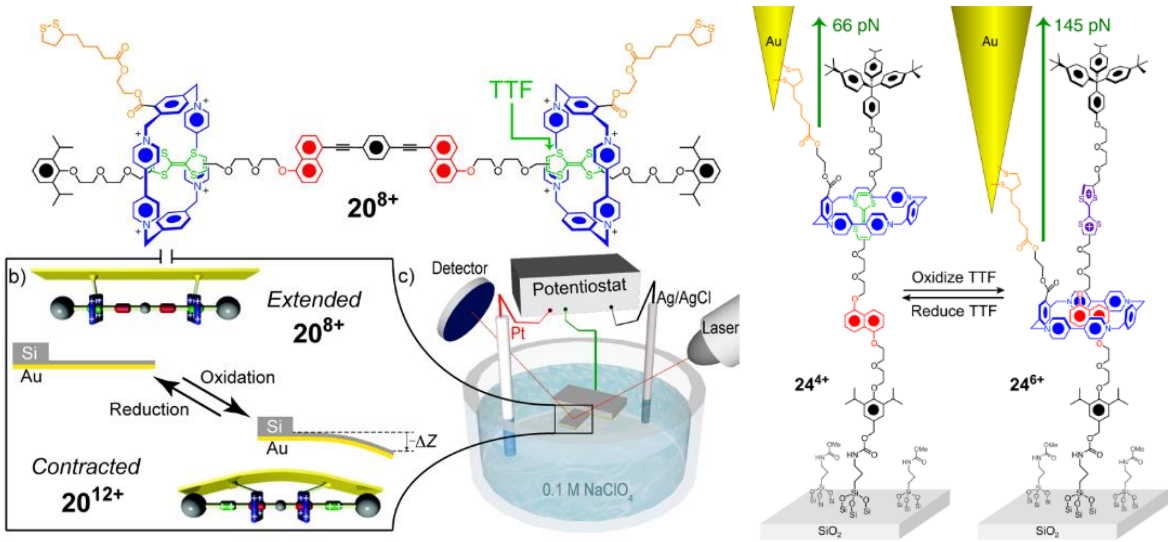

Figure 1.22 *The rotaxane powered device described by Stoddart et al.(left) and the system for the force measurements of a single [2]rotaxane on a AFM tip (right).*[47, 48]

The same research group also reported an analogous [2]rotaxane analogous that was tethered between to the tip of a gold atomic force microscope (AFM) cantilever and a silica support. This allowed the group to measure the force of switching of a single rotaxane upon electrochemical oxidation by using the tip as a dynamometer. The variation corresponded to 79 pN between the GSCC and the MSCC which is a very high value for a single molecule[48] (Figure 1.22). By retraction of the AFM they were also able to measure the force needed to make the ring slip from the stopper unit. All these examples were intentionally chosen to show how rational design and the application of the principles of host guest chemistry have been used to overcome the challenges posed by the synthesis of artificial molecular systems based on the MIMs in the last decades, and as Richard Feynman once said: "*What would be the utility of such machines? Who knows? I cannot see exactly what would happen, but I can hardly doubt that when we have some control of the arrangements of things on a molecular scale we will get an enormously greater range of possible properties that substances can have, and of the different things we can do*".[49]

1.2 Electron Paramagnetic Resonance Spectroscopy (EPR)

Electron Paramagnetic Resonance spectroscopy (EPR) is a magnetic resonance technique, similar to NMR that works with magnetic fields and frequencies that can interact only with the unpaired electrons of paramagnetic species.

This spectroscopic technique has been developed in the first half of the 20th century since the discovery, by Stern and Gerlach in 1921, that a beam of silver atoms passing through a magnetic field was split in two lines resulting in an accumulation in discrete points on the receiving screen rather than a continuous distribution.[50] This first observation led to the introduction in 1925 by Uhlenbeck and Goudsmith, of the concept of spin as an intrinsic property of the electron.[51] Three years later, in 1928 Dirac derived his quantum mechanics theory in which the relativistic interpretation of the electron spin was an essential part. [52] The first EPR spectroscopy experiment was made by E.K. Zavoisky by recording the EPR spectra of $CuCl_2 \cdot 2H_2O$ in 1944.[53]

The rotation of the electron on its axis, with an intrinsic angular momentum is called "Spin" $\vec{S}$, and because the electron is a negatively charged particle this rotation generates a magnetic field giving rise to and electronic magnetic moment $\vec{\mu}$. The electron can be considered as a spinning bar magnet or a dipole. These "spinning magnets" are randomly oriented but when exposed to an external magnetic field (B_0), because of the Zeeman effect (Figure 1.23), a quantization of the energetic levels of the electron spin orientation is observed, with an energy difference (ΔE) corresponding to:

$$\Delta E = g \cdot \mu_B \cdot B_0$$

Where g is a dimensionless proportionality constant that strictly depends on the magnetic moment and the gyromagnetic ratio of the electron, μ_B is the Bohr magneton and B_0 is the value of the applied external magnetic field. The number of different spin states depends on the quantum number *I* that gives the number of possible spin states (N) corresponding to:

$$N = 2nI + 1$$

The electron has I = 1/2 and the possible spin states are +1/2 (parallel to B_0) and –1/2 (antiparallel to B_0). The difference in population between the two spin states is about 10^{-3}, maintained by the relaxation phenomena and when a radiation of the appropriate wavelength is applied, under these premises, the population of the two states can be changed. The interacting frequency is absorbed by the electrons in the lowest energy spin state to populate the high energy spin state. By measuring the absorbed energy of the transition, it is possible to obtain a signal characteristic of the investigated system. The EPR spectrum of the free electron is consists of a single absorption line with the maximum absorption centred

at a *g* value 2.002319 [54] and can be represented as a gaussian curve but due to technical reasons it is represented as first derivative.

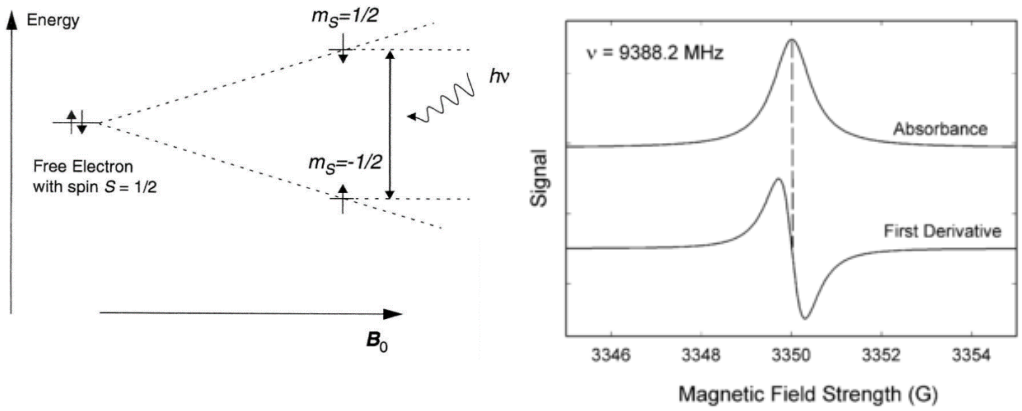

Fig. 1.23 *The electron Zeeman Effect (left) and the EPR spectra of the free electron (right).*

The CW-EPR experimental setup is composed by a microwave (MW) frequency source, generally working in the X-band corresponding to about 10 GHz, a resonating cavity linked to a receiver and an electromagnet, and it works by transmitting a constant microwave frequency and at the same time sweeping the intensity of the magnetic field. The detector measures the decrease in intensity of the frequency reflected from the cavity (Figure 1.24). The measurement is not made directly on the frequency irradiated from the MW source, but the sample is irradiated with a second sinusoidal frequency, called modulation frequency that allows to obtain a narrower and stronger signal. The use of this modulation results in an experimental spectrum represented in the first derivative, allowing also to observe the hyperfine structure of the signal. For this reason, to calculate the number of spin present in the sample, the double integral of the signal has to be evaluated.

This experimental setup is characterized by a high sensitivity, the instrument can detect paramagnetic species in concentration of about 10^{-7}M. The timescale of the analysis, due to the fast relaxation of the electrons, is in the sub microsecond range and this allows one to obtain many useful information on the fast-dynamic equilibria, i.e. the association dissociation process in the formation of an inclusion complex, that characterizes many supramolecular systems. Such information are not always accessible with other techniques, like NMR spectroscopy due to the nature of the physical phenomena it detects, the relaxation of the nuclear spin is much slower compared to the relaxation of the unpaired electron The experimental NMR spectra, obtained by the investigation of fast equilibria usually yields signals that are time mediated averages that makes the accurate measurements of the investigated equilibria more challenging.[55] The analysis of the EPR spectra can provide many useful information about the investigated system by the measurement of the characteristic parameters like the g-value, the hyperfine splitting constant and the line width.

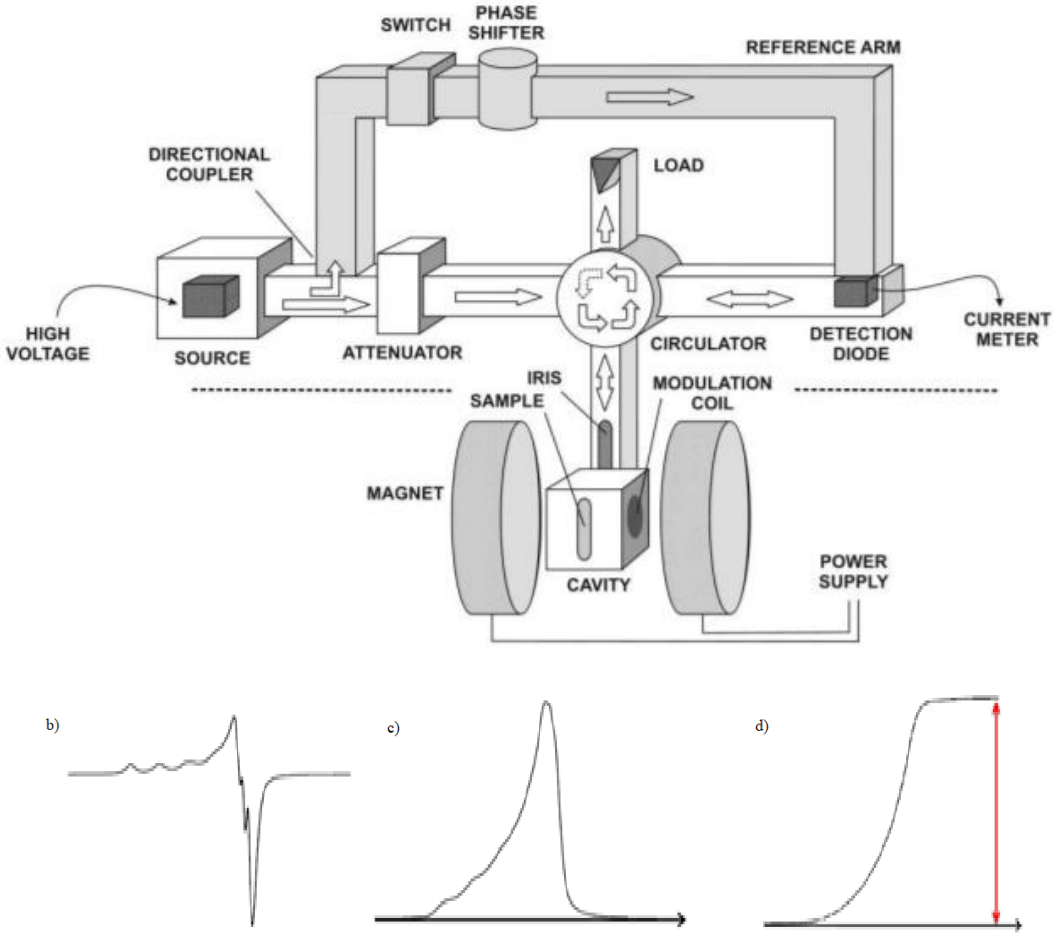

Fig. 1.24 *Schematic representation of a CW-EPR spectrometer (top), b) the spectra recorded by the EPR instrument in first derivative, c) absorption curve (first integral) d) second integral.*

1.2.1 Relevant parameters in an EPR spectra:

Except the case of the free electron, electrons occupy the orbitals of the atoms they belong to, and orbitals occupied by the unpaired electrons are called Single Occupied Molecular Orbital (SOMO). Because the electron occupies an orbital, in addition to its spin angular momentum, the total spin angular momentum of the system is slightly increased due to the interaction of the spin angular momentum of the electron and the orbital. This interaction is called spin orbit coupling and means that the value of magnetic field for the resonance of the electron (at a given excitation frequency) is slightly different from the value of the free electron. This value is usually expressed in Gauss (G) and is obtained by measuring the value of the field at the centre of the curve. The deviation from the field value of the free electron strictly depends on the nature of the atom occupied by the unpaired electron and the deviation is usually small for organic radicals, among them it is smaller for σ systems, larger for π systems and for systems containing heteroatoms. In paramagnetic metals the variation is usually very large. In Figure 1.25 are reported some values for known organic radicals.

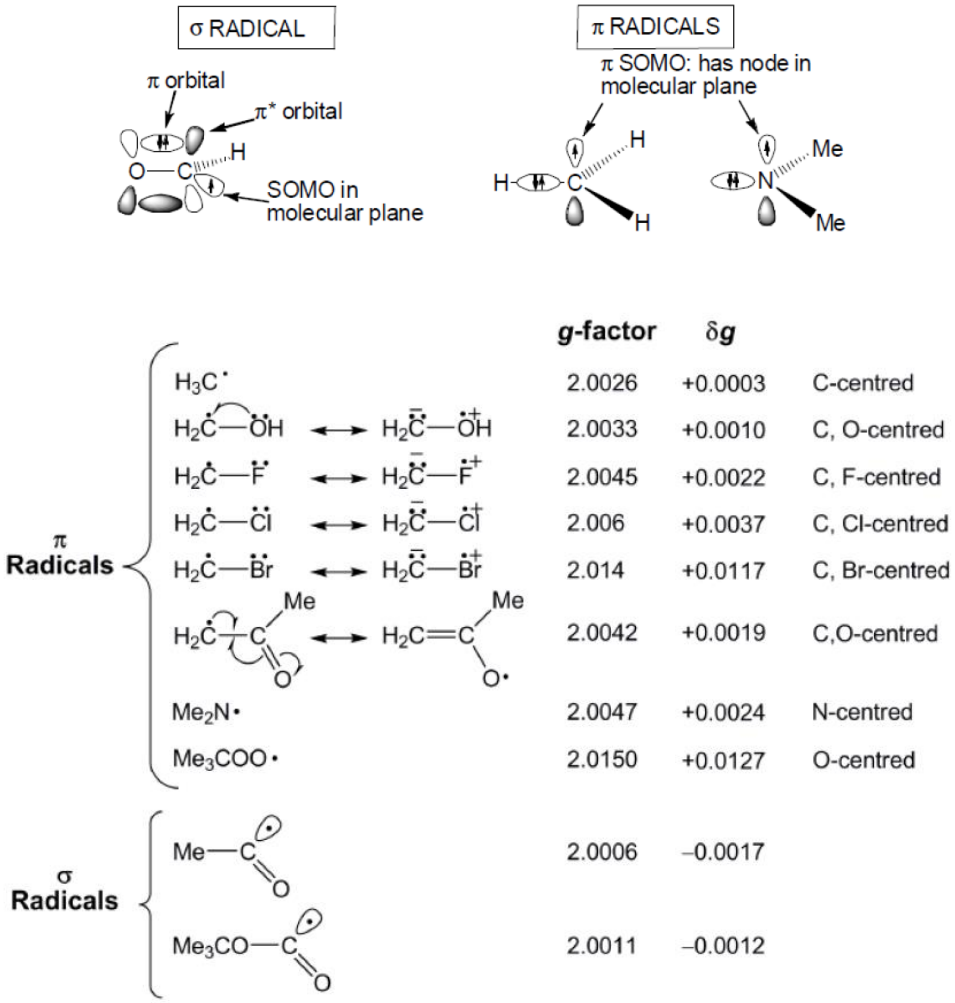

Figure 1.25 *Electronic configuration in σ based radicals (top left) and π based radicals (top right) and g values for some organic radicals (bottom).*

When the unpaired electron is located on an atom with spin ≠ 0 like ^{1}H, ^{13}C, ^{14}N, ^{31}P, etc. the magnetic moments of the electron and of the nuclei influence each other resulting in a splitting of the spectral lines, called hyperfine splitting, with a line separation determined by the value of the *hyperfine splitting constant* (*a*). Conceptually it is similar to the splitting of the lines in NMR spectroscopy determined by the coupling constant called *J*. The number of lines, resulting from the splitting of the signal depends from the equation:

$$(2nI_{tot,1} + 1)(2nI_{tot}, 2+ 1)(2nI_{tot}, 3+ 1)\ldots\ldots\ldots (2I_{tot}, k+ 1)$$

Where *I* is the spin quantum number, n the number of equivalent nuclei with the same *I*. The relative intensities of the split peaks follows the rule of Tartaglia's triangle as in NMR spectroscopy. The simplest example of the hyperfine splitting constant can be observed in the spectra of the hydrogen radical ($H^{\bullet}$), hydrogen has spin ½ as well as the electron, by application of the above-mentioned

equation the resulting lines are two, due to the contribution of the hydrogen atom in the splitting of the energy of the possible spin states of the molecule.

Similarly, if an unpaired electron interacts with a ^{14}N atom who has I=1 the experimental spectra will be characterized by 3 lines, separated by the value of the nitrogen hyperfine splitting constant, a_N. (Figure 1.26).

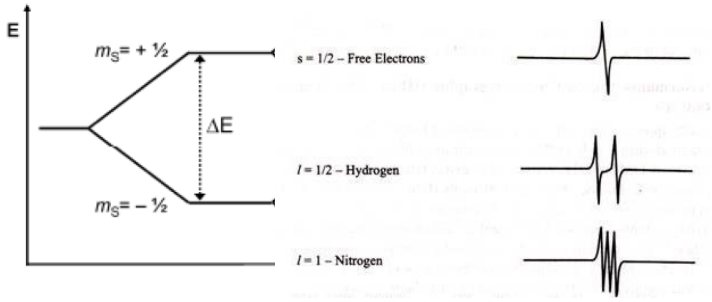

Figure 1.26 *Energy separation of the interaction of two interacting spin with I= ½ (left), experimental spectra of various spin systems (right).*

Similarly, the presence of many magnetic nuclei coupled with the unpaired electron will give rise to more complex spectra: the coupling with one nuclei with I=1 and one with I= ½ like ^{14}N and ^{1}H, respectively, will give rise to a signal composed of 6 spectral lines, as reported by the diagram in Figure 1.27 (in this case with $a_N > a_H$).

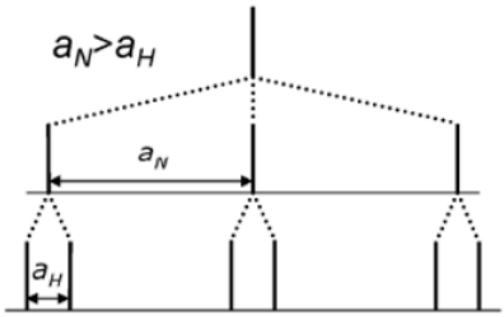

Figure 1.27 *Diagram for the coupling between the unpaired electron and one nucleus with I=1 and a second nucleus with I= ½ with $a_N > a_H$.*

The value of the hyperfine splitting constant of the unpaired electron with the coupled nucleus is related to the nature of the SOMO orbital: orbitals with a prevalent *s*-character give rise to strong coupling (*i.e.*132G for the formyl radical) while *p*-based orbitals are characterized by smaller *a* values, like for the methyl radical in which a node is present at the nucleus that disrupts the spin interaction between the unpaired electron and the hydrogen atom. So, in principle, there would be no mechanism for the interaction to occur. However, in the methyl radical, hyperfine splitting is actually detected. This

observation can be explained in terms of the spin polarization effect: the most important and stable electronic configuration of the methyl radical is the one in which the electron of the hydrogen atom involved in the bond with the carbon's sp^2 orbital, and the unpaired electron, located on the p orbital of the carbon atom have opposite sign. This spin orientation determines a net unpaired negative spin density in the *s* orbital of the proton that generates a hyperfine splitting constant with a negative sign, thus giving rise to a signal constituted by a quartet with 1:3:3:1 intensity pattern (Figure 1.28). This spin polarization effect is described by the McConnell equation[56]:

$$a = Q\,\rho$$

that describes the proportional dependence of the hyperfine splitting constant a, with the spin density ρ or, in other words, the probability of the unpaired electron to be located on a particular atom and Q is an empirical constant.

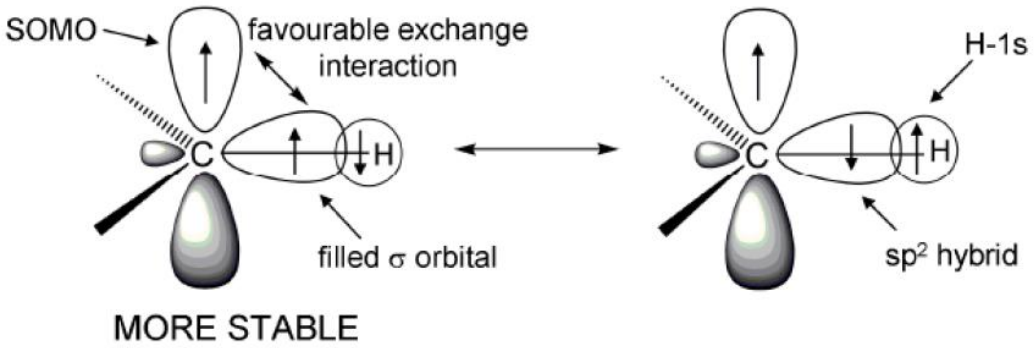

Figure 1.28 *Electronic configuration in the methyl radical.*

This splitting can also be observed between the unpaired radical and distant nuclei, like in the case of conjugate systems in which the various resonance forms are characterized by the delocalization of the unpaired electron on different nuclei. For example, the naphthalene radical shows an EPR spectra characterized by 25 lines (Figure 1.29).

Another parameter to evaluate in the EPR spectra is the line width, strongly depending on the relaxation time of the unpaired electron. The unpaired electron has a relaxation time ca. 10^6 times faster than the relaxation of nuclei because the magnetic moment of the electron, compared to that of the nuclei, is about 1000 times greater, and the relaxation timescale depends roughly on the square root of the magnetic moment. The broadening caused by variation of the relaxation time is referred as homogeneous while the line width determined by other phenomena is called inhomogeneous. Many phenomena can contribute to a variation in the line width but the most important regarding supramolecular systems are the time-dependent effects, also called dynamic effects, that can be both intramolecular or intermolecular and the broadening results for dynamic fluctuations in the local field experienced by the

unpaired electron. Some of these effects are: the slow tumbling of the molecule in a viscous liquid, the interaction with other paramagnetic species, a variation in the rate of rotation of the paramagnetic centre around a bond modulated by the steric hindrance of the system. The mobility of the paramagnetic species is described by the correlation time, τ_c, corresponding to the time needed for the molecule to turn of ca. one radian. This parameter can be very useful for the examination of the formation of inclusion complexes between a paramagnetic probe and a host molecule, the formation of the complex strongly affects τ_c and thus the line width of the paramagnetic molecule.

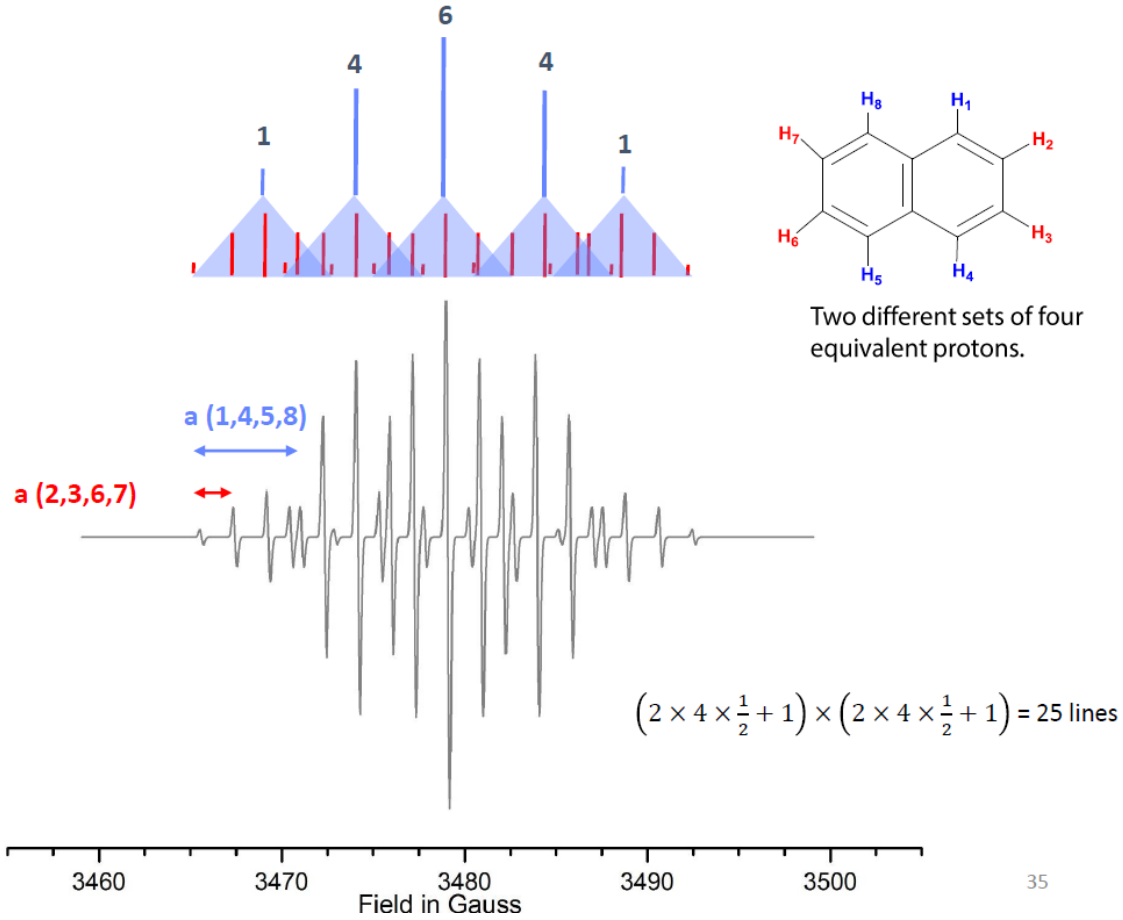

Figure 1.29 *The EPR spectra of the naphthalene radical.*

An example of this effect can be observed in the work of Kaifer *et al.* in which they demonstrated the encapsulation of a 4-trimethylammonium-TEMPO probe inside the cavity of a resorcinarene supramolecular capsule formed by self-assembling of six resorcinarene monomers in a nonpolar media like CH_2Cl_2. The spectra of the probe consist of three spectral lines due to the coupling of the unpaired electron with the nitrogen atom. By increasing the concentration of resorcinarene components of the supramolecular capsule the fraction of paramagnetic nitroxide included in the capsule increases, affecting the line shape in the high field region with a broadening determined by a slower mobility of the probe when included in the cavity as shown in Figure 1.30.[57]

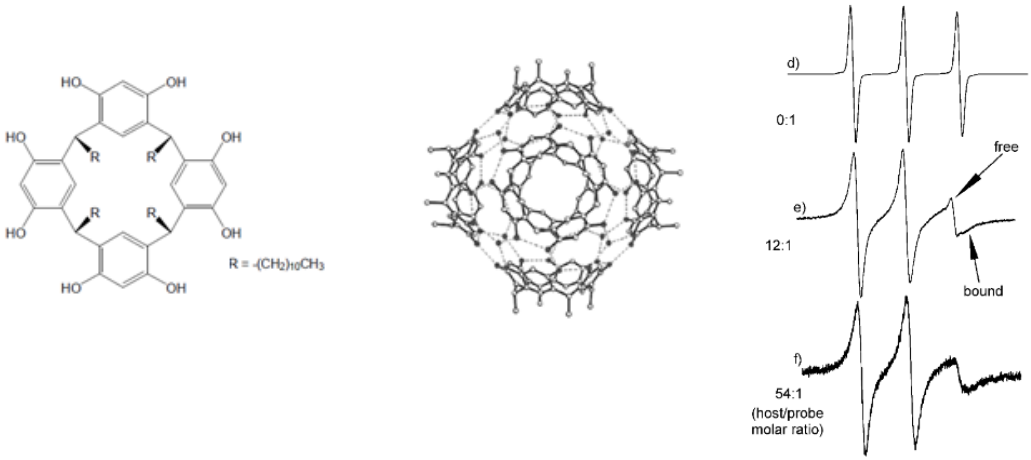

Figure 1.30 *Monomeric constituents of the resorcinarenes supramolecular capsule (left), ball and stick representation of the supramolecular capsule [58] (middle) and broadening of the high field EPR lines of 4-trimethylammonium-TEMPO due to the inclusion of the probe in the resorcinarene capsule (right).[57]*

1.2.2 Organic radicals

All the properties discussed above makes EPR spectroscopy a useful complementary technique for the investigation of supramolecular assemblies but in order to make these kinds of systems suitable for EPR investigation a paramagnetic centre must be added. For this purpose, organic radicals are good candidates, because of the wide range of properties and for the possibility of chemical modification. Many different organic radicals were reported so far in the literature [59] since the discovery of the triphenylmethyl (trityl) radical reported for the first time by Gomberg in 1900 [60] paving the way for the free radical chemistry. Just one year later, in 1901, Piloty *et.al.* reported the first free radical based on the nitroxide structure [61] but it took more than five decades for the first EPR investigation of these structures by Holden et.al.[62] Many organic radicals are transient species characterized by very short lifetime but some of them, thanks to their structural features, can be stabilized by electronic effects (*i.e.* resonance) like the trityl and nitroxyl radicals.

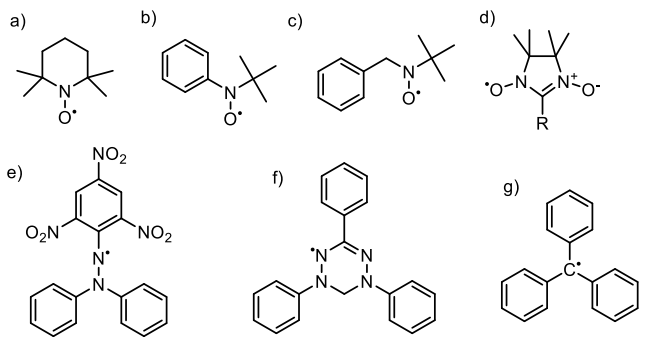

Figure 1.31 *Some of the most important organic radicals: a) TEMPO, b) DMEPN c) BTBN d) Nitronyl Nitroxide, e) DPPH, f) Verdazyl radical g) Trityl radical.*

Their persistency depends on their reactivity that can be tuned varying the structural features around the radical centre. In this way it's possible to obtain radicals characterized by a very long lifetime (years) even without peculiar precautions. These kinds of radicals, as described by Griller and Ingold, can be called stable meaning that they "can be isolated and handled as pure compounds"[63] because their paramagnetic nature is retained even for years. In Figure 1.31 some very well-known organic radicals are reported.

The nitroxide radical is one of the most studied among the organic radicals and consists of an aminoxyl (N-O•) paramagnetic unit characterized by a π_{N-O} three electron bond resulting from the overlap of the $2p_z$ orbitals of the nitrogen and oxygen atoms with an electronic structure composed by two main canonical forms as shown in Figure 1.32, with the unpaired electron occupying the π* orbital of both nitrogen and oxygen, with a slightly higher spin density on the oxygen.[59] Because of this stabilized electronic structure the product of dimerization is not observed, the formation of the dimer is thermodynamically unfavoured (with a gain in energy of about 35 kcal/mol) respect to the gain in energy due to the electronic stabilization which is 30 kcal/mol (Figure 1.32). The EPR spectra of the aminoxyl group embedded in the 2,2,6,6-tetramethylpiperidine-N-oxyl (TEMPO, Figure 1.31, a) is characterized by three EPR lines because of the coupling between the unpaired electron and the ^{14}N nucleus. Benzyl-*tert*-butyl nitroxide (BTBN) radical (Figure 1.31, c) instead is characterized by 9 EPR lines due to the coupling of the unpaired electron also with the two ^{1}H nuclei in the β position.

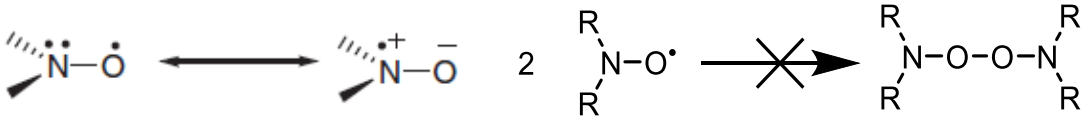

Figure 1.32 *Resonance structures of the aminoxyl group (left) and the not observed dimerization pathway. (right)*

The persistency of nitroxyl radicals is strictly dependent on the structural features in which the aminoxyl group is comprised. The BTBN radical for example, with the two hydrogen atoms in β position can then react via disproportion to afford the corresponding diamagnetic hydroxylamine and nitrone derivatives. (Figure 1.33).

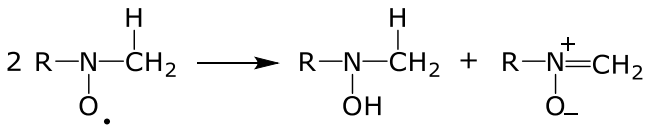

Figure 1.33 *The disproportion reactions between two nitroxyl radicals in which hydrogen atoms are present in the β position.*

Conversely, TEMPO in which the hydrogens in the β positions are replaced by methyl groups cannot undergo disproportion, this radical is highly persistent and can be stored for years. The nitroxyl group

has some properties that can be successfully exploited in the investigation of supramolecular architectures and among them, the high sensitivity to the surrounding environment: the presence of hydrogen bond donors, or a more polar environment results in an increase of a_N value (Figure1.34). These variations arise from the hydrogen bond or dipolar interaction mediated stabilization of the resonance structures in which the unpaired electron is located on the nitrogen. This effect was well described in 1973 by Silver *et al.* that described the spectroscopic variations of 4-oxo-TEMPO in various solvents (Table 1.1).[64]

Solvents	g-Factor	a_N (Gauss)	$a_{O(17)}$ (Gauss)
Benzene	2.0062	14.45	*19.29*
1-Butanol	2.0060	15.01	*19.11*
Water	*2.0058*	*16.01*	*17.86*

Table 1.1 *Variations of the g-factor, a_N and $a_{O(17)}$ for 4-oxo-TEMPO in different solvents ordered in increasing polarity.*[64]

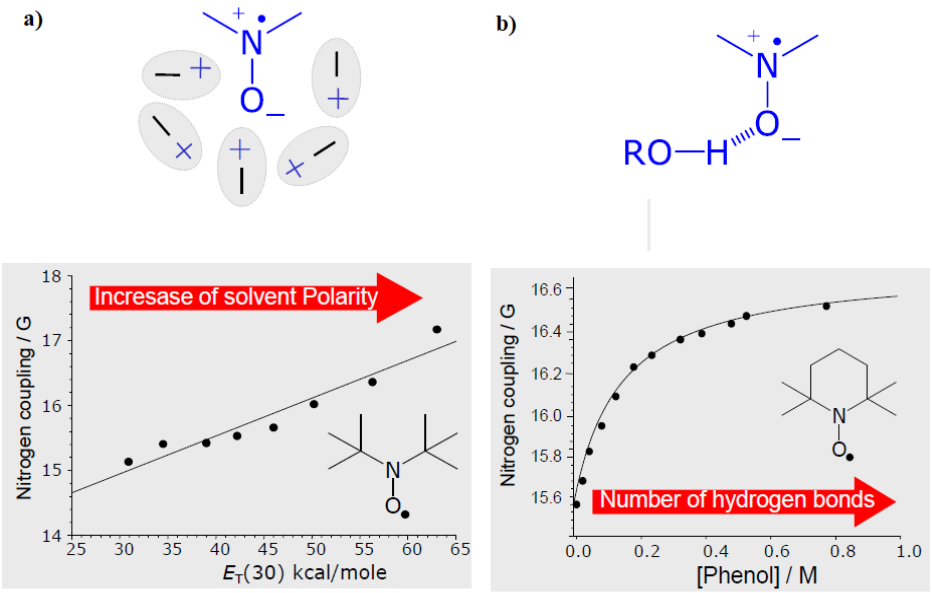

Figure 1.34 *The effect on the g value of: a) dipolar interactions b) hydrogen bonding.*

This feature can be exploited for the investigation of the formation of an inclusion complex between a nitroxyl probe and a host whose cavity has a different polarity compared to the surrounding media.

Another important advantage of the nitroxyl group is the possibility of chemical modification of the structure in which the nitroxyl group is comprised. Since their discovery many different derivatives have been synthesized. For the TEMPO radical, *i.e.*, the main modifications explored are on the 4 position yielding derivatives like 4-oxo-TEMPO, 4-amino-TEMPO and 4-carboxy-TEMPO. (Figure 1.35). Other modifications regarded also the 2 and 6 positions with more hindered substituents or spirocyclic groups to increase the stability of these radicals towards bioreduction phenomena. These strategies

allowed the application of these radicals in many fields like bio imaging[65] and as a polymerization catalyst.[66]

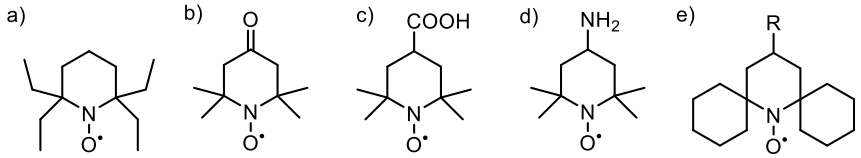

Figure 1.35 *Some derivatives of TEMPO, a) 2,2,6,6-tetraethyl-TEMPO, b) 4-oxo-TEMPO, c) 4-carboxy-TEMPO, d) 4-amino-TEMPO, e) bis-spirocyclohexyl-TEMPO.*

The robust stability of this radical scaffold, even in harsh conditions is what mainly allows the opportunity of wide chemical modification directly on the paramagnetic species, without any need of protection/deprotection or successive oxidations that can interfere with the structure in which the radical is present.

Another important radical, derived from the aminoxyl group is the nitronyl nitroxide (NN, Figure 1.36), which is a stable and persistent radical, based on the imidazole ring. This structure contains both the aminoxyl and nitrone groups with the unpaired electron delocalized between the nitrogen atoms of the two groups. The resulting EPR spectra is composed by 5 lines with a 1:2:3:2:1 intensity ratio. They were first synthesized by Ullman *et al.* in 1968 resulting from the condensation of a bis-hydroxylamine and benzaldehyde in benzene, followed by oxidation of the dihydroxy-imidazolidine precursor with lead dioxide to give the blue coloured radical.[67] This radical can be irreversibly converted to iminyl-nitroxide (IN) which have a red to orange colour and 7 line spectrum characterized by a 1:1:2:1:2:1:1 ratio due to the spin coupling of the unpaired electron with two non-equivalent nitrogen atoms.

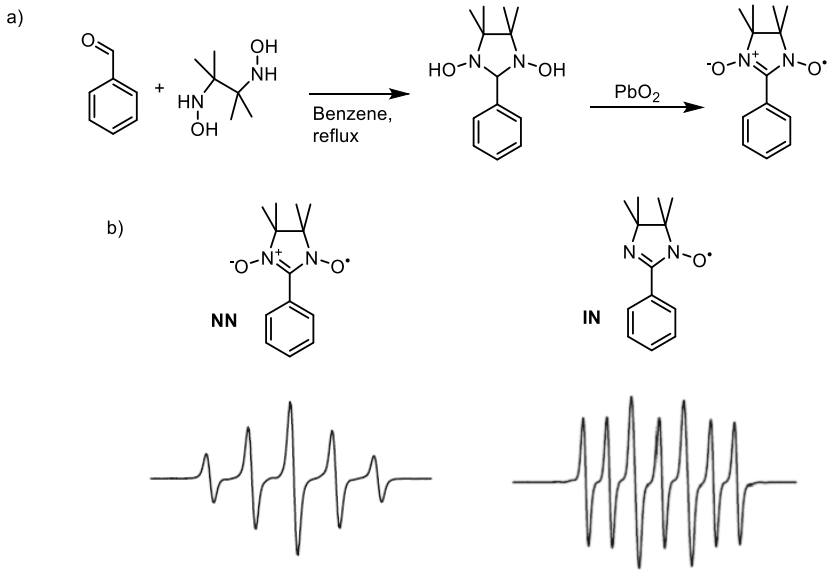

Figure 1.36 *a) The synthesis of NN presented by Ullman et al. b) Nitronyl nitroxide (NN) and Iminyl nitroxide (IN) and their corresponding EPR spectra.*

The conversion of NN to IN can take place in presence of nitric oxide (NO), as shown by the work of Kalyanaraman *et al.*,[68] which is an important biological signalling molecule. In the cardiovascular system, nitric oxide influences the degree of vasodilatation of blood vessels, mediates the aggregation of platelets, it is a neurotransmitter in the central nervous system and plays a key role in the immune system as cytotoxic mediator. Because of this reactivity, NN radicals have been used for the determination of the NO release mediated by the homolytic S-N bond cleavage in S-nitrosothiols adducts (S-NO-albumin and S-NO glutathione) in biological media,[69] and also the role of ascorbate and protein thiols on this process was investigated. The labelling of different amino acids by Peng *et al.* was used to measure the nitric oxide levels in different tissues.[70] Despite the challenging synthesis, NN radicals are widely used as spin labels for biological macromolecules, like oligonucleotides. Their presence allowed to obtain many information on the structural features and on the dynamics exerted by this kind of molecules.[71]

NN radicals are also good candidates for the synthesis of organic based magnetic materials because of their ability to organize themselves in ordered structures thanks to the ability of the N-O groups to interact via hydrogen bonding, π-stacking and the chelation of metal cations to form mixed organic-inorganic hybrid structures. These abilities can be exploited for the synthesis of purely organic ferromagnetic materials, like in the example reported by Kinoshita *et al.* in which *p*-nitrophenyl-nitronylnitroxide was studied in the crystal phase. The β-phase orthorhombic crystals were showing a bulk intermolecular ferromagnetic coupling at 0.65 K, in these conditions the spin of the NN radicals are parallel ($S \geq 1$).[72] The ferromagnetic coupling can take place also via intramolecular alignment of the spins of the unpaired electrons when the two radical centres are linked by a spacer characterized by an optimized composition and geometry that prevents the natural antiparallel pairing of the spins of the unpaired electrons (Figure 1.37).

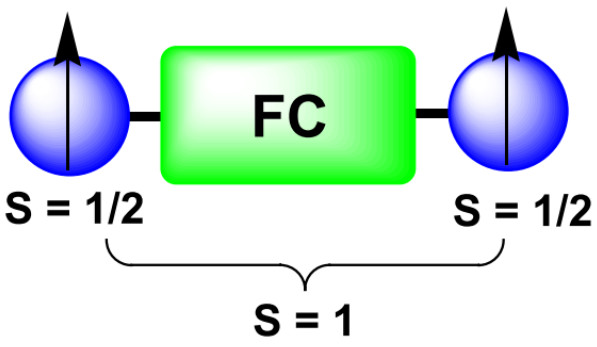

Figure 1.37 *Schematic representation of intramolecular ferromagnetic interaction in a diradical.*[73]

Zoppellaro *et al.* for instance reported the synthesis and characterization of pyrazolylbipyridine-bis nitronyl nitroxide (Figure 1.38) that exhibited ferromagnetic properties thanks to the efficient propagation of the spin polarization through bond.[73]

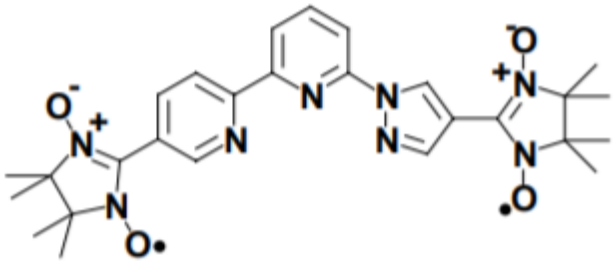

Figure 1.38 *The pyrazolylbipyridine-bis nitronylnitroxide synthesized by Zoppellaro et al.*

The properties shown by NN radicals makes them very good candidates for the synthesis of organic based spin crossover magnetic materials which are considered as a holy grail by chemists and physicists.[59]

Another possibility, as already mentioned, is the exploitation of the coordinating properties of the NN group toward metal cations for the synthesis of organic-inorganic hybrid complexes. Also in this case the magnetic properties in the solid state are due to the parallel spin alignment between the unpaired electrons of the organic radical and the metal cation. The fine tuning of the geometry of the complex is crucial. NN radicals can act both as a monodentate ligand and as a bidentate ligand (Figure 1.39).[74]

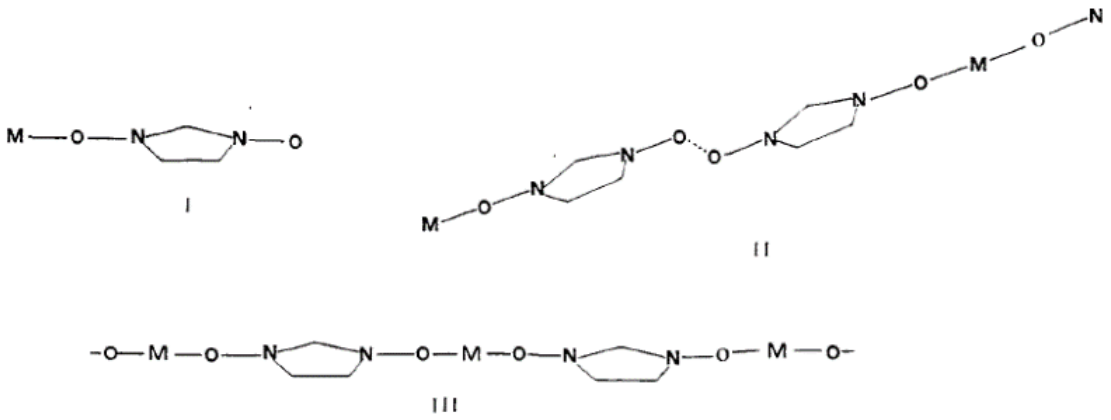

Figure 1.39 *Schematic representation of the chelating properties of NN radical towards metal cations, I and II represents a monodentate ligand to the metal M, in III the radical acts as a bidentate ligand.*[74]

In their pioneering work on this topic, Caneschi *et al.* reported in 1988 the investigation of a complex between 2,4,4,5,5-pentamethyl-4,5-dihydro-l-imidazolyl-1-oxy-3-oxide and copper(II) trifluoroacetylacetonate ($Cu(tfac)_2$). The resulting adduct was characterized by a square pyramidal geometry yielding a ferromagnetic coupling between the spin of the radical and copper unpaired electrons.[75]

1.3 The use of organic radicals for the investigation of supramolecular architectures.

Combining the already mentioned properties of EPR spectroscopy and of organic radicals can be a valuable analytical method to be exploited for the investigation of supramolecular systems. In particular, the timescale of EPR analysis, its sensitivity and the sensitivity of organic radicals to the surrounding environment allows to obtain structural and dynamic information on the investigated system. This method can be achieved by applying two main approaches: spin probing and spin labelling. So far there are many examples of both approaches in literature, developed to address the need of new analytical methods for the characterization of supramolecular systems with always increasing levels of complexity.

1.3.1 Spin probing.

The spin probing approach consists in the exploitation of small organic radicals that interacts with the investigated system through non-covalent interactions. One of the main applications of this approach is in the investigation of the complexation properties of a host molecule. Some of the most investigated hosts are macrocyclic compounds like CDs, CBs, calixarenes etc. but this method can be applied also for the investigations of different kinds of hosts like the self-assembled monolayer of monolayer protected gold nanoparticles (AuNPs), micelles and liposomes. Virtually, the properties of any host molecule that interacts with the probe can be explored with this method, if the probe is designed in such a way that the formation of the complex induces a variation in the spectroscopic parameters of the EPR spectra of the paramagnetic probe. The use of TEMPO radical relies mostly on the variation of a_n, resulting from the different polarity of the surrounding environment experienced by the nitroxyl group. The width of the EPR lines can also be a useful parameter to consider, since it depends on the mobility and the tumbling rate of the probe that usually changes while the probe is involved in the inclusion complex. However, the observed changes exerted by TEMPO radicals are usually small, yielding therefore no clear distinction between the free and complexed probe and limiting in this way the number of information that can be obtained. To overcome this limitation, other derivatives of the nitroxyl radical can be used, like the BTBN radical, because of its unique structural features that allows to obtain more detailed information on the investigated system. The EPR spectra of this probe is composed of 9 spectral lines and this can be easily interpreted on the basis of the coupling of the unpaired electron with the nitrogen atom and the two hydrogens with a_N and $a_{2H\beta}$ respectively. The presence of the hydrogen atoms in β position gives to this radical the sensitivity towards the conformational changes in its structure, according to the Heller-McConnel equation:[76]

$$a_{2H\beta} = \rho_N (B_0 + B_2\langle\cos^2\theta\rangle)$$

This means that $a_{2H\beta}$ depends on the spin density $\rho_{N,}$ of the alpha atom, in this case nitrogen, and from the dihedral angle θ comprised between the plane of the H_β-C-N bonds and the symmetry axis of the 2*pz* orbital of the nitrogen occupied by the unpaired electron (Figure 1.40), The closer the planes are, the more important will be the probability for the unpaired electron to interact with the H_β atoms. The transition to an eclipsed conformation from a staggered conformation is therefore expected to result in an increase of $a_{2H\beta}$.

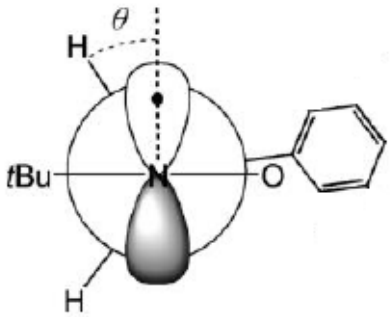

Figure 1.40 *The dihedral angle θ comprised between the plane of the H_β-C-N bonds and the symmetry axis of the 2pz orbital of the nitrogen occupied by the unpaired electron in the BTBN probe.*

As a result, when there is a change in the conformation of the probe, *i.e.* due to the formation of an inclusion complex with a host, the resonance field for the $M_I(2H_\beta) = \pm 1$ lines change significantly for the free and complexed species. If the timescale of formation/dissociation of the complex are comparable to the timescale of the EPR analysis, the resulting experimental spectra will be characterized by two separate sets of signals for the free and complexed probes. Lucarini *et al.* exploited this approach to examine the formation of an inclusion complex between the BTBN probe and many guests, like CDs, calixarenes and sodium dodecylsulphate (SDS) micelles.[77] In their works they varied the concentration of host added to a solution of the probe and observed the rise of the signals characteristic of the complexed probe (Figure 1.41).

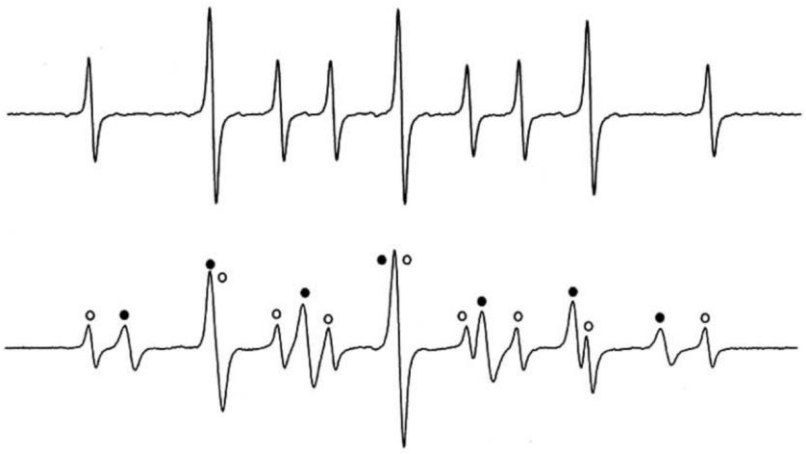

Figure 1.41 *EPR spectra of BTBN probe in water (top) and in presence of β-CD (bottom), Empty (°) and full symbols (•) indicate the lines of the free and included radicals, respectively.*

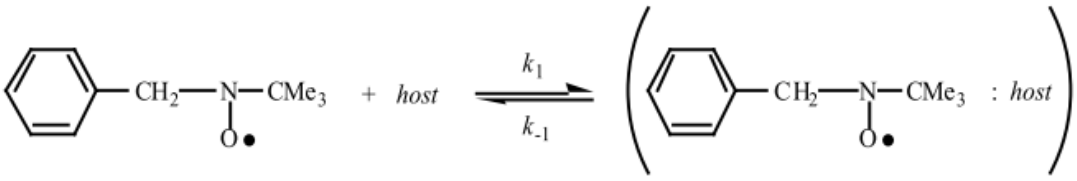

Figure 1.42 *The equilibrium involved between the probe and a host.*

Quantitative information on the equilibria depicted in Figure 1.42 were obtained by considering the expression for the equilibrium constant K:

$$K = \frac{k_1}{k_{-1}}$$

in which k_1 is the association rate constant and k_{-1} is the dissociation rate constant. When the concentration of the host is in large excess compared to the probe the equation can be written also as:

$$K = \frac{x_{host}}{x_{free}\,[host]_0}$$

in which x_{host} and x_{free} are the molar fractions of the complexed and free probes, respectively, and $[host]_0$ is the actual concentration of the host. The composite EPR spectra can be easily simulated by using a two-jump model and by repeating the same experiments and simulations at different temperatures it is possible to determine k_1 and k_{-1} at each temperature. By this approach they were able to obtain the equilibrium and rate constants for the formation of the inclusion complex between the BTBN probe and various guests, the analysis of the obtained results allowed them also to assess the features of the host affecting the complexation equilibria, *i.e.* at 294K with α-CD K= 14.3 M^{-1}, in presence of β-CD as a host K= 1281 M^{-1} and with γ-CD K= 50.7 M^{-1}. These values underline the importance of the size of the host on the complexation equilibria, for the BTBN probe the optimal host is represented by β-CD.

By plotting the values of k_1 and k_{-1} obtained at the different temperatures in van't Hoff plots it was also possible to obtain the thermodynamic parameters for the interactions and their evaluation allows to assess the nature of the interactions. For example, the interaction of BTBN radical with β-CD is slightly exothermic, with a $\Delta G°_{294\,K}$= -4.18 kcal/mol^{-1} with an enthalpic contribution corresponding to a $\Delta H°$ = -4.83 kcal/mol^{-1} while the entropic contribution is $\Delta S°$= -2.2 cal/$mol^{-1}K^{-1}$. From this results becomes clear the predominance of the negative enthalpic contribution to the value of the Gibbs energy term respect to the slightly negative entropic contribution. The entropy of activation is mainly determined by the negative contribution of the more restricted conformational and motional freedom of the probe in the cavity of the β-CD which is almost completely counterbalanced by the release of water molecules from the cavity of the host, from the solvation shell of the probe and their reorganization.[78] An analogue of the BTBN probe, in presence of SDS micelles, showed an opposite thermodynamic profile for the interaction, with a large positive entropy of activation corresponding to $\Delta S°$= 9.61 cal/$mol^{-1}K^{-1}$ resulting

from the desolvation of the probe caused by its solubilization in the hydrophobic interior of the micelles due to hydrophobic effects. The small and negative enthalpic contribution has only a minor contribution.[79]

Thanks to the potential of this approach, and the versatility of the probe, as well as the possibilities of chemical modification on its structure, BTBN was used for the investigation of many hosts. On the other hand, as already mentioned, the presence of the benzylic hydrogens affects the persistence of the paramagnetic probe, that can react via disproportion to afford the corresponding EPR silent hydroxylamine and nitrone derivatives. Nevertheless, the lifetime of the probes can vary between minutes and hours, which is generally a sufficient time to perform several EPR analyses. For this reason, the diamagnetic amine precursor of the BTBN probe or its derivatives are oxidized in situ directly in the EPR capillary. This method can also be used to study hosts of higher complexity, as an example, it was used by our research group for the investigation of the complexation equilibria between hydrogenated (**I-III**) and fluorinated (**IV-VI**) derivatives of BTBN radical and the hydrogenated (**NP1)** or fluorinated (**NP2**, **NP3a**, **NP3b**) monolayer of self-assembled monolayer protected gold nanoparticles (AuNPs) with different sizes. The aim of the study was to evaluate their possible use in drug delivery applications (Figure 1.43).[80] In this case the spin probes were used to simulate a drug molecule intercalating in the fluorinated monolayer of the AuNPs to rationalize the role of lipophilic and fluorophilic interactions in the design of the monolayer.

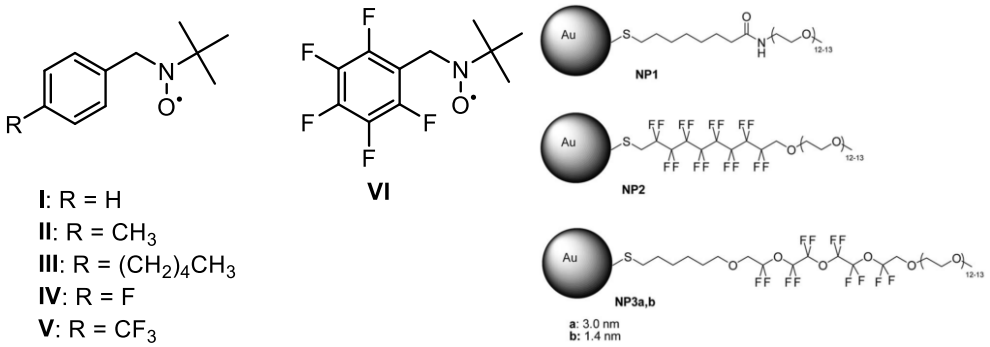

Figure 1.43 *The spin probes used for the investigation of various AuNPs.*[80]

The amine precursors of the probes were oxidized in situ with oxone and good EPR spectra were recorded for all the probes in water. They were all characterized by the usual 9 lines easily interpreted on the basis of the coupling of the unpaired electron with the nitrogen and the β-hydrogens atoms. When the EPR spectra were recorded in presence of AuNPs new signals were observed (Figure 1.44) and attributed to the probes intercalated in the monolayer of the nanoparticles. In this case we observed a decrease of a_N as a result of a lower polarity inside the monolayer and the variation of $a_{2H\beta}$ due a change of the geometry of the probe. The same trend was observed for all the probes **I-VI**. By increasing the absolute concentration of AuNPs the new signals became dominant in the EPR spectra. Following the

method described above, it was possible to easily obtain the equilibrium constants K_{eq} for the intercalation of the probes in the monolayer of the AuNPs. (Figure 1.45).

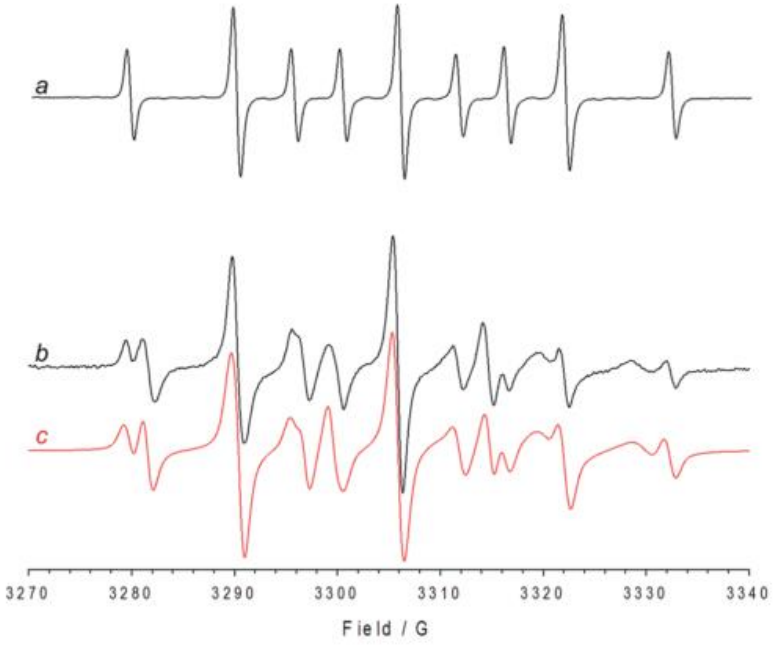

Figure 1.44 *a) EPR spectra of probe* ***V*** *recorded in water at 298 K, and b) in presence of* ***NP3b*** *1.3 mM, c) computational simulated EPR spectra.*

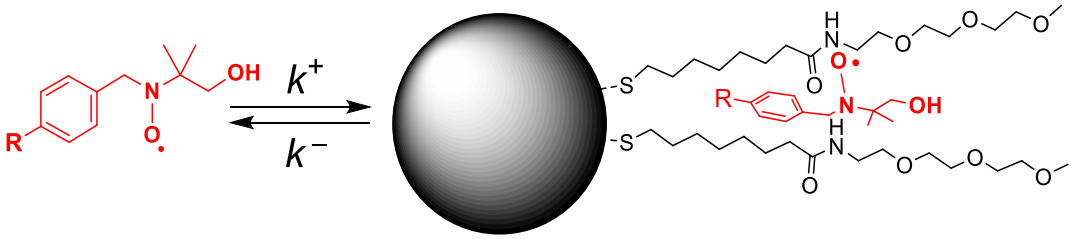

Figure 1.45 *The investigated partition equilibria between the probes and the AuNPs.*

The AuNPs characterized by a fluorinated monolayer **NP2** and **NP3a**,**b** displayed an increased affinity for both hydrogenated and fluorinated probes, *i.e.***NP1** was characterized by K_{eq} = 2.2 M^{-1} for probe **II** and K_{eq} = 4.0 M^{-1} for probe **V** while for **NP2** those values increased to K_{eq} = 5.7 M^{-1} for probe **II** and K_{eq} = 29 M^{-1} for probe **V**. in the case of **NP1** there was 1.8 fold increase by comparing the ratio of K_{eq} (K_V/K_{II}) of **V** and **II** and 5.1 fold increase in the case of **NP2** for the same probes. The variations observed for **NP1** were found to be very similar to those obtained by repeating the same experiments with SDS micelles that are expected to interact with the probes only by hydrophobic interactions. The same trend is observed with **NP3a,b** and in this case K_{eq} of **V** increased 25 and 22 times for **NP3a** and **NP3b** respectively (K_{eq} = 100 M^{-1} for **NP3a** and K_{eq} = 90 M^{-1} for **NP3b**) compared to **NP1**. With **NP3a**, the comparison between probe **VI** with a perfluorinated phenyl ring (K_{eq} = 80 M^{-1}) and probe **I** (K_{eq} = 6.2 M^{-1}) led to a 12.9-fold increased affinity of **VI**. In general, the partition equilibrium of the probe inside

the monolayer was favoured raising the hydrophobicity and the degree of fluorination of the probes and it grows significantly more when probes and monolayers are both fluorinated, thanks to the contribution of fluorophilic interactions.

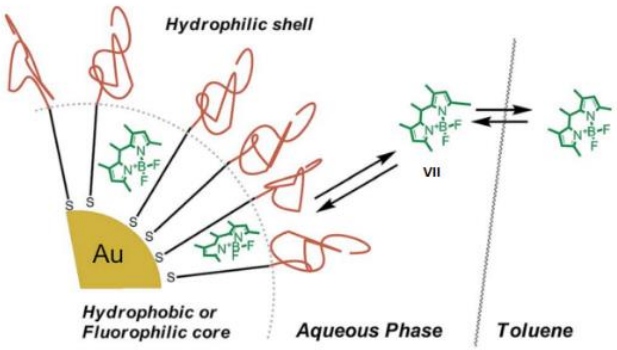

Figure 1.46 *The phase transfer equilibria of* ***VII*** *in a biphasic mixture of water/toluene in presence of AuNPs.*

The position of the fluorinated chain in the monolayer affects the binding affinity of small molecules: the rigid monolayer of **NP2,** in which the fluorinated chains are close to the gold core, displays a lower binding affinity for the probes respect to the flexible monolayer of **NP3a,b**, whose fluorinated chains are located in the middle of the monolayer and thus resulting more accessible to guests. The size of the nanoparticles was also found to affect the repartition equilibria of the probe in the monolayer, **NP3a** with a diameter of 3nm was characterized by higher affinity for the probes respect to **NP3b** with a diameter of 1.4 nm. Reducing the inter ligand space with a tighter packing of the monolayer thiols results in a more efficient interaction with guests. In this work we have also performed fluorescence delivery studies using the hydrophobic dye **VII** in a water/toluene biphasic mixture in presence or in absence of AuNPs (Figure 1.46), the presence of the nanoparticles in the aqueous layer resulted in a slowing down the rate of phase transfer of **VII** from the aqueous layer to the organic phase (Figure 1.47).

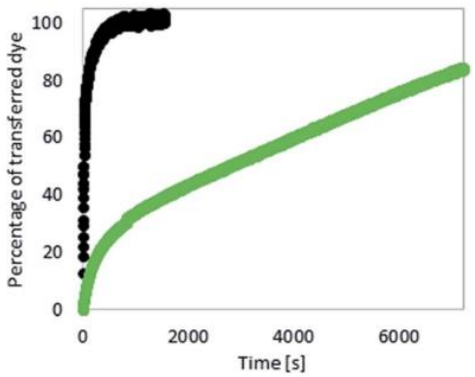

Figure 1.47 *Kinetic profile for the phase transfer of* ***VII*** *in the biphasic water/toluene mixture in absence spin labelling (black line) and in presence of* ***NP3a*** *(green line).*

The spin probing approach has also been exploited for biological applications and nitroxides were extensively studied as magnetic resonance imaging (MRI) contrast agents.[81]

1.3.2 Spin labelling for the investigation of supramolecular systems.

Spin labelling consists in the grafting, through covalent bond(s) of organic radicals to another molecule. This approach was developed and named by H. McConnel in 1965 [82] and was immediately recognized as an extremely useful approach, extensively used in the following 40 years in the investigation of biological membranes, proteins, peptides DNA and RNA. The covalent functionalization of these biological structures allowed scientists to obtain many useful biophysical information on their structural and dynamic properties.[83]

With the rise of supramolecular chemistry, and the need of new analytical approaches, led scientists to consider spin labelling outside the context of biology as a tool to exploit basic principles for the rational design of the building blocks used to assembly supramolecular aggregates.

Radicals based on the nitroxyl group are probably the most studied and used as labels thanks to the wide variety of chemical modification possibilities. In an example reported by Lucarini *et al.* the detection of the intramolecular inclusion of a TEMPO label linked with a flexible aliphatic chain to a β-CD was described. The non-complexed TEMPO fragment was characterized by a_N= 17.00 G while when involved in the interlocked *lasso*-type complex the value decreased to a_N= 16.55 G. (Figure 1.48) By this method it was also possible to distinguish the intermolecular complexation with another β-CD (a_N= 16.48) and the partial complexation of the radical through the upper rim of the CD (a_N= 16.80).[84] These differences are caused by the different environment experienced by the radical fragment, between the polar aqueous media and the hydrophobic cavity of the β-CD. Addition of SDS or 2,6-di-*O*-methyl-β-cyclodextrin (DM- β -CD) was found to be able to influence the complexation equilibria in the non-interlocked derivative.

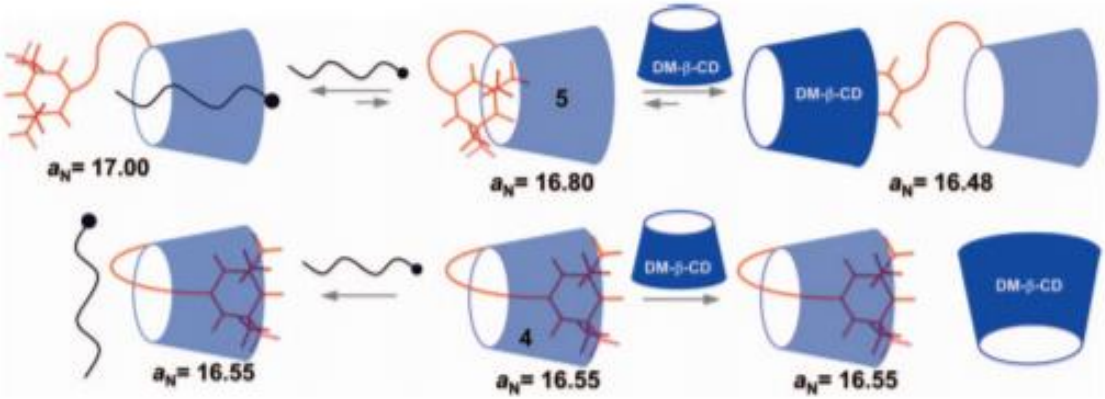

Figure 1.48 *The different inter and intramolecular binding modes between TEMPO and β-CDs.*[84]

The spin labelling approach can be particularly useful in the investigation of mechanically interlocked molecules such as rotaxanes, this method was used for the investigation of the chemically responsive, acid/base fuelled, switching in a [2]rotaxane based on the dibenzylammonium/bipyridium electron poor thread and the electron rich dibenzo[24]crown-8 (DB24C8) macrocycle. The spin labels represented by TEMPO units, were covalently grafted on the ring component and on one side of the thread to act as stoppering unit. The EPR spectra of the rotaxane consists of three lines indicating a diradical system with no interaction between the radical centres. The shuttling of the macrocycle from the dialkylammonium station to the bipyridinium station observed after the addition of a base, in this case DIPEA, resulted in evident spectral changes, from the three spectral lines to five. The two new exchange lines are attributable to the through space spin coupling ($J_{NO\bullet-NO\bullet} > 0$) between the two radical fragments caused by the reduction of the distance between the two spin labels. The initial state was restored by the addition of trifluoroacetic acid (TFA) resulting in the shuttling of the macrocycle back to the dialkylammonium station and switching off the magnetic interaction between the nitroxides. This cycle was repeated several times (Figure 1.49).[85] Further investigations of this [2]rotaxane by the means of PELDOR analysis, a pulsed EPR technique allowed to obtain measurements of the distances between the radical centres in the two co-conformations.[86]

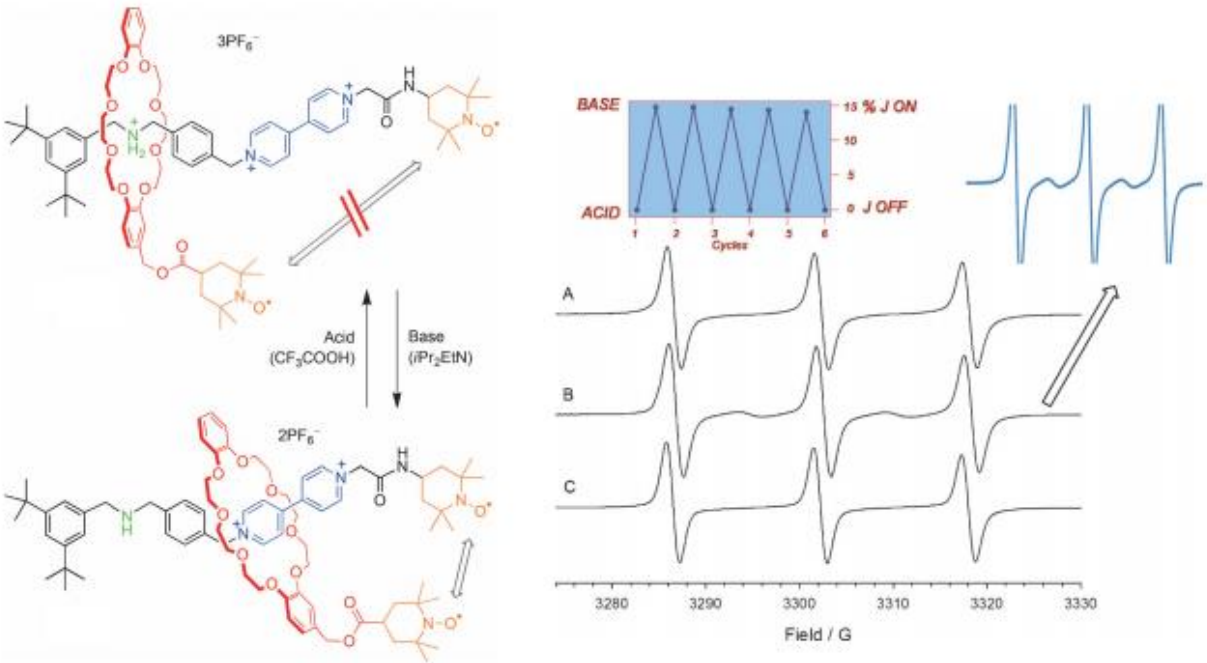

Figure 1.49 *The reversible switching acid base responsive [2]rotaxane (left) and the EPR spectra of a) the rotaxane in its initial state, b) after the addition of DIPEA, c) after the addition of TFA (right).*[85]

In another work,[87] my research group investigated the switching properties of a bis spin labelled "Stoddart-Heath" type" bistable [2]rotaxane, **Rot1**$^{2\bullet4+}$, consisting of a dumbbell containing the electron rich tetrathiafulvalene (TTF) and 1,5-dioxynaphtalene (DNP) units and a ring represented by the spin

labelled electron deficient $CBPQT^{4+}$ macrocycle (**CBPQTNO$^{\bullet}$**). In this rotaxane, the shuttling of the ring between the TTF and DNP station can be realized by electrochemical oxidation of the TTF to its EPR active radical cation $TTF^{\bullet+}$. Both the dumbbell and the macrocycle were labelled with nitroxide radicals, for the dumbbell a bulky spirocyclohexyl piperidine-N-oxyl was used as stoppering unit. The single station rotaxanes as well as the corresponding dumbbells were synthesized (Figure 1.49) for comparison studies. The synthesis was performed by inducing the formation of the pseudorotaxane in DMF at -10°C and then adding the alkyine spirocyclohexyl radical stopper in the presence of $[Cu(MeCN)_4]PF_6$ and (benzyltriazolylmethyl)amine (TBTA) to interlock the pseudorotaxane by the copper catalysed alkyne azide cycloaddition, the so called "click" reaction. The formation of the rotaxanes and of the dumbbells was detected by ^{1}H-NMR spectroscopy even if the radical fragments causes a broadening of the NMR signals. In all cases, the upfield shift of TTF (**Rot1$^{2\bullet 4+}$/Dumb1$^{\bullet}$**, **Rot3$^{2\bullet 4+}$/Dumb3$^{\bullet}$**) or DNP (**Rot4$^{2\bullet 4+}$/Dumb4$^{\bullet}$**) for the rotaxane, compared to the corresponding dumbbell, proton signals was clearly observed, confirming that the **CBPQTNO$^{\bullet}$** encircles the corresponding TTF station. The EPR spectra of the rotaxanes and of the dumbbells (Figure 1.50) were characterized by different spectral features, allowing us to distinguish the different kinds of nitroxide labels: the nitroxides used as stoppers in the dumbbells were characterized by a_N = 15.40G while for the wheel's nitroxide pendant a_N = 15.82 G.

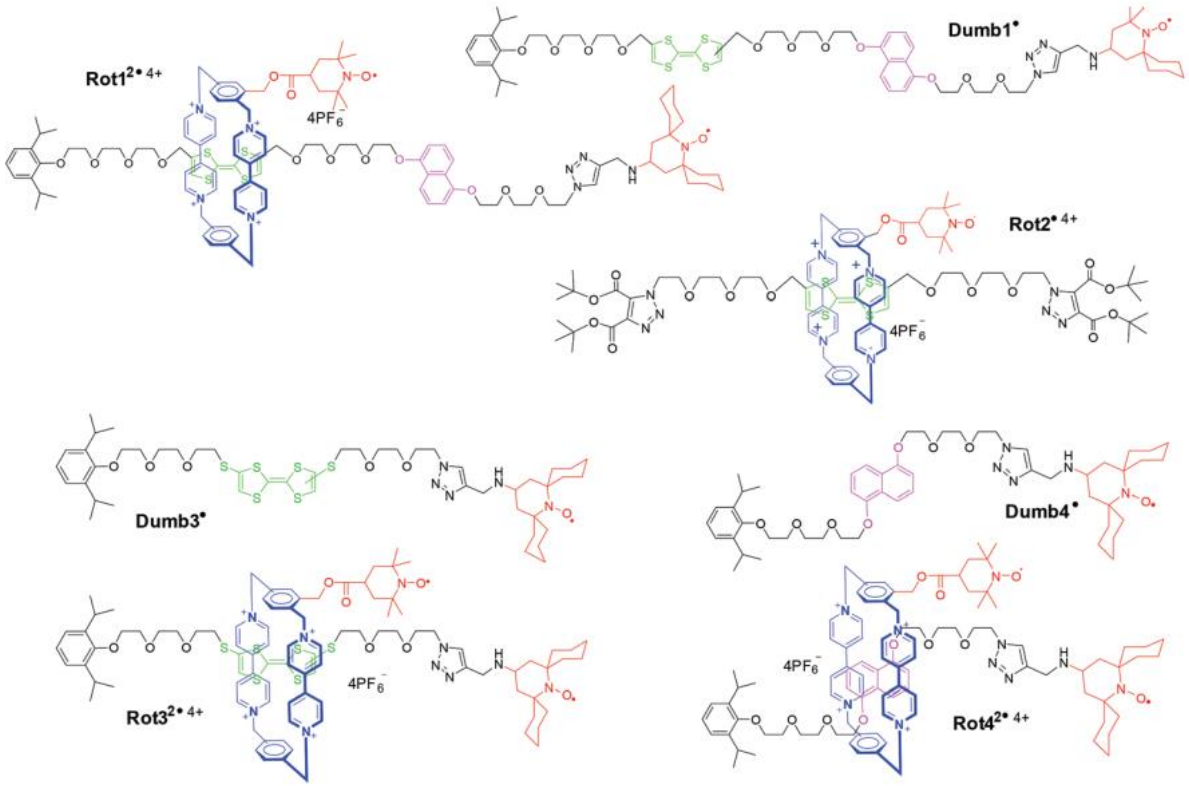

Figure 1.50 *The spin labelled [2]rotaxanes and the corresponding dumbbells.*[87]

The EPR spectra of **Rot3**$^{2\bullet4+}$ and **Rot4**$^{2\bullet4+}$ (Figure 1.50 a and d) were composed by 5 spectral lines, characteristic of a diradical system with a strong spin exchange ($J_{NO\bullet-NO\bullet}$) between the nitroxide units and the broadening of the second and fourth spectral lines suggests that the spin exchange coupling constant, *J*, is modulated by conformational dynamics. This exchange can be attributed to a through space spin exchange mechanism, usually observed when two radicals are spatially close, with a distance typically below 10Å. Conversely, the bistable rotaxane **Rot1**$^{2\bullet4+}$ was characterized by only a three-line spectrum with a non-symmetrical shape due to the superimposition of the signals of both the wheel and the dumbbell radical labels, that contributes to the overall spectra in a 1:1 ratio. The two radicals do not display spin exchange ($J_{NO\bullet-NO\bullet}$ = 0) owing to a longer distance between them, so confirming that **CBPQTNO**$^{\bullet}$ encircles preferentially the far TTF station as indicated by the ^{1}H-NMR investigations. To test the electrochemical properties of the spin labelled rotaxanes and threads we treated them with 1 equivalent of $Fe(ClO_4)_3$, a mono electronic oxidizing agent, in degassed acetonitrile (ACN).

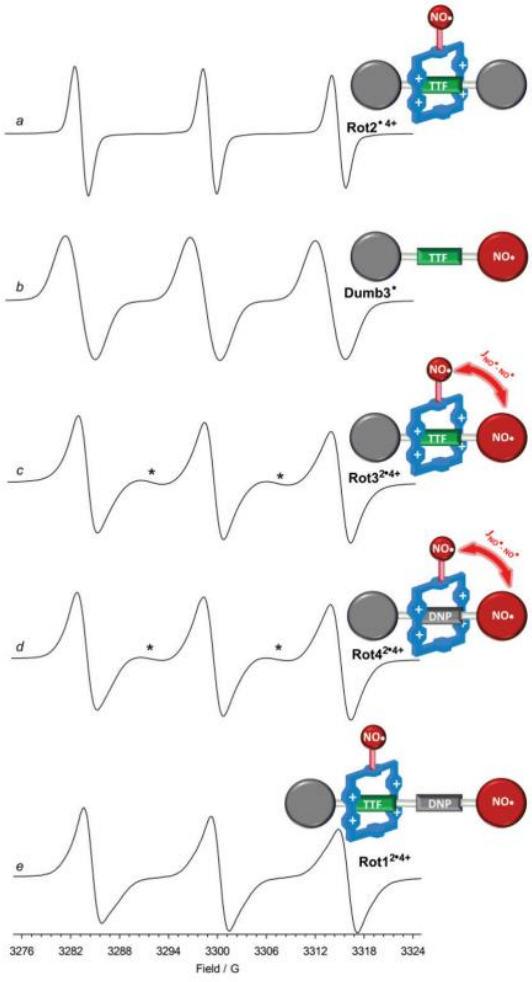

Figure 1.51 *EPR spectra of the spin labelled rotaxanes and dumbbells.*

The first rotaxane/dumbbell pair investigated were the single station **Rot3**$^{2\bullet4+}$ and **Dumb3**, upon oxidation of TTF to TTF$^{\bullet+}$ the EPR spectra of **Dumb3** (Figure 1.51, a) was composed by the signals of the nitroxide, of TTF$^{\bullet+}$ and new lines whose position was consistent with a strong spin exchange ($J_{TTF\bullet+}$–

$_{NO}$•) between the N-O• terminal unit and TTF$^{•+}$. Conversely, the EPR spectrum of **Rot3**$^{2•4+}$ (Figure 1.51 c) was characterized by the presence of exchange lines together with those of the starting nitroxide and TTF$^{•+}$ monoradical. The linewidth and the symmetric resonating field values suggested that the exchange lines derived from the through space spin exchange between the two nitroxides ($J_{NO•–NO•} > 0$). These observations suggested that the ring component is forced to stay on the TTF station due to the absence of other binding sites and that the CBPQT^{4+} ring acts as an "attenuator" preventing the exchange interaction between the TTF$^{•+}$ and both nitroxides. The results were confirmed by recording the EPR spectra of **Rot2**$^{•4+}$ and after addition of the oxidizing agent, no indication of spin exchange between the nitroxide label on the ring and the internal TTF$^{•+}$ was observed (Figure 1.51 b). After the analysis of the single station dumbbell and rotaxane derivatives we started to investigate the oxidized bistable rotaxane **Rot1**$^{2•4+}$ and the corresponding dumbbell **Dumb1**•.

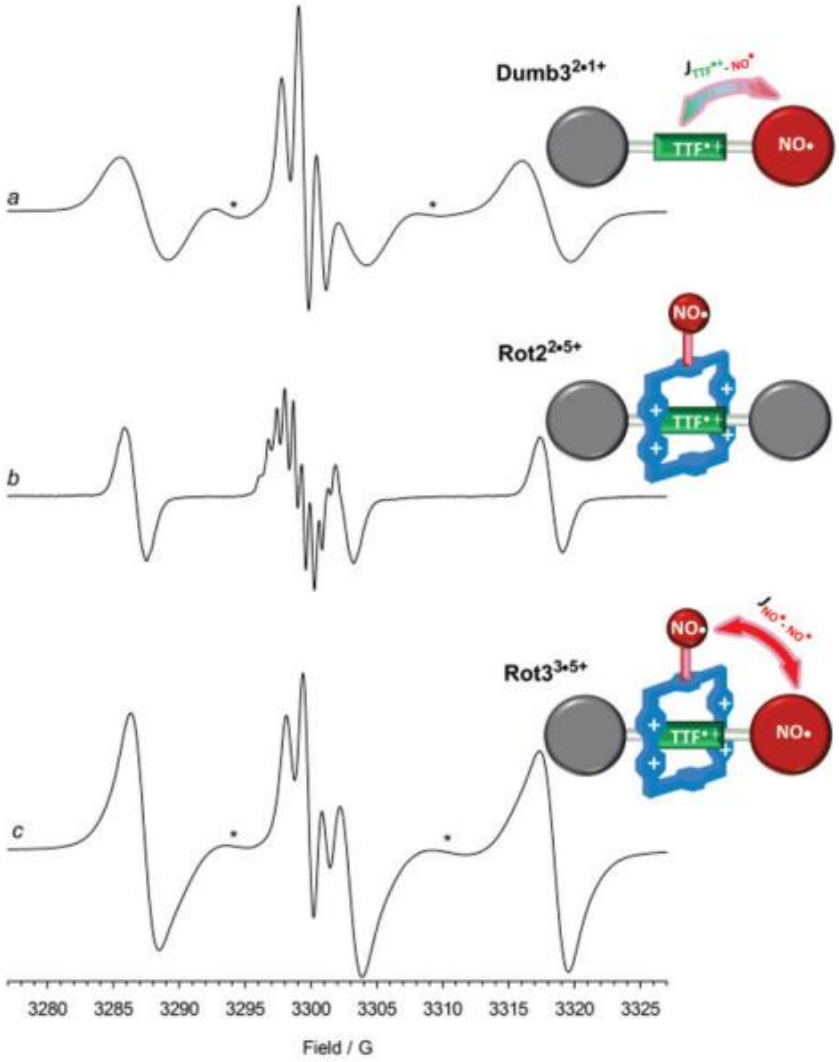

Figure 1.52 *EPR spectra of a)* ***Dumb3***•*, b)* ***Rot2***$^{•4+}$ *c)* ***Rot3***$^{•4+}$ *after oxidation with 1 equivalent of* $Fe(ClO_4)_3$*, star symbols specifies the exchange lines in ACN at 328K.*

Upon oxidation of **Dumb1**$^{\bullet}$, the observed EPR spectra is composed of the signals of the nitroxide and TTF$^{\bullet+}$, exchange lines were also observed at low field while at high field the broadening of the signals led to a more difficult detection. The spin exchange was attributable to the exchange between N-O$^{\bullet}$ and TTF$^{\bullet+}$ due to the position of the exchange lines despite of the long distance between them. The exchange can be justified by the flexibility of the glycolic chains that allows the interaction between the radical centres. However, due to the small number of possible conformations in which the nitroxide and TTF$^{\bullet+}$ are sufficiently close, the exchange interaction was very small.

The same behaviour was observed in the rotaxane **Rot1**$^{2\bullet4+}$, in which, after oxidation with $Fe(ClO_4)_3$ nitroxide and TTF$^{\bullet+}$ signals are present as well as the exchange lines that resonates at fields corresponding to the symmetric centre between the resonance fields of the terminal nitroxide and the TTF radical cation (Figure 1.52, left). The interaction was possible thanks to the shuttling of the ring on the DNP station. Also in this case, the interaction is weak and modulated by conformational dynamics. To assess the reversibility of the switching, the experiments on **Rot1**$^{2\bullet4+}$ were repeated in an electrochemical cell, where the TTF radical cation was electrogenerated by a positive potential (*ca.* +0.5V) in deoxygenated ACN. The EPR spectra recorded in these conditions showed all the spectral features observed for the oxidation with $Fe(ClO_4)_3$ (Figure 1.53, right). The inversion of the sign of the current reduced TTF$^{\bullet+}$ to its neutral form and the starting EPR spectra of **Rot1**$^{2\bullet4+}$ was restored. These experiments were repeated in many cycles confirming the reversible nature of the process.

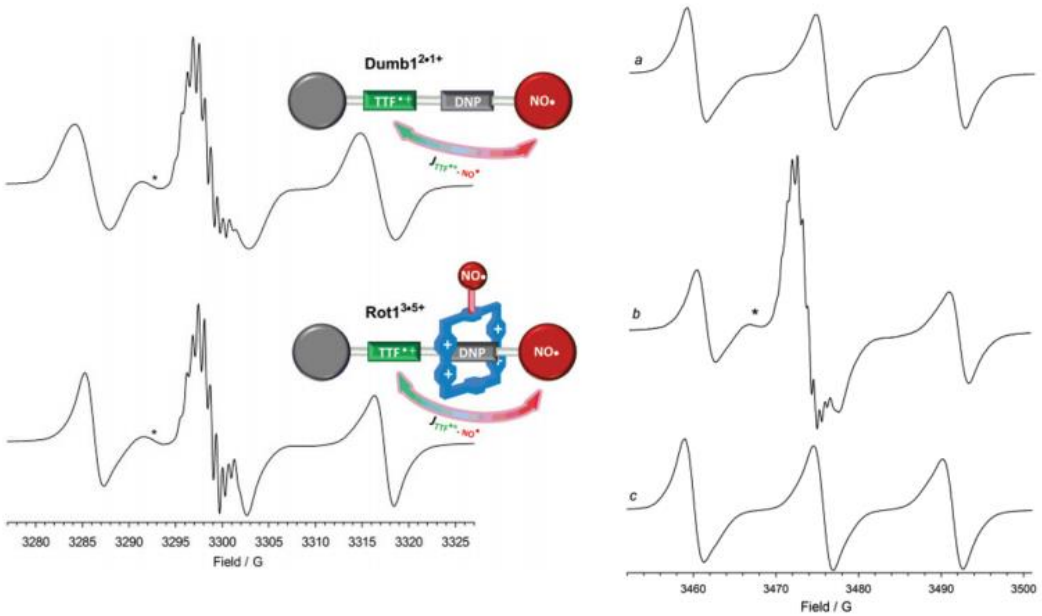

Figure 1.53 *EPR spectra of* ***Dumb1*** *and* ***Rot1***$^{2\bullet4+}$ *after oxidation with* $Fe(ClO_4)_3$ *(left), and reversible oxidation and reduction of* ***Rot1***$^{2\bullet4+}$ *in an electrochemical cell (right) at 328K in 0.1* Bu_4NPF_6*/ACN at (a)* E_{appl}*= 0 V, (b)* E_{appl}*= +0.5 V and (c)* E_{appl}*= -0.5 V. Star symbols specifies the exchange lines.*

1.4 Aim of the thesis

The always increasing complexity in the design and synthesis of molecular machines, inspired by the vastness of potential applications in many fields like nanoelectronics, biomedical applications and material sciences requires also new analytical approaches capable to characterize the nanoscale processes exerted by these kinds of systems. These information are not always accessible with common techniques, making the rational design of functional supramolecular systems even more challenging. In this context, EPR spectroscopy can be a very useful tool for the investigation of supramolecular architectures due to its sensitivity, timescale of analysis and possibility of exploiting both spin probing and spin labelling approaches whose versatility enables the investigation of many different phenomena. Nevertheless, in order to use EPR spectroscopy, paramagnetic species such as organic radicals, must be introduced in the system in form of probes or labels. The synthesis of the spin probes or the spin labelling can be challenging but despite this drawback this approach offers several advantages.

My Ph.D. was devoted to the application of EPR as an analytical tool for the investigation of supramolecular systems, realized by the synthesis and characterization of suitable spin probes and labels. The 2nd chapter will be focused on the investigation of an important non-covalent interaction, analogue of hydrogen bond (HB), called halogen bond (XB). The nature of this interaction has been widely debated from the scientific community and information on its properties lags by far, especially in the solution phase, compared to other non-covalent interaction. The study of this interaction has been realized by the design and synthesis of a suitable spin probe containing both the BTBN motif and the XB donor 4-iodo-2,3,5,6-tetrafluoro phenyl group. The use of these spin probes allowed us, by performing complexation experiments with XB acceptors, to measure the kinetic and thermodynamic parameters for this interaction in solution (Figure 1.54).

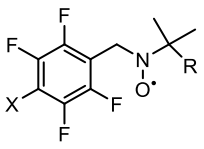

2: X= I, R= CH_3
2-H: X = H R= CH_3
3: X= I, R= CH_2OH
3-H: X= H, R= CH_2OH

Figure 1.54 *The XB bond donor probes **2**, **3** and the derivatives **2-H** and **3-H** with the XB inactive hydrogen atom in para position.*

The 3rd chapter will be focused on the synthesis of a derivative of a DB24C8 containing the BTBN motif for the investigation of its host properties toward guests such as alkali metal cations and organic guests. The EPR analysis enabled the measurement of the degree of complexation and to discriminate different guests from the experimental EPR readout. The formation of a pseudorotaxane with a thread molecule

containing both the dialkylammonium and bipyridinium recognition sites, and the switching of the ring between the two stations of the guest was detected directly in solution (Figure 1.55).

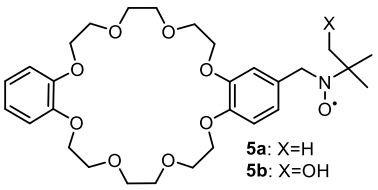

Figure 1.55 *The DB24C8 labelled with the BTBN motif for complexation investigations.*

The 4th chapter is devoted to the development and optimization of a mild and high yielding synthetic method for the synthesis of spin labelled [2]rotaxanes by exploiting the active metal template copper catalysed azide alkyne cycloaddition (AT-CuAAC). The rotaxanes were designed to contain nitronyl nitroxide radicals (NN) as stoppers in the thread shaped molecule. Derivatives of different length and composition were synthesized as well as the corresponding non-interlocked threads. The EPR investigation of these NN labelled rotaxanes provided many useful information on the conformational dynamics in solution. Thanks to variable temperature EPR experiments and the comparison between the [2]rotaxanes and the corresponding threads we were able to measure the apparent activation energies for the conformational variations. Their ability form complexes with metal cations, and the effect it has on the EPR spectra of the spin labelled rotaxanes and threads was also investigated (Figure 1.56).

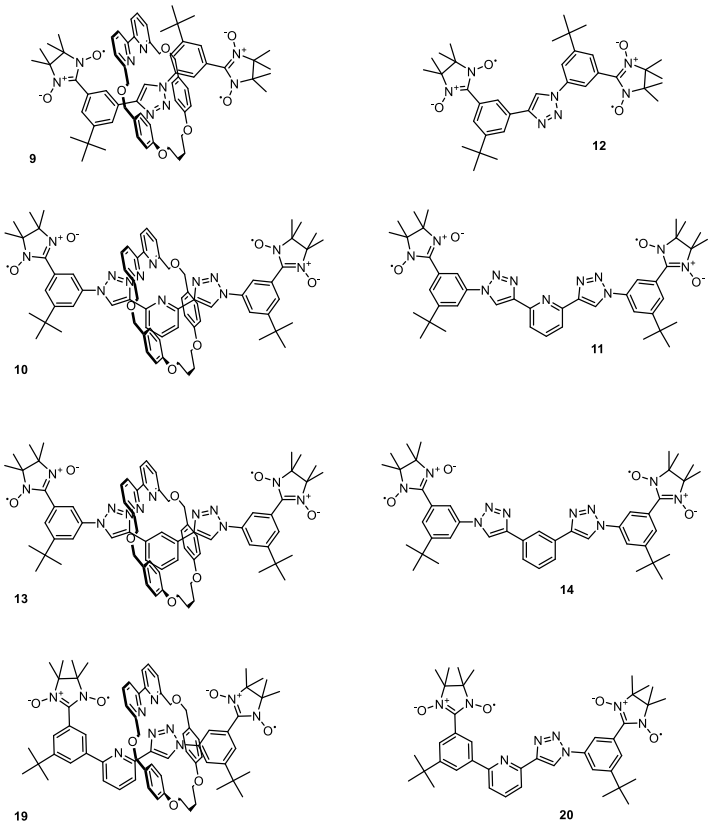

Figure 1.56 *The NN-labelled [2]rotaxanes and the corresponding threads.*

1.5 References

1. P. Murphy and L. A. J. O'Neil, "What is Life? The Next Fifty Years: "Speculations on the Future of Biology", Cambridge University Press, 1997
2. A. Sorrenti, J. Leira-Iglesias, A. J. Markvoort, T. F. A. de Greef and T. M. Hermans, *Chem. Soc. Rev.*, 2017, **46**, 5476 - 5490.
3. V.Balzani, M. Venturi, "*Chemistry: reading and writing the book of nature*", London, royal society of chemistry, 2014
4. (a) J. Lehn, *Angew. Chem. Int. Ed. Engl.*, 1990, **29**, 1304 - 1319; (b) K. D. Hänni and D. A. Leigh, *Chem. Soc. Rev.*, 2010, **39**, 1240-1251

5 Ł. Albrecht, G. Dickmeiss, F. C. Acosta, C. Rodríguez-Escrich, R. L. Davis, and K. A. Jørgensen, *J. Am. Chem. Soc.*, 2012, **134,** 2543 - 2546.

6 S. Gürbüz, M. Idrisa and D. Tuncel, *Org. Biomol. Chem.*,2015, **13**, 330 - 347.

7 N. M. Khashab, A. Trabolsi, Y. A. Lau, M. W. Ambrogio, D. C. Friedman, H. A. Khatib, J. I. Zink and J. F. Stoddart, *Eur. J. Org. Chem*,. 2009, **11**, 1669 – 1673.

8 M. Rězanka, M. J. Langton and P. D. Beer, *Chem. Commun.*, 2015, **51**, 4499 - 4502.

9 L. Pauling, J. Am. Chem. Soc., 1931, 53, 1367 - 1400.

10IUPAC, A.D. McNaught and A. Wilkinson, "Compendium of chemical terminology" 2nd ed. (the "Gold Book"), Blackwell scientific publications, Oxford, 1997.

11 G. Cavallo, P. Metrangolo, R. Milani, T. Pilati, A. Priimagi, G. Resnati, and G. Terraneo, *Chem. Rev*., 2016, **116**, 2478 - 2601.

12 R. H. S. Winterton, *Contemporary Physics*, 2006, **11**, 559 - 574.

13 E.V. Anslyn, D.A. Dougherty, "Modern Physical Organic Chemistry", University Science Books; Sausalito, CA, 2005.

14 W. Blokzijl and J.B. Engberts, *Angew. Chem. Int. Ed. Engl.*, 1993, **32**, 1545 - 1579.

15 D. J. Cram, *Chem. Int. Ed. Engl.*, 1986, **25**, 1039 - 1057.

16 J.M. Lehn, *Chem. Soc. Rev.*, 2007, **36**, 151 - 160.

17 A. Villers, *Compt. Rend. Acad. Sci*. 1891, 435 - 438.

18 E.M.M. Del Valle, *Process Biochemistry*, 2004, **39** 1033 – 1046.

19 S. M. N. Simones, A. Rey-Rico, A. Concheiroc and C. Alvarez-Lorenzo, *Chem. Commun.*, 2015, **51**, 6275 -6289.

20 F. Zhao, H. Yin, J. Li, *Biomaterials*, 2014, **35**, 1050 - 1062.

21 S. Tamesue, Y. Takashima, H. Yamaguchi, S. Shinkai, and A. Harada, *Angew. Chem.*, 2010, **122**, 7623 - 7626

22 M Nakahata, Y. Takashima, H. Yamaguchi and A. Harada, *Nature Communications*, 2011, **2**, 511

23 C.J. Pedersen, *J. Am. Chem. Soc.*, 1967, **89** 26, 7017 - 7036.

24 A. Gerus, K. Ślepokura, Panek, A. Turek, and J. Lisowski, *J. Org. Chem.*, 83, **12**, 6748 - 6753.

25 P. Waeles, C. Clavel, K. Fournel-Marotte and F. Coutrot, *Chem. Sci.*, 2015, **6**, 4828 - 4836.

26 P.R. Ashton, C.G. Claessens, W. Hayes, J.F. Stoddart, S. Menzer, A.J. White and D.J. Williams, *Angew. Chem. Int. Ed. Engl.*, 1995, **34**, 1862 - 1865.

27 H- Tseng, S.A. Vignon, P.C. Celestre, J. Perkins,, J.O. Jeppesen, A. Di Fabio, R. Ballardini, M.T. Gandolfi, M. Venturi, V. Balzani and J.F. Stoddart, *Chemistry - A European Journal*, 2004, **10**, 155 - 172

28 M. F. Czar and R. A. Jockusch, *Chem. Phys. Chem*, 2013, **14**, 1138 - 1148

29 E. Wasserman, *J. Am. Chem. Soc*. 1960, **82**, 4433 - 4434.

30 T. Harrison, S. Harrison, *J. Am. Chem. Soc*. 1967, **89**, 5723 - 5724.

31 C. Dietrich-Buchecker, J.P. Sauvage, *Tetrahedron Letters*, 1983, **24**, 5095 - 5098.

32 P. R. Ashton, E. J. T. Chrystal, P.T. Glink, S. Menzer, C. Schiavo, N. Spencer, J.F. Stoddart, P.A. Tasker, A. J. P. White, D. J. Williams, *Chem.–Eur. J.* 1996, **2**, 709 - 728.

33 P. R. Ashton, T. T. Goodnow, A. E. Kaifer, M. V. Reddington, A. M. Z. Slawin, N. Spencer, J. F. Stoddart, C. Vicent, D. J. Williams, *Angew. Chem. Int. Ed. Engl.*, 1989, **28**, 1396 – 1399.

34 M. Asakawa, P. R. Ashton, R. Ballardini, V. Balzani, M. Belohradsky´, M. T. Gandolfi, O. Kocian, L. Prodi, F. M. Raymo, J. F. Stoddart, and M. Venturi, *J. Am. Chem. Soc.*, 1997, **119**, 302 – 310.

35 A. D. McNaught and A. Wilkinson, "*The IUPAC Compendium of Chemical Terminology*", Blackwell Science, Oxford, 2nd edn, 1997
36J., A. Pinczewska, and S. M. Goldup, *J. Am. Chem. Soc.*, 2013, **135**, 13318 - 13321.
37 C. P. Collier, G. Mattersteig, E. W. Wong, Y. Luo, K. Beverly, J. Sampaio, F. M. Raymo, J. F. Stoddart, J. R. Heath, *Science*, 2000, **289**, 1172 - 1175
38 H. V. Schröder, S. Sobottka, M. Nößler, H. Hupatz, M. Gaedke. B. Sarkar and C. A. Schalley. *Chem. Sci.*, 2017, **8**, 6300 - 6306.
39 V. Balzani, A. Credi, F. Raymo J.F.Stoddart, *Angew. Chem. Int. Ed.*, 2000, **39**, 3348 - 3391.
40 P. Boyer, *Biochim. Biophys. Acta*, 1993, **1140**, 215 - 250
41 D. S. Goodsell, "Our Molecular Nature: The Body' s Motors, Machines, and Messages", Copernicus, New York, 1996.
42 J. Wu, "Introduction to neural dynamics and signal transmission delay", Walter de Gruyter, Berlin, 2011.
43 V. Balzani, M. Clemente-Leon, A. Credi, B. Ferrer, M. Venturi, A. H. Flood and J. F. Stoddart, *PNAS*, 2006, **103**, 1178 - 1183.
44 P. R. Ashton, R. Ballardini, V. Balzani, I. Baxter, A. Credi, M. C. T. Fyfe, M. T. Gandolfi, M. Gomez-Lopez, M.-V. Martınez-Diaz, A. Piersanti, N. Spencer, J. F. Stoddart, M. Venturi, A. J. P. White and D. J. Williams, *J. Am. Chem. Soc.*, 1998, **120**, 11932 – 11942.
45 G. Ragazzon, C. Schäfer, P. Franchi, S. Silvi, B. Colasson, M. Lucarini and A. Credi, *PNAS*, 2018, **115**, 9385-9390.
46 C. Biagini, F. Di Pietri, L. Mandolini, O. Lanzalunga, and S. Di Stefano, *Chem. Eur. J*., 2018, **24**, 10122 - 10127.
47 Y. Liu, A. H. Flood, P. A. Bonvallet, S. A. Vignon, B. H. Northrop, H.-R. Tseng, J. O. Jeppesen, T. J. Huang, B. Brough, M. Baller, S. Magonov, S. D. Solares, W. A. Goddard, C.-M. Ho and J. F. Stoddart, *J. Am. Chem. Soc.*, 2005, **127**, 9745 - 9759.
48 B. Brough, B. H. Northrop, J. J. Schmidt, H.-R. Tseng, K. N. Houk, J. F. Stoddart and C.-M. Ho, *PNAS*, 2006, **103**, 8583 - 8588.
49 a) R. P. Feynman, *Eng. Sci*. 1960, **23**, 22-36; b) R. P. Feynman, *Saturday Rev*., 1960, ***43***, 45 - 47.
50 W. Gerlach, O. Stern, *Zeitschrift für Physik*., 1922, **9,** 349 - 352.
51 S. Goudsmit and G. E. Uhlenbeck, *Physica*, 1926, **6**, 273 - 290.
52 P. A. M. Dirac, *Proc. R. Soc. Lond. A*, 1928, **117**, 610 - 624.
53 E. Zavoisky, E. 1945 *Fizicheskiĭ Zhurnal, 1945,* **9**, 211 - 245.
54 G: Gabrielse, D. Hanneke, *CERN Courier*., 2006, **46,** 8, 35 - 37.
55H. J. Schneider, F. Hacket, V. Rüdiger, *Chem. Rev*. 1998, **98**, 1755-1786.
56 H.M. McConnell, *J. Chem. Phys.*, 1956, **24**, 764 - 766.
57 E. Mileo, S. Yi, P. Bhattacharya and A. E. Kaifer, *Angew. Chem. Int. Ed.*, 2009, **48**, 5337 - 5340.
58 M. Yamanaka, A. Shivanyuk, and J. Rebek, *J. Am. Chem. Soc.*, 2004, **126**, 2939 - 2943.
59 R. G. Hicks, *"Stable Radicals Fundamentals and Applied Aspects of Odd-Electron Compounds"*, 2010, John Wiley & Sons Ltd.
60 M. Gomberg, *J. Am. Chem. Soc.*, 1900, **22**, 757 - 771.
61 O. Piloty and B. G. Schwerin, *Berichte der Deutschen Chemischen Gesellschaft* , 1901, **34**, 1870 - 1887.
62 A. N. Holden, W. A. Yager and F. R. Merity, *J. Chem. Phys*., 1951, **19**, 1319.
63 D. Griller and K. U. Ingold, *Chem Access Res.*, 1976, **9**, 13 - 19.
64 H. Hayal and B. L. Silver *J. Phys. Chem.*,1973,***77,*** 72 - 78.
65 B. Goodson, *J. Magn. Reson*., 2002, **155**, 157 - 216.
66 C. Wetter, J. Gierlich, C. A. Knoop, C. Müller, T. Schulte and A. Studer, *Chem Eur. J*., 2004, **10**, 1156 - 1166.
67 J. H. Osiecki, and E. F. Ullman, *J. Am. Chem. Soc.*, 1968, ***90***, 1078 - 1079.
68 J. Joseph, B. Kalyanaraman, and J. S. Hyde, *Biochem. Biophys. Res. Co*., 1993, **192**, 926 - 934.
69 G. Scorza, D. Pietraforte and M. Minetti, "*Free Radical Biology and Medicine"*, 1997, **22**, 633 - 642.
70 J. Zhang, M. Zhao, G. Cui and S. Peng. *Bioorg. Med. Chem*, 2008, **16**, 4019 - 4028.
71 A. Okamoto, T. Inasaki and I. Saito, *Tetrahedron Lett.*, 2005, **46**, 791 - 795.
72 M. Tamura, Y. Nakazawa, D. Shiomi, K. Nozawa, Y. Hosokoshi, M. Ishikawa, M. Takahashi, M. Kinoshita, *Chem. Phys. Lett.*, 1991, **186**, 401 - 404.
73 G. Zoppellaro, V. Enkelmann, A. Geies, and M. Baumgarten, *Org. Lett*., 2004, **6**, 4929 - 4932.

74 S.J. Lippard, *"Progress in Inorganic Chemistry"*, 1991, John Wiley & Sons Ltd.
75 A. Caneschi, D. Gatteschi, A. Grand, J. Laugier, L. Pardi, and P. Rey, *Inorg. Chem.* 1988, **27**, 1031 - 1035.
76 C. Heller and H. M. McConnell, *J. Chem. Phys.*, 1960, **32**, 1535.
77 P. Franchi, M. Lucarini and G. F. Pedulli, *Curr. Org. Chem.*, 2004, **8**, 1831 – 1849.
78 M. Lucarini, B. Luppi, G.F. Pedulli, B.P. Roberts, *Chem. Eur. J.*, 1999, **5**, 2048.
79 G.Brigati, P. Franchi, M. Lucarini, G.F. Pedulli, L. Valgimigli, *Res. Chem. Intermed.*, 2002, **28**, 131 - 141.
80 M. Boccalon, S. Bidoggia, F. Romano, L. Gualandi, P. Franchi, M. Lucarini, P. Pengo and L. Pasquato, *J. Mater. Chem. B*, 2015, **3**,432 – 439.
81 R.C. Brasch, D.A. London, G.E. Wesbey, T.N. Tozer, D.E. Nitecki, R.D. Williams, L.D. Tuck, D.P. Lallemand, *Radiology*, 1983, **147**, 773 – 779.
82 T.J. Stone, T. Bauckman, P. L. Nordio and H. M. McConnel, *Proc. Nat. Acad. Sci. U.S.A.*,1956, **54**, 1010 -1017.
83 D. Bardelang, M. Hardy, O. Ouari and P. Tordo, *"Encyclopedia of Radicals in Chemistry, Biology and Materials"*, 2012, John Wiley & sons, Ltd.
84 P. Franchi, M. Fanı`, E. Mezzina, and M. Lucarini, *Org. Lett.*, 2008, **10**, 1901 - 1904.
85 V. Bleve, C. Schfer, P. Franchi, S. Silvi, E. Mezzina, A. Credi, and M. Lucarini, *ChemistryOpen*, 2015, **4**, 18 - 21.
86 P. Franchi, V. Bleve, E. Mezzina, C. Schaefer, G. Ragazzon, M. Albertini, D. Carbonera, A. Credi, M. DiValentin and M, Lucarini, *Chem. Eur.J.*, 2016, **22**, 8745 – 8750.
87 V. Bleve, P. Franchi, L. Gualandi, F. Romano, E. Mezzina and M. Lucarini, *Org. Chem. Front.*, 2018, **5**, 1579 -1585.

2. EPR investigation of Halogen bond interaction in solution.

2.1 The Halogen bond interaction

Non-covalent interactions between molecules or between different regions of a single molecule are the driving force that allows molecular recognition or the determination of the three-dimensional conformation of a molecule's structure. In Proteins, *i.e.*, the folding of the aminoacidic sequence is crucial for its functionality as a misfolding can result in altered properties not allowing the protein to complete its specific task.[1] During the last decades great efforts were made to comprehend the nature and characteristics of many different non-covalent interactions that allowed the rational design of molecules enabling their targeted use as drugs or as functional materials. Despite the wide knowledge of many non-covalent interactions like hydrogen bonding or π-interactions, the comprehension of some of them still widely lacks. One of those is Halogen bonding (XB),[2] a non-covalent interaction that involves halogen atoms as donors, was initially observed two centuries ago by J.J. Colin who observed the blue/black coloured complex between amylose and iodine in 1814.[3] He also observed the formation of a liquid with a metallic lustre upon mixing of dry iodine and dry gaseous ammonia,[4] but the exact composition was determined only 50 years later by F. Guthrie.[5] In the following years, a great variety of XB adducts was prepared, but the interaction involving electrophilic halogen atoms and electron rich species was regarded just as charge transfer interactions and information about its nature remained fragmented and non-conclusive for a long time. We had to wait until 1961 with the work of R. Zingaro and R. Hedges,[6] who were investigating the formation of complexes between halogens and phosphine oxides and sulphides, to read for the first time the name halogen bond as term to describe this selective interaction. In 2009, in order to take a comprehensive look at this interaction, the international union of pure and applied chemistry (IUPAC) decided to systematically investigate this interaction with the objective to: "take a comprehensive look at intermolecular interactions involving halogens as electrophilic species and classify them".[7] In 2013, at the end of this research project IUPAC was able to conclusively classify this interaction with the definition: "A halogen bond occurs when there is evidence of a net attractive interaction between an electrophilic region associated with an halogen atom in a molecular entity and a nucleophilic region in another, or the same, molecular entity".[8]

2.1.1 The nature of halogen bond interaction

Halogen bond interaction is considered an analogue of the hydrogen bonding interaction and because of that, throughout the years has also been referred as "inverse hydrogen bonding" by W. Klemperer *et al.*[9] and involves an electrophilic halogen atom as donor and electron rich species as acceptors (Figure 2.1). The counterintuitive electrophilic behaviour of the halogen atom has puzzled scientists for a long time

since halogen atoms were generally regarded as sites with a high electronic density because of their intrinsically high electronegativity. Nevertheless, when a halogen atom is covalently bonded to another atom, the electronic density of the halogen is mainly localised perpendicular to the axis of the covalent bond, centred on the halogen atom while on the elongation of the bond lies a region of depleted electron density called "σ-hole" (Figure 2.2) whose electrostatic potential is less negative or, in some cases, even positive.[10]

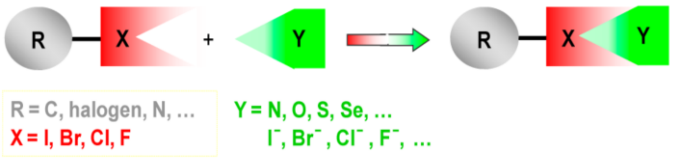

Figure 2.1 *Schematic representation of the XB interaction*

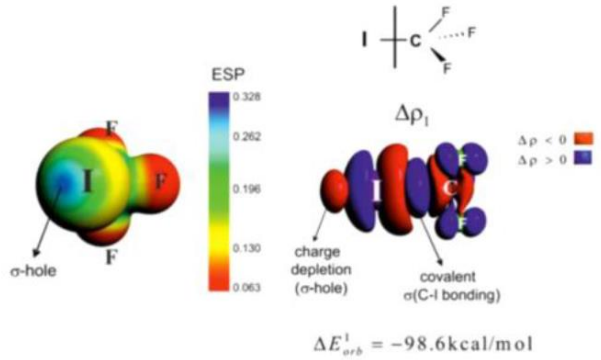

Figure 2.2 *Molecular electrostatic potential of CF_3I*

This anisotropic distribution of the electronic density is what determines the ability of the halogen atom to behave as electrophile and was first observed in 1952 when the X-ray structure of solid Cl_2 was determined and characterized by the short and perpendicular contacts between the nonbonded charge concertation of a chlorine atom and the charge depletion of another Cl atom resulting in a tightly packed structure. [11] In Figure 2.3 the polar flattening, corresponding to the σ-hole area can be seen, and its coordination with the high electronic density zone of another Cl_2 molecule, orthogonal to the plane of the Cl-Cl bond.

Acceptors are generally characterized by a region of high electronic density like molecules containing heteroatoms (N, S, O, etc..). Ethers, alcohols, carbonyl containing compounds, amines are some of the main XB acceptors reported in literature but also other electron rich compounds such as conjugated π-systems can be suitable acceptors. Experimental data revealed that the intermolecular distance between the halogen atom and the acceptor is smaller compared to the sum of Van der Waals radii of the atoms. The peculiar position of the depleted electron density also results in a highly directionality of XB, which is even more pronounced than that of HB.[2] The angle of the R-X···:N interaction is close to 180° for short and strong interactions while this value slightly decreases for longer and weaker XB interactions with

values comprised between 170° and 150°. The directionality of XB has been extensively studied, Hassel *et al.* for example reported the structure of infinite chains formed by bromine and dioxane containing "halogen molecules bridges" in which the angle between the Br_2 and the oxygen of dioxane is 178.34° by considering the axis of the Br-Br bond (Figure 2.4, top). [12] The directionality of this interaction is also reflected by observing the structure of the complex between Br_2 and benzene that also forms infinite chains with the σ-hole pointing towards the π bonding orbital of the C=C bonds as depicted in Figure 2.4 (bottom).[13]

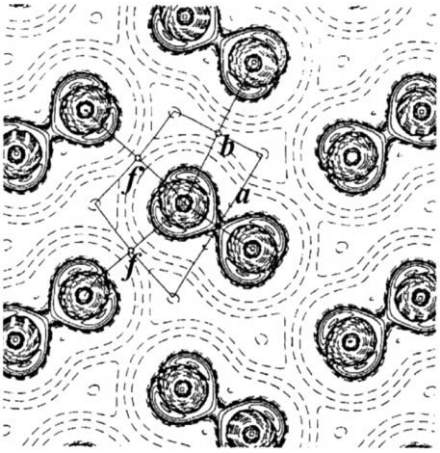

Figure 2.3 *Laplacian distribution for the (100) plane distribution of solid chlorine, black full lines correspond to high electronic density zones.*[11]

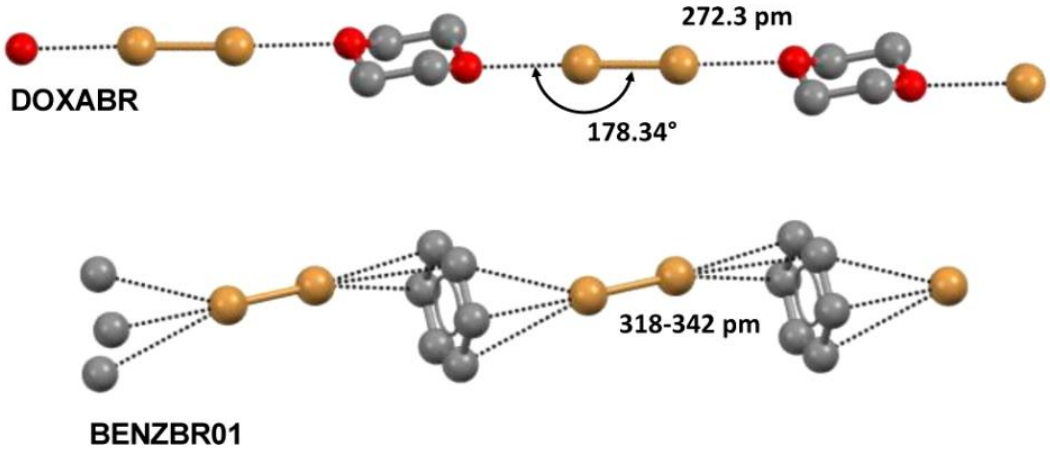

Figure 2.4 *Ball and stick representation of the infinite chains formed by dioxane (top) and benzene (bottom) with* Br_2.[12, 13]

The strength of this interaction strictly depends on the polarizability of the halogen atom and follows the order F < Cl < Br < I <At. The XB ability of astatine has been calculated to be higher than iodine, but due to its intrinsic radioactive decay with short half-life, no XB bonded complex has been described. The electronegativity of the halogen atoms and their polarizability determines the size and the magnitude

of the positive character of electrostatic potential of the *σ-hole*. Figure 2.5 shows a comparison between the molecular electrostatic potentials of CF_4, CF_3Cl, CF_3Br, CF_3I and clearly shows the decrease of the electronic density depletion area, and its extension, corresponding to the *σ-hole*, in the order CF_3I > CF_3Br > CF_3C > CF_4.[14] The positive polarization of the *σ-hole* also depends on the hybridization of the atom next to the considered halogen atom, usually represented by a carbon. For organic halides the strength of the XB donor increases by increasing the *s* character of the *sp*-hybridization of the carbon, in order C(*sp*)-X > C(sp^2)-X > C(sp^3)-X.[2] Another factor that influences the strength of the XB donor is the electron withdrawing character of the group bonded to the XB donor halogen atom, the more electron withdrawing it is, the stronger will be the interaction. Figure 2.6 reports the plot of the XB distances between XB donors and an acceptor that shows how the distance between the donor and the acceptor drops increasing the degree of fluorination of the phenyl ring bonded to the halogen atom.[15]

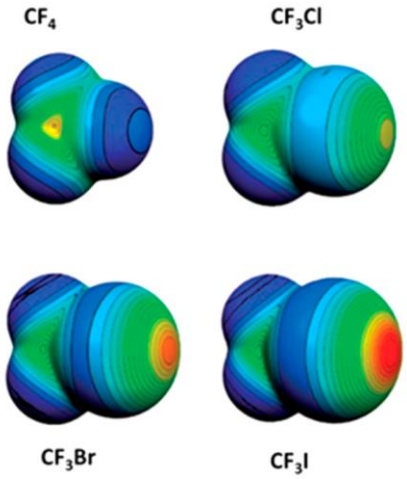

Figure 2.5 *Molecular electrostatic potential of CF_4, CF_3Cl, CF_3Br, CF_3I.*[13]

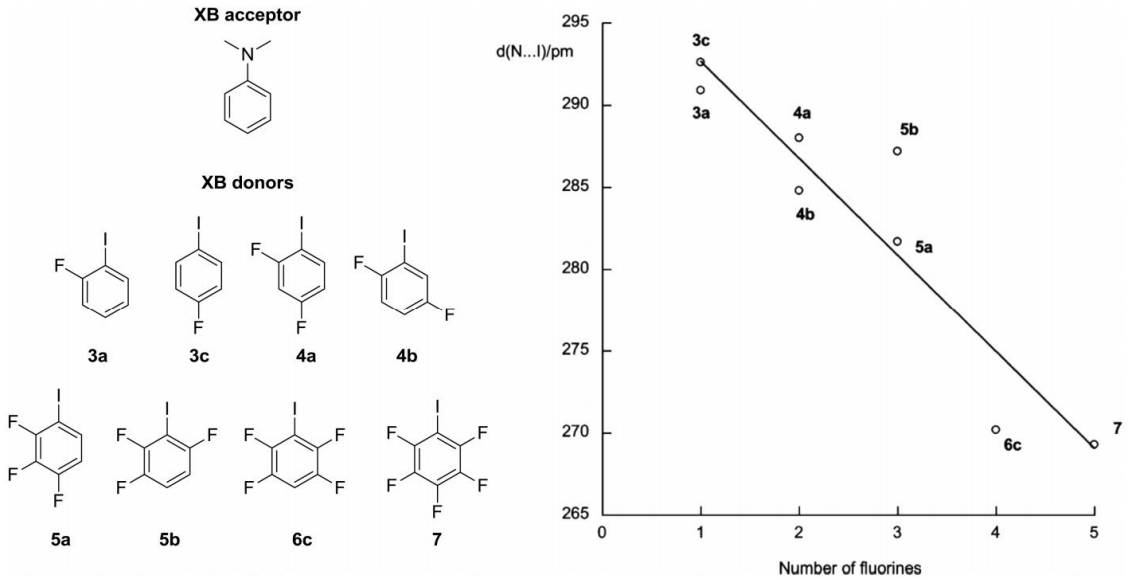

Figure 2.6 *Intermolecular distance in pm (right) between the XB donors (left, bottom) and the acceptors (left, top).*[14]

The XB interactions can be very strong, in some cases even stronger than HB, and can compete with other non-covalent interactions in molecular recognition events. The tight similarity to HB but the higher lipophilicity of halogen atoms, compared to HB donor groups, makes this interaction an interesting candidate in the design of molecular recognition patterns especially in the case of drug that requires an accurate balance between lipophilicity and hydrophilicity to allow them to be absorbed and to cross cell's membranes.[2] Due to its peculiar properties, XB interaction has been used extensively for the design and realization of self-assembling systems, crystal engineering and in drug design. Nowadays, in the pharmaceutical market almost 40% of the drugs contains one or more halogen atoms.[2] Therefore the rationalization of the XB bond interactions in the process of drug design must be precisely considered. However, because of the long debate that involved the scientific community on the nature of this interaction, experimental data regarding its properties still widely lacks, especially for the solution phase, if compared to other non-covalent interactions like HB and π-interactions. In this context we tried to give a contribution to the understanding of XB by the means of EPR spectroscopy by preparing a small set of XB donor spin probes based on the benzyl-*tert*-butyl nitroxide (BTBN) motif, and recording the possible EPR experimental spectral changes when the probe is involved in a XB bonded complex with an acceptor.[16]

2.2 Results and discussion

We have chosen the BTBN motif for the synthesis of the spin labelled XB donor probes because its high sensitivity to conformational changes is well known,[17] and could be exploited for the characterization of the XB interaction. Moreover, the intrinsic sensitivity of the nitroxyl group to the surrounding environment could assess eventual self-assembly processes. The XB donor backbone of the probe was designed to contain the 4-iodo-2,3,5,6-tetrafluoro-phenyl group, known to be one of the best XB donors groups due to the high polarization of the C-X bond when fluorine atoms are present at the *meta* and *ortho* positions respect to the iodine atom.[18]

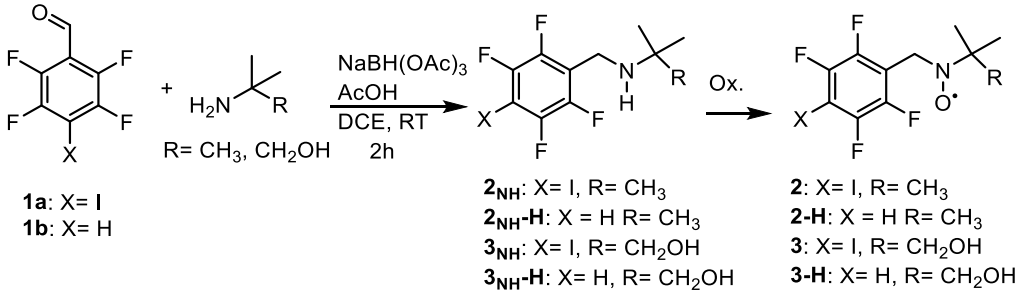

Scheme 2.1 *Synthesis of the XB donor spin probes.*

The synthesis of the spin probes was achieved by obtaining the key intermediate 4-iodo-2,3,5,6-tetrafluorobenzaldehyde that was synthesized following the procedure developed by Dumele *et al.*,[19]

starting from 2,3,5,6-tetrafluorobenzoic acid that was subjected to lithiation with 2 equivalents of n-BuLi in THF at -78°C followed by reaction with I_2 to afford 4-iodo-2,3,5,6-tetrafluorobenzoic acid. Reduction with DIBAL-H in anhydrous Et_2O afforded 4-iodo-2,3,5,6-tetrafluorobenzaldehyde **1a** in 40% yield. 2,3,5,6-tetrafluorobenzaldehyde was obtained under the same conditions omitting the lithiation/iodination step. Attempts to react **1a** following a classical reductive amination protocol, by condensation of the aldehyde with the corresponding amine, refluxing them in toluene in a Dean-Stark apparatus and then reducing the imine intermediate with $NaBH_4$ in MeOH/THF mixture failed. The treatment with the reducing agent caused the dehalogenation of the substrate affording only N-*tert*-butyl-2,3,5,6-tetrafluorobenzylamine $\mathbf{2_{NH}}$**-H** or $\mathbf{3_{NH}}$**-H**. To obtain the XB donor precursor of the spin probe, a mild one pot protocol developed by *Shah et al.*[20] was used. The aldehyde and the amine are condensed an reduced in situ with $NaBH(OAc)_3$ and glacial acetic acid in 1,2-dichloroethane (DCE) yielding the amine precursor of the spin probes $\mathbf{2_{NH}}$ and $\mathbf{3_{NH}}$. The analogues with the XB inactive hydrogen atom in para position were synthesized starting from 2,3,5,6-tetrafluorobenzaldehyde **1b** that was subsequently condensed with *tert*-butylamine or 2-methyl-2-amino-1-propanol to give $\mathbf{2_{NH}}$**-H** and $\mathbf{3_{NH}}$**-H**. The amine precursors were then oxidized to the corresponding paramagnetic spin probe with 3-chloro-perbenzoicacid (MCPBA) in the EPR cavity prior to the analysis to afford nitroxyl spin probes **2, 2-H, 3** and **3-H** (Scheme 2.1).

EPR analyses of **2** and **3** in C_6F_6 revealed a spectrum composed of 9 spectral lines, with each line presenting a triplet hyperfine structure. The spectrum was interpreted on the basis of the coupling of the unpaired electron with the nitrogen, the two benzylic protons and the fluorine atoms at the *ortho* position in the phenyl ring. For example, probe **2** (1.0 mM) was characterized by a_N = 15.64 G, $a_{2H\beta}$ = 12.00 G and a_{2F} = 0.92 G. The value of $a_{2H\beta}$ of **2** shows a significant increase compared to that of BTBN ($a_{2H\beta}$ = 7.66 G) in the same experimental conditions and this dramatic difference was attributed the steric hindrance due to the presence of fluorine atoms at the ortho positions that increases the importance of conformations in which the dihedral angle θ between the symmetry axis of the $2p_z$ orbital, occupied by the unpaired electron, and the planes of the H-C-N bonds, is close to 30°, according to the Heller-McConnel equation (Figure 2.7).[21] Accordingly, eventual variations of the probe conformation resulting from the formation of the XB bonded complex is expected to be connected to a variation of the value of $a_{2H\beta}$.

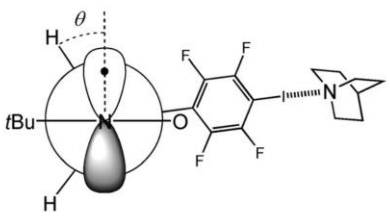

Figure 2.7 *One of the possible conformations of probe* ***2*** *while involved in a XB bonded complex with quinuclidine, a XB acceptor.*

Actually, upon addition of quinuclidine (Q), to probe **2**, we observed a significant decrease of $a_{2H\beta}$ ($a_{2H\beta}$ = 11.47 G) and, to a lesser extent, a variation of a_{2F} (a_{2F} = 0.84 G) reflecting a geometrical variation of the probe while involved in the XB complex (Figure 2.8).

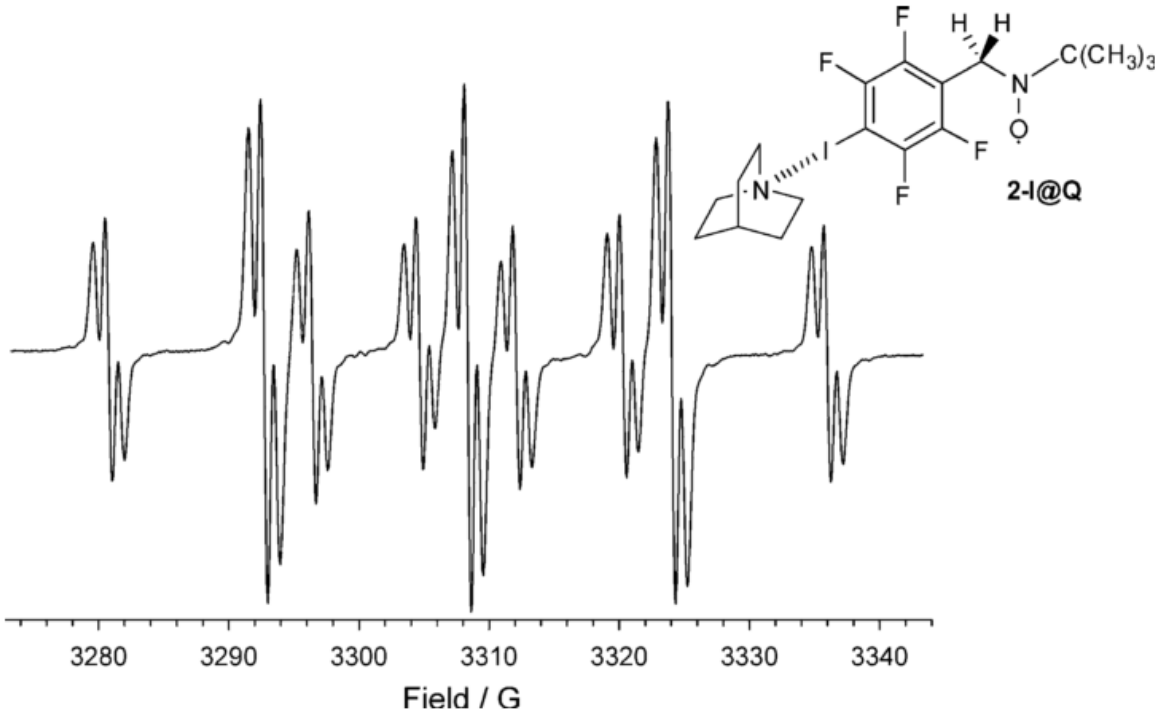

Figure 2.8 *EPR spectrum of **2** recorded in C6F6 at 298 K in presence of Q (1M).*

It is important to observe that the nitrogen's splitting constant does not change significantly (a_N = 15.60 G) and this implies that the spectroscopic variation caused by the interaction between probe **2** and quinuclidine are caused by a specific interaction that takes place far away from the paramagnetic centre. If those variations were caused by a general medium effect, like a change in polarity of the surrounding media, the value of a_N would have been affected. Repeating the same experiments with the XB inactive probe **2-H** confirmed that the spectroscopic variations are due to an XB interactions, because after the addition of a large excess of quinuclidine, probe **2-H** did not show any significant spectroscopic variation. In particular probe **2-H** was characterized by a_N = 15.65 G, $a_{2H\beta}$ = 11.97 G and a_{2F} = 0.89 G while after the addition of quinuclidine the splitting constant changed to a_N = 15.69 G, $a_{2H\beta}$ = 11.91 G and a_{2F} = 0.87 G.

By performing an EPR titration we monitored the variation of $a_{2H\beta}$ in function of the concentration of quinuclidine (grey circles, Figure 2.9). The theoretical dependence (black line) of $a_{2H\beta}$ on XB acceptor concentration, represented in the plot, was obtained by numerically fitting of the experimental data and considering the value of the equilibrium constant for the formation of XB complex (K_{XB}) as adjustable parameter.

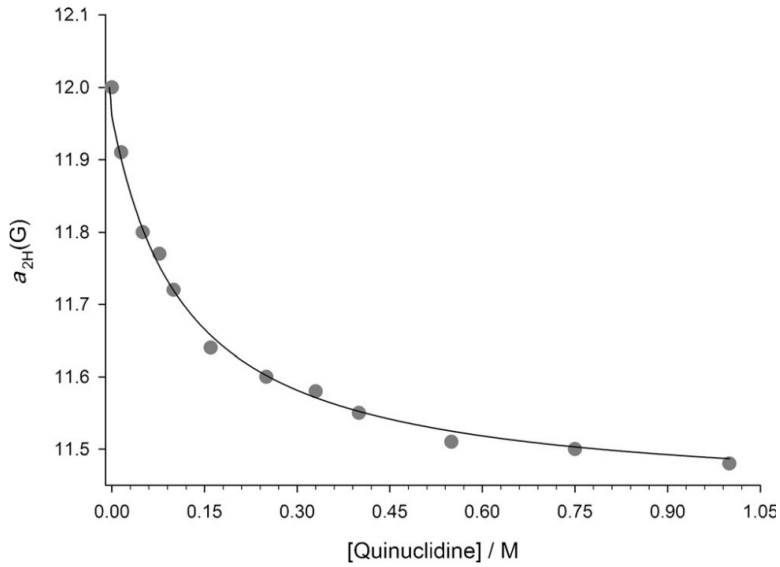

Figure 2.9 *Plot of $a_{2H\beta}$ of probe **2** (ca 0.1 M) versus the concentration of quinuclidine at 294 K in C_6F_6.*

To obtain the molar fractions of the free probe and of the probes involved in the XB complex we had to take into account that the rate of formation and dissociation of the XB complex is larger compared to the timescale of the EPR analysis and the experimental spectrum represents in this case a concentration weighted average. However, under these conditions it is possible to obtain the values of the molar fractions values for the free and complexed probes by using equation 2.1:

$$a_{EPR} = a_2 X_2 + a_2@Q X_2@Q \qquad (2.1)$$

in which a_2 corresponds to the $a_{2H\beta}$ value of probe **2**, a_2@Q is the benzylic splitting of **2** involved in the XB complex with Q and X_2, X_2@Q are the molar fractions of the free and complexed nitroxide. The variations of $a_{2H\beta}$ represented in Figure 2.8 were well modelled by the proposed 1:1 binding isotherms using standard curve fitting method assuming K_{XB}= 8.2 M^{-1}.

This value is lower than that reported in literature for the XB interaction between pentafluoriodobenzene (C_6F_5I) and Q in cyclohexane at 298 K (K_{XB}= 20 M^{-1}) and could be due to the presence of the *para*-methylene unit in the probe's structure whose weak electron-donating character lowers the polarization of the electronic density of the halogen atom, resulting in a weaker XB donor ability compared to the strong EWG fluorine atom in *para* position of C_6F_5I.

The XB donor ability of probe **3** was also investigated under the same conditions ([**2**] = 0.1 mM, C_6F_6, 294 K). The values of the hyperfine splitting constants for probe **3** were found to be very similar to those of probe **2**, with a_N = 15.54 G, $a_{2H\beta}$ = 12.50 G and a_{2F} = 0.86 G. The addition of Q resulted in spectroscopic changes similar to those of probe **2**. The correlation between the variation of the values of $a_{2H\beta}$ and a_{2F} was also in this case verified by repeating the same experiments with the XB inactive probe **3-H** whose spectroscopic parameters remained almost unchanged after the addition of [Q] = 0.1

M. However, after the addition of an excess of Q (up to 0.7 M) to **3-H**, $a_{2H\beta}$ value decreased to 12.20 G. This variation can be attributed to the presence of the hydroxyl group that interacting with Q via hydrogen bonding, affects the conformation of the probe. In presence of [Q] = 0.7 M, the EPR spectra of probe **3** was characterized by a_N = 15.30 G, $a_{2H\beta}$ = 11.92 G and a_{2F} = 0.85 G but in this case the EPR titration with Q revealed a deviation from the proposed model caused by the presence of the hydroxyl group whose HB ability influences the geometry of the probe and the value of $a_{2H\beta}$ for concentrations of Q above 0.1 M. The deviation from the proposed 1:1 binding model is shown in Figure 2.10 that reports the trend of $a_{2H\beta}$ versus the concentration of Q for probe **3**.

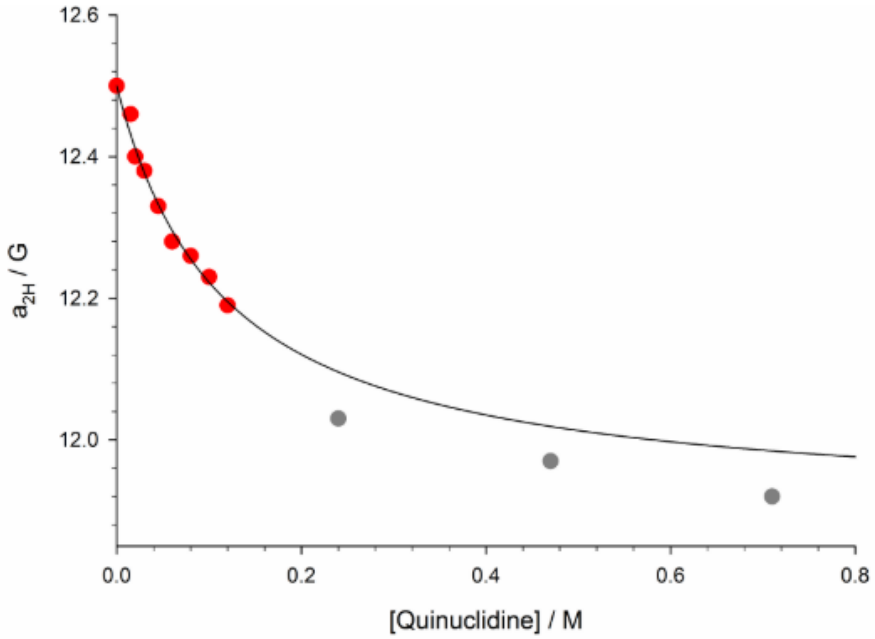

Figure 2.10 *Plot of the dependence of $a_{2H\beta}$ for probe **3** versus the concentration of Q at 294 K in C_6F_6. Red points correspond to the measured $a_{2H\beta}$ values for concentrations of Q below 0.1M. Values above this concentration (grey points) were not taken into account for the determination of K_{XB}. The black line represents the theoretical dependence of $a_{2H\beta}$ from [Q].*

However, for concentrations below 0.1 M the variation of $a_{2H\beta}$ for probe **3** was found to be coherent with the behaviour of probe **2** and for this range of concentration we were able to obtain the equilibrium constant for the interaction between **3** and Q which was found to be K_{XB}= 8.6 M^{-1}, in excellent agreement for the value found for probe **2**. Because of the ability of **3** to interact with Q both via XB and HB, we decided to limit further experiments to probe **2** whose XB donor ability was then assessed with various XB acceptors. Triethylamine (Et_3N, Figure 2.11), 1,4-diazabicyclo[2.2.2]octane (DABCO, Figure 2.12), tri-butyl phosphine oxide (Bu_3PO, Figure 2.13) were tested as XB acceptors in trimethylpentane (TMP) at 223 K with probe **2**. The presence of the XB acceptor resulted in all cases in a variation of $a_{2H\beta}$ of probe **2** allowing us to obtain K_{XB} for the XB interaction with each acceptor.

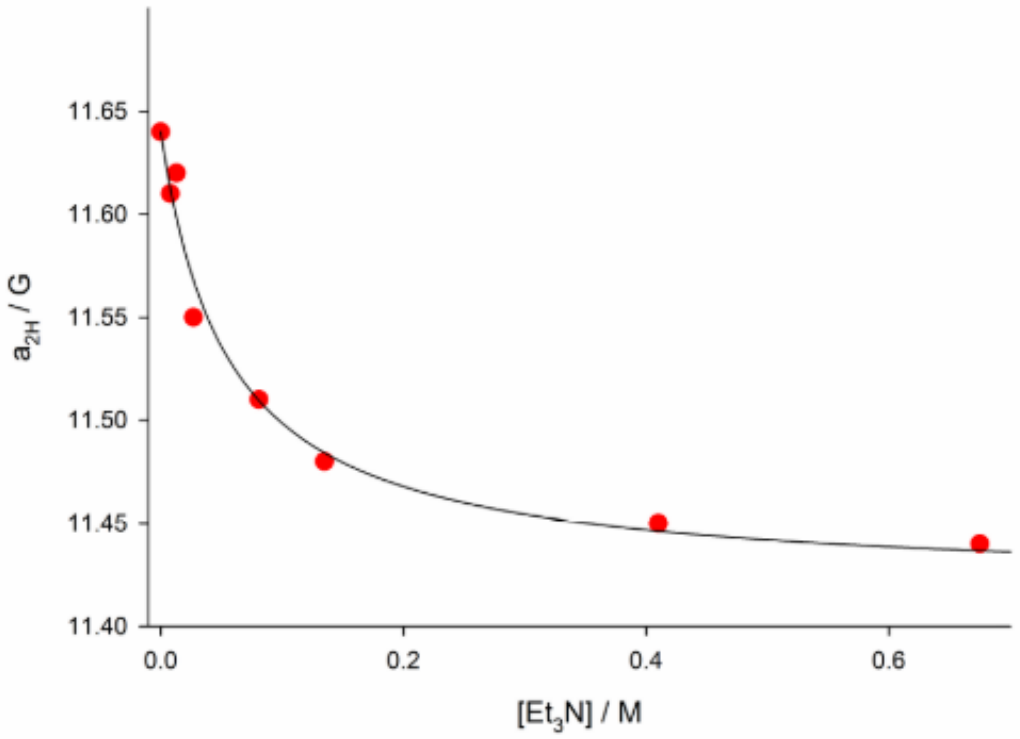

Figure 2.11 *Plot of the dependence of* $a_{2H\beta}$ *for probe* ***2*** *(ca. 0.1 mM) versus the concentration of triethylamine at 223 K in TMP. Red dots correspond to experimentally determined* $a_{2H\beta}$ *values, black line represents the theoretical dependence of* $a_{2H\beta}$ *from* [Et_3N].

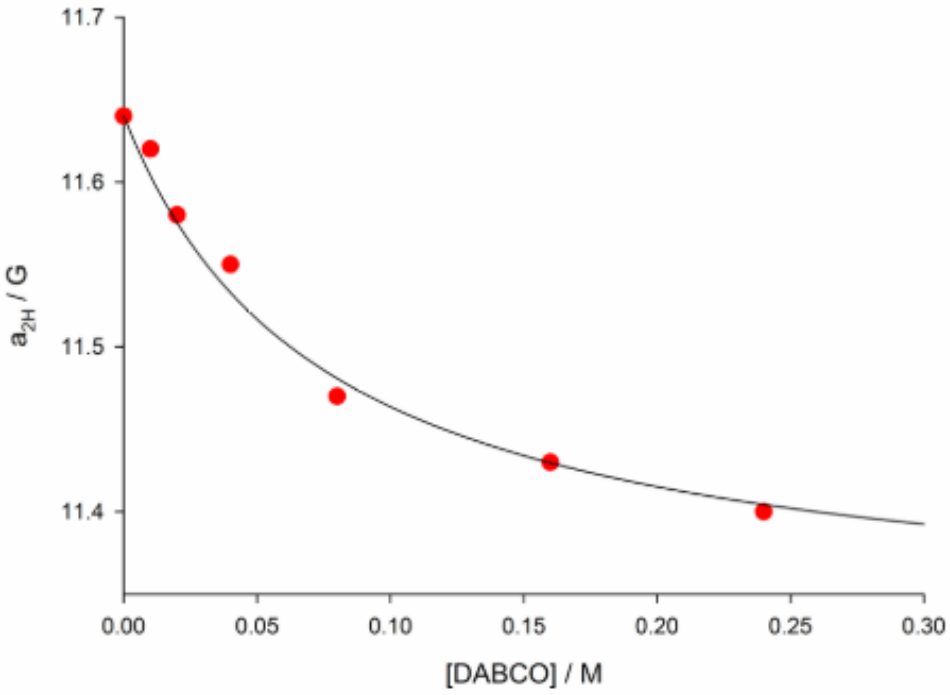

Figure 2.12 *Plot of the dependence of* $a_{2H\beta}$ *for probe* ***2*** *(ca. 0.1 mM) versus the concentration of DABCO at 223 K in TMP. Red dots correspond to experimentally determined* $a_{2H\beta}$ *values, black line represents the theoretical dependence of* $a_{2H\beta}$ *from [DABCO].*

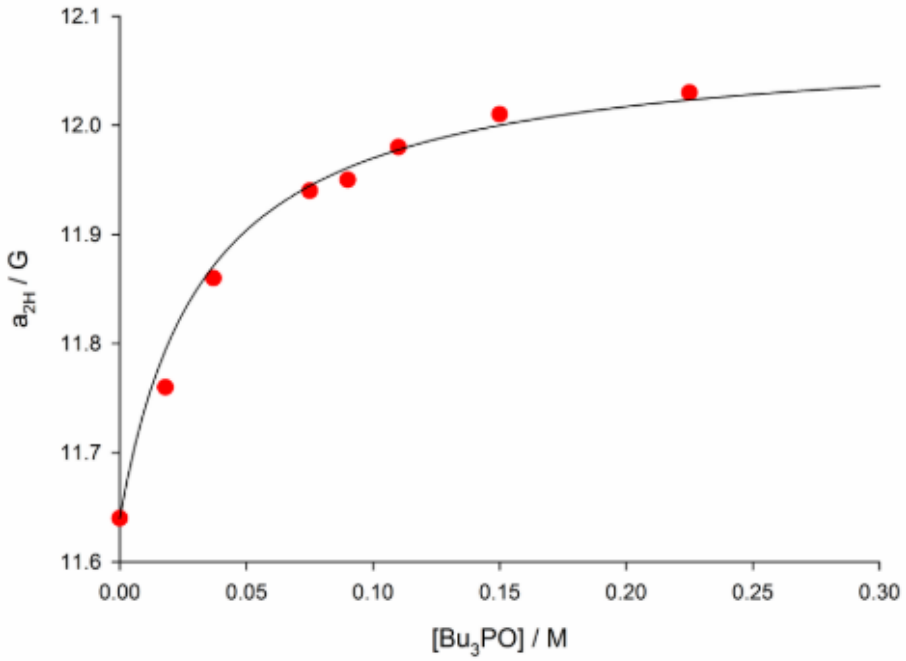

Figure 2.12 *Plot of the dependence of $a_{2H\beta}$ for probe **2** (ca. 0.1 mM) versus the concentration of Bu_3PO at 223 K in TMP. Red dots correspond to experimentally determined $a_{2H\beta}$ values, black line represents the theoretical dependence of $a_{2H\beta}$ from [Bu_3PO].*

Table 2.1 *Equilibrium constants for the XB interaction of probes **2** and **3** with various XB acceptors determined by EPR titrations.*

Probe	XB acceptor	Solvent	T [K]	K_{XB} [M^{-1}]
2	Quinuclidine	C_6F_6	294	8.2 ± 1
3	Quinuclidine	C_6F_6	294	8.6 ± 2
2	Quinuclidine	TMP	294	11 ± 2
2	Quinuclidine	TMP	274	25 ± 4
2	Quinuclidine	TMP	243	51 ± 8
2	Quinuclidine	TMP	223	109 ± 15
2	Quinuclidine	TMP	203	220 ± 20
2	Et_3N	TMP	223	18 ± 3
2	DABCO	TMP	223	13 ± 2
2	Bu_3PO	TMP	223	29 ± 5
2	Quinuclidine	ACN	243	30 ± 4
2	Cl^-	ACN	243	25 ± 5

All the XB acceptors caused a decrease of $a_{2H\beta}$ values except Bu_3PO that produces an increase of the β-hydrogens hyperfine splitting constant. However, also in this case, it was possible to obtain K_{XB} for the interaction. The experimental results are summarized in Table 2.1 and were found to be in good

agreement with those previously reported in literature. [18,22] The measured K_{XB} values were found to follow the order quinuclidine>Bu_3PO>Et_3N>DABCO.

When we tried to measure the affinity of chloride anion towards the XB donor we observed no variations in the spectroscopic parameters of probe **2** and this could be due to the absence of XB interaction between the donor and the acceptor or to the absence of conformational variation between the free and complexed probe. To better understand the behaviour of the probe in presence of Cl^- we repeated the EPR experiment in presence of Q as competitive ligand for **2**. The EPR titration was then carried out by addition of Bu_4NCl to a solution of **2** in ACN in presence of Q (0.38 M). Under these competing conditions the addition of Cl^- resulted in a variation of $a_{2H\beta}$ caused by the displacement of quinuclidine as XB acceptor by the chloride anion (Figure 2.14).

This competition experiment allowed us to determine the equilibrium constant for the XB interaction between chloride anion and **2** by considering equation 2.2:

$$[\mathbf{2}@Q] / [\mathbf{2}@Cl] = (K_{Cl}\,[Cl]) / K_{XB}\,[Q] \qquad (2.2)$$

in which [**2**@Q] is the concentration of **2** involved in the XB complex with quinuclidine, [**2**@Cl] is the concentration of **2** involved in the XB complex with chloride anion, K_{Cl} and K_{XB} the equilibrium constants for the association in the XB complex, respectively, of Cl^- and Q, [Cl] the concentration of chloride anion and [Q] the concentration of quinuclidine. By this method it was possible to determine the equilibrium constant for the XB interaction between chloride anion and probe **2** that corresponds to K_{Cl} = 25 M^{-1}. It is worth noting that even if K_{Cl} is modest in comparison to those of the best synthetic chloride receptors using halogen bonding alone as recognition interaction,[18,23] it is however sufficiently high to be detected by our competitive EPR method.

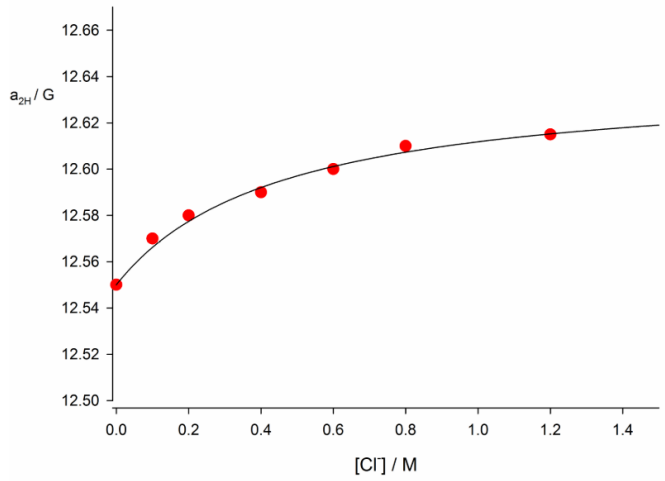

Figure 2.14 *Plot of the dependence of $a_{2H\beta}$ for probe **2** (ca. 0.1 mM) versus the concentration of $Bu_4N^+Cl^-$, at 243 K in ACN in presence of quinuclidine 0.38 M. Red dots corresponds to experimentally determined $a_{2H\beta}$ values, black line represents the theoretical dependence of $a_{2H\beta}$ from [Q].*

To have a deeper understanding of the XB interaction we repeated the EPR titrations with **2** and Q at various temperatures in order to determine the thermodynamic parameters for the formation of the XB complex. The measurements of the variation of $a_{2H\beta}$ of **2** caused by the addition of increasing amounts of Q were carried out in 2,2,5-trimethylpentane (TMP) in the 203-298 K temperature range. The experimental dependence is shown in Figure 2.15.

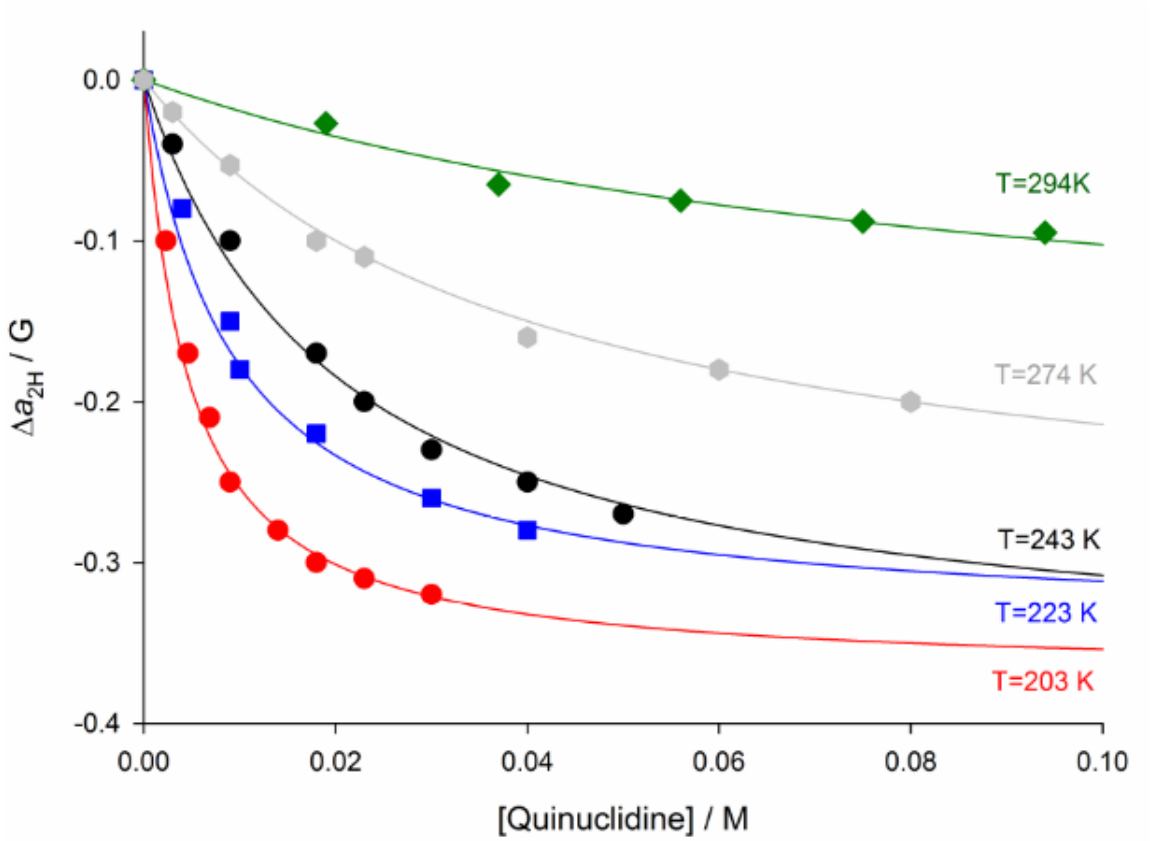

Figure 2.15 *Plot of the dependence of $a_{2H\beta}$ for probe **2** (ca. 0.1 mM) versus the concentration of* Q*, at various temperatures TMP. Dots corresponds to experimentally determined variation of $a_{2H\beta}$, solid lines represent the theoretical dependence of $a_{2H\beta}$ variation from [Q].*

The numerical fitting of each curve and the exploitation of equation 2.1 gave us the value of K_{XB} at each temperature. The enthalpic and entropic parameters were calculated from the corresponding van't Hoff plot (Figure 2.16).

The enthalpic contribution, corresponding to ΔH = -3.9 kcal mol^{-1}, was found to be consistent with the range of enthalpic variations reported in the literature for the formation of XB complexes with the same or other nitrogen containing acceptors.[22] The loss of entropy, corresponding to ΔS = -8.6 kcal mol^{-1}, was also found to be consistent with the range of entropic variations reported in literature for various XB complexes.[22]

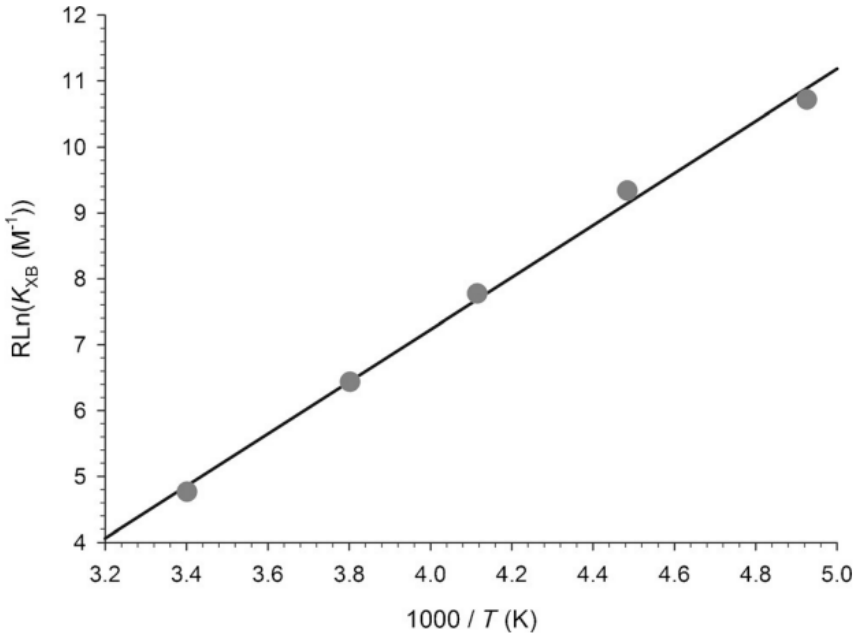

Figure 2.16 *Van't Hoff plot for the temperature dependence of K_{XB} for the formation of a XB complex between 2 and Q, in TMP.*

2.3 Conclusions

In this work, we have developed a new method for the detection and characterization of the XB interaction in solution. It was realized by the use of specifically designed XB donor spin probes and EPR spectroscopy. It represents the first direct EPR method for the detection of this interaction in solution and has proven to be a reliable and sensitive analytical approach. This method can be exploited also in fluorinated solvents (*i.e.* C_6F_6) that must be avoided for obvious reasons when investigating XB interaction by the means of ^{19}F-NMR. The experimental data obtained with this method was found to be in good agreement with those obtained by other methods, previously reported in literature. This method can also be used when the formation of the XB adduct does not induce variations in the probe's conformation, like in the case of chloride anion by performing competitive EPR experiments in presence of quinuclidine. With this approach we were also able to obtain the thermodynamic parameters for the XB interaction by performing VT-EPR experiments.

2.4 References

1 J.M. Berg, J.L. Tymoczko, L. Stryer, "*Biochemistry*", 5th ed., New York, W H Freeman; 2002.
2 G. Cavallo, P. Metrangolo, R. Milani, T. Pilati, A. Priimagi, G. Resnati and G. Terraneo, *Chem. Rev.* 2016, **116**, 2478−2601.
3 M. M. Colin, H. Gaultier de Claubry, *Ann. Chim*., 1814, **90**, 87−100.
4 M. Colin, *Ann. Chim.*, 1814, **91**, 252−272.
5 F. Guthrie, *J. Chem. Soc.*, 1863, **16**, 239−244.
6 R. A. Zingaro, M. Hedges, *J. Phys. Chem.*, 1961, **65**, 1132−1138.
7 Project No. 2009-032-1-100. Categorizing Halogen Bonding and Other Noncovalent Interactions Involving Halogen Atoms. *Chem. Int.* 2010, **32**, 20−21.
8 G. R. Desiraju, P.S. Ho, L. Kloo, A.C. Legon, R Marquardt, P. Metrangolo, P. Politzer, G. Resnati, K. Rissanen, (IUPAC Recommendations 2013), *Pure Appl. Chem*., 2013, **85**, 1711−1713.
9 S. E. Novick, K.C. Janda, W. Klemperer, *J. Chem. Phys.*, 1976, **65**, 5115 - 5121.
10 T. Clark, M. Hennemann, J. S. Murray and P. Politzer, *J Mol Model*, 2007, **13**, 291–296.
11 V. G. Tsirelson, P. F. Zhou, T. H. Tang, R. F. W. Bader, *Acta Crystallogr., Sect. A: Found. Crystallogr.*, 1995, **51**, 143−153.
12 O. Hassel, J. Hvoslef, *Acta Chem. Scand*., 1954, **8**, 873.
13 O. Hassel, K. O. Stromme, *Acta Chem. Scand*, 1958, **12**, 1146.
14 T. Clark, M. Hennemann, J. S. Murray, P. Politzer, *J. Mol. Model.*, 2007, **13**, 291-296.
15 C. Prasang, A. C. Whitwood, D.W. Bruce, *Crystal Growth & Design*, 2009, **9**,5319-5326.
16 L. Gualandi, E. Mezzina, P. Franchi, and M. Lucarini, *Chem. Eur. J*., 2016, **22**, 16017 – 16021
17 P. Franchi, M. Lucarini and G. F. Pedulli, *Curr. Org. Chem.*, 2004, **8**, 1831 – 1849.
18 M. G. Sarwar, B. Dragisic, L. J. Salsberg, C. Gouliaras, M. S. Taylor, *J. Am. Chem. Soc*., 2010, **132**, 1646–1653.
19 O. Dumele, N. Trapp, F. Diederich, *Angew.Chem. Int. Ed.*, 2015, **54**, 12339 –12344; *Angew. Chem.*, 2015, **127**, 12516 –12521.
20 A. F. Abdel-Magid, K. G. Carson, B. D. Harris, C. A. Maryanoff, R. D. Shah, *J. Org. Chem*., 1996, **61**, 3849-3862.
21 C. Heller, H. M. McConnell, *J. Chem. Phys*., 1960, **32**, 1535.
22 F. Biedermann, H.-J. Schneider, *Chem Rev.*, 2016, **116**, 5216 – 5300.
23 E. Dimitrijevic, O. Kvak, M. S. Taylor, *Chem. Commun*. 2010, **46**, 9025–9027.

3. EPR sensing of metal and organic cations using a novel spin-labelled dibenzo-24-crown-8-ether.

Since their discovery by the Nobel prize Charles Pedersen[1] half a century ago, crown ethers and their derivatives have been extensively used for the synthesis of MIMs.[2] Crown ethers are macrocyclic molecules constituted by repeating ethylene glycolic units (Figure 3.1a). The host properties of these macrocycles are widely appreciated and used as binding motif for many supramolecular assemblies. They can interact very well with both inorganic and organic cations because of the presence of the oxygens, that can be good acceptors for hydrogen bonding and charge transfer interactions. Metal cations, like Na^+, K^+ are known to be good guests. Organic cations, like protonated amines are also widely used because of their good binding with crown ethers. The possibility of modification in the crown ether structure allowed many researchers to expand the recognition pattern of these macrocycles. Dibenzo crown-ethers are for example derivatives of crown ethers in which two ethylene glycolic units have been replaced by two catechol rings (figure 3.1b). The presence of these fused phenyl rings also allows to exploit π interactions with guests like Dibenzylammonium hexafluorophosphate.[3]

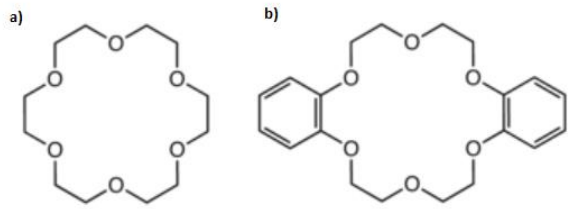

Figure 3.1 *a) a crown ether, b) a dibenzo-crown ether.*

In the literature there are several different examples of functionalized crown ethers that were used for their self-assembly properties as sensors,[4] in the synthesis of stimuli responsive rotaxanes [5] and in functional materials.[6]

The binding properties of this class of macrocycles has been explored by the means of many analytical techniques like ^{1}H-NMR and UV-vis spectroscopy.

3.1 Spin labelled crown ethers

Because of its favourable characteristics for the investigation of supramolecular assemblies, EPR spectroscopy has already been used for the characterization of inclusion complexes of crown ethers, and this was achieved in general by labelling the crown ether with persistent nitroxide derivatives like TEMPO and proxyl radicals. An example of this approach is the work by Ishizu and co-workers[7] in

which they describe the synthesis of a benzo-15-crown-5 ether labelled with a TEMPO radical (Figure 3.2).

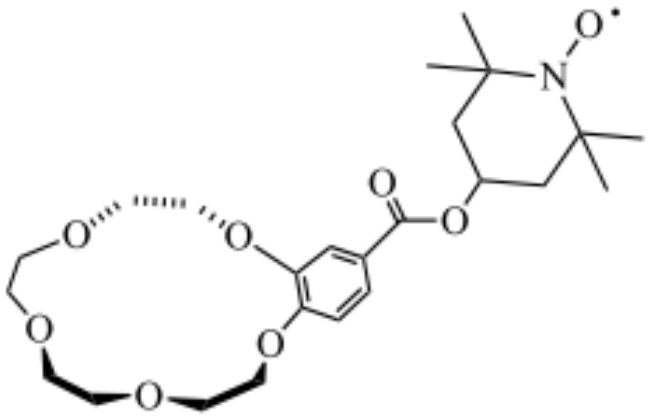

Figure 3.2 *The spin labelled benzo-15-crown-5 ether reported by Ishizu and co-workers.*[7]

The EPR analysis of this macrocycle was characterized by the presence of three spectral lines, with a 1:1:1 relative intensity, consistent with a TEMPO monoradical and with a line separation determined by the nitrogen hyperfine splitting constant a_N = 15.86 G and a g-factor g_0 = 2.0058. To investigate the complexing properties towards alkali metal cations of this macrocycle, the EPR experiments were repeated in presence NaSCN and KSCN as metal cation sources. The addition of NaSCN did not produce any significant change in the spectral features of the spin labelled crown ether. On the contrary, the addition of half equivalent of KSCN to a solution of the macrocycle resulted in a dramatical change of EPR spectra. The three- line spectrum changed to a 5- line spectrum (see figure 3.3), resulting from the through space spin-spin coupling between the radical labels of two macrocycles. This behaviour has been attributed to the formation of a 2:1 sandwich-like complex between the macrocycle and K^+. The separation of the new lines in the spectra was found to be a_N = 7.92 G corresponding to half of the original a_N of the macrocycle confirming the diradical nature of the complex. Complexes with other metals were however not reported.

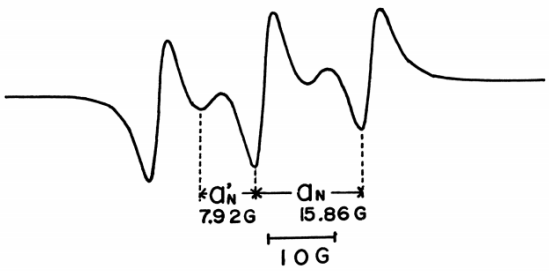

Figure 3.3 *The EPR spectra of the spin labelled crown ether reported by Ishizu and co-workers in presence of 0.5 eq. of KSCN.*[7]

Other examples of spin labelled crown ethers have been described but their ability to report the formation of an inclusion complexes with guest was poor, mainly due to very small variations in the EPR spectra or to a poor complexing ability of the labelled macrocycle. These variations regarded mainly the nitrogen hyperfine splitting constant. The introduction of the nitroxyl radical directly on the glycolic chains (Figure 3.4), as reported by Eastman *et al.*,[8] was not favourable for the complexation of metals.

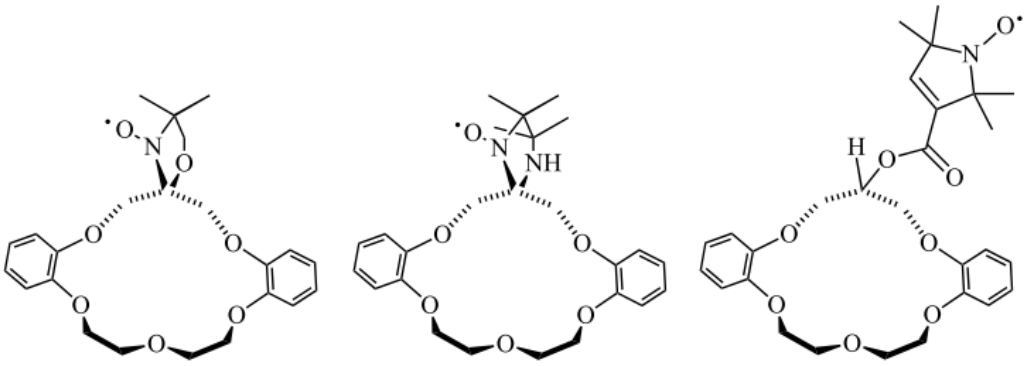

Figure 3.4 *The spin labelled crown ethers reported by Eastman et al.*[8]

The EPR investigation of the macrocycles, in presence of NaSCN was however characterized by only small spectral changes, that cannot be directly attributed to the formation of a complex between the labelled crown ethers and Na^+.

Further investigations revealed that the conformation of the three crown ethers was characterized by intramolecular interactions between the hydrogens of the propylene bridge and the glycolic oxygens that disrupted the ability of the cavity of the crown ethers to host the metal ion. Moreover, X-ray diffraction also revealed that the nitroxyl fragment points outwards, away from the cavity of the macrocycle, preventing in this way interactions between the paramagnetic centre and the metal ion, if the complex is somehow present in solution. Further attempts were made by Dugas *et al.*[9]who reported the synthesis of di- and tetra-spin labelled 18-crown-6 ethers (Figure 3.5). In this case the addition of KSCN as potassium source resulted in a variation of the EPR parameters of the crown ethers. In particular, the di-spin labelled 18-crown-6 EPR spectra was characterized by 3 spectral lines, characteristic of a biradical with no interaction between the radical fragments ($J = 0$) while in presence of K^+ a five-line spectra was observed, characteristic of a diradical with a spin-spin coupling between the paramagnetic centres ($J \neq 0$). The different spectra result from an altered conformation induced by the cation complexed within the cavity of the macrocycle with the two spin labels closer to each other, allowing the through space spin-spin interaction. The spectral variations were however found to be very small and do not allowed further investigations on the host properties of the spin labelled crown ether. Moreover, the host properties of these macrocycles with other metal cations were not described.

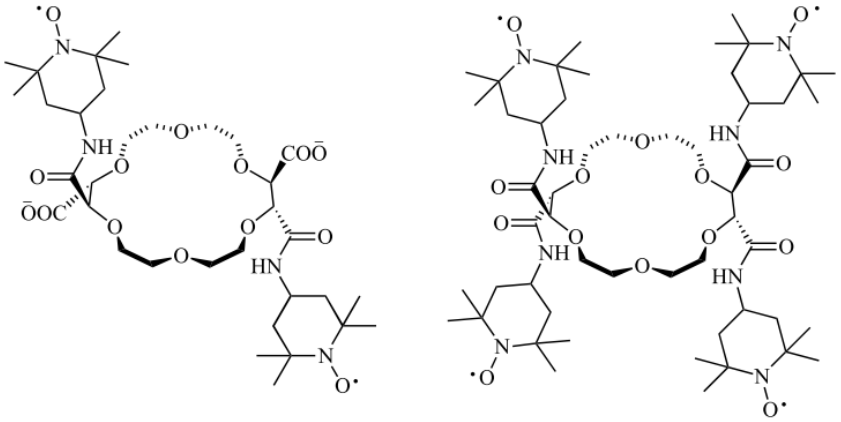

Figure 3.5 *The diradical (left) and tetra-radical (right) 18-crown-6 ethers reported by Dugas et al.*[9]

All the examples reported relied on the measurement of the variation of the nitrogen hyperfine splitting constant (a_N) or of the spin-spin exchange constant (J) for the detection of the presence of inclusion complexes between crown ethers and metal cations. However, these two parameters usually led to small changes, and in the case of a_N, it was not exclusively related to the formation of an inclusion complex, because its variation may also result from a general media effect, caused by a variation the polarity of the surrounding media.

To improve the reporting of the sensing ability of spin labelled crown ethers, we decided to introduce the benzyl-*tert*-butyl nitroxide (BTBN) group on the structure of a dibenzo-24-crown-8 ether (DB24C8). The choice of the BTBN group was inspired by the idea to use the β-hydrogens hyperfine splitting constant ($a_{2H\beta}$) to report the formation of inclusion complexes because of its high sensitivity to changes in the host's conformation that usually are induced by the complexation event. In particular, the variation of the resonance field of the $M_I(2H_\beta) = \pm 1$ lines can be a specific indication of the inclusion of a guest. Moreover, in crown ethers in which a fused macrocycle is present like the dibenzo-24-crown-DB24C8, the label can be introduce directly on one phenyl ring, minimizing the steric hindrance of the label and thus hopefully avoiding negative effects on the host performances of the crown ether. For these reasons we decided to design and synthesize two new mono-spin labelled DB24C8 bearing the BTBN structure label, fused with one of the two phenyl rings.[10]

3.2 Results and discussion

The synthesis of the amine precursor (**4a**) of BTBN functionalized DB24C8 spin probe **5a** was carried out by reductive amination with *tert*-butyl amine (Scheme 3.1) of formyl-DB24C8, that was synthesized according to the procedure reported by Liu and co-workers.[11] Formyl DB24C8 was refluxed in methanol with *tert*-butylamine in methanol and the formation of the imine intermediate was checked via TLC. Once the condensation was complete, the imine intermediate was reduced with $NaBH_4$. the reaction was quenched with 1M HCl and MeOH removed *in vacuo*. The product was resuspended in 1M NaOH and

the aqueous layer extracted with DCM that was dried on $MgSO_4$ and removed *in vacuo* to yield the crude product. Pure compound **4a** was obtained after purification on silica gel. The amine precursor **4b** of spin probe **5b** was synthesized under the same conditions by condensation of formyl-DB24C8 and 2-methyl-2-amino-1-propanol.

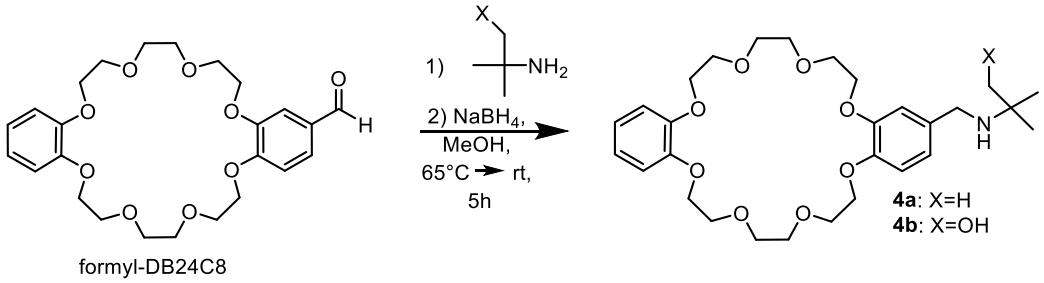

Scheme 3.1 *Synthesis of the amine precursors **4a** and **4b**.*

The EPR active spin probes were obtained by *in situ* oxidation of the amine precursors **4a** and **4b** with MCPBA directly into the EPR capillary affording the spin probes **5a** and **5b** (Figure 3.6).

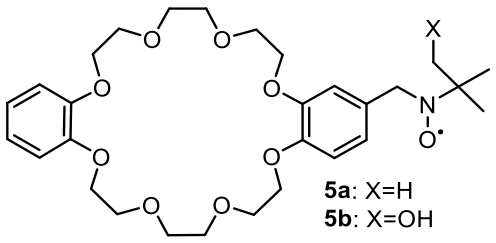

Figure 3.6 *The spin labelled DB24C8 **5a** and **5b**.*

The X-band EPR spectra of probe **5a** 1.0 mM in methylene chloride (DCM) in presence of MCPBA 1.0 mM showed the characteristic spectra of the BTBN radical, with 9 spectral lines (see Figure 3.7a) resulting from the coupling of the unpaired electron with the nitrogen (a_N = 15.32 G) and the two hydrogens in β position ($a_{2H\beta}$ = *8.06 G*). Similar results were obtained for probe **5b** that was characterized, under the same conditions, by a_N = 15.38 G and $a_{2H\beta}$ = 8.48 G.

3.2.1 Complexation studies with metal cations.

To evaluate the host properties of the spin labelled macrocycles, alkali metal iodides or picrates ($\mathbf{M}^+$) were used as guests. Despite their almost complete insolubility in DCM, when the host precursors **4a** or **4b** were added to a $\mathbf{M}^+$ saturated DCM solution, full solubilization of the salt was observed, indicating the formation of an inclusion complex with the hosts. The subsequent addition of MCPBA to the solution

oxidized the diamagnetic host to the corresponding paramagnetic EPR active spin labelled crown ethers, allowing us to record their respective EPR spectra that were characterized by the presence of additional lines, caused by the variation of $a_{2H\beta}$.and attributable to the probe involved in the complex with $\mathbf{M}^+$ and in equilibrium with the free **5a** or **5b**, respectively. Further metal salt was then added until its precipitation was observed, in this case the signals of the complexed spin labelled crown ethers were the only observable lines, as shown in Figure 3.7 c) for probe **5a** in DCM in presence of Na^+.

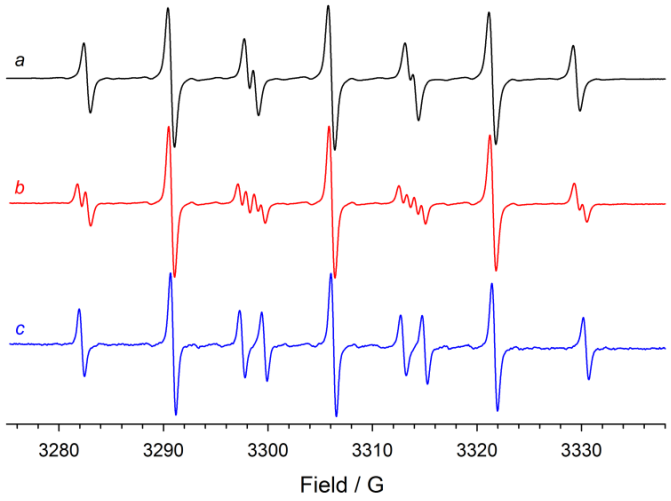

Figure 3.7 *EPR spectra of a)* ***5a*** *in DCM at 298K b) in presence of Na^+ 7 mM, c) in a Na^+ saturated solution.*

The experiments repeated with probe **5b** and K^+ under the same conditions gave a similar readout, as shown in Figure 3.8 that reports the experimental EPR spectra with increasing amounts of K^+.

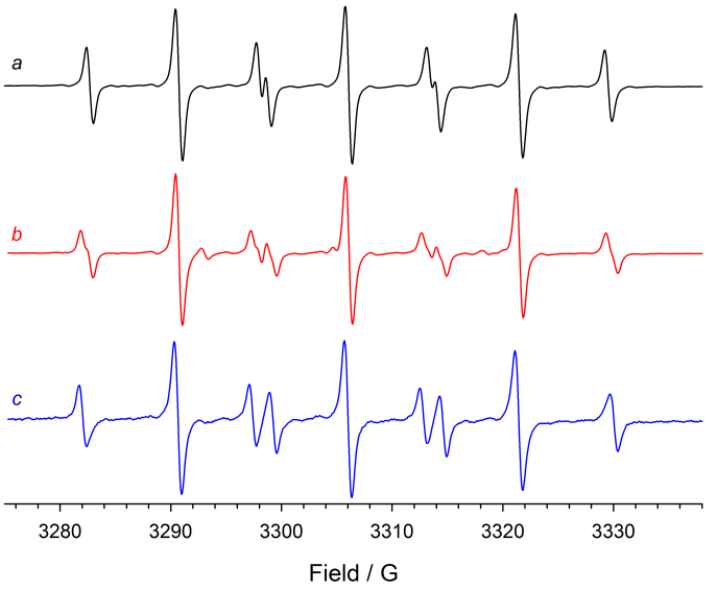

Figure 3.8 *EPR spectra of a)* ***5b*** *in DCM at 298K b) in presence of K^+ 7 mM, c) in a K^+ saturated solution.*

Other than Na^+ and K^+ also Cs^+ showed the same behaviour. Li^+ on the contrary, did not show any variation in the EPR spectra of the free spin labelled macrocycles, but this is consistent with the data reported in literature, which reports the poor interactions of this alkali metal cation with large crown ethers.[12] The presence of two distinct sets of signals for the free and complexed spin labelled DB24C8 indicates that the complexation equilibria (Scheme 3.2) is slower compared to the timescale of the EPR.

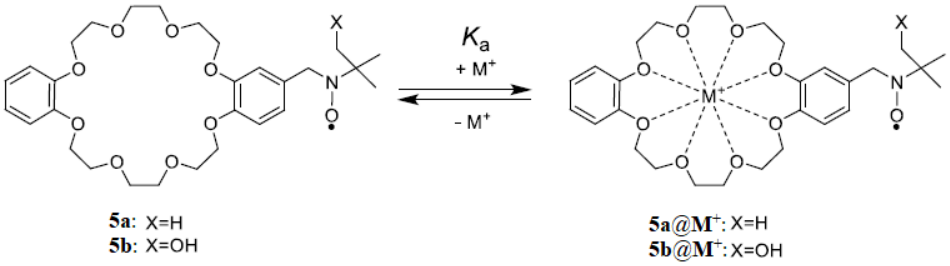

Scheme 3.2 *The complexation equilibria between* ***5a*** *and* ***5b*** *and an alkaline metal cation* ***M***$^+$.

The main variations regarded $a_{2H\beta}$, while only significantly smaller variations were observed for a_N indicating that the variations of $a_{2H\beta}$ are caused by a specific interaction with $\mathbf{M}^+$ when included in the cavity of the crown ether backbone of the spin labelled DB24C8. The almost negligible variations of a_N indicates that the changes in the spectrum are not due to a general medium effect, i.e. a variation of the polarity of the environment surrounding the probe. The observed variations result from different dihedral angle comprised between the planes of the H-C-N bonds and the symmetry axis of the p_z orbital of the nitrogen occupied by the unpaired electron, according to the Heller-McConnel equation[13] and are induced by the inclusion of the metal within the DB24C8 backbone of the probe. This behaviour was observed both for probes **5a** and **5b**.

In addition, $a_{2H\beta}$ showed an increase inversely proportional to the cation size, larger with Na^+ ($a_{2H\beta}$ = 8.73 G) and smaller with Cs^+ ($a_{2H\beta}$ = 8.47 G) as reported in table 3.1 for probe **5a** and in table 3.2 for probe **5b**.

Table 3.1 *EPR parameters for host* ***5a****.*

Solvent	Guest	a_N/G	$a_{2H\beta}$ /G
DCM	-	15.32	8.06
ACN	-	15.38	8.35
DCM	Li^+	15.32	8.06
DCM	Na^+	15.37	8.73
ACN	Na^+	15.38	8.72
DCM	K^+	15.36	8.56
ACN	K^+	15.42	8.69
DCM	Cs^+	15.36	8.47
DCM	$Bn_2NH_2^+$	15.44	8.47
DCM	$\mathbf{6}^{3+}$	15.43	8.58
DCM	$\mathbf{6}^{2+}$	15.54	9.94

Table 3.2 *EPR parameters for host* ***5b****.*

Solvent	Guest	a_N/G	$a_{2H\beta}$ /G
DCM	-	15.38	8.48
DCM	Na^+	15.36	9.07
DCM	K^+	15.35	8.98
DCM	Cs^+	15.33	8.86
DCM	$Bn_2NH_2^+$	15.42	8.90
DCM	$\mathbf{6}^{3+}$	15.39	9.01
DCM	$\mathbf{6}^{2+}$	15.549	10.0

The EPR experiments were then repeated in ACN to obtain quantitative information on the host properties of the spin labelled crown ethers. In this solvent alkali metal iodides are soluble. However, the changes in the EPR spectra, observed in ACN, between the free and complexed probes, were smaller compared to those recorded in DCM thus not allowing to observe separate EPR signals for the free and complexed species. Under these conditions, the degree of complexation *p*(%) can be obtained by measuring the apparent values of $a_{2H\beta}$ recorded by the instrument and by using equation 3.1:

$$p(\%) = \frac{[\mathbf{5a}@\mathrm{M}^+]}{[\mathbf{5}]_0} \times 100 = \frac{a_{\mathrm{EPR}} - a_{free}}{a_{complex} - a_{free}} \times 100 \quad (3.1)$$

where $[\mathbf{5}]_0$ represents the total concentration of nitroxide, a_{EPR} and a_{free} are, respectively, the $a_{2H\beta}$ of the sample measured by the EPR instrument in presence of $\mathbf{M}^+$ and the $a_{2H\beta}$ measured for the spin labelled DB24C8 without the addition of any metal cation. a_{complex} is the value of the benzylic hydrogens hyperfine splitting measured with a saturated $\mathbf{M}^+$ solution, and representing the maximum variation recorded for the investigated cation.

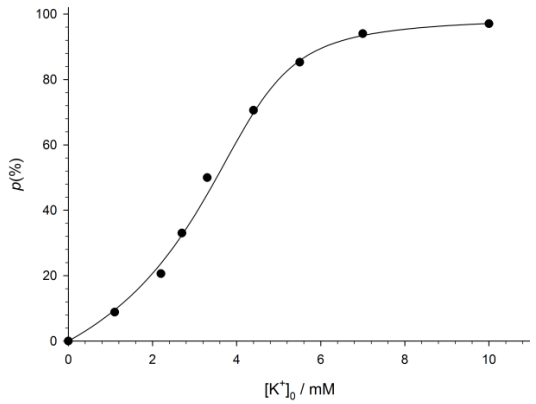

Figure 3.9 *Dependence of the complexation degree, p(%) as function of* K^+ *for nitroxide* ***5a*** *(0.15 mM) at 298 K in ACN produced by oxidation of* ***4a*** *(5 mM). Black dots represents p(%) calculated in the EPR titration while the line represents the theoretical dependence of p(%) on* K^+ *concentration calculated by means of equations 3.1, 3.2, 3.3 and by introducing* K_a*= 6900* M^{-1}*.*

The dependence of p(%) on the concentration of K^+ is reported in Figure 3.9 and was obtained by performing an EPR titration in ACN at 298 K with KI and by using equation 3.1 in which was introduced the a_{EPR} value as the experimental readout of the instrument.

However, the sigmoid dependence could not be well-modelled assuming a 1:1 binding model and an association constant value (K_a) corresponding to the value reported in literature for the unlabelled DB24C8 in ACN corresponding to K_a = 6900 M^{-1}.[14] This deviation can be rationalized by considering that the BTBN derivatives are generally less stable compared to more sterically hindered nitroxides. The paramagnetic nitroxyl group can decay by reacting via disproportion to afford the corresponding hydroxylamine and nitrone derivatives (Figure 3.10)

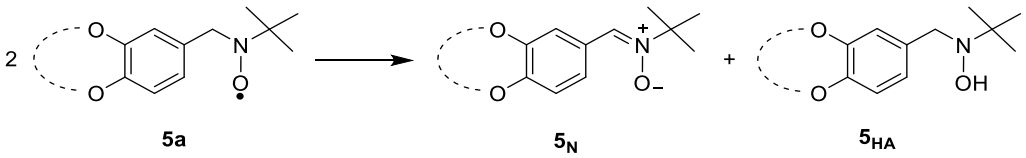

Figure 3.10 *The decay of paramagnetic host* ***5a*** *to afford the corresponding nitrone and hydroxylamine EPR silent derivatives.*

The EPR silent derivatives must be considered hosts for the metal ions as well. The steady state, resulting from a similar rate of formation and destruction of the paramagnetic species, was reached after mixing the host, M^+ and MCPBA in ACN for few minutes. EPR experiments, by measuring the double integral of the experimental spectra, revealed that the concentration of nitroxide at this concentration did not exceed 3% of the diamagnetic precursor. The main metal receptor species present in the sample are thus represented by the starting amine and the degradation products of the paramagnetic host. As a consequence, the fraction of metal M^+ available for complexation, M_{eff}^+, is much lower than the total amount of $\mathbf{M}^+$ added to the sample (M_0^+). The amount of M_0^+ inversely depends on the concentration of diamagnetic host in solution. By varying the initial concentration **4a** and the concentration of MCPBA in a sample with a constant amount of metal it was possible to observe how, increasing the concentration of starting amine the ratio of complexed to free nitroxide decreases. In Figure 3.11 are reported the EPR experiments in presence of a constant amount of metal and an almost constant ratio of nitroxide and starting amine obtained by optimizing the amount of MCPBA added prior to the analysis ($[\mathbf{4a}]_0/[\mathbf{5a}]_0 \approx$ 60). The equilibrium constant for the investigated equilibria can be obtained, under these conditions, by considering equations 3.2 and 3.3:

$$K_a = \frac{[\boldsymbol{CE_{dia}}@M^+]}{([\boldsymbol{CE_{dia}}]_0 - [\boldsymbol{CE_{dia}}@M^+])([M^+]_0 - [\boldsymbol{CE_{dia}}@M^+])} \quad (3.2)$$

$$K_a = \frac{[\mathbf{5a}@M^+]}{([M^+]_{eff} - [\mathbf{5a}@M^+])([\mathbf{5a}]_0 - [\mathbf{5a}@M^+])} \quad (3.3)$$

In which $[\mathbf{CE_{dia}}]_0$ is the total amount of EPR silent crown ether derivatives ($[\mathbf{4a}]+[\mathbf{5_N}]+[\mathbf{5_{HA}}]=[\mathbf{4a}]_0$) corresponding to the initial amount of starting amine, $[M^+]_{eff}=[M^+]_0-[\mathbf{CE_{dia}}@M^+]$ is the effective concentration of metal cation available in solution for the inclusion with spin probe and $[\mathbf{5a}]_0$ is the total amount of nitroxide that can be determined quantitatively by double integration of the EPR spectrum. Because the amount of paramagnetic DB24C8 is considerably smaller compared to the amount of diamagnetic hosts, the amount of M^+ involved in the complex with **5a** has been omitted in equation (3.2).

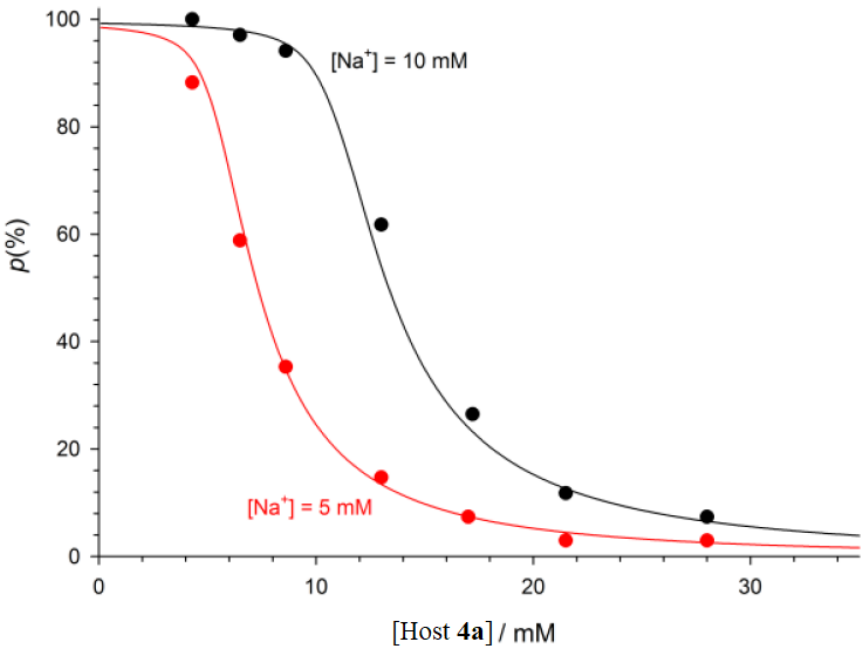

Figure 3.11 *Complexation degree, p(%) of nitroxide complexation determined by EPR (dots) as function of diamagnetic host* ***4a*** *concentration. The lines represent the theoretical dependence of p(%) on host* ***4a*** *concentration at two different Na^+ concentrations, obtained by the means of equations (3.1) – (3.3) by introducing $[\mathbf{5a}]_0 = [\mathbf{4a}]_0/60$ and $K_a = 1.3 \times 10^4\ M^{-1}$.*[12]

The dependence of the complexation degree *p*(%) of **5a** on $\mathbf{M^+}$ or on the concentration of **4a** was well-modelled by considering the reported equilibria, solving equations (3.1),(3.2) and (3.3) and assuming for all the **5a** derivatives present in solution a K_a value similar to that reported in literature for unsubstituted DB24C8.[12]

3.2.2 Complexation studies with organic cations.

We have then started to investigate the host properties of **5a** towards organic cations, like dibenzylammonium ($Bn_2NH_2^+$) in DCM at 298 K and also in this case we observed a variation of $a_{2H\beta}$ that resulted in the appearance of a new set of signals overlapped with those of **5a**, indicating the formation of an inclusion complex with a slower rate of formation and dissociation compared to the

EPR timescale. The measured EPR parameters, in presence of $Bn_2NH_2^+$ (a_N = 15.44 G and $a_{2H\beta}$ = 8.47 G), were found to be different from those recorded with the various alkali metal cations (that were also different from each other), meaning that the instrument can discriminate between different guests as the readout of the instrumental EPR analysis was different from each guest. This feature inspired us to use a guest composed by two recognition sites for the spin labelled hosts to see if the formed pseudorotaxane could show any difference upon the shuttling of the macrocycle between the two stations. The guest that was used, guest $\mathbf{6^{3+}}$, was composed of a stopper, a dibenzylammonium station and a bipyridinium station with a methyl group linked to it (Figure 3.12).

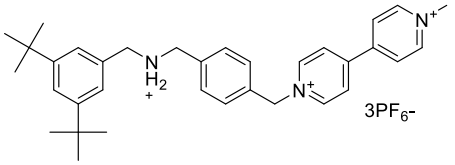

Figure 3.12 *Guest* $\boldsymbol{6^{3+}}$.

Analogous to the thread shaped molecule present in the acid-base switchable [2]rotaxane developed by Balzani *et al.* and based on the DB24C8- $R_2NH_2^+$/BPY^{2+} recognition motive,[15] we used it in EPR experiments in presence if **5a**. The experiments were carried out by adding $\mathbf{6^{3+}}$ to a solution of **5a** and MCPBA. First of all, we observed the complete solubilization of $\mathbf{6^{3+}}$ in DCM, solvent in which $\mathbf{6^{3+}}$ is poorly soluble, as a first evidence of formation of the pseudorotaxane. The EPR spectra, recorded in DCM at 298K and with 1 eq. of $\mathbf{6^{3+}}$ of the pseudorotaxane **5a**@$\mathbf{6^{3+}}$ was characterized by spectroscopic parameters (a_N = 15.42 G and $a_{2H\beta}$ = 8.58 G, figure 3.13b) close to those recorded for $Bn_2NH_2^+$ as guest (aN = 15.44 G and a2H = 8.47 G, Table 3.1) indicating that the paramagnetic host encircles mainly the $R_2NH_2^+$ station, in agreement with the observations reported in literature.[13]

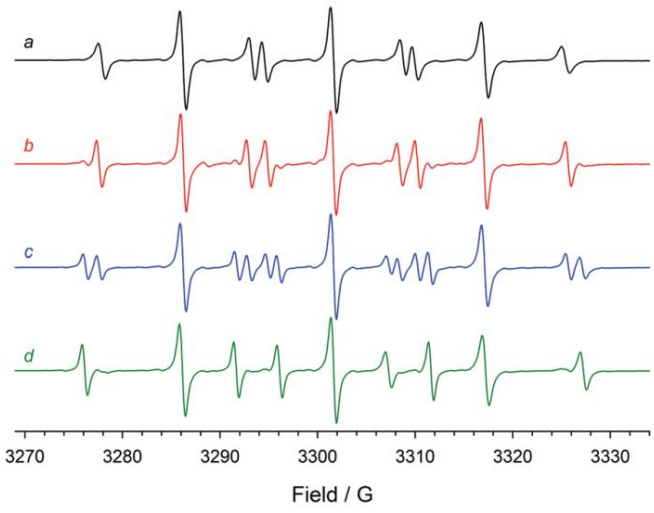

Figure 3.13 *a) EPR spectra of host* ***5a*** *in DCM at 298 K, b) in presence of 1 eq.* $\boldsymbol{6^{3+}}$ *c) guest* $\boldsymbol{6^{3+}}$ *+ 0.5 eq. DIPEA d) guest* $\boldsymbol{6^{3+}}$ *+ 1.0 eq. DIPEA.*

When 0,5 eq. of the non-nucleophilic base diisopropylethylamine (DIPEA) were added (Figure 3.13c), the EPR spectra of the sample was characterized by the rise of new signals, along with the starting signals of **5a**@**6**$^{3+}$but with different hyperfine splitting constants (a_N = 15.54 G and $a_{2H\beta}$ = 9.94 G). These signals were attributed to a new complex in solution, **5a**@**6**$^{3+}$, with **5a** that encircling the BPY^{2+} station after the shuttling between the two recognition sites (Figure 3.14).

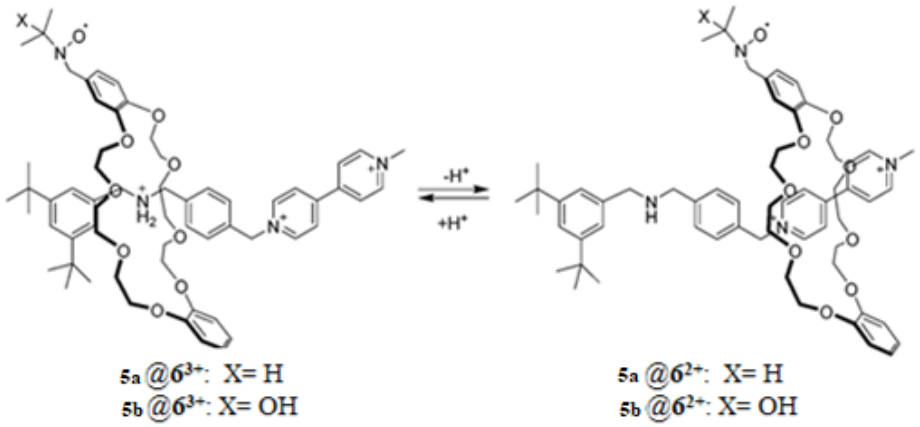

Figure 3.14 *Shuttling of the spin labelled macrocycles **4a** and **4b** between the two stations of host **6**.*

Also in this case, the signals of the two paramagnetic species were observed at the same time, indicating that the equilibrium between **5a**@**6**$^{3+}$ and **5a**@**6**$^{2+}$, and thus the shuttling of the macrocycle, is slower compared to the EPR timescale. Upon addition of an excess of DIPEA, the new signals of **5a**@**6**$^{2+}$ became predominant (Figure 3.13d), while the addition of trifluoroacetic acid (TFA), after the DIPEA treatment, restored the initial EPR spectrum by protonating again the ammonium site and allowing the macrocycle to shuttle back in its initial position. Similar results were obtained by using **5b**.

The corresponding [2]rotaxanes **R4a**$^{3+}$ and **R4b**$^{3+}$ (Scheme 3.3) were also synthesized by reacting the spin labelled crown ethers precursors in presence of the non-methylated precursor of thread **6**$^{3+}$ (**6a**$^{2+}$). The formed diamagnetic pseudorotaxane **4a**@**6a**$^{3+}$ (or **4b**@**6a**^{3}) and 3,5-di-tert-butylbenzyl bromide were refluxed in DCM for 5 days followed by Purification on SiO_2.

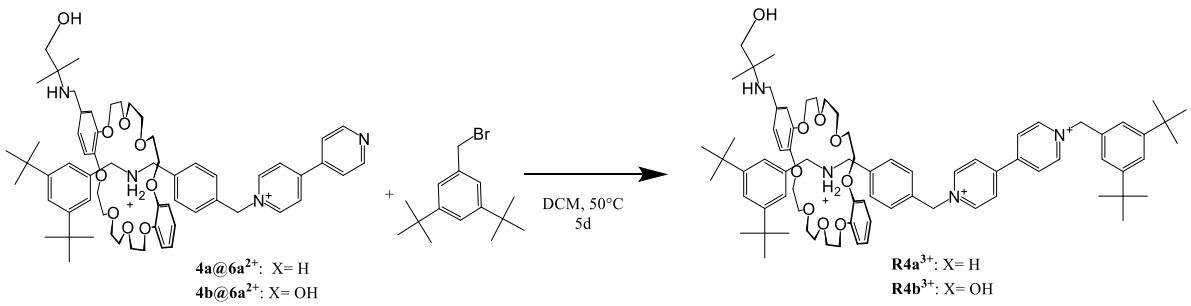

Scheme 3.3 *Synthesis of rotaxane **R4a**$^{3+}$ and **R4b**$^{3+}$.*

When we added the oxidant and recorded the EPR spectrum of the rotaxanes, we observed an EPR spectra different from the expected 9-line spectrum. A possible explanation of this unexpected result can be due to oxidation of the dibenzyl amine function on the thread shaped molecule, that was not observed with the pseudorotaxane, since the complex was formed after mixing the already oxidized host with the guest. Deprotonation of the thread may be due to a proton transfer between the dibenzylamine unit on the thread and the N-*tert*-butylamine on the macrocycle. Moreover, the addition of DIPEA to the sample did not result in any observation that led to assume that a switching process was taking place. Instead, we observed a charge transfer between DIPEA and the bipyridinium unit to generate its EPR active radical cation ($BPY^{+\bullet}$). Because of these unexpected results, we concluded that labelling such a system with non-persistent radical units, therefore requiring the treatment with an oxidizing agent to generate the paramagnetic species, may not result in useful EPR data for its characterization.

3.3 Conclusions

In conclusion, we have synthesized two new spin probes based on the DB24C8 crown ether labelled with the BTBN group derivatives. The β-hydrogens hyperfine splitting constant of hosts **5a** and **5b** was found to be susceptible to the presence of cations that formed a 1:1 complex with the host. Moreover, the timescale of the EPR analysis, faster compared to the investigated equilibria, allowed us to access it and to discriminate between different guests. Quantitative measurements on the complexation events were found to be consistent with those previously reported in literature by the means of other methods, confirming that EPR spectroscopy can be successfully used to measure the equilibrium constants for the complexation of cations with spin labelled crown ethers.

This approach has proven to be useful even in the investigation of complex systems like pseudo rotaxanes, in which the switching between two different recognition sites can be monitored by the measurement of the EPR parameters.

3.4 References

1 C. J. Pedersen, *J. Am. Chem. Soc.*, 1967, **89**, 7017.
2 F. M. Raymo and J. F, Stoddart, *Chem. Rev.*, 1999, **99**, 1643−1663.
3 P. R. Ashton, E. J. Chrystal, P. T. Glink, S. Menzer, C. Schiavo, N. Spencer, J. F. Stoddart, P. A. Tasker, A. J. White and D. J. Williams, *Chemistry – A European Journal*, 1996, **2** 709 - 728.
4 G. W. Gokel, W. M. Leevy, and M. E. Weber, *Chem. Rev.*, 2004, ***104***, 2723–2750.
5 P. R. Ashton, R. Ballardini, V. Balzani, I. Baxter, A. Credi, M. C. T. Fyfe, M. T. Gandolfi, M. Gomez-Lopez,M.-V. Martinez-Dıaz, A. Piersanti, N. Spencer, J. F. Stoddart, M. Venturi, A. J. P. White and D. J. Williams, *J. Am. Chem. Soc*., 1998, **120**, 11932-11942.
6 M. Zhang, D. Xu, D. X. Yan, J. Chen, S. Dong, B. Zheng and F. Huang, *Angew. Chem. Int. Ed.*, 2012, **51,** 7011-7015.
7 K. Ishizu, H. Kohama and K. Mukai, *Chem. Lett.*, 1978, 227 – 230.

8 M. P. Eastman, D. E. Patterson, R. A. Bartsch, Y. Liu, and P. G. Eller *J. Phys. Chem.*, 1982, **86**, 2052 – 2058.
9 H. Dugas, P. Keroack, and M. Ptak, *Can. J. Chem.*, 1984, **62**, 489 – 497.
10 L. Gualandi, P. Franchi, A. Credi, E. Mezzina and M. Lucarini, *Phys. Chem. Chem. Phys*, 2018, DOI: 10.1039/c8cp04362k
11 D. Liu, D. Wang, M. Wang, Y. Zheng, K. Koynov, G. K. Auernhammer, H-J. Butt and T. Ikeda, *Macromolecules*, 2013, **46**, 4617−4625.
12 R. Frański, *Rapid Commun. Mass Spectrom.* 2009, **23**, 3488 – 3491.
13 C. Heller and H. M. McConnell, *J. Chem. Phys.*, 1960, **32**, 1535.
14 Y. Takeda, *Bull. Chem. Soc. Jpn.*, 1983, **56**, 3600; Y. Takeda, Y. Kudo and S. Fujiwara, *Bull. Chem. Soc. Jpn.*, 1985, **58**, 1315.
15 P. R. Ashton, R. Ballardini, V. Balzani, I. Baxter, A. Credi, M. C. T. Fyfe, M. T. Gandolfi, M. Gomez-Lopez, M.-V. Martınez-Diaz, A. Piersanti, N. Spencer, J. F. Stoddart, M. Venturi, A. J. P. White and D. J. Williams, *J. Am. Chem. Soc.*, 1998, **120**, 11932 – 11942.

4. Use of active metal template approach for the synthesis of novel spin labelled [2]-rotaxanes

The development of the revolutionary approach for the synthesis of MIMs by Sauvage *et al.*[1] has risen an always growing attention by the scientific community in the exploitation of metal ions for the synthesis of interlocked molecules. The method developed by Sauvage *et al.* was based on the so-called passive metal (PT) template approach according to which the metal cation plays only the role of pre-organizing the components of the target catenane before the interlocking reaction(s). The catenane synthesized in their work consisted of two interlocked macrocyclic molecules containing a diphenolphenanthroline unit and ethylene glycolic chains and was obtained in an unprecedented 42% yield by adding half equivalent of Cu^+ to a solution of the precursors that led to the formation of a 1:2 cross-like complex between them. This complex was then subjected to a Williamson ether synthesis reaction with diiodotetraoxatetradecan in presence of a base that closed the macrocyclic molecules interlocking them in the [2]catenane. However, this synthesis required harsh conditions (high temperature, a coordinating solvent like DMF) and this approach was further improved by changing the ring closure reaction. The same group described lately the synthesis of a similar [2]catenane by exploiting a ring closing metathesis (RCM) reaction by using a Grubbs I catalyst to interlock the macrocyclic components of the [2]catenane in 92% yield (Figure 4.1). The passive metal template however requires not only components capable of coordinating the metal cation but also needs to exploit secondary non-covalent interactions to maximize the yield of the target interlocked molecules. As an example in the RCM reaction developed by Sauvage and co-workers, the C-H···O interaction between the hydrogen of the phenanthroline and the glycolic chains on the opposite side of the copper coordinating centre of the phenanthrolines, maximizes the catenation yield by keeping the glycolic chains close to the phenanthroline's core and avoiding intercomponent cyclization.[2]

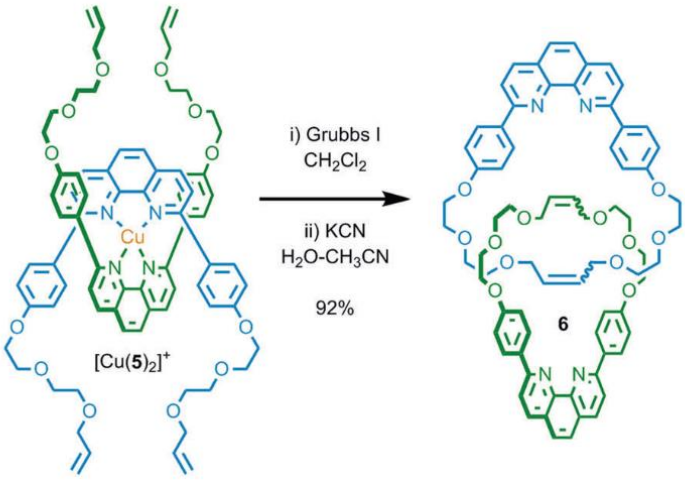

Figure 4.1 *The RCM mediated catenation developed by Sauvage and co-workers.*[2,3]

Passive metal template approach has been a milestone in the synthesis of MIMs and its potentiality has been widely demonstrated over the years. Nevertheless, this methodology does not consider the ability of some metal cations to be involved in the formation of covalent bonds and is used only for the coordination of the components in a thermodynamically favourable complex whose geometry favours the mechanical interlocking of the components themselves.[3]

4.1 The active metal template approach

With the aim to improve the exploitation of metal ions in the formation of mechanical bonds, in 2006 Leigh and co-workers,[4] developed a method to take advantage of the ability of metal ions to form covalent bonds other than just using them as templates for the self-assembly of the precursors of the mechanically interlocked molecule. The approach was used for the synthesis of a [2]rotaxane that was obtained thanks to the ability of copper (I) to coordinate the pyridine unit present in the macrocycle and the alkyne and azide functionalized half-threads. Following the coordination of the different components of the target [2]rotaxane, the Cu^{I} inside the cavity of the pyridine-functionalized macrocycle catalysed the azide-alkyne cycloaddition (CuAAC) "click" reaction, allowing the formation of a 1,2,3-triazole 5-membered ring that interlocks the macrocycle (Figure 4.2).

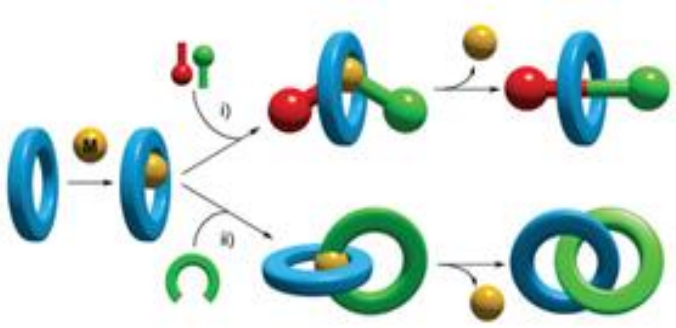

Figure 4.2 *Schematic representation of the AT-CuAAC method for the synthesis of rotaxanes and catenanes.*[3]

The mechanism of formation of the mechanical bond, with the closure of the triazole ring is however still debated since many different pathways are possible, strictly depending on the characteristics of the various components, like the size of macrocycle and the steric hindrance of the thread precursors. The mechanism proposed by Leigh and co-workers is, in this case, a monometallic mechanism that begins with the formation of the complex between the macrocycle and Cu^{I} followed by the coordination of the alkyne half-thread. The subsequent coordination of the azide component leads then to the formation of a productive complex in which the copper cation catalyses the formation of the triazole link between the half-threads. (Figure 4.3).[5]

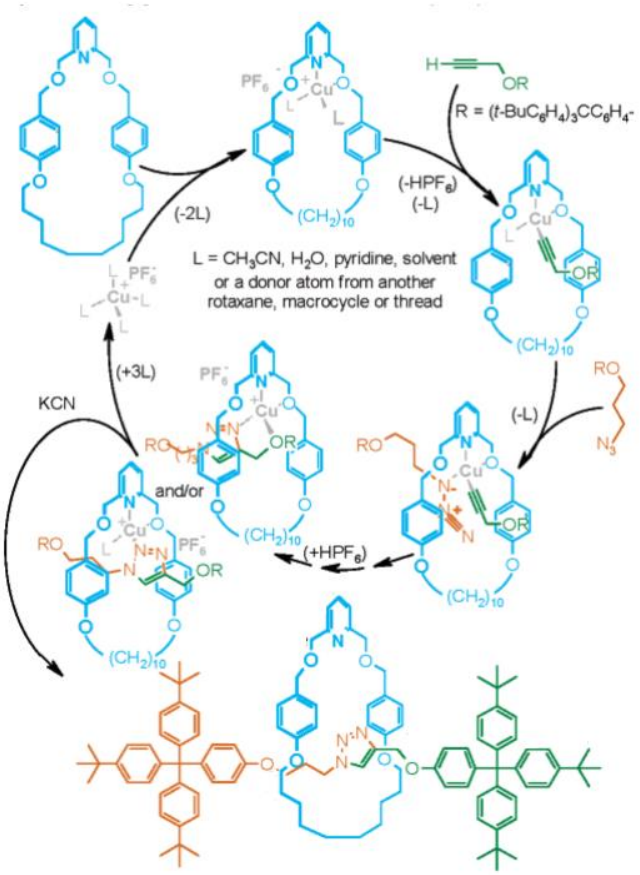

Figure 4.3 *Proposed mechanism for the formation of the rotaxane using the AT-CuAAC developed by Leigh and co-workers.*[5]

Conversely to the thermodynamic nature of the passive template approach, the active template mechanical bond formation is a kinetically driven process.[6] The requirements for the formation of the mechanical bond are the same of formation of the bond(s) catalysed by the metal ion: the covalent bond can take place only when the components are in a favourable arrangement around the metal ion inside the macrocycle, with a precise stereochemistry of the complex. In principle, this method allows also to use sub-stoichiometric amounts of metal respect to the macrocycle. If the product of the reaction is a worse binding site for the metal than the free macrocycle, the metal can then dissociate from the product and form a new productive complex with another macrocyclic molecule.[6] The AT-CuAAC has been further developed until reaching in some cases quantitative yields in terms of mechanical bond formation.[7] In an elegant paper Goldup *et al.*, for example, reported the exploitation of a 2,-2'-bypiridine containing macrocycle in the synthesis of rotaxanes that were obtained by pre-forming the Cu^{I}-macrocycle complex and then adding both 3,5-di-*tert*-butyl phenylazide and 3,5-di-*tert*-butyl phenylacetylene half threads to the reaction mixture (Figure 4.4). Thanks to this strategy they were able to get the target rotaxanes in excellent yields and also to assess the effect of the size of the macrocyclic compound on the formation of the mechanical bond.[8] This approach has been used also for the synthesis of catenanes.[9]

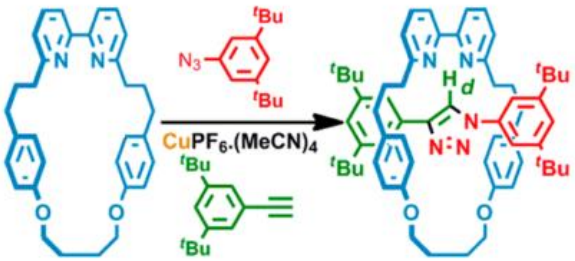

Figure 4.4 *Example of synthesis of a [2]rotaxane with the method developed by Goldup and co-workers.*[8]

The coupling of active template and the click reaction (AT-CuAAC) has proven to be a successful approach for the synthesis of MIMs as testified by the always growing number of research groups adopting this strategy for the synthesis of catenanes and rotaxanes.

The click reaction is particularly suitable for the active template approach since it requires mild reaction conditions and is usually fast and selective. The availability of wide variety of different substrates, azides and alkynes precursors, allows to use this reaction to access a large variety of chemical structures. Nevertheless, many different metal catalysed reactions have been successfully used for the synthesis of mechanical bonds but click chemistry, thanks to its advantages, always had a privileged role in supramolecular chemistry.

The possibility to obtain interlocked molecules in high yields is a great opportunity for the investigation of these systems, whose synthesis is often challenging and time-consuming, allowing chemists to access the target MIMs in larger amount compared to the classical low yielding methods and making them easier to study. This is particularly true for the synthesis of spin labelled [2]rotaxanes in which the synthesis is made even more challenging thanks to the presence of a paramagnetic centre that usually do not withstands harsh reaction conditions. In this context we decided to use the AT-CuAAC approach for the synthesis of [2]rotaxanes bearing nitronyl nitroxides (NN) radicals as stoppers. The NN radical (Figure 4.5a), already introduced in chapter 1, was chosen because of its conjugated nature, that allows in some cases to observe through-bond spin-spin coupling.[10] Moreover, their good persistence makes them good candidates for the spin labelling. Their more stable derivatives, imino-nitroxyl radicals (IN, figure 4.5b), were not considered valuable spin labels since the presence of two non-equivalent couplings with the two different nitrogen atoms would have made the analysis of eventual spin-spin coupling between two IN more difficult and without any relevant benefit. This work is aimed to the exploitation of paramagnetic centres, introduced at the extremities of the thread and working as stoppers, to the analysis of its structural and dynamic properties and the influence of the mechanical bond on the spin-spin coupling between the two radical centres. Because both the macrocycle and some of the obtained [2]rotaxanes can be good ligands for metal ions, another aspect of this work is devoted to the assessment of the effects that the presence of the metal ion coordinated in the rotaxane can have on its EPR properties.

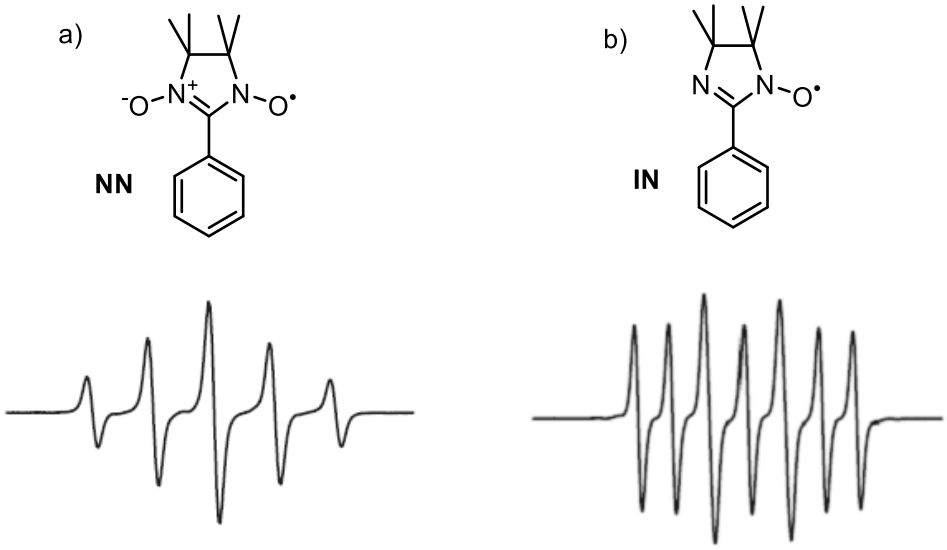

Figure 4.5 *a) NN radical b) IN radical.*

4.2 Spin-spin coupling in diradicals

When two unpaired electrons are present in a single molecule, the dipolar coupling interaction (J) between them depends on many factors such as distance between the radical centres and the degree of conjugation. If the two unpaired electrons are located on distant sites of the molecule the interaction is negligible ($J \approx 0$). The EPR spectra will be characterized by the overlapping of the signals of the 2 unpaired electrons, and these kinds of molecules composed of two independent radicals are called biradicals *i.e.* two distant nitroxyl radicals in a molecule have an EPR spectrum characterized by the overlapping of the characteristic three lines separated by the same a_N of the corresponding mono radicals.

Diradicals instead are molecules characterized by the presence of two unpaired electrons showing dipolar interactions between them ($J \neq 0$). The magnitude of the dipolar coupling depends on the overlapping of the non-bonding molecular orbitals occupied by the unpaired electrons. This overlapping may be due to the short distances between two isolated unpaired electrons, typically below 10 Å, in this case the mechanism is a through-space (TS) interaction. Another possible mechanism is through delocalization of the unpaired electrons within the structure of a conjugated molecule, in this case the mechanism is a through bond spin-spin interaction (TB). In these molecules, the EPR spectra show additional lines, resulting from the coupling of the unpaired electron with distant nuclei. Thus, two interacting TEMPO nitroxide groups present a five lines spectrum due to the coupling of the electron with two equivalent nitrogen atoms with lines separation equal to $a_N/2$. Similarly, two interacting NN radicals will show 9 lines (with lines separation equal to $a_N/2$) due the coupling with four equivalent nitrogen atoms.

4.3 Results and discussion

4.3.1 Synthesis of the NN-spin labelled [2]rotaxanes

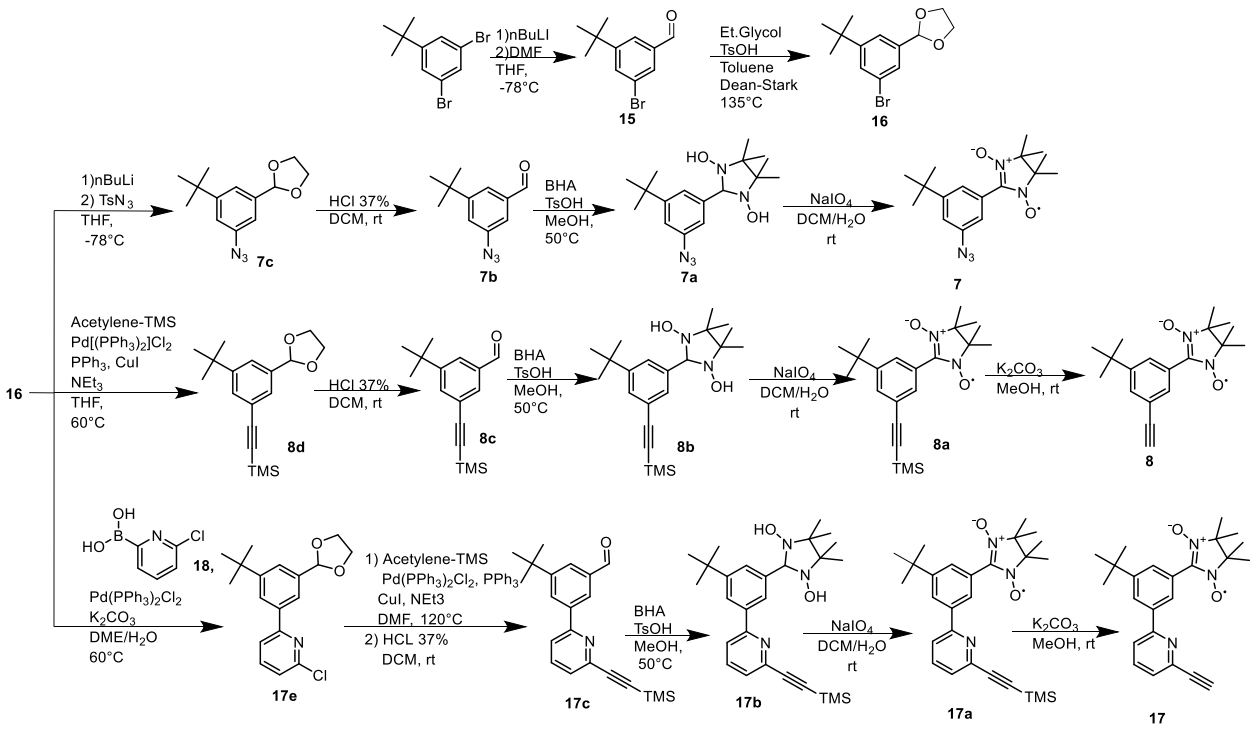

Scheme 4.1 *Synthesis of the NN-labelled half threads*

The synthesis of the paramagnetic half-threads (Scheme 4.1) started with 3-bromo-5-(*tert*-butyl)-benzaldehyde (**15**) that was synthesized starting from 3,5-dibromo-*tert*-butyl benzene according to the procedure reported in literature.[11] The protection of the aldehyde functionality as 1,3 dioxolane was achieved by condensation of **15** with ethylene glycol in toluene in a Dean-Stark apparatus to yield compound **16**. This was the key intermediate for the divergent synthesis of the NN-labelled half-threads that was subjected to lithiation with *n*-BuLi and subsequent reaction with tosyl-azide (TsN_3) in THF at -78 °C to yield compound **7c**. The acetal protecting group was removed by treatment with 37% HCl in DCM to give the free aldehyde **7b** that was then condensed with 2,3-bis-hydroxylamino-2,3-dimethyl-butane (BHA)[12] in degassed methanol and in presence of a catalytic amount of *para*-toluenesulfonic acid (TsOH) that afforded the radical precursor dihydroxy-imidazolidine **7a**. Oxidation of **7a** with $NaIO_4$ in a DCM/H_2O biphasic mixture yielded azide functionalized NN-labelled half-thread **7**. Half-thread **8** was instead obtained by reacting **16** with trimethylsilyl acetylene (TMS-acetylene) in a palladium assisted Sonogashira cross-coupling to give compound **8d** that was then subjected to deprotection of the aldehyde function with acid treatment affording compound **8c**. The condensation with BHA that gave the NN-precursor **8b** was carried out in the same conditions as for **7a**. Similarly, the oxidation to the radical stopper **8a** was carried out by using the same protocol as for **7**. Treatment of **8a** with K_2CO_3 deprotected the alkyne functionality to give compound **8**.

For the synthesis of the ethinyl(pyridyl) functionalized paramagnetic half-thread **17,** compound **16** was subjected to a palladium assisted Suzuki-Miyuara cross-coupling with 6-chloropyridyl-2-boronic acid (**18**)[13] to give compound **17e**. It was subsequently reacted with TMS-acetylene in DMF at 120°C. The following steps (acetal hydrolysis, condensation with BHA, oxidation and deprotection of the alkyne) were performed under the same conditions as for **8** and afforded compound **17**.

The NN labelled half-threads **7**, **8**, **17** were then used for the synthesis of the target rotaxanes (Scheme 4.2) and the corresponding threads (Scheme 4.3).

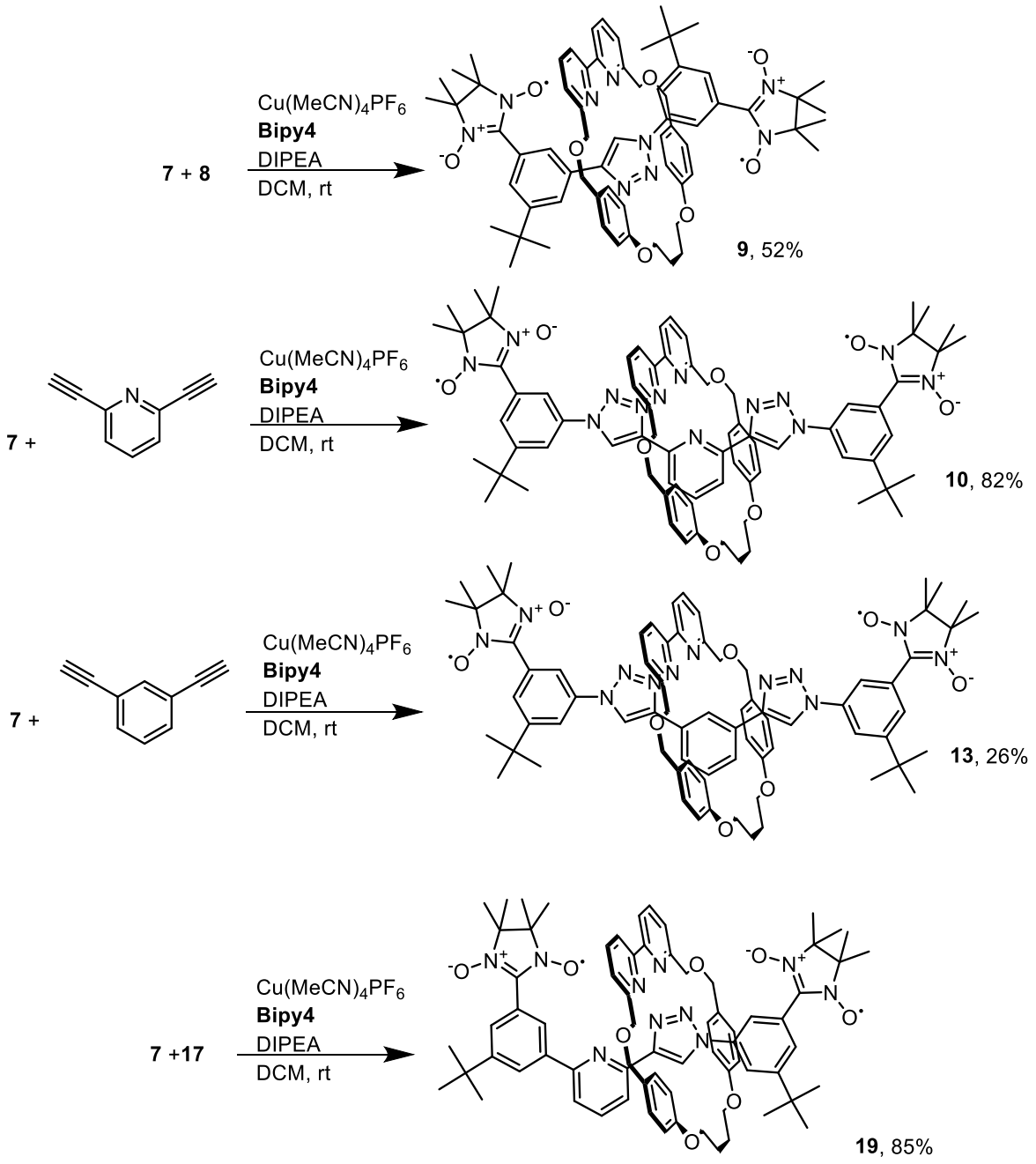

Scheme 4.2 *Synthesis of the NN labelled [2]rotaxanes.*

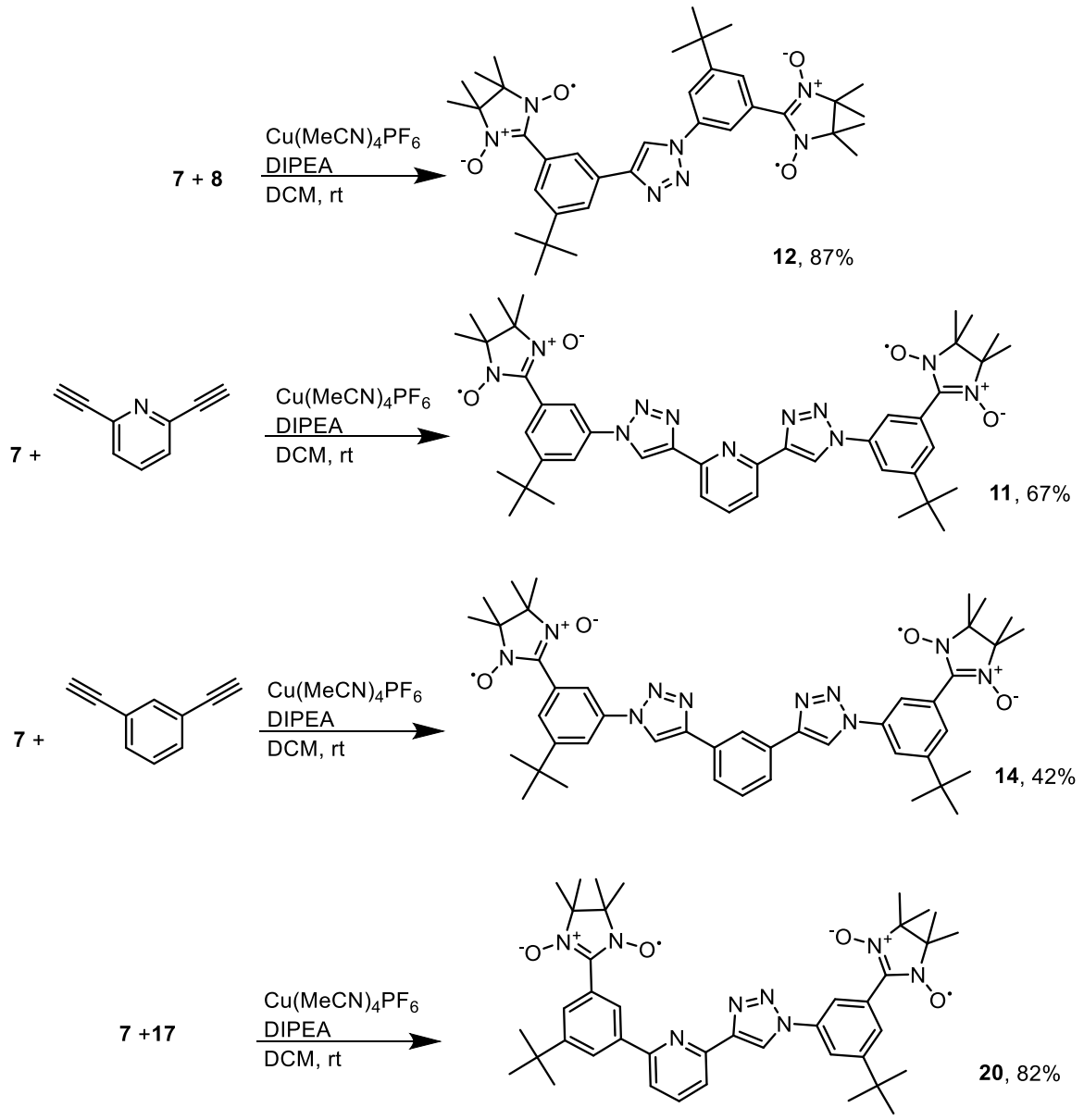

Scheme 4.3 *Synthesis of the NN labelled threads.*

The rotaxanes were obtained by using the 2,2'-bipyridine containing macrocycle (**Bipy4**, Figure 4.5) synthesized by Goldup and co-workers and exploiting the AT-CuAAC developed and optimized by the same research group.[8] This method implies the use of copper(tetrakis-acetonitrile) hexafluorophosphate as catalyst for the click reaction and by mixing the macrocycle (1 eq.) and a sub-stochiometric amount of copper (0.96 eq.) to form the Cu^{I}/**Bipy4** complex before the addition of the azide and alkyne half-threads to the reaction vessel. The addition of DIPEA starts the reaction that leads to the target interlocked molecules. The reaction is monitored *via* TLC analysis and once complete, copper is removed upon treatment with a saturated ethylenediaminetetraacetic acid/ammonia 17.5 % solution ($EDTA/NH_3$) that removes the copper from the reaction mixture.

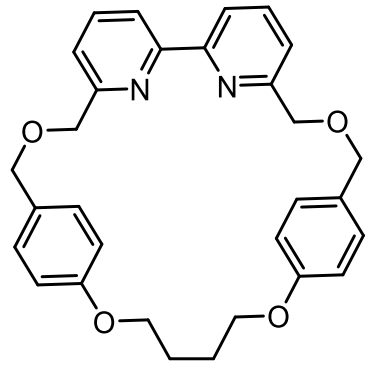

Figure 4.5 *Macrocyclic compound* ***Bipy4****.*[8]

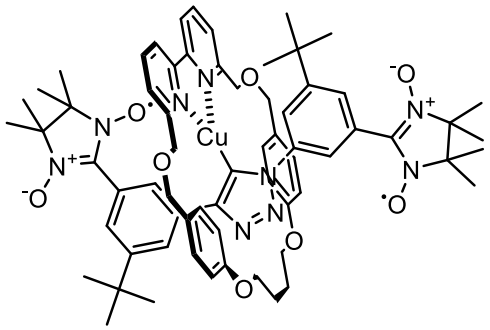

Figure 4.6 *The triazolide of rotaxane* ***9****.*

The rotaxanes were then carefully purified on SiO_2 gel chromatography with DCM/EtOAc as eluent to remove any traces of IN decomposition products. The radical rotaxanes were found to be fairly persistent, upon storage at 4°C for few months the EPR analysis evidenced the presence of just a 5-10% of IN derivatives, produced by decomposition of the diradical. For this reason, before each EPR analysis the samples were purified again via column chromatography. The first rotaxane obtained was **9**, synthesized using half-threads **7** and **8**. Actually, the triazolide[14] intermediate (with the copper directly bonded to the triazole and coordinated with the bipyridine in the macrocycle, Figure 4.6) was isolated after column chromatography. Thus, a second demetallation step with formic acid was performed to remove the copper from the cavity of the rotaxanes. In the triazolide intermediate the bond between the triazole and the copper atom is stabilized both by the coordination of Cu^{I} with the bipyridine of **Bipy4** and by the steric hindrance caused by the NN and *tert*-butyl stoppering fragments that makes it less accessible to external agents. The acid treatment resulted however in a decrease of the yield of **9** due a partial degradation of the NN radical. Longer derivatives **10** and **13** with 5 aromatic rings between the spin labels in the thread shaped molecule, were synthesized by reacting the **Bipy4**-Cu^{I} complex in presence of 2 equivalents of **7** and respectively, one equivalent of 2,6-diethynyl pyridine or 2,6-diethynylbenzene. Derivative **19**, with 4 phenyl rings between the NN labels, was synthesized under the same conditions by using radicals **7** and **17**. The corresponding free threads **11**, **12**, **14**, and **20** were synthesized in absence of the macrocycle.

4.3.2 EPR investigation of the NN labelled [2]rotaxanes

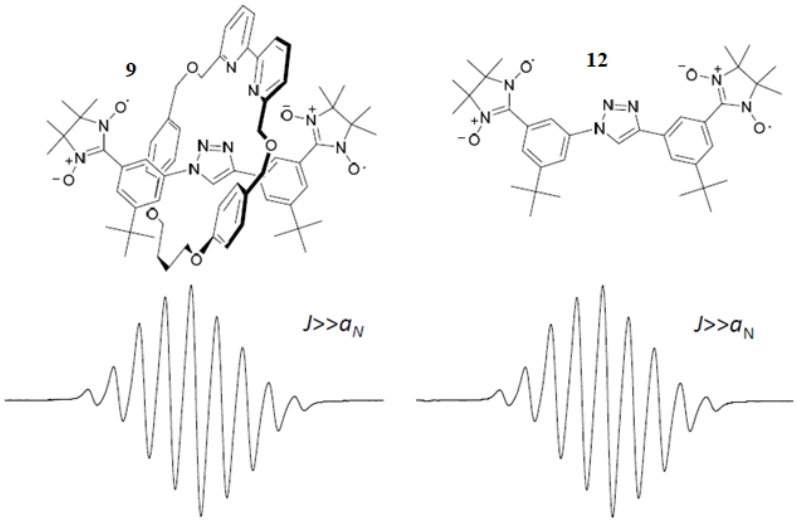

Figure 4.7 *EPR spectra of* ***9*** *and* ***12*** *recorded in DCM at 298K.*

The EPR spectrum of rotaxane **9** (g= 2.0068*;* a_N= 7.56 G, see figure 4.7), recorded in CH_2Cl_2 was characterized by the presence of 9 lines, indicating a strong spin-spin interaction between the radical fragments with an exchange constant J larger than a_N ($J >> a_N$). For comparison the spectrum (see Figure 4.7) of the corresponding free thread **12** (g= 2.0068; a_N= 7.52 G) showed a very similar pattern. In this case the spin-spin interaction can be due a) to the short distance between the NN labels, and/or b) to the conjugation relation between the two radicals. Both the through space and through bond mechanisms can therefore be hypothesised.

We have then recorded the EPR spectrum of rotaxane **10** in ACN (g= 2.0060*;* a_N = 7.43 G) and in toluene (Figure 4.8) at room temperature. In this case the spectrum presents 5 lines, with a smaller average value of J ($\bar{J}$) compared to that of thread **11** (g= 2.0069; a_N = 7.50 G, in ACN) that was instead characterized by a 9 lines spectrum with a strong spin-spin interaction between the two radicals ($J >> a_N$).

The experiments were repeated at different temperatures and rotaxane **10** showed a clear line width alternation, whose magnitude depends on the temperature and the solvent. At room temperature, the selective line broadening is so strong that results in an EPR spectrum characterized by 5 lines. The temperature-mediated spectral changes were found to be reversible. To understand the differences between the spectroscopic properties of **10** and **11** we had to take into account the modulation of the spin-exchange. A model to explain the line width alternation in a biradical in solution was proposed by Luckhurst in 1966.[15] In this model we assume that each electron interacts equally with two nitrogen nuclei, then in the absence of spin exchange the biradical behaves as two single radicals and the EPR spectrum would consist of five lines separated by a_N, the nitrogen hyperfine splitting. As mentioned in paragraph 4.2, if there is a strong scalar exchange interaction, J, between the two electrons such that $J >> a_N$, the spectrum will consist of nine lines separated by $a_N/2$. In a situation in which the exchange

integral J is modulated between two values such that the average J ($\bar{J}$) is still greater than a_N we might expect to find that the widths of the 1st, 3th 5th, 7th and 9th lines are unaffected since their positions are independent of the modulation, but that all other lines are broadened by it since their positions depend on J. If we rely on this model and assume the contribution of through-bond mechanisms is negligibly small for biradicals **10** and **11**, a modulation of the exchange interaction could be observed when the molecule passes from one conformation to the other having different overlap between the wave functions and thus different J values. Therefore, the observed temperature dependent spectra can be analysed in terms of the modulated exchange interaction. For the sake of simplicity, only two extreme conformations are assumed. One is a strongly interacting conformation with a spin exchange, $J >> a_N$. The other is a less interacting conformation with $J = 0$. It should also be clear that the model is a simplification, the exchange integral can assume many values and the number of values depends on the flexibility of the molecule. Similarly, it may be wrong to think of the modulation as a jump process and instead, there may be a continuous variation in J as the molecule passes from one conformation to the next. Nevertheless, the final conclusion still holds that any process which modulates the exchange integral will produce an alternating linewidth provided that $\bar{J} > a_N$. To better understand the effect of the modulation of the spin exchange we analysed the conformational properties of the thread shaped molecule **11**.

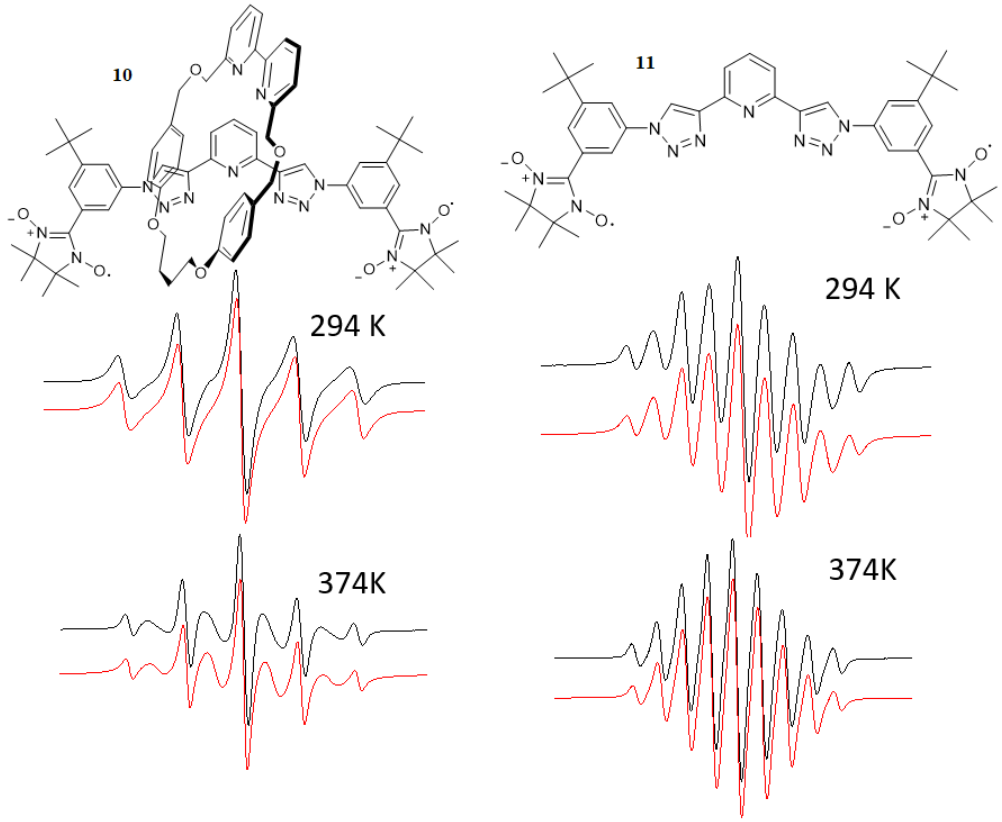

Figure 4.8 *EPR spectra of **10** and **11** recorded in toluene at 294 K and at 374 K. In red are reported the corresponding theoretical simulations.*

In analogy to the known conformational preference of 2,2'-bipyridines[16] the 2,6-bis(1,2,3-triazol-4-yl)pyridines skeleton is expected to predominantly adopt the *anti–anti* conformation due to favourable electrostatic interactions, whereas repulsive interactions due to lone pair repulsion disfavour the *syn–syn* conformation (Figure 4.9).

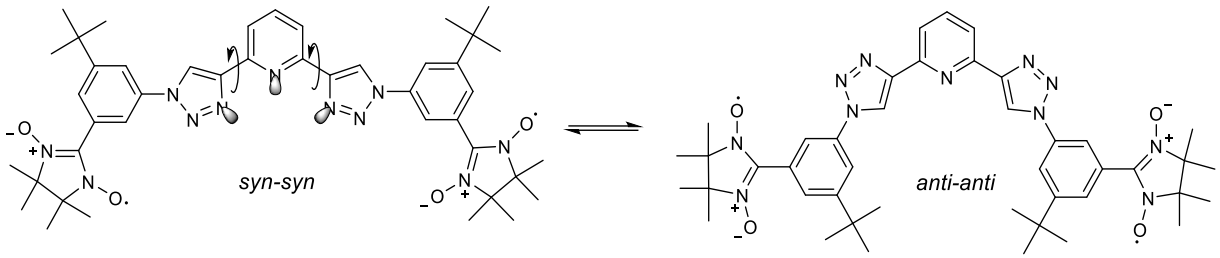

Figure 4.9 *Possible conformations of thread* ***11***.

DFT calculations on a 4-(2-pyridyl)-1,2,3-triazole model system [17] predicted a significant stabilization of the *anti*-conformer by 6.4 kcal/mol (over the *syn* conformer) in the gas phase. Calculations confirmed that the lone pair repulsion is the main reason of the significant destabilization observed in the *syn-syn* conformation. Experimental verification of the predicted strong conformational preference for the *anti–anti* conformation was successively obtained both in the solid state and in solution by single-crystal X-ray structural analyses and NMR measurements, respectively[18] Based on this, we safely assumed that both diradical **10** and **11** should be considered only in the *anti-anti* conformations.

For the *anti-anti* conformer three main different conformations around the phenyl-triazole bonds are possible. According to the relative position of the radical units, we termed these conformers as "far-far", "close-far" and "close-close" conformations (see Figure 4.10). Clearly, they are characterized by different distances between radical centres and thus by different *J* values.

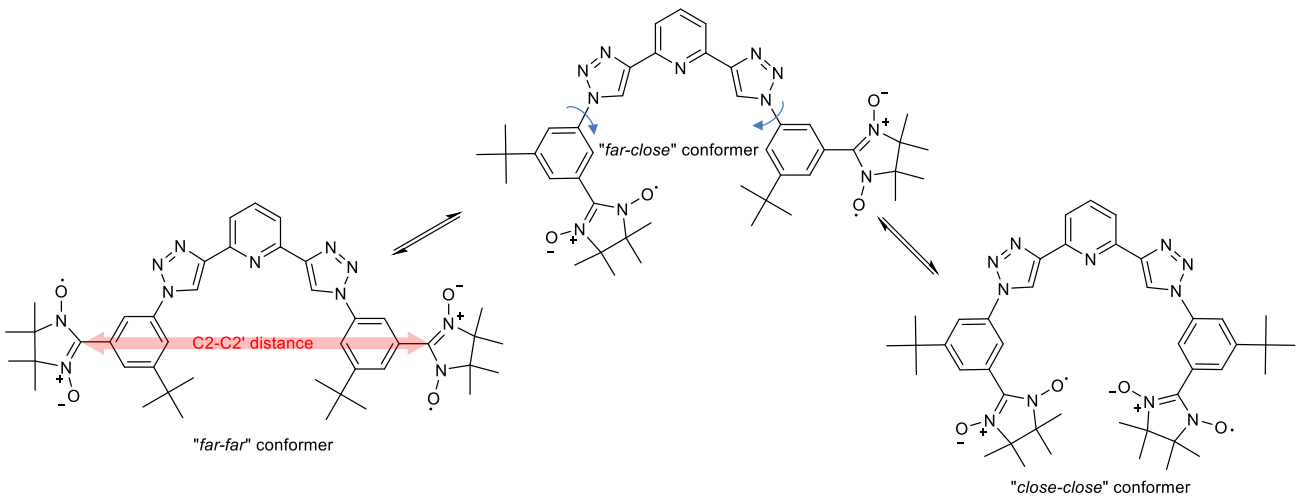

Figure 4.10 *The three possible conformation by considering the rotation of the phenyl triazole-bond of the anti-anti conformation of thread* ***11***.

We made an estimation of these distances by performing stochastic dynamics (SD) simulations in the gas-phase at 298 K by using the AMBER* force field. The simulations were run at 298 K for 20 ns with time steps of 1.5 fs and an equilibrium time of 2 ns before. In order to use reliable parameters, the nitronyl nitroxide moiety was modelled as indicated in Scheme 4.4.

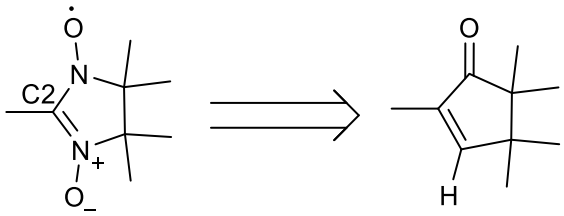

Scheme 4.4 *Simplified model for the NN used in the computational simulations.*

Estimates of distance between C2-C2' (<*r*>) from MD calculations were then calculated. As expected for the different conformers, very different distance profiles were obtained with ⟨*r*⟩ corresponding to 16.0 Å for the "far-far" conformation, 11.5 Å for the "close-far" conformation and 7.1 Å for the "close-close" conformer.

Table 4.1 *distances between C2-C2' in the three main conformations of* ***11***.

Conformer	C2-C2' distance (Å)
far-far	16.0
close-far	11.5
close-close	7.1

Many experimental and theoretical studies have been devoted to the dependence of the exchange coupling upon structural parameters. In particular, it has been shown that the exchange coupling constant *J* decreases exponentially with the distance[19] and that it depends on the orientation of the orbitals containing the unpaired electron with respect to each other.[20] Keeping mind this, we can assume that no spin exchange should be observed for the "*far-far*" conformation, while strong exchange is expected for the "*close-close*" conformer.

To confirm these conclusions, we prepared a new thread (**14**) where the pyridine unit was replaced by a phenyl ring. Removing of the nitrogen atom of the pyridine should give rise to the disappearance of lone pair repulsions between triazoles and pyridine allowing the thread **14** to adopt *syn-syn like* conformations (see Scheme 4.5) in which the distance between nitroxide fragments is larger compared to the *anti-anti* conformation of thread **11** Actually, the EPR spectra of **14** are characterized by a five-line pattern(see Figure 4.11) and shows a clear indication of a decrease in the average value of *J* ($\bar{J}$). When the spectrum of **14** is recorded in toluene, $\bar{J}$ is so small to be comparable to a_N and lines due to forbidden transitions are clearly visible (Figure 4.11).[21]

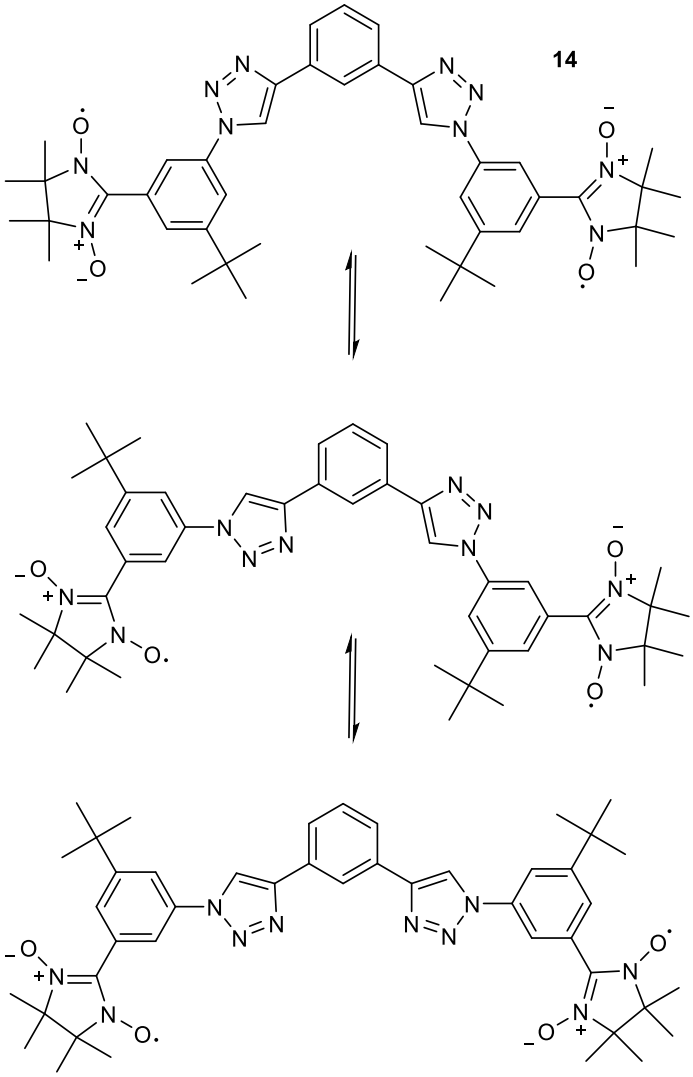

Scheme 4.5 *Possible conformations of thread* ***14*** *around the two triazole-phenyl bonds.*

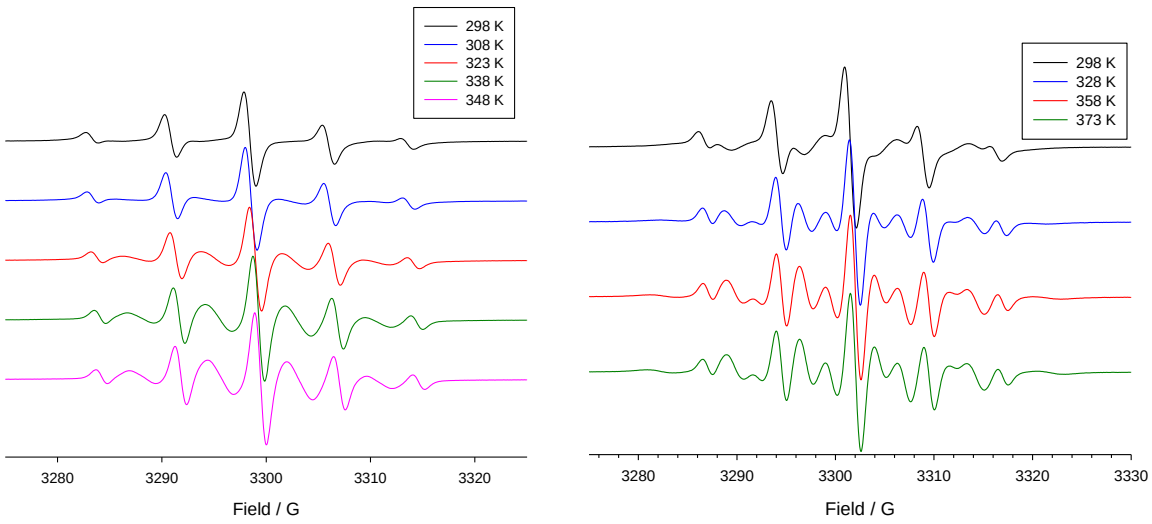

Figure 4.11 *EPR spectra of thread* ***14*** *recorded in ACN (left) and toluene (right) at different temperatures.*

Rotaxane **13** was instead characterized by a five lines spectrum even at high temperatures. If we compare these spectra with those of free thread **14** it is clear that rotaxanation produces a reduction of the average value of *J* in both solvents (see Figure 4.12).

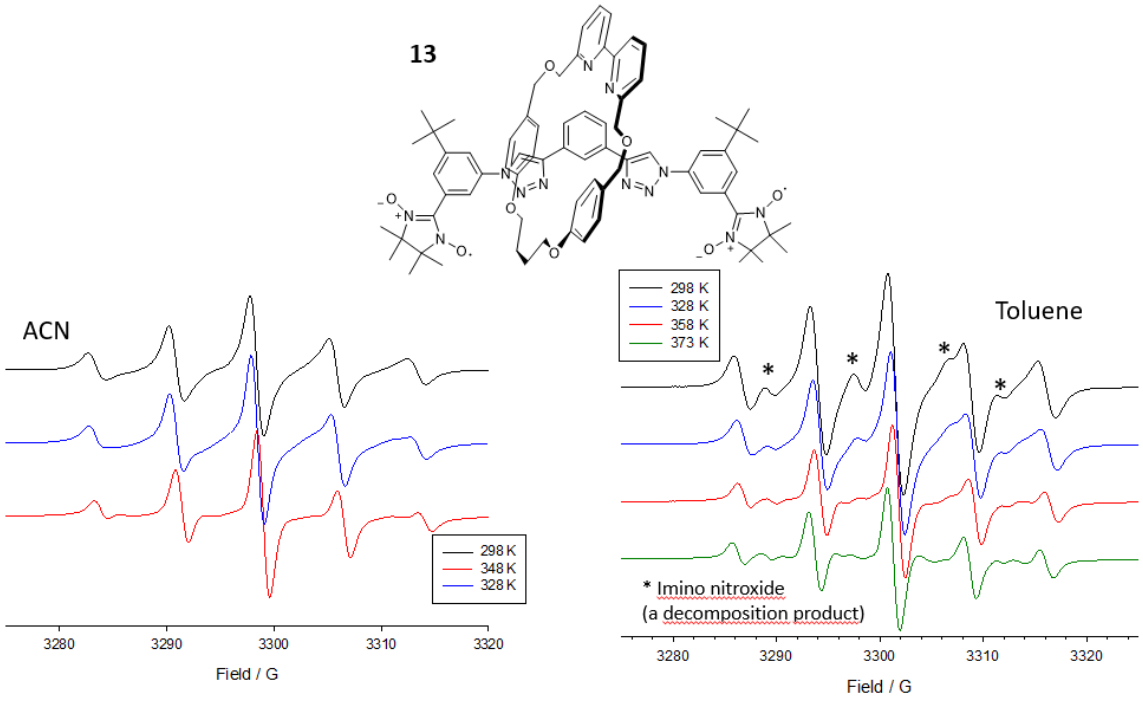

Figure 4.12 *Rotaxane **13** (top), and its EPR spectra recorded in ACN and toluene at different temperatures (bottom).*

We then tried to better understand the origin of the differences of the line widths between threads and rotaxanes, that is between **10** and **11** and between **13** and **14**. Actually, these differences may rise from two different phenomena. The broader line width observed in the rotaxanes can result from a decrease in the average value of *J* ($\bar{J}$) or a decrease in the rate of exchange, or both. In the first hypothesis a decrease on ($\bar{J}$) is expected if rotaxanation would induce an increase in the number of conformations having larger distance between radical fragments, that is an increase of *far-far* conformations. In the second hypothesis a decrease in the rate of spin exchange is obtained if rotaxanation would induce a decrease in the rate of rotation around phenyl-triazole bonds. As long as $\bar{J} >> a$ it is impossible to distinguish between these alternatives. In other words, rotaxanation could reduce the average value of *J* or the rate of exchange, or both. Evidence for the first hypothesis were however obtained by recording EPR spectra of **10** and **11** at different temperatures in ACN and by measuring the corresponding exchange interaction rates.

Exchange broadened EPR spectra were simulated (a_N=7.50 G) by using density matrix theory (which covers the full ranges of rate exchange) and by assuming the simplified two-jump model including a strongly interacting conformation ($J >> a_N$) and another less interacting conformation with $J = 0$. The simulations (red lines) reported in Figure 4.13 of experimental spectra of **10** recorded in toluene at

different temperatures (black lines) show the excellent agreement between the experimental and theoretical spectra calculated by this model.

Figure 4.13 *EPR spectra (black lines) of* ***10*** *recorded in toluene at different temperatures and the corresponding theoretical simulations (red lines).*

The Arrhenius relationship between apparent EPR exchange interaction rates and the temperature is shown in Figure 4.14 for **10** and **11** in ACN. From the slope of the plot, the apparent activation energies for the intramolecular dynamics were evaluated as listed in Table 4.2. The apparent activation energies in the rotaxane **10** and in the free thread **11** were found to be very similar, suggesting that rotaxanation does not have a significant effect on the energy barrier for bond rotation.

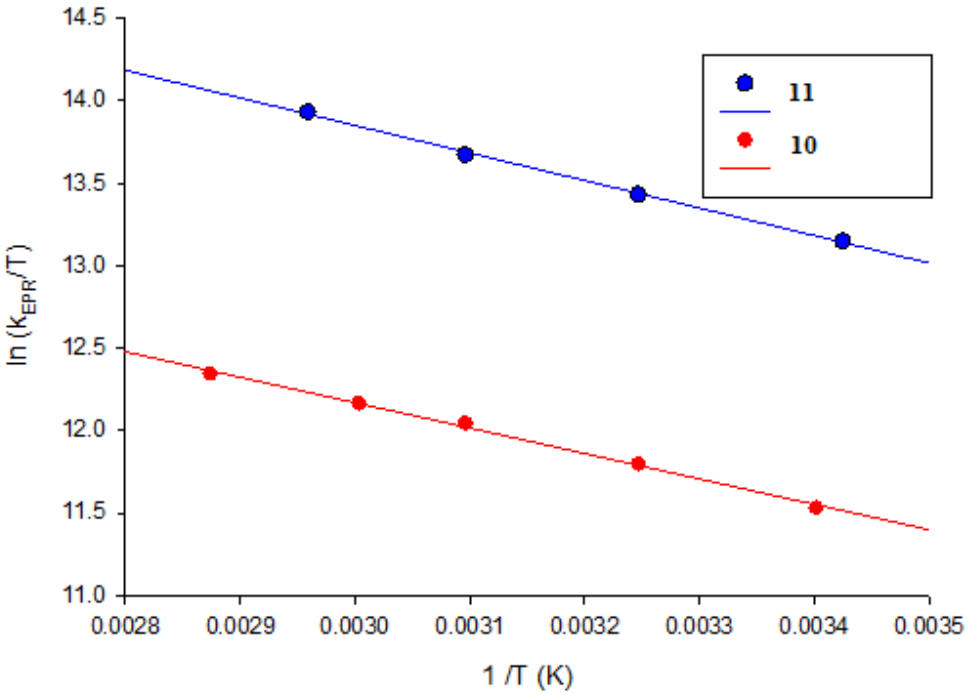

Figure 4.14 *Arrhenius plot of the EPR exchange interactions rates for* ***10*** *and* ***11****.*

In toluene the spectra of **11** were almost completely averaged even at room temperature and accurate determination of activation energy was not possible.

Table 4.2 *Apparent activation energies for the intramolecular dynamics of* ***10*** *and* ***11****.*

Radical	**Solvent**	k_{EPR} **(298K)** s^{-1}	$\Delta H^{\#}$ **kcal/mol**
11	ACN	1.8×10^{8}	3.3
10	ACN	3.3×10^{7}	3.1
11	Toluene	$\approx3\times10^{8}$	--
10	Toluene	1.5×10^{7}	4.5

From these results it is clear the presence of the macrocycle in the rotaxane **10** (and presumably **13**) produces an alteration in the conformational equilibria, compared to that of corresponding thread, giving rise to an increase in the importance of the *far-far* conformations in which the two paramagnetic labels are not interacting.

Non-symmetrical rotaxane (**19**) and thread (**20**) biradicals having only one triazole ring were also prepared and investigated by EPR. Results similar to those observed with **10** and **11** were obtained (data not shown).

4.3.3 Effect of the protonation on the NN-labelled [2]rotaxanes

In literature[17] is reported that proton coordination by nitrogen atoms of the pyridine and traizole rings has a dramatic effect on the equilibrium between conformations of the triazole-pyridine-triazole core present in **10** and **11**. In particular, coordination of the proton converts the *anti–anti* conformation to the *syn–syn* conformation (Figure 4.15).

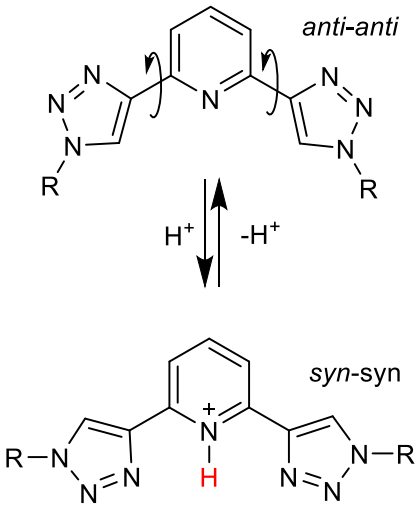

Figure 4.15 *Conversion of the anti-anti to the syn syn conformation induced by protonation of the pyridine.*

When thread **11** is in the *syn-syn* arrangement three main conformations result from the rotation of the phenyl-triazole bonds. Each conformation is characterized by very large distances between radical centres. Therefore, no exchange (*J=0)* can be hypothesised for all these conformations (see Figure 4.16).

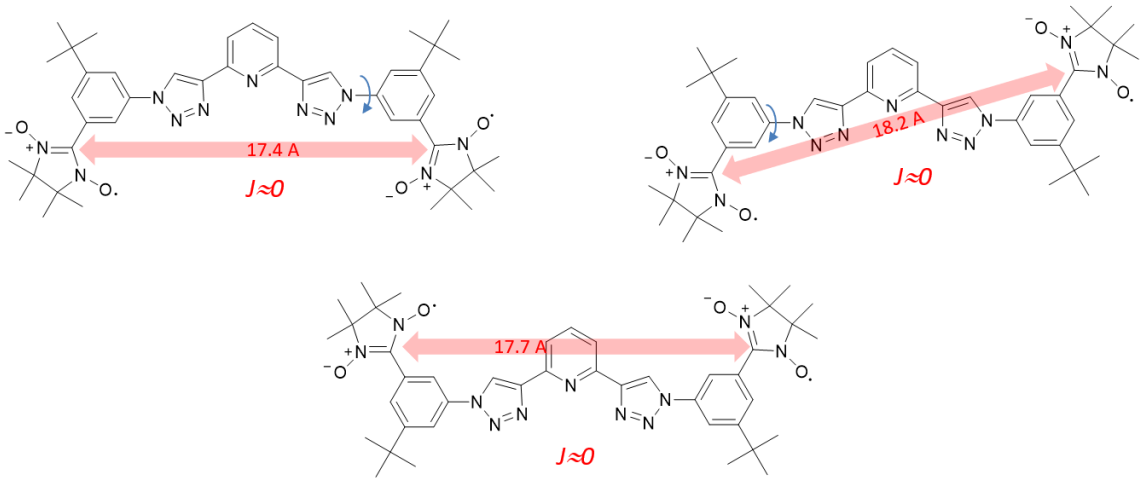

Figure 4.16 *Distances between the spin labels in three possible conformations in the syn-syn conformer of* ***11****.*

Actually, the EPR spectra of **11** recorded in ACN in the presence of increasing amounts of trifluoracetic acid (TFA), showed the disappearance of the nine-lines spectrum due to the contribution of the *anti-anti* conformation and the increase of the five-lines spectrum due to the *syn-syn* conformation (Figure 4.17).

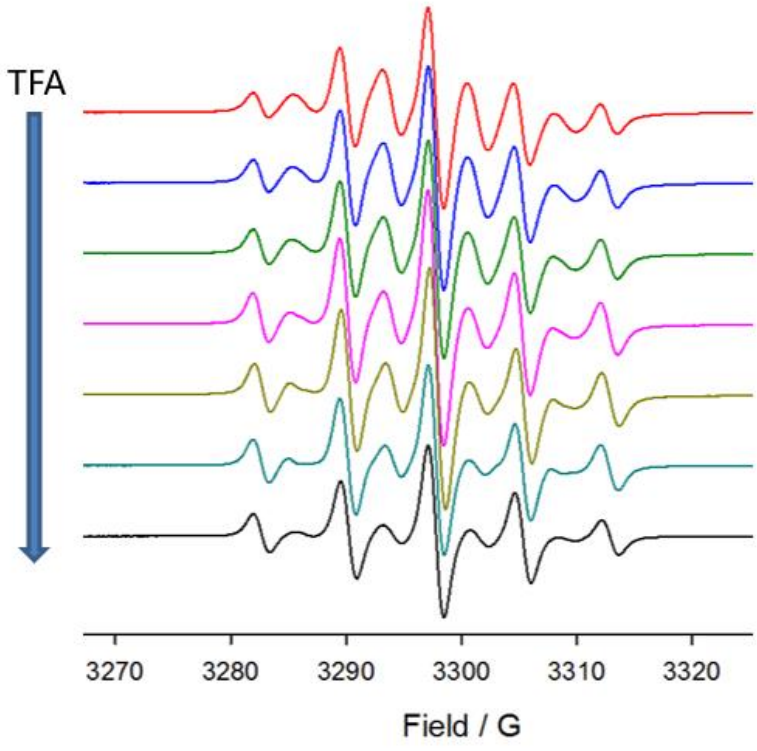

Figure 4.17 *EPR titration of thread* ***11*** *with TFA recorded in ACN at 298 K.*

The spectra can be reproduced by superimposing the signals of the two conformations in different relative amounts. This suggests that the protonation equilibrium between the two species must be slow in the EPR time scale. We have previously show with **14** that the rate of triazole-phenyl-triazole rotation is comparable to EPR time scale. Thus, we could conclude proton transfer between 2,6-disubstituted pyridine and its conjugate acid is the rate limiting process.[22]

Rotaxane **10** shows extreme broadening. In this case, the reduction of ($\bar{J}$) due to the increase of *syn-syn* conformations would simply produce an increase in the intensity of five lines spectrum. Actually, increasing amount of TFA in ACN produced an increase in the height of EPR lines (Figure 4.18).

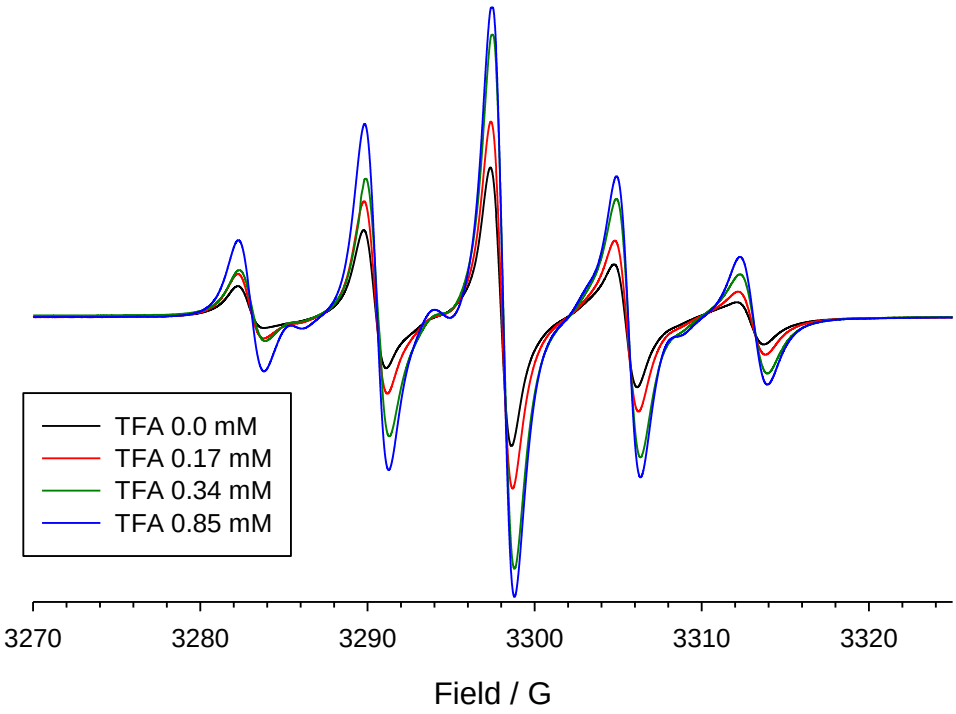

Figure 4.18 *EPR titration of rotaxane **10** with TFA recorded in ACN at 298 K.*

4.3.4 Effect of metal coordination on the NN labelled [2]rotaxanes.

The triazole-pyridine-triazole motif, present in **10** and **11** is already known to be a good ligand for metal cations.[17] Moreover also the bipyridinium unit in the macrocyclic component of the [2]rotaxanes constitutes a binding site for metals.[23] Therefore, we decided to assess if the host guest properties of both rotaxanes and threads by the means of EPR spectroscopy.

The EPR spectrum of **11** was recorded in the presence of iron(II) trifluoromethanesulfonate ($Fe(OTf)_2$) in ACN and is reported in Figure 4.19. It shows mainly one broad signal with a trace of unresolved hyperfine structure. Lines separation is about ¼ of nitrogen coupling. All these observations suggest the formation of a tetraradical whose structure could be similar to that reported by Hecht and co-workers[17] (Figure 4.20), in which the unpaired electron is coupled with 8 nitrogen atoms. Reversible interconversion between tetraradical and diradical forms was demonstrated by addition of an excess of

2,2'-bypiridine to a solution containing the Fe(II)-**11** complex. Under these conditions the EPR spectra returned to the original biradical signal. We have also recorded the EPR spectrum of the derivative lacking pyridine ring (**14**) in the presence of $Fe(OTf)_2$ in ACN. As expected, no significant changes were evident in this case.

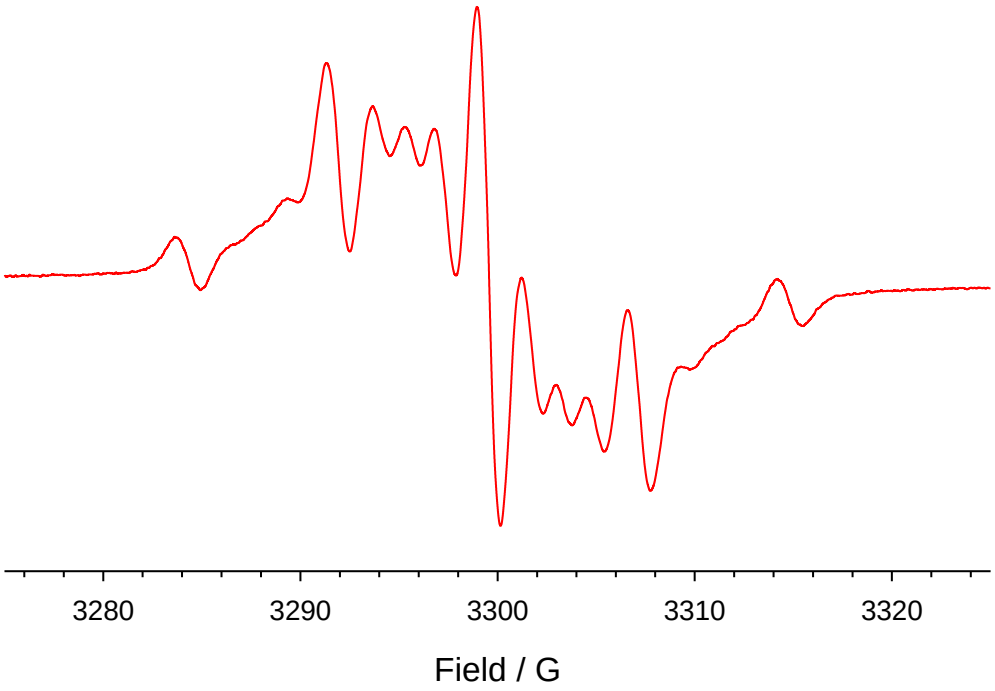

Figure 4.19 *EPR spectrum of* ***11*** *in presence of* $Fe(OTf)_2$ *in ACN at 298 K.*

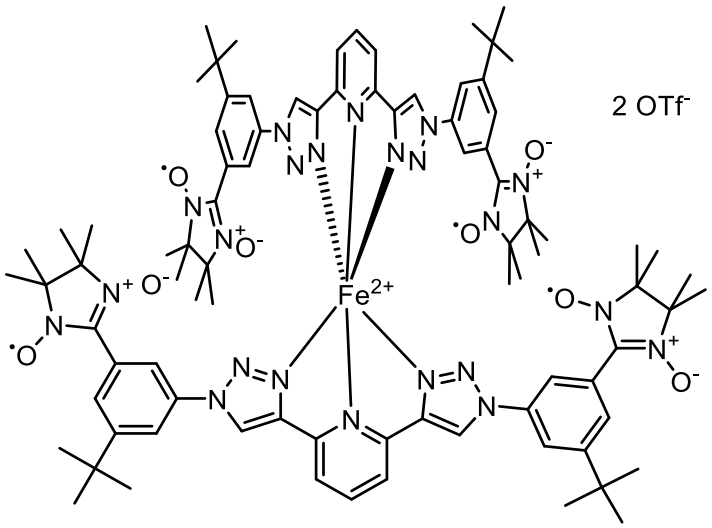

Figure 4.20 *The tetraradical complex* $\mathbf{11}_2$***@****$Fe(OTf)_2$.*

We performed an EPR titration in ACN by adding increasing amount of Fe(II) to a solution of **11**. After the addition of half equivalent of Fe(II) (respect to nitroxide) the spectra did not change anymore confirming the 1:2 stoichiometry of the complex (see Figure 4.21).

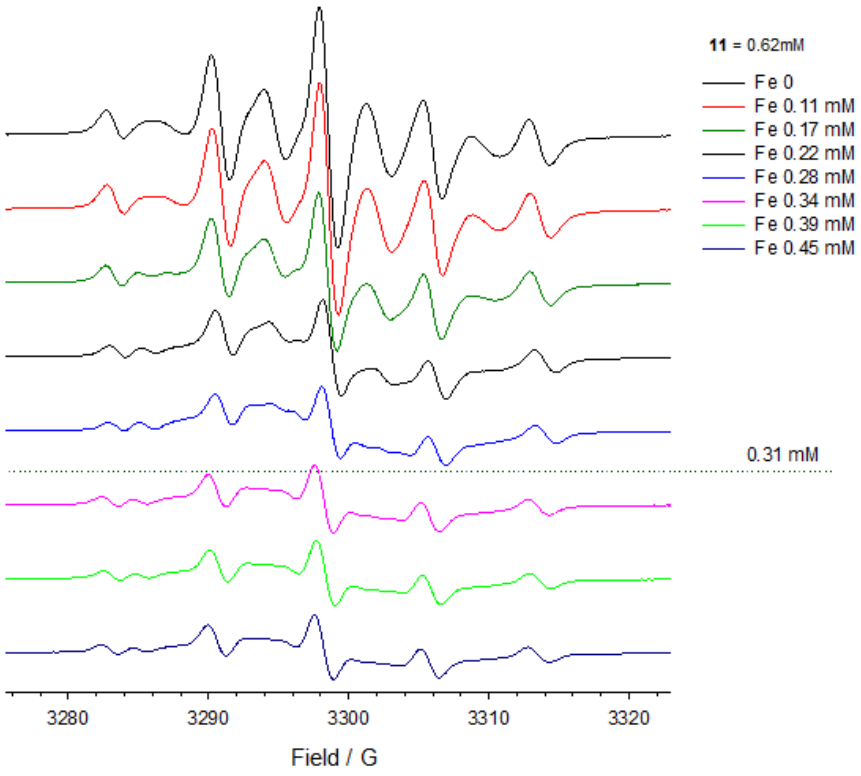

Figure 4.21 *The EPR titration of* ***11*** *with* $Fe(OTf)_2$ *in ACN at 298 K.*

The EPR spectrum of rotaxane **10** in the presence of $Fe(OTf)_2$ in ACN is reported in Figure 4.22. In this case a very broad line (line width larger than 50 G) was obtained. No evidence of hyperfine structure was visible. This signal is clearly different if compared to that obtained with **11** in the presence of Fe(II). The double integrated signal remains constant after addition of Fe(II) indicating that the total amount of radical species does not change.

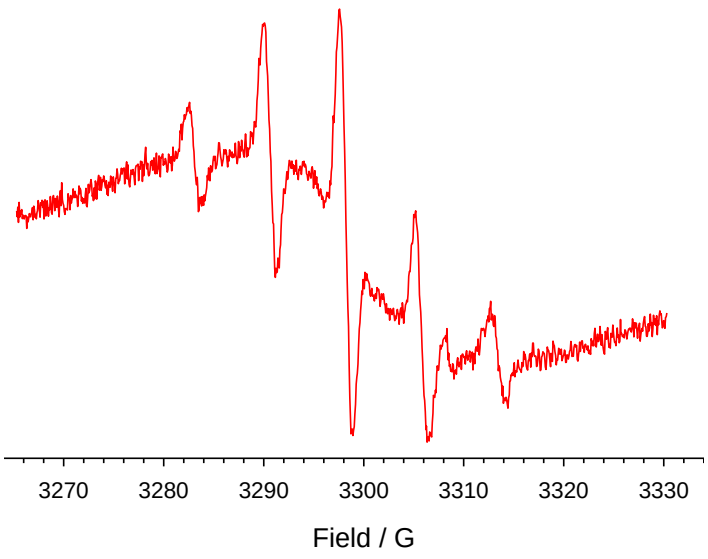

Figure 4.22 *EPR spectrum of rotaxane* ***10*** *recorded in ACN at 298 K and in presence of* $Fe(OTf)_2$.

We performed also an EPR titration in ACN by adding increasing amount of Fe(II) in the presence of **10**. In the present case the spectra stopped to change after the addition of more than one equivalent of Fe(II) suggesting the formation of a 1:1 complex. The addition of 2,2'-bipyridine restored the original spectrum of **10** (Figure 4.23). This peculiar signal was observed also with other metal cations and the nature of its origin is still under investigation in our laboratories.

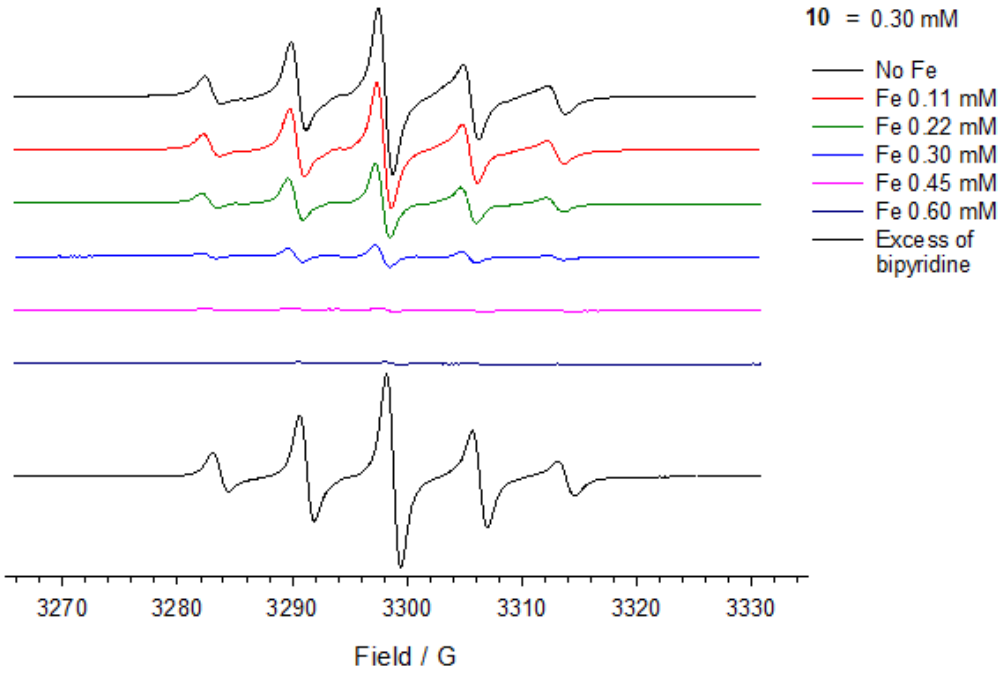

Figure 4.23 *EPR titration of* ***10*** *in ACN at 298 K, with* $Fe(OTf)_2$.

4.4 Conclusions

We have developed and optimized a method for the synthesis of NN spin labelled [2]-rotaxanes, and their corresponding free threads, in high yields and in mild conditions, compatible with the presence of the radical stoppers. The presence of the paramagnetic fragments as stoppering units allowed us to obtain, by the means of EPR spectroscopy, information on the conformational equilibria exhibited by the investigated structures. The mechanical bond has a significative effect on conformation populations increasing the importance of conformations in which the radical fragments are far apart while is doesn't seem to have an effect on the activation energy for phenyl-triazole bond rotation. The switching from the *anti-anti* to the *syn-syn* conformer was detected by protonation of the triazole-pyridine-triazole core present in **10** and **11**. The metal binding abilities were then investigated by performing EPR titrations that revealed the formation of a 2:1 tetraradical complex between **11** and Fe(II) and a 1:1 complex between **10** and Fe(II). The magnetic properties of the complexes between the rotaxanes/threads and metal cations are currently under investigation in our laboratories.

4.5 References

1 C. Dietrich-Buchecker, J. -P. Sauvage, *Tetrahedron Letters*, 1983, **24**, 5095 - 5098.
2 B. Mohr, J.-P. Sauvage, R. H. Grubbs and M. Weck, *Angew. Chem., Int. Ed. Engl*., 1997, **36**, 1308 - 1310.
3 J. E. M. Lewis, P. D. Beer, S. J. Loeb and S. M. Goldup, *Chem.Soc.Rev*., 2017, **46**, 2577 – 2591.
4 J. D. Crowley, S. M. Goldup, A.-L. Lee, D. A. Leigh and R.T. McBurney, *Chem. Soc. Rev*., 2009, **38**, 1530 - 1541.
5 V. Aucagne, K. D. Hanni, D. A. Leigh, P. J. Lusby, and D. B. Walker, *J. Am. Chem. Soc*. 2006, **128**, 2186-2187.
6 M. Denis, S. M. Goldup, *Nature Reviews Chemistry*, 2017, **1**, 0061.
7 E. A. Neal and S. M. Goldup, *Chem. Sci.*, 2015, **6**, 2398 – 2404.
8 H. Lahlali, K. Jobe, M. Watkinson and S. M. Goldup, *Angew. Chem. Int. Ed.*, 2011, **50**, 4151 – 4155.
9 J. E. M. Lewis, F. Modicom, and S. M. Goldup *J. Am. Chem. Soc.*, 2018,***140***, 4787 - 4791.
10 K. Higashiguchi, K. Yumoto, and K. Matsuda, *Org. Lett.*, 2010, 12, 5284 – 5286.
11 PHENEX PHARMACEUTICALS AG; C. Gege, C. Steeneck, O. Kinzel, G. Kleymann, T. Hoffmann, WO2013/178362, 2013, A1
12 C. Hirel, K. E. Vostrikova, J. Pécaut, V. I. Ovcharenko and P. Rey, *Chem. Eur. J*., 2001, **7**, 2007-2014.
13 A. Bouillon, J.-C. Lancelot, J. S. de Oliveira Santos, V. Collot, P. R. Bovy, S. Rault, *Tetrahedron*, 2003, **59**, 10043-10049.
14 J. Winn, A. Pinczewska, and S. M. Goldup, *J. Am. Chem. Soc.*, 2013, ***135***, 13318–13321.
15 G. R. Luckhurst, *Mol. Phys.*, 1966, **10**, 543-550.
16 S. T. Howard, *J. Am. Chem. Soc.*, 1996, **118**, 10269 –10274.
17 R. Meudtner, M. Ostermeier, R. Goddard, C. Limberg and S.Hecht, *Chem. Eur. J*., 2007, **13** 9834-9840.
18 D. Zornik, R. M. Meudtner, T. E. Malah, C. M. Thiele and S. Hecht, *Chem. Eur. J*., 2011, **17**, 1473 – 1484.
19 a) K. Yamaguchi, M. Okumura, J. Maki, T. Noro, H. Namimoto, M. Nakano, T. Fueno, K. Nakasuji, Chem. Phys. Lett. 1992, **190**, 353−360. (b) G. L. Closs, M. D. E. Forbes, P. J. Piotrowiak, *J. Am. Chem. Soc.*, 1992, **114**, 3285−3294.
20 V. Barone, A. Bencini, A. Di Matteo, *J. Am. Chem. Soc*., 1997, **119**, 10831−10837.
21 G. R. Luckhurst and G. F. Pedulli, *Mol. Phys.*, 1971, **20**, 1043-1055.
22 J. Emsley, V. Gold and R. A. Lee, *J. Chem. Soc., Perkin Trans. II*, 1986, **11**, 1861-1865.
23 M. Denis, J. Pancholi, K. Jobe, M. Watkinson and S. M. Goldup, *Angew. Chem. Int. Ed.*, 2018, ***57***, 5310.

5. Experimental section

5.1 Materials and methods

All reagents and solvents were used as received, without further purification.

Reactions were monitored by TLC chromatography and the formation of the products was visualized with UV, I_2 or ninhydrin. In some cases, the reactions were also monitored by the means of GC-MS, ESI-MS and NMR analyses.

Column Chromatography was performed on Merck silica gel (230–400 mesh).

NMR analysis were recorded on Varian Mercury 400 MHz, Bruker AV400 and AV3-400 spectrometers at 298 K, using the solvent peaks as internal standards. Chemical shifts are reported in parts per million (ppm, δ scale).

ESI-MS Mass spectrometry analyses were performed on Waters ZMD 4000, ZQ 4000 and TQD mass spectrometers, the sample was prepared in methanol or acetonitrile.

LC-MS analysis was performed with a Waters TQD mass spectrometer equipped with UHPLC injection with a BEH C18 column; ACN/hexane gradient + 0.2% formic acid.

GC-MS was performed on an Agilent 7890 Gas Chromatographer paired with Agilent 5973 Mass selective detector, CH_2Cl_2 was used as solvent for the preparation of the samples.

EPR spectra has been recorded on Bruker-ELEXYS spectrometer by using the following instrument settings: microwave power 0.79 mW, modulation amplitude 0.04 mT, modulation frequency 100 kHz, scan time 180 s, 2K data points.

UV-visible experiments were performed on a JASCO V-550 spectrometer.

5.2 Experimental section of chapter 2

2,3,5,6 tetrafluoro-4-iodobenzaldehyde **1**,[1] was synthesized according to literature procedure.

2,3,5,6-tetrafluorobenzaldehyde (**1-H**) was obtained by reduction of 2,3,5,6-tetrafluoro-benzoic acid following the same procedure used for **1**.[1]

2,3,5,6 tetrafluoro-benzoic acid was purchased from TCI.

Synthesis of compound 2_{NH}:

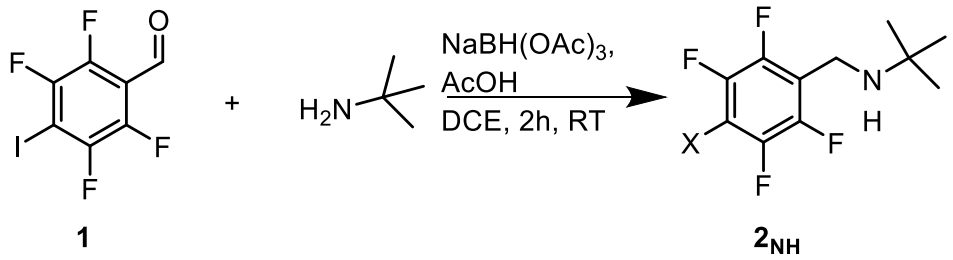

1 **2_{NH}**

A stirred mixture of **1** (250 mg, 0,82 mmol) and *tert*-butylamine (90µL, 0,86 mmol, 1,05 eq.) in dry DCE (9,25mL), under N_2, was treated with $NaBH(OAc)_3$ (226 mg, 1,06 mmol 1,3 eq.) and then with glacial acetic acid (1,4 eq.). The mixture was stirred for 2 h and then the reaction was quenched with 1M NaOH (10 mL). The aqueous phase was extracted with DCM (3x10 mL), the organic phases washed with brine (30 mL), dried on $MgSO_4$ and filtered. The solvent was removed under reduced pressure. The crude product was purified on SiO_2 (c-Hex/Et_2O 9:1) to give a colourless solid (207 mg, 0.57mmol, 70%). ^{1}H-NMR (400 MHz, CD_3CN) δ: 3,81 (s, 2H), 1,12 (s, 9H); ^{19}F-NMR (376 MHz, CD_3CN) δ -123.81 (m), -144.61(m); GC-MS (*m/z*, %): 361 [M^+, 6], 346 [M^+ - 15, 34], 288 [M^+ - 73, 29], 161 [M^+-234, 12].

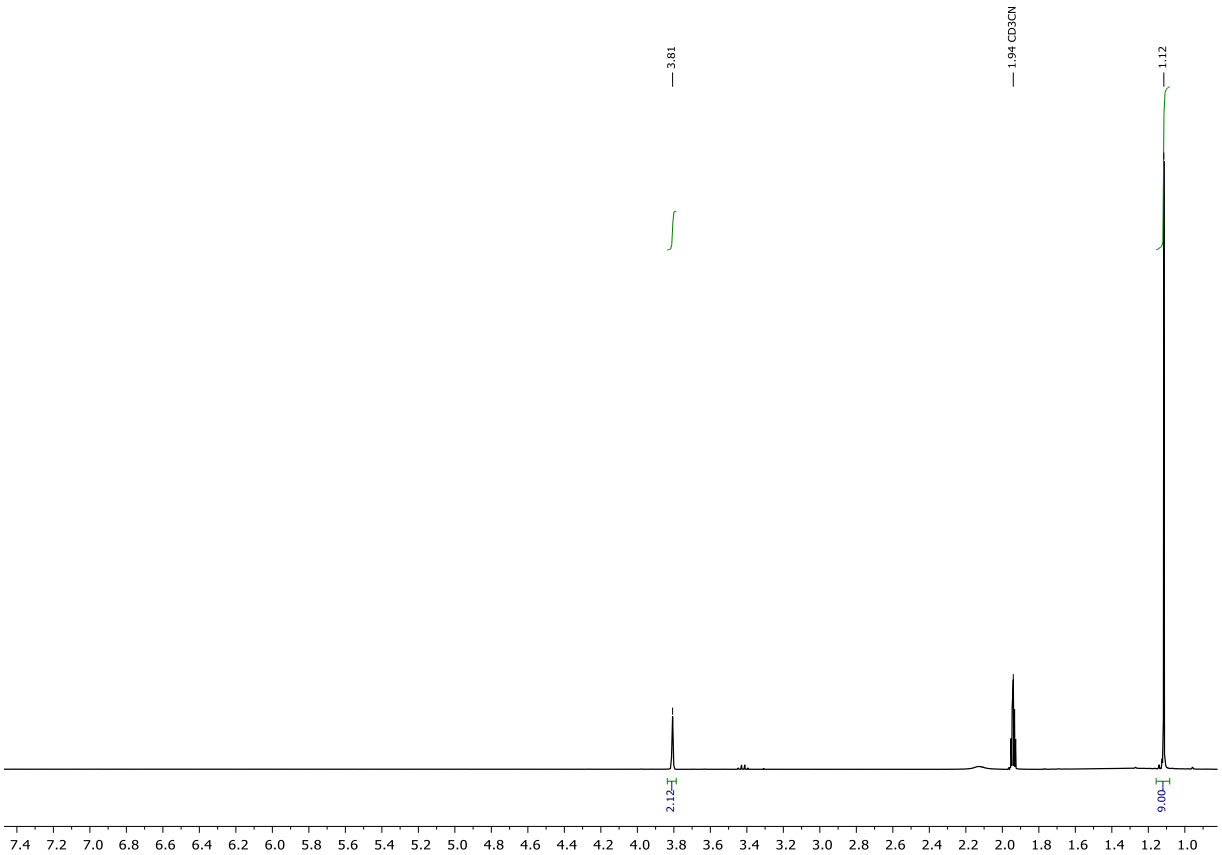

Figure 5.1 *^{1}H-NMR (400 MHz, CD_3CN) of compound* ***2*****$_{NH}$**.

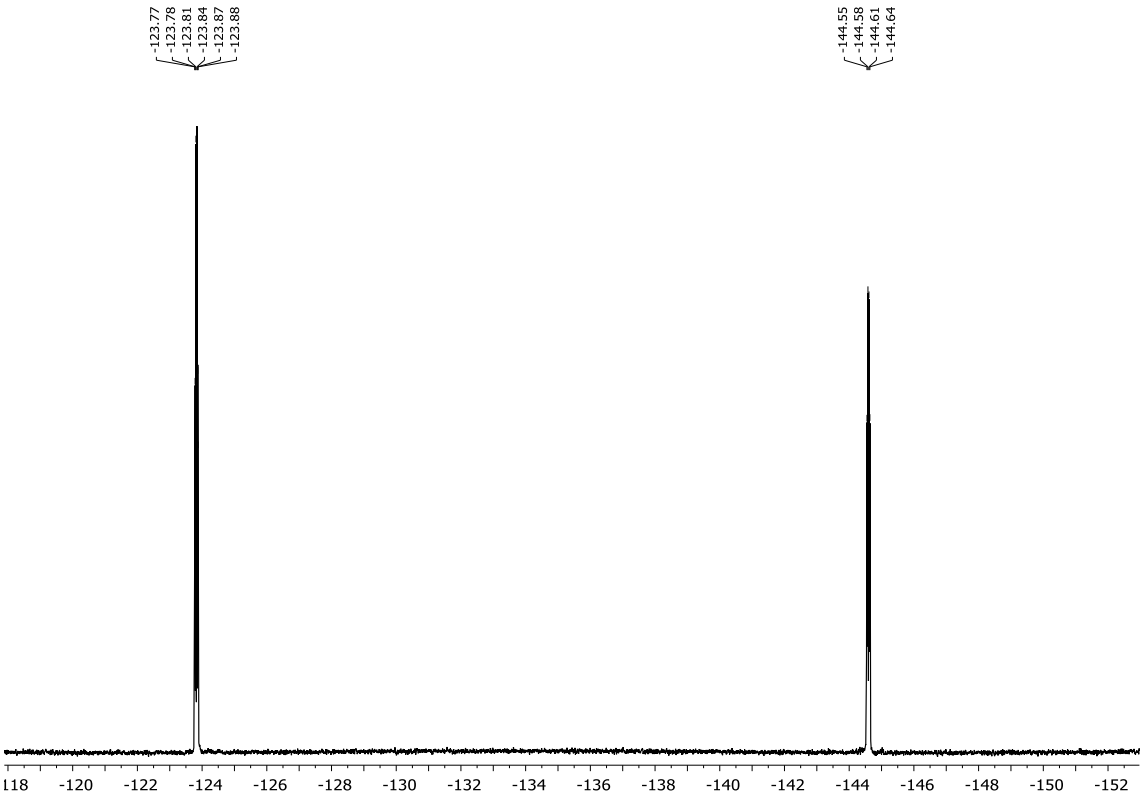

Figure 5.2 *^{19}F NMR (376 MHz, CD_3CN) of compound* ***2*****$_{NH}$**.

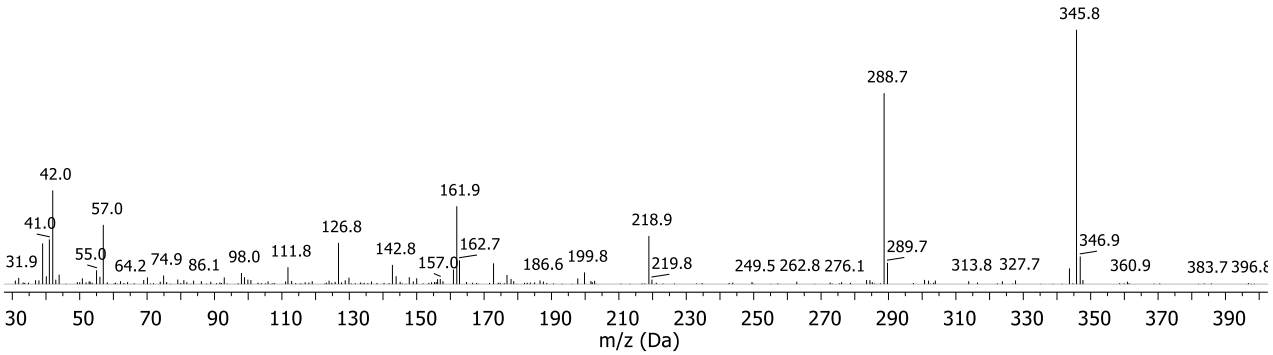

Figure 5.3 *EI-MS spectrum of compound* ***2*****$_{NH}$**.

Synthesis of compound 2$_{NH}$-H:

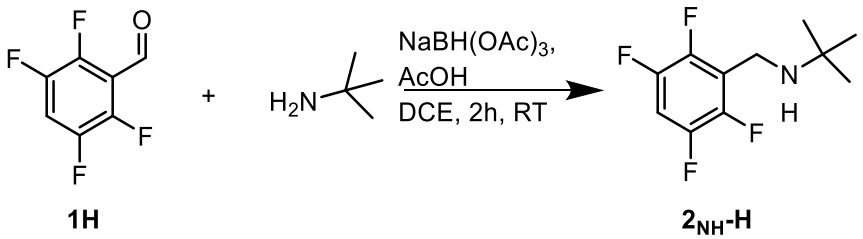

A stirred mixture of **1-H** (250 mg, 1.40 mmol) and *tert*-butylamine (154 µL, 1.47 mmol, 1.05 eq.) in dry DCE (9 mL), under N_2, was treated with $NaBH(OAc)_3$ (226 mg, 2,54 mmol 1.3 eq.) and then with glacial acetic acid (112 µL, 1.96 mmol, 1.4 eq.). The mixture was stirred for 2 h and then the reaction was quenched with 1M NaOH (10 mL). The aqueous phase was extracted with DCM (3x10 mL), the organic phases washed with brine (30 mL), dried on $MgSO_4$ and filtered. The solvent was removed under reduced pressure. The crude product was purified on SiO_2 (c-Hex/Et_2O 9:1). Isolated as a colorless oil (198 mg, 60%); ^{1}H-NMR (400 MHz, CD_3CN) δ: 7,21 (tt, *J* = 10.3, 7.6 Hz, 1 H) 3,82 (s, 2H), 1,12 (s, 9H); ^{19}F NMR (376 MHz, CD_3CN) δ -141.92 (ddd, *J* = 21.6, 13.1, 10.4 Hz), -147.02 (ddd, *J* = 21.0, 13.1, 7.6 Hz); GC-MS (*m/z*, %): 235 [M^+, 0,33], 220 [M^+ - 15, 100], 163 [M^+- 73, 80].

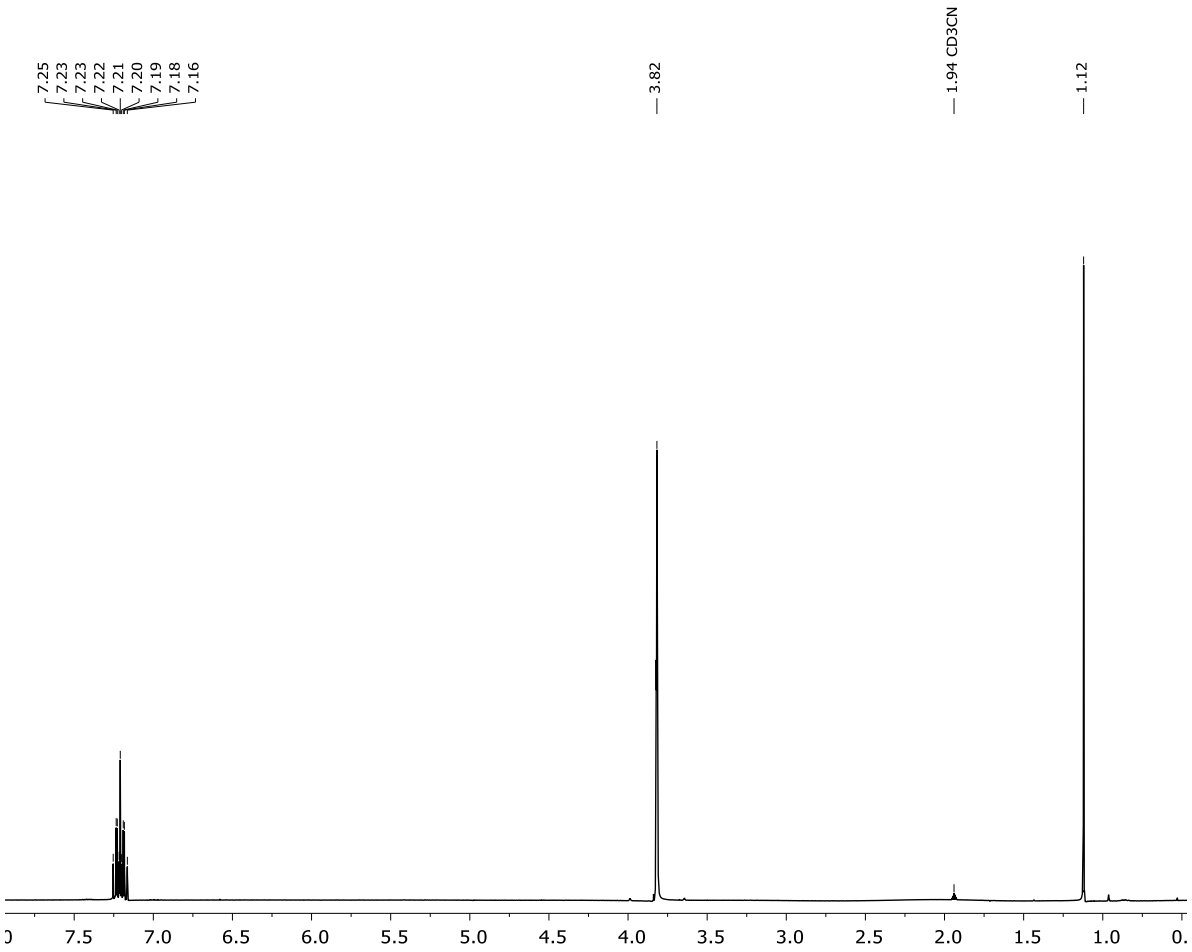

Figure 5.4. *^{1}H-NMR (400 MHz, CD_3CN) of compound* ***2*** $_{\mathbf{NH}}$***-H.***

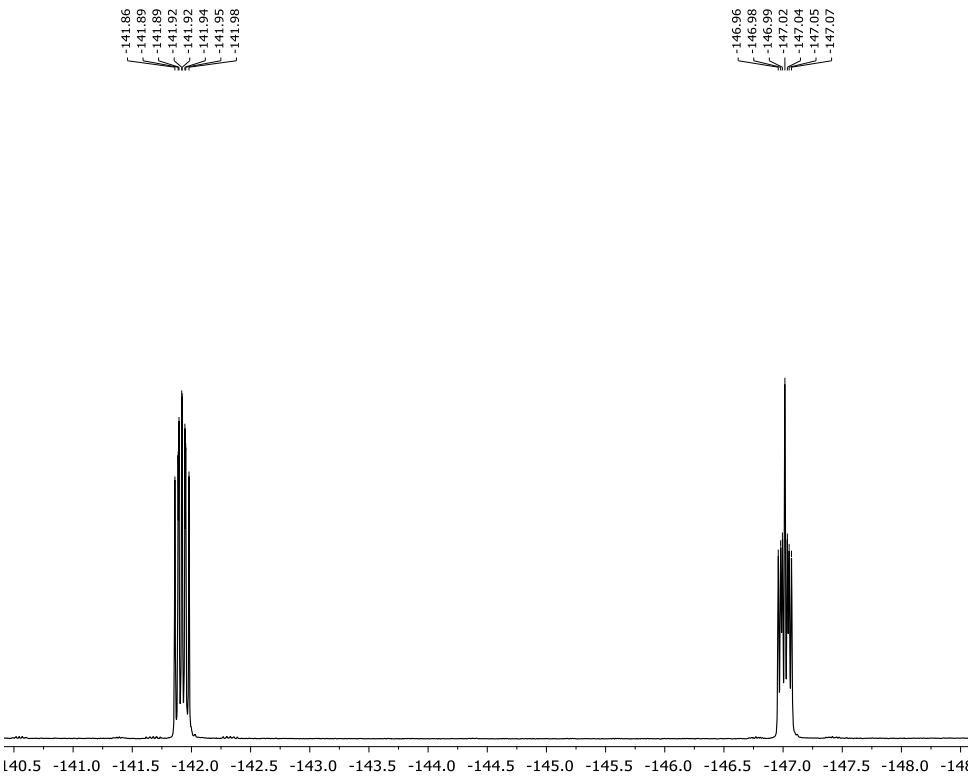

Figure 5.5. *^{19}F NMR (376 MHz, CD_3CN) of compound* ***2*** $_{\mathbf{NH}}$ ***-H.***

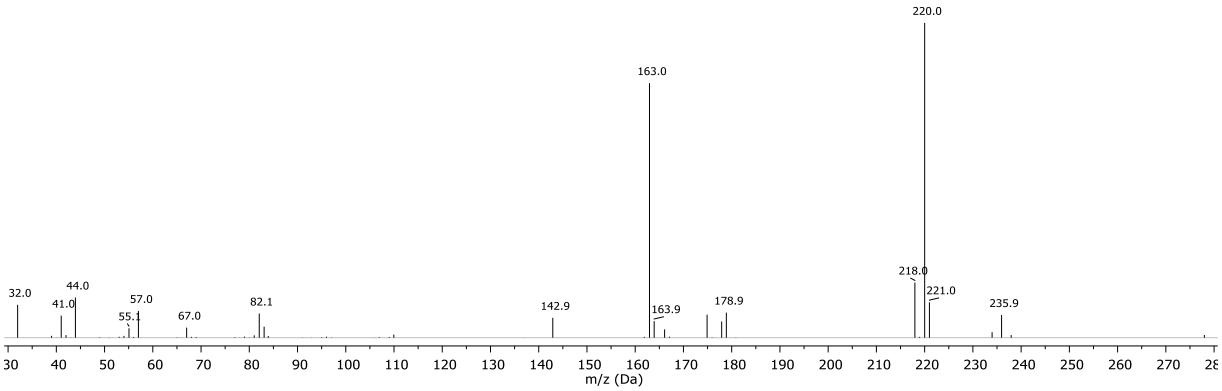

Figure 5.6. *EI-MS spectrum of compound* ***2$_{NH}$-H****.*

Synthesis of compound 3$_{NH}$:

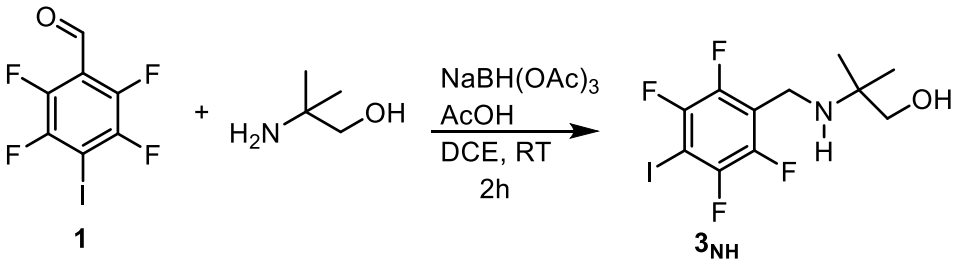

A stirred mixture of **1** (250 mg, 0.82 mmol) and 2-methyl -2-amino 1-propanol (77 mg, 0.86mmol, 1.05 eq.) in dry DCE (9 mL), under N_2, was treated with $NaBH(OAc)_3$ (226 mg, 1.06 mmol 1,3 eq.) and then with glacial acetic acid (1,4 eq.). The mixture was stirred for 2 h and then the reaction was quenched with 1M NaOH (10 mL). The aqueous phase was extracted with DCM (3x10 mL), the organic phases washed with brine (30 mL), dried on $MgSO_4$ and filtered. The solvent was removed under reduced pressure. The crude product was purified on SiO_2 gel chromatography(c-Hex/EtOAc 3:1) to give a colourless solid (197 mg, 64%); ^{1}H-NMR (400 MHz, CD_3CN) δ: 3,80 (s, 2H), 3,28 (s, 2H) 1,05 (s, 9H); ^{19}F NMR (376 MHz, CD_3CN) δ -123.73 (m), -144.50 (m); GC-MS (*m/z*, %): 362 [M^+-18, 2], 346 [M^+ -32, 100], 288,9 [M^+- 88, 81].

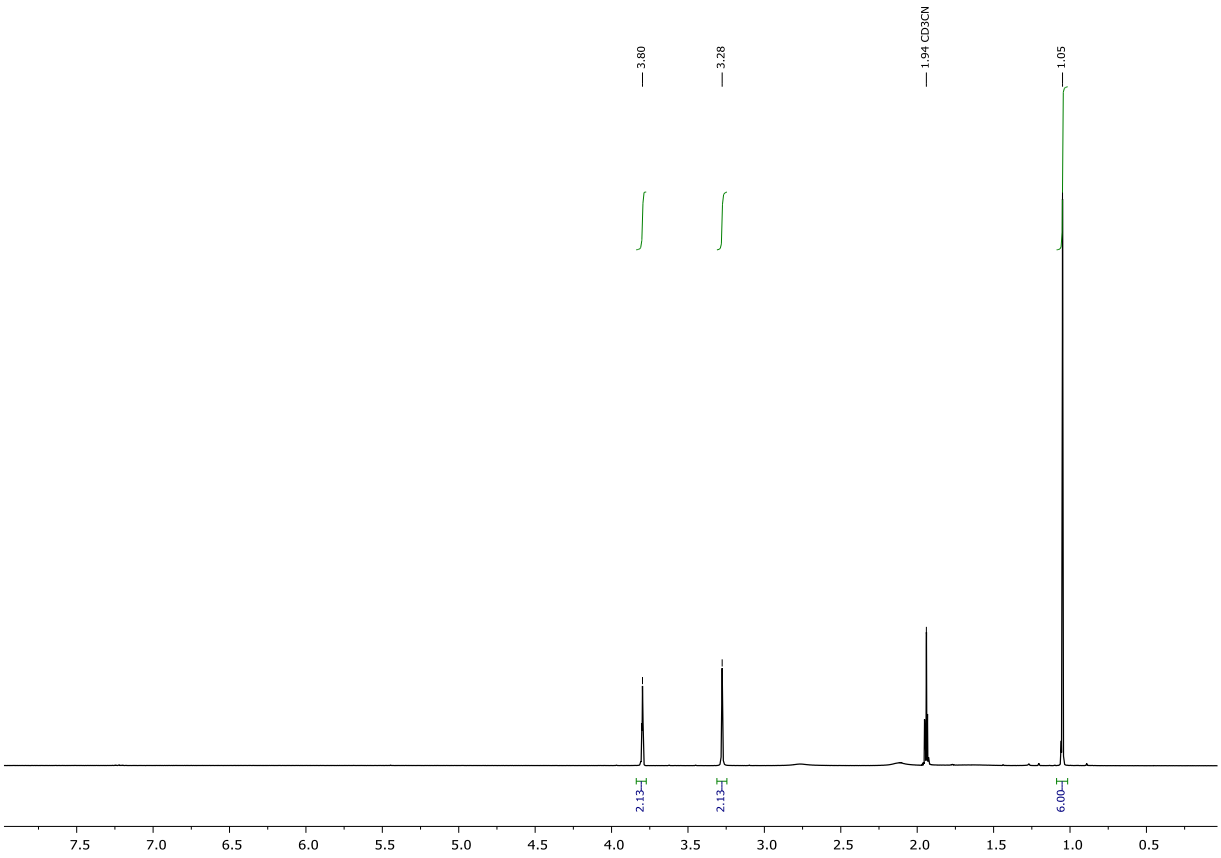

Figure 5.7. *[1]H-NMR (400 MHz, CD_3CN) of compound* ***3*****$_{NH}$.**

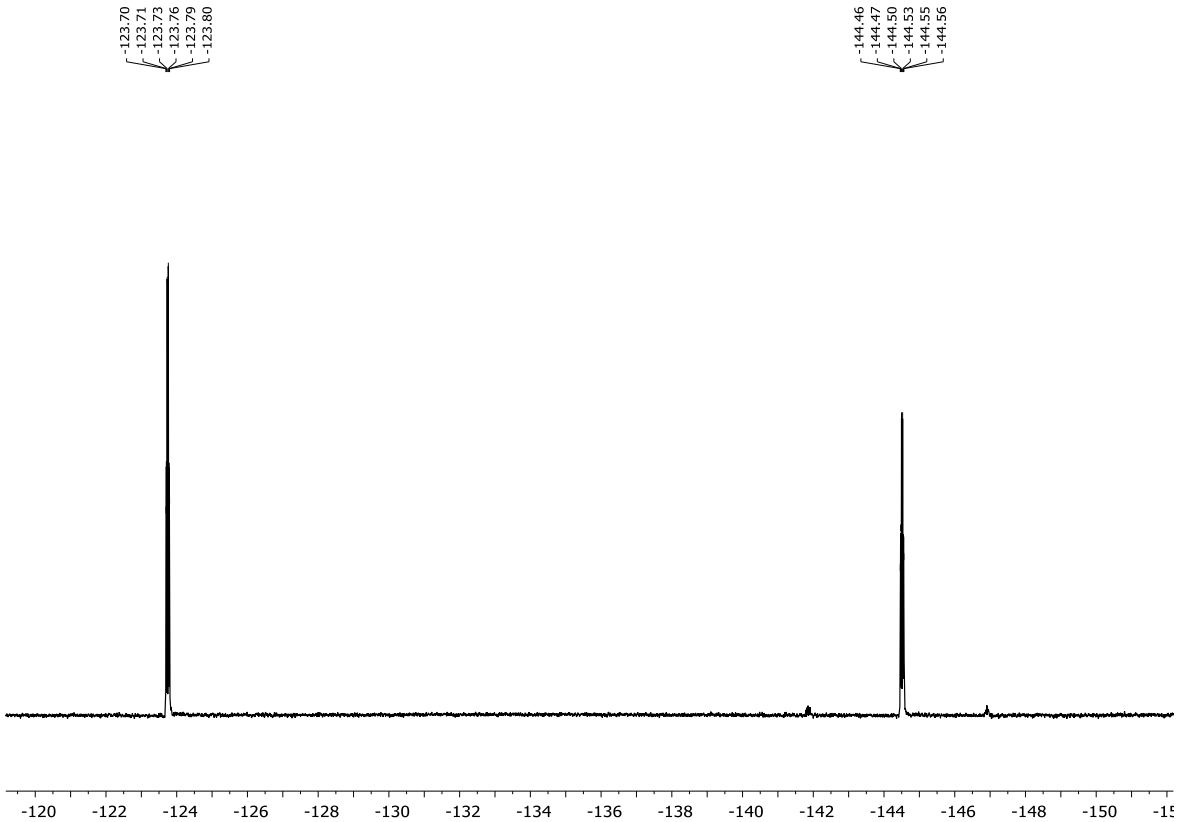

Figure 5.8. *[19]F NMR (376 MHz, CD_3CN) of compound* ***3*****$_{NH}$.**

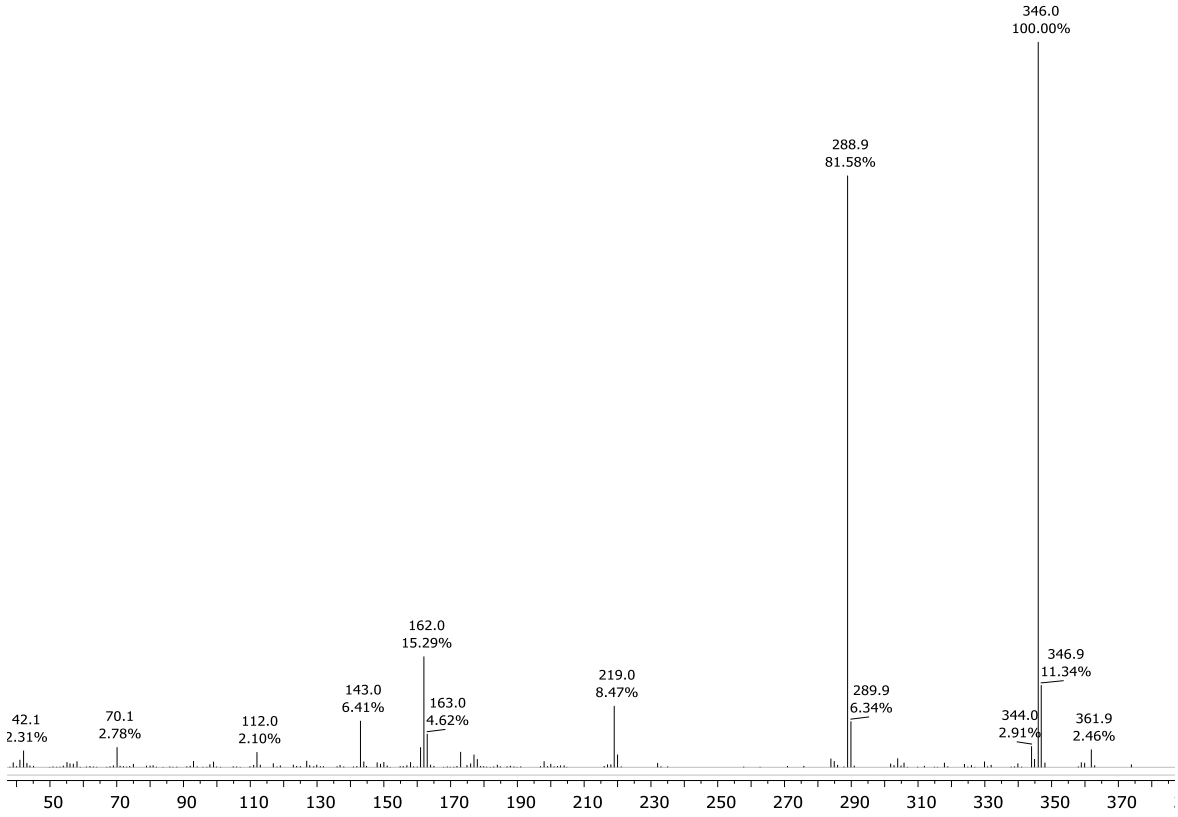

Figure 5.9. *EI-MS spectrum of compound* ***3*****$_{NH}$**.

Synthesis of compound 3$_{NH}$-H.

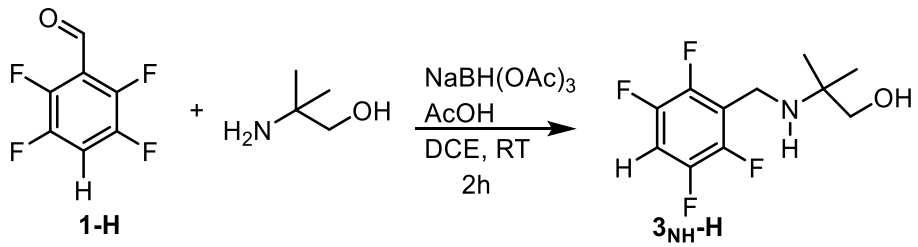

A stirred mixture of **1-H** (250 mg, 1.40 mmol) and 2-methyl -2-amino 1-propanol (77 mg, 0,86 mmol, 1.05 eq.) in dry DCE (9 mL), under N_2, was treated with $NaBH(OAc)_3$ (226 mg, 2,54 mmol 1,3 eq.) and then with glacial acetic acid (112 µL, 1.96 mmol, 1,4 eq.). after 2 h The reaction was quenched with 1M NaOH and the aqueous phase extracted with DCM. The organic phases were washed with brine, dried on $MgSO_4$ and the solvent removed under reduced pressure. The crude product was purified on silica (c-Hex/Et_2O 9:1) to give **3$_{NH}$-H** as a colourless solid (193 mg, 55%); ^{1}H-NMR (400 MHz, CD_3CN) δ: 7,22 (tt, *J* = 10.3, 7.6 Hz, 1H) 3.82 (s, 2H), 3.20 (2, 2H) 1,12 (s, 9H); ^{19}F NMR (376 MHz, CD_3CN) δ -141.86 (ddd, *J* = 21.5, 13.2, 10.4 Hz), -146.91 (ddd, *J* = 21.1, 13.1, 7.5 Hz); GC-MS (EI, *m/z, %*): 236 [M^+-15, 3], 220 [M^+ - 32, 100], 163 [M^+- 88, 98].

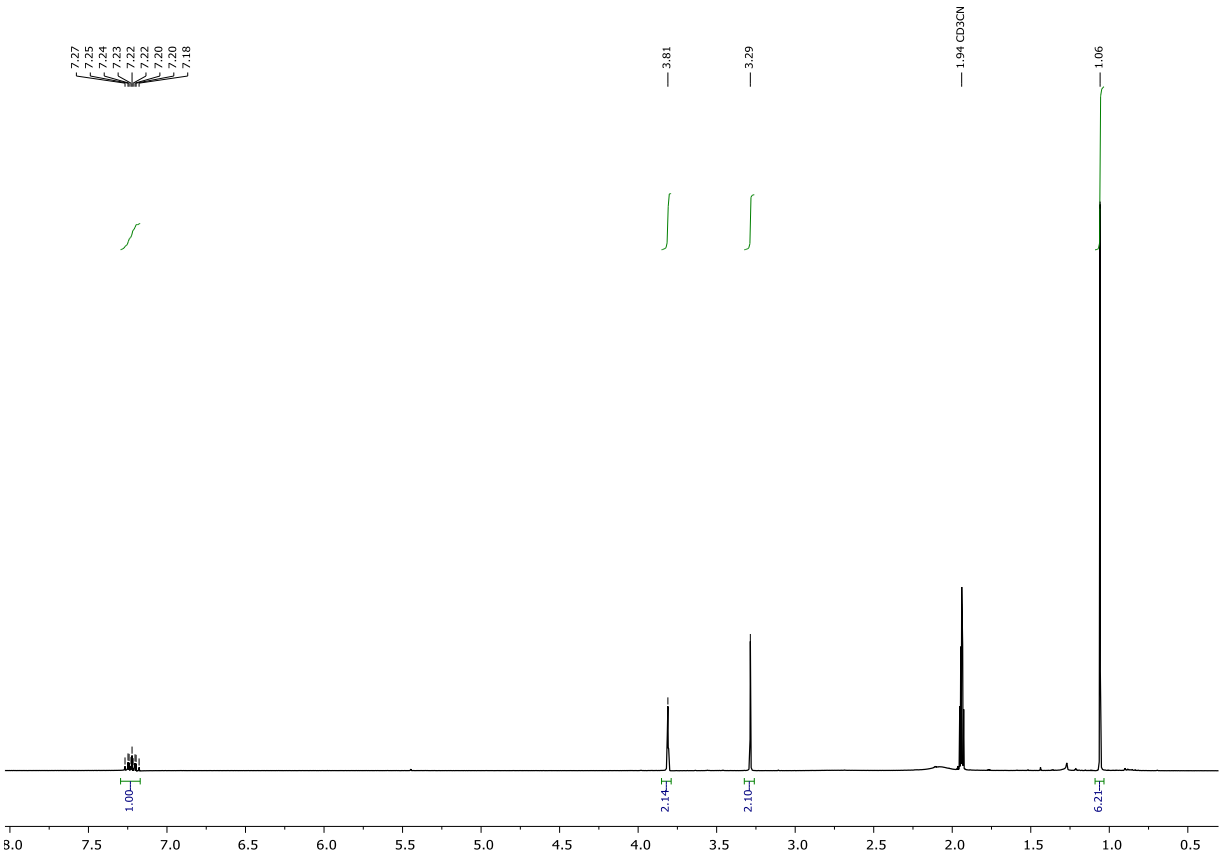

Figure 5.10. *^{1}H-NMR (400 MHz, CD_3CN) of compound* ***3*** $_{\mathbf{NH}}$ ***-H.***

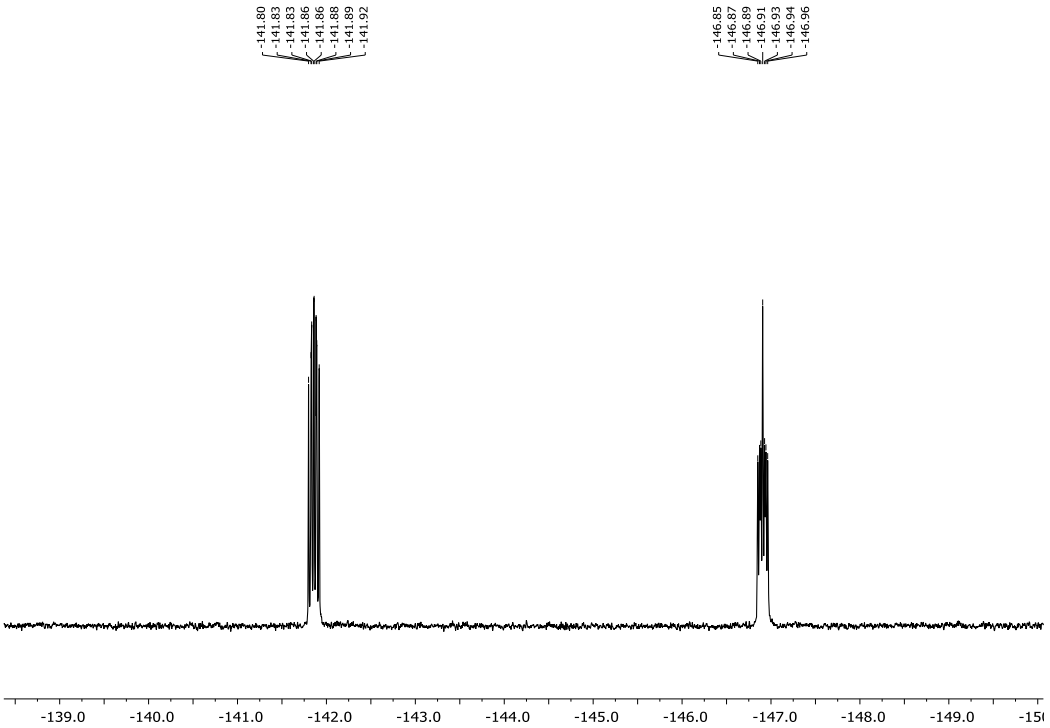

Figure 5.11 *^{19}F NMR (376 MHz, CD_3CN) of compound* ***3*** $_{\mathbf{NH}}$ ***-H.***

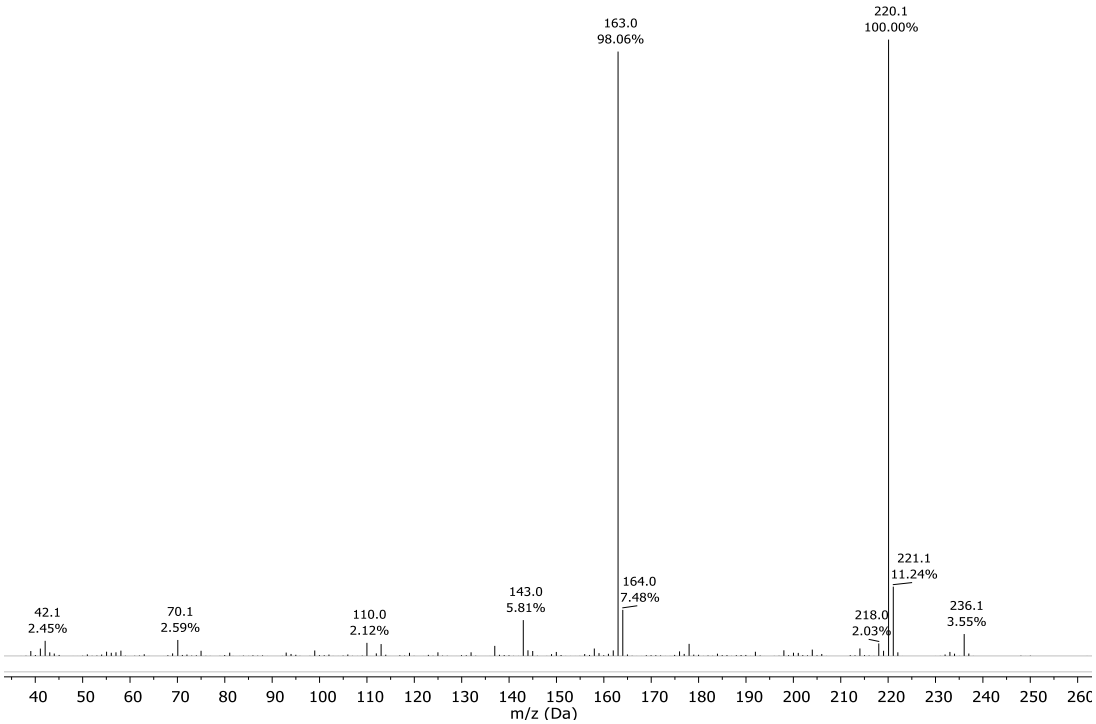

Figure 5.12. *EI-MS spectrum of compound* ***3$_{NH}$-H****.*

5.3 Experimental section of chapter 3

Formyl-DB24C8[2] and compound **6a**$^{2+}$[3] were synthesized according to procedures reported in literature.

Synthesis of N-tertbutyl-4-aminomethyl-Dibenzo[24]crown-8 (4b)

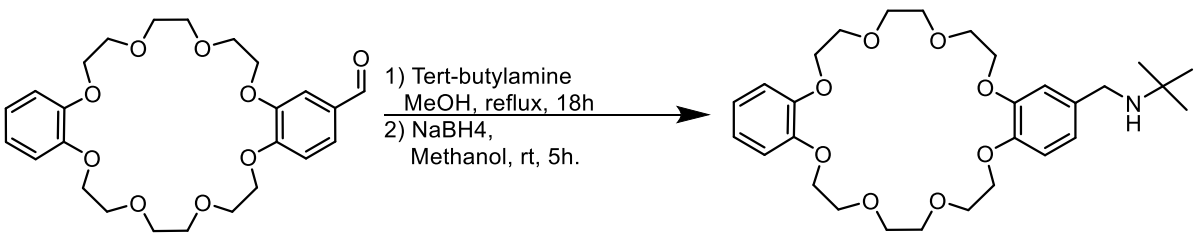

4a

A stirred mixture of formyl-DB24C8 (250 mg, 0.52 mmol) and *tert*-butylamine (82 μL, 0.788 mmol, 1.5 eq.) in dry methanol 19 mL was refluxed for 18 h. the formation of imine intermediate was checked with tlc (DCM/MeOH 9:1). The mixture was then cooled to room temperature and $NaBH_4$ (78 mg, 2.1 mmol, 4 eq.) was added in small portions. The mixture was stirred at RT for 5 h and the reaction quenched with 1M HCl (3 mL). Methanol was evaporated under vacuum and the residue suspended in 1M NaOH (10 mL), stirred for 15 min and the aqueous layer was extracted with DCM (4x10 mL), washed with water and brine (40 mL each) and dried with $MgSO_4$. The solvent was removed in vacuo to obtain a yellowish solid. The crude product was purified via column chromatography on SiO2 (eluent DCM/MeOH/NH_4OH 25% 90:10:1) to obtain an off white sticky solid (176 mg, 63%) ^{1}H-NMR (400MHz, $CDCl_3$) δ 1.18 (s, 9 H), 3.65 (s, 2 H), 3.82 (s, 8 H), 3.88-3.91 (m, 8 H), 4.09-4.18 (m, 8H), 6.77-6.95 (m, 7 H); ^{13}C NMR (101 MHz, CD_2Cl_2) δ 149.64, 149.43, 148.56, 121.94, 115.43, 114.87, 114.61, 71.57, 70.38, 69.83, 54.00, 47.05, 28.88. ESI-MS (+, *m/z*, %): 534.2 [M+H$^+$, 100], 556 [M+Na$^+$, 5].

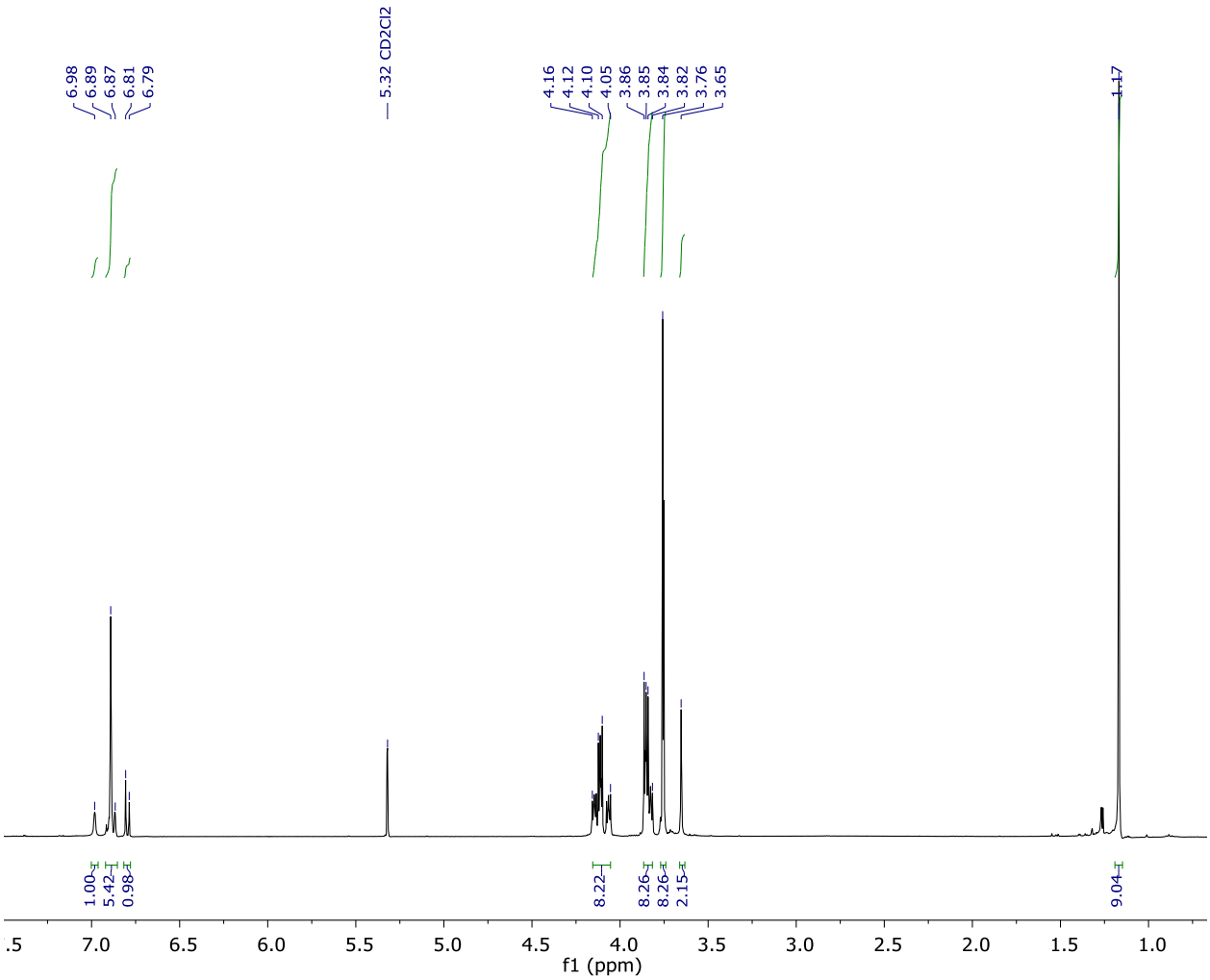

Figure 5.13 *^{1}H-NMR of compound **4a** in CD_2Cl_2.*

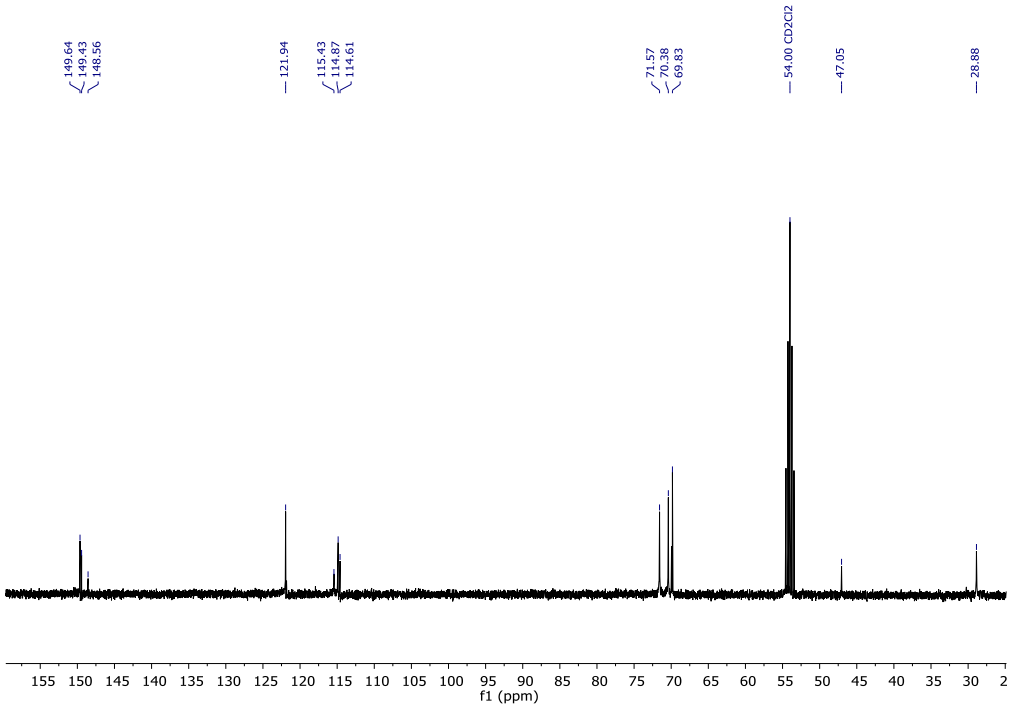

Figure 5.14 *^{13}C NMR of compound **4a** in CD_2Cl_2.*

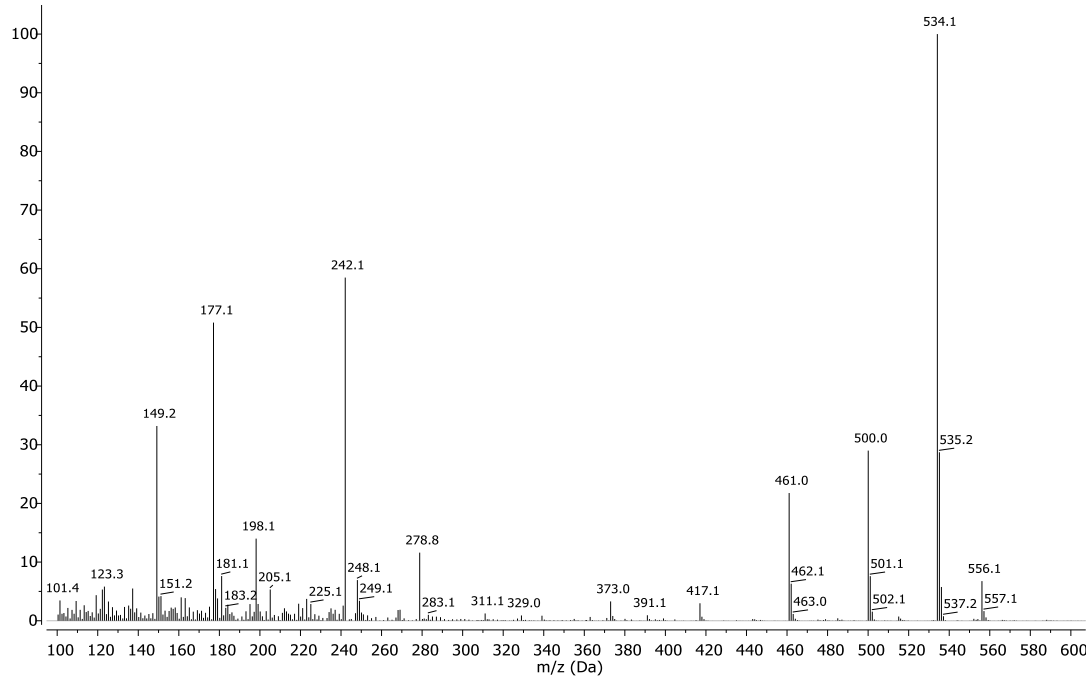

Figure 5.15 *Mass spectrum (ESI+) of* ***4a*** *in methanol.*

Synthesis of ((N-2-methyl-propan-1-ol)-2-aminomethyl)-dibenzo[24]crown-8 (4b):

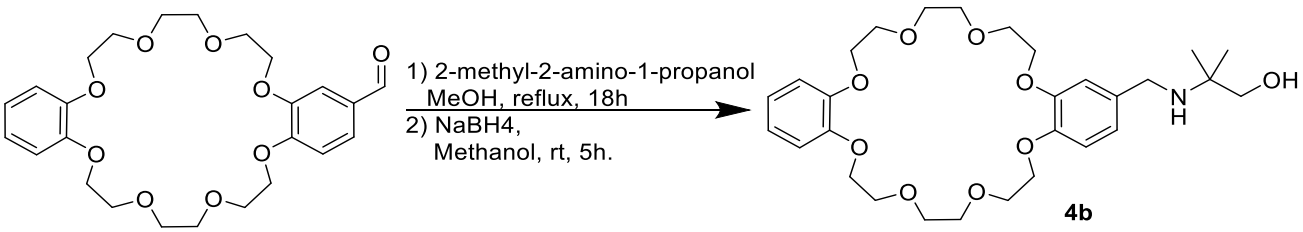

Following the same procedure for **4a**, Formyl-DB24C8 (250 mg, 0.52 mmol, 1 eq.) and 2-amino-2-methyl-1-propanol (49 mg, 0.54 mmol, 1.05 eq.) were refluxed in methanol for 18 h. The formation of imine intermediate was observed via TLC (DCM/MeOH 9:1). The mixture was then cooled to room temperature and $NaBH_4$ (78 mg, 2.1mmol, 4 eq.) was added to the reaction mixture in small portions. The mixture was stirred at RT for 5 h and the reaction quenched with 1M HCl (3mL). Methanol was evaporated under vacuum and the residue suspended in 1M NaOH (10 mL), stirred for 15 min and the aqueous layer extracted with DCM (4x10 mL), washed with water and brine (40 mL each) and dried with $MgSO_4$. The solvent was removed in vacuo to obtain a yellowish solid. The crude product was purified via column chromatography on SiO_2 gel chromatography (eluent DCM/MeOH 9:1 then DCM/MeOH/NH_4OH 90:10:1) to obtain a white sticky solid (160 mg, 55%).

^{1}H-NMR (400MHz, CD_2Cl_2) δ 1.11 (s, 6 H), 3.28 (s, 2 H), 3.60 (s, 2 H), 3.76 (s, 8 H), 3.83-3.86 (m, 8 H), 4.09-4.14 (m, 8H), 6.81-6.89 (m, 7 H); ^{13}C NMR (101 MHz, CD_2Cl_2) δ 149.64, 148.52, 134.98, 121.93, 121.32, 114.86, 71.59, 70.40, 69.82, 68.81, 54.00, 46.50, 24.42. ESI-MS (+, *m/z*, %) 550 [M+H$^+$, 75], 572 [M+Na$^+$, 100].

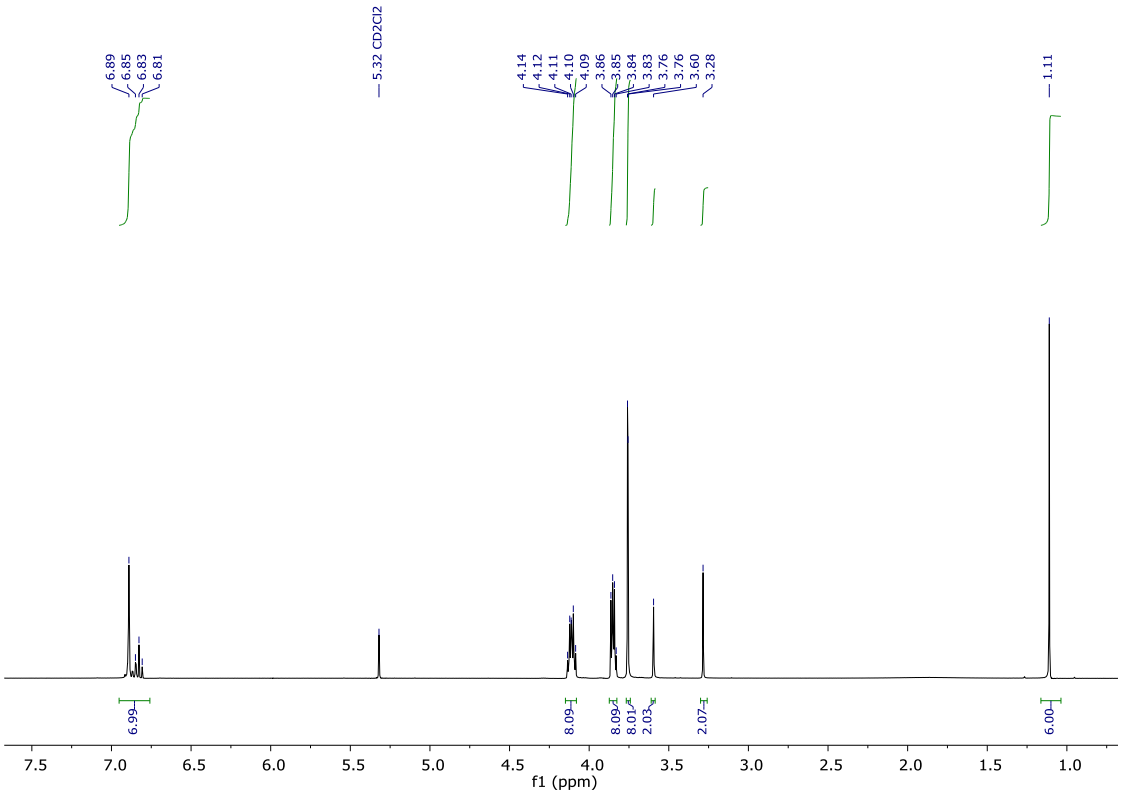

Figure 5.16 *[1]H NMR of compound* ***4b in CD_2Cl_2.***

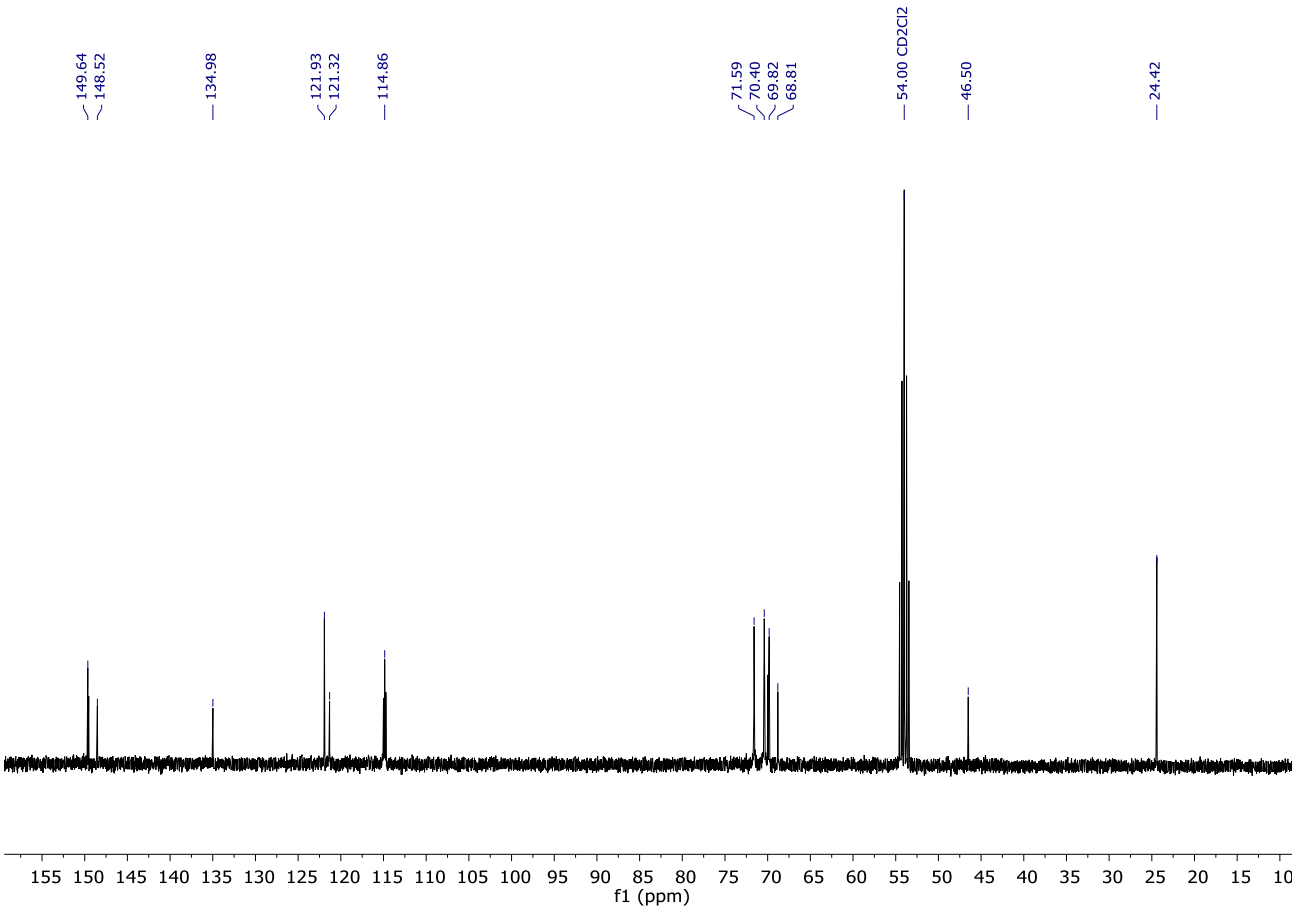

Figure 5.17 *^{13}C NMR of compound **4b** in CD_2Cl_2.*

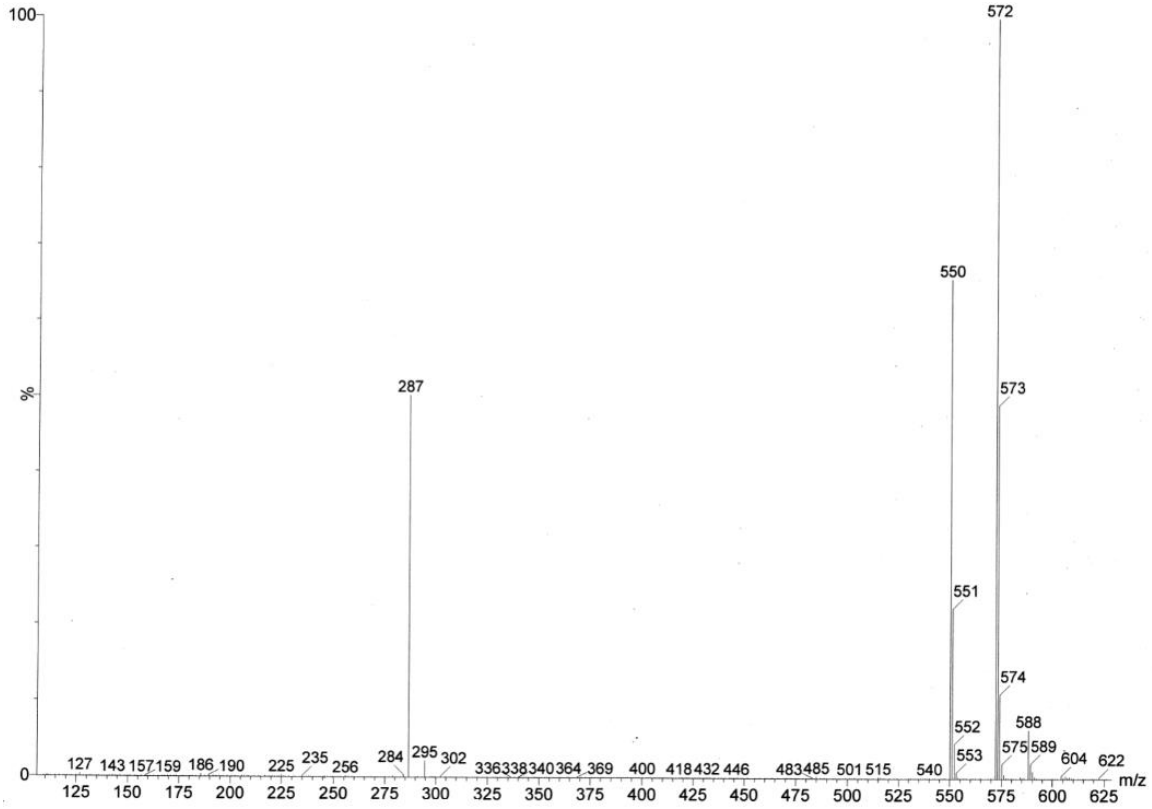

Figure 5.18 *ESI-MS spectrum of **4b** in methanol.*

Compound 6^{3+}:

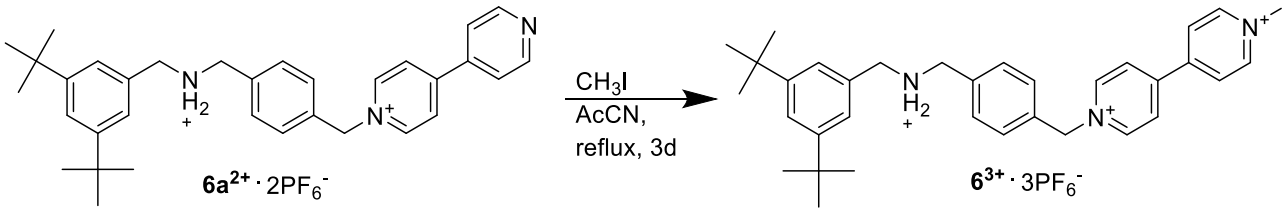

Compound **$6a^{2+}$** (50 mg, 65 μmol) was dissolved in ACN (5 mL) and then methyl iodide (12 μL, 0.194 mmol, 3 eq.) was added. The mixture was heated under reflux for 3d. The solvent was removed *in vacuo* and the crude mixture subjected to column chromatography on SiO_2 (eluent DCM/MeOH 9:1 then 7:1 and finally MeOH/H_2O/NH_4Cl 2M 7:2.5:0.5). Methanol was removed in vacuo and the solution was then treated with aqueous NH_4PF_6 The precipitate was filtered and washed with water to afford title compound as a white solid (34 mg, 56%) ^{1}H-NMR (400MHz, $(CD_3)_2CO$) δ 1.30 (s, 18 H), 4.62 (s, 2 H), 4.69 (s, 2 H), 4.73 (s, 3 H), 6.22 (s, 2H), 7.45 (s, 2 H), 7.56 (s, 1 H), 7.71-7.77 (m, 4H), 8.77 (m, 4 H), 9.35 (m, 2 H), 9.45 (m, 2 H). ^{13}C NMR (101 MHz, acetone-d_6) δ = 152.54, 151.59, 147.77, 146.92,

135.56, 133.76, 132.21, 131.21, 130.68, 128.48, 127.75, 125.08, 124.37, 65.09, 53.25, 51.92, 35.50, 31.59, 29.84. ESI-MS (+, m/z, %): 784 $[M\text{-}PF_6, 20]^+$.

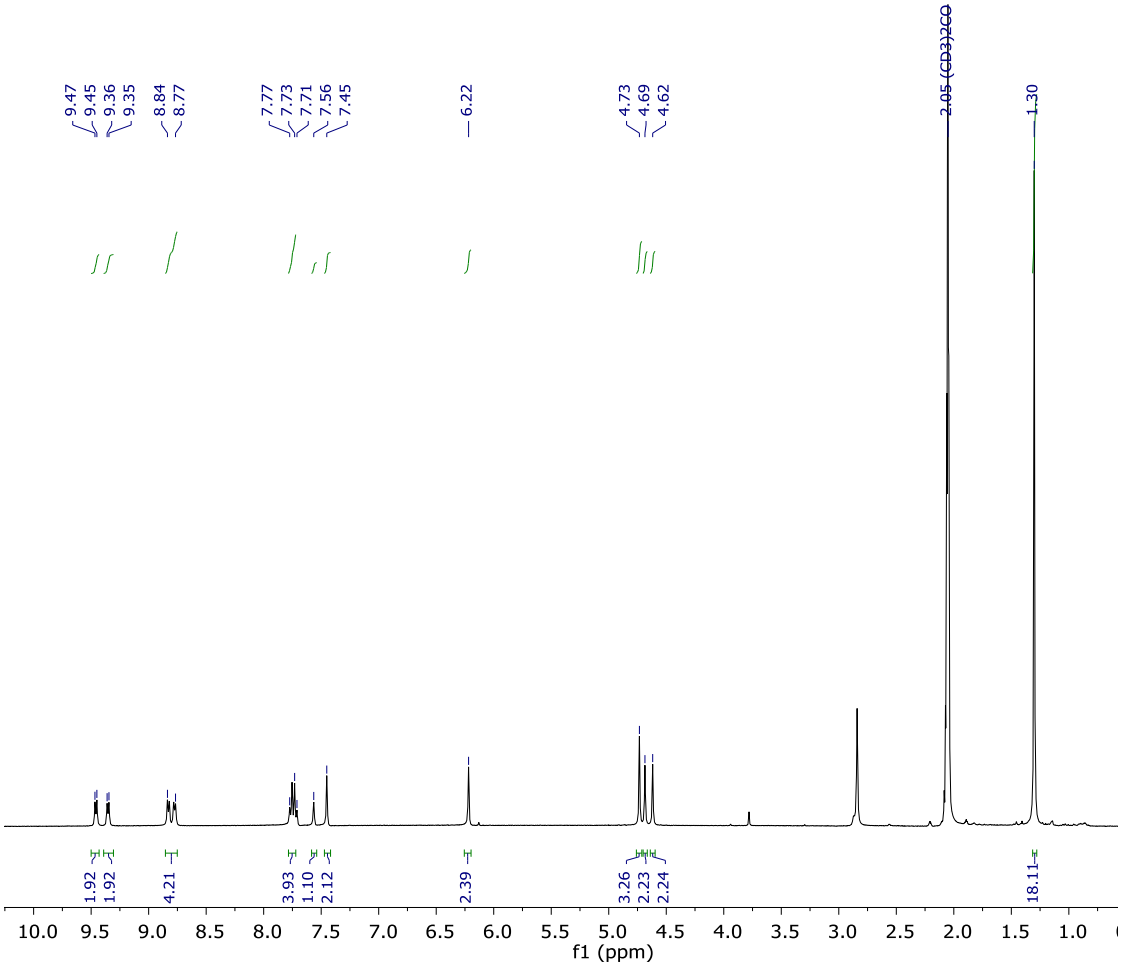

Figure 5.19 *^{1}H NMR of compound* ***6***$^{3+}$ *in Acetone-d_6.*

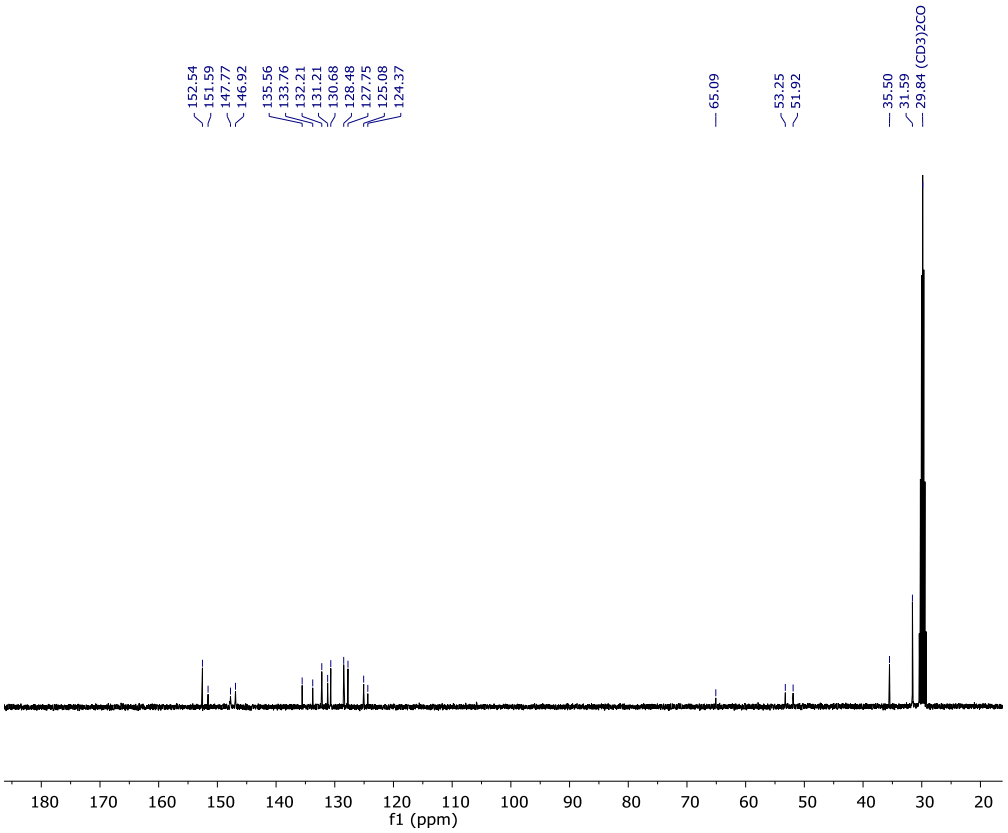

Figure 5.20 *^{13}C NMR of compound **6**$^{3+}$ in Acetone-d_6.*

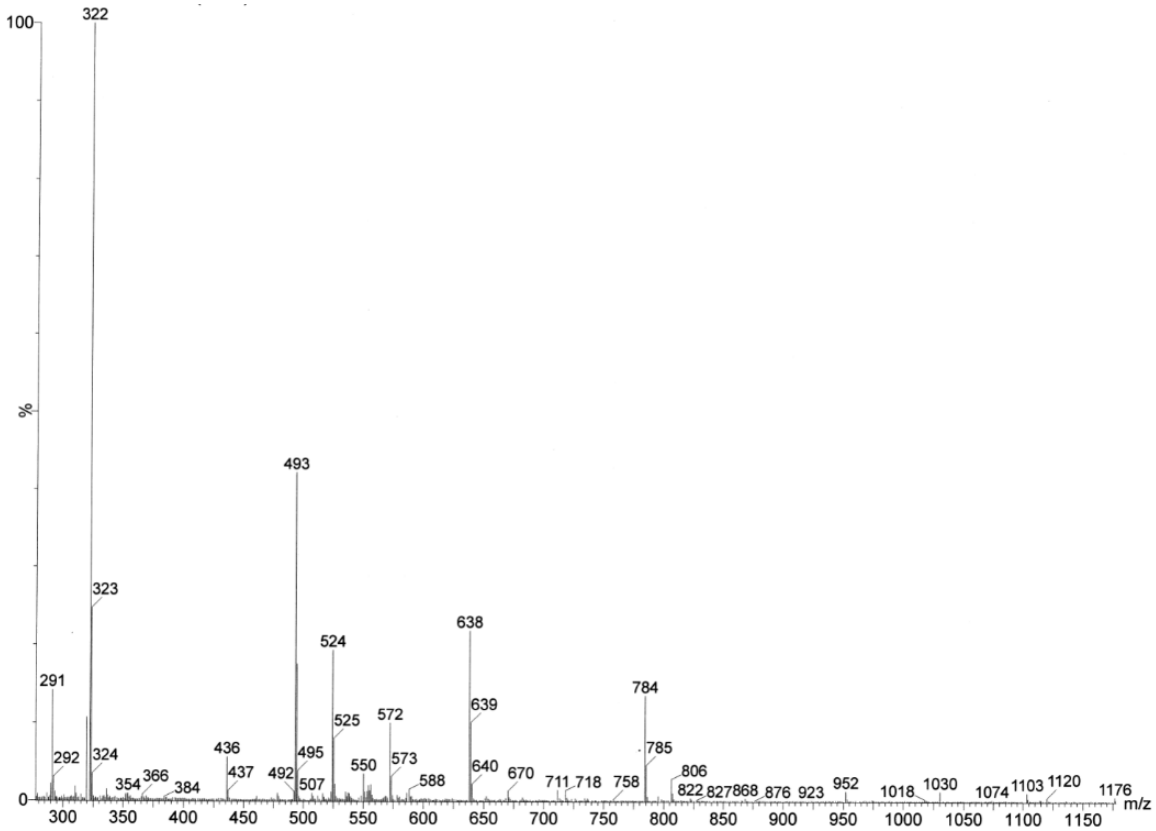

Figure 5.21 *ESI-MS spectrum of **6**$^{3+}$ in methanol.*

Rotaxane R4a^{3+}:

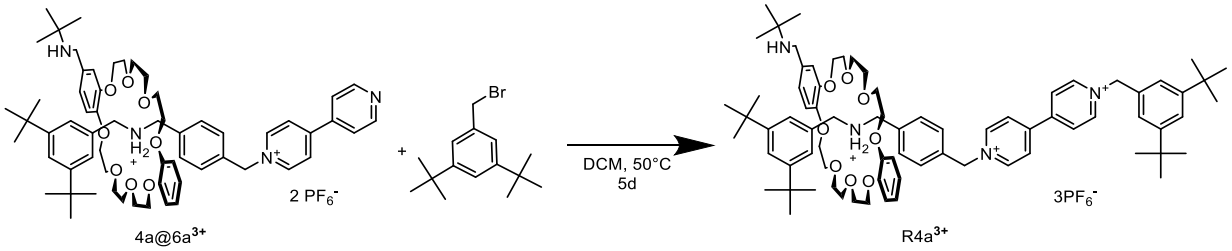

Compound **6a**$^{2+}$ (30 mg, 0.039 mmol, 1 eq.) was added to a stirred mixture of **4a** (52 mg, 2.5 eq.) in dry DCM. 3,5-Di tertbutyl benzyl bromide (60mg, 0.21 mmol, 5,5 eq.) was added and the mixture was heated under reflux for 5 days. The solvent was removed *in vacuo* and the crude mixture subjected to column chromatography on SiO_2 (eluent DCM/MeOH 9:1 then 7:1 and finally MeOH/H_2O/NH_4Cl 2M 7:2.5:0.5). Methanol was removed in vacuo to obtain a yellowish solid insoluble in water. Acetone was added to dissolve the residue and the resulting solution treated with aqueous NH_4PF_6. Acetone was removed *in vacuo*, the precipitate filtrated and washed with water to afford rotaxane **R4a**$^{3+}$ as a white solid (10 mg, 15%) ^{1}H-NMR (400MHz, $(CD_3)_2CO$) δ 1.24 (s, 18 H), 1.31 (s, 18 H), 1.58 (s, 9H), 3.55-4.31 (m, 26 H), 4.42 (s, 2 H), 4.84 (m, 4 H), 5.86 (s, 2H), 6.15 (s, 2H), 6.80-6.98 (m, 7 H), 7.23-7.40 (m, 4 H), 7.46 (s, 2H), 7.53 (s, 1H), 7.62 (s, 3H), 8.79 (m, 4 H), 9.19 (m, 2 H), 9.56 (m, 2 H). ESI-MS (+, *m/z*): 1651 [M+3 HPF_6]$^+$, 1506 [M+2HPF_6]$^+$.

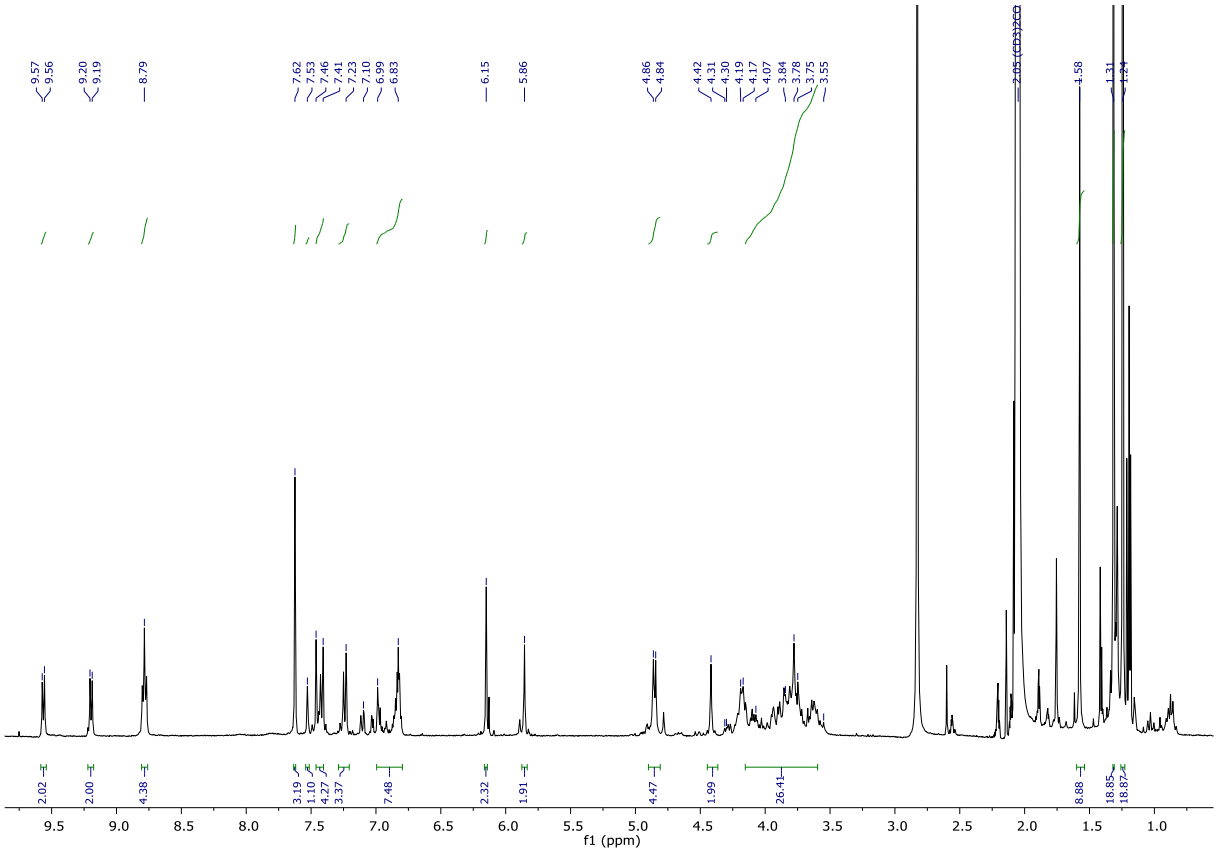

Figure 5.22 *^{1}H NMR of rotaxane* ***R4a***$^{3+}$ *in Acetone-d_6.*

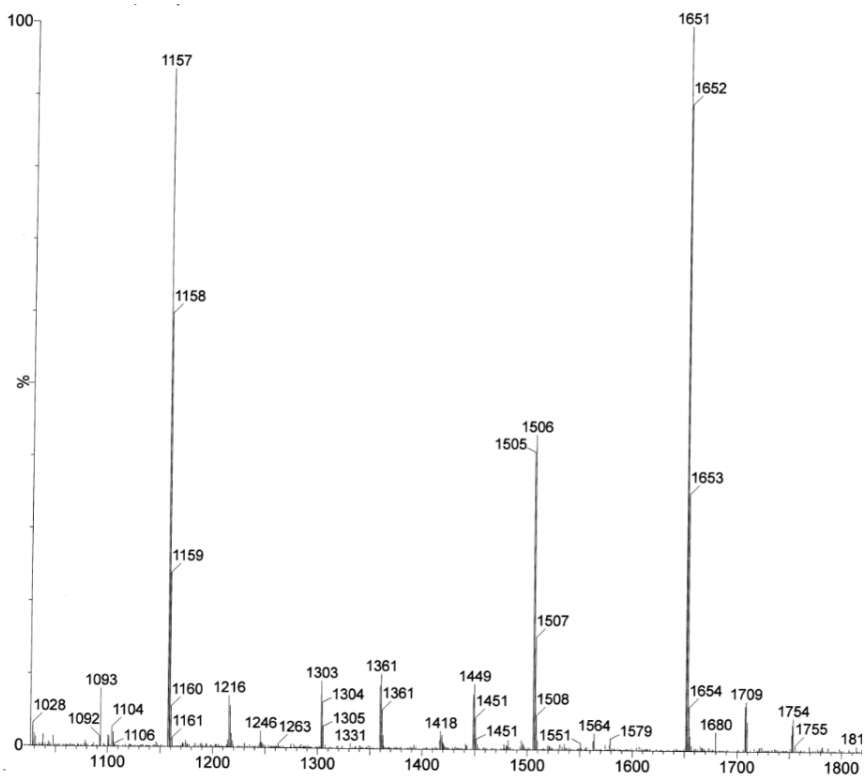

Figure 5.23 *ESI-MS spectrum of* ***R4a***$^{3+}$ *in methanol.*

Rotaxane R4b^{3+}:

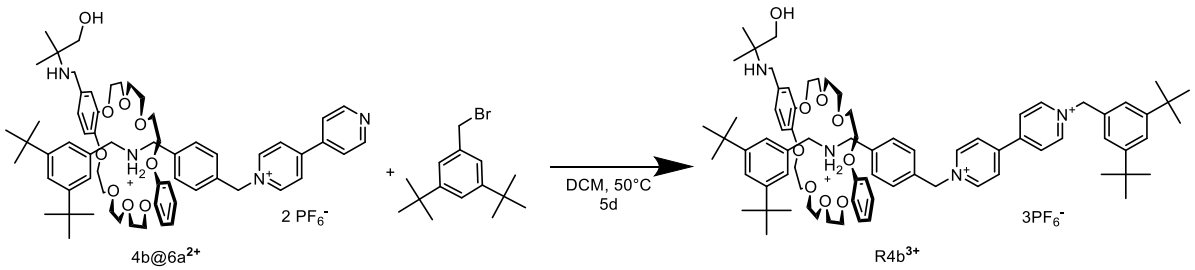

Compound **6a**$^{2+}$ (30 mg, 39 μmol) was added to a stirred mixture of **4b** (53 mg, 97 μmol, 2.5 eq.) in dry DCM (3 mL). 3,5-Di tertbutyl benzyl bromide (60 mg, 0.21 mmol, 5.5 eq.) was added and the mixture was heated under reflux for 5 days. The solvent was removed *in vacuo* and the crude mixture subjected to column chromatography (eluent DCM/MeOH 9:1 then 7:1 and finally MeOH/H_2O/NH_4Cl 2M 7:2.5:0.5). Methanol was removed *in vacuo* to obtain a yellowish solid insoluble in water. Acetone was added to dissolve the residue and the resulting solution treated with a NH_4PF_6 aqueous solution. Acetone was removed *in vacuo* and the precipitate filtrated and washed with water to afford rotaxane **R4b**$^{3+}$ as a white solid (16 mg, 24%) ^{1}H-NMR (400MHz, $(CD_3)_2CO$) δ 1.24 (s, 18 H), 1.31 (s, 18 H), 1.51 (s, 6H), 3.57-4.30 (m, 28 H), 4.40 (s, 2 H), 4.84 (m, 4 H), 5.86 (s, 2H), 6.15 (s, 2H), 6.80-7.11 (m, 7 H), 7.23-

7.43 (m, 4 H), 7.46 (s, 2H), 7.52 (s, 1H), 7.63 (s, 3H), 8.78 (m, 4 H), 9.18 (m, 2 H), 9.54 (m, 2 H). ESI-MS (+, *m/z*): 1667 $[M+3\ HPF_6]^+$, 1522 $[M+2HPF_6]^+$.

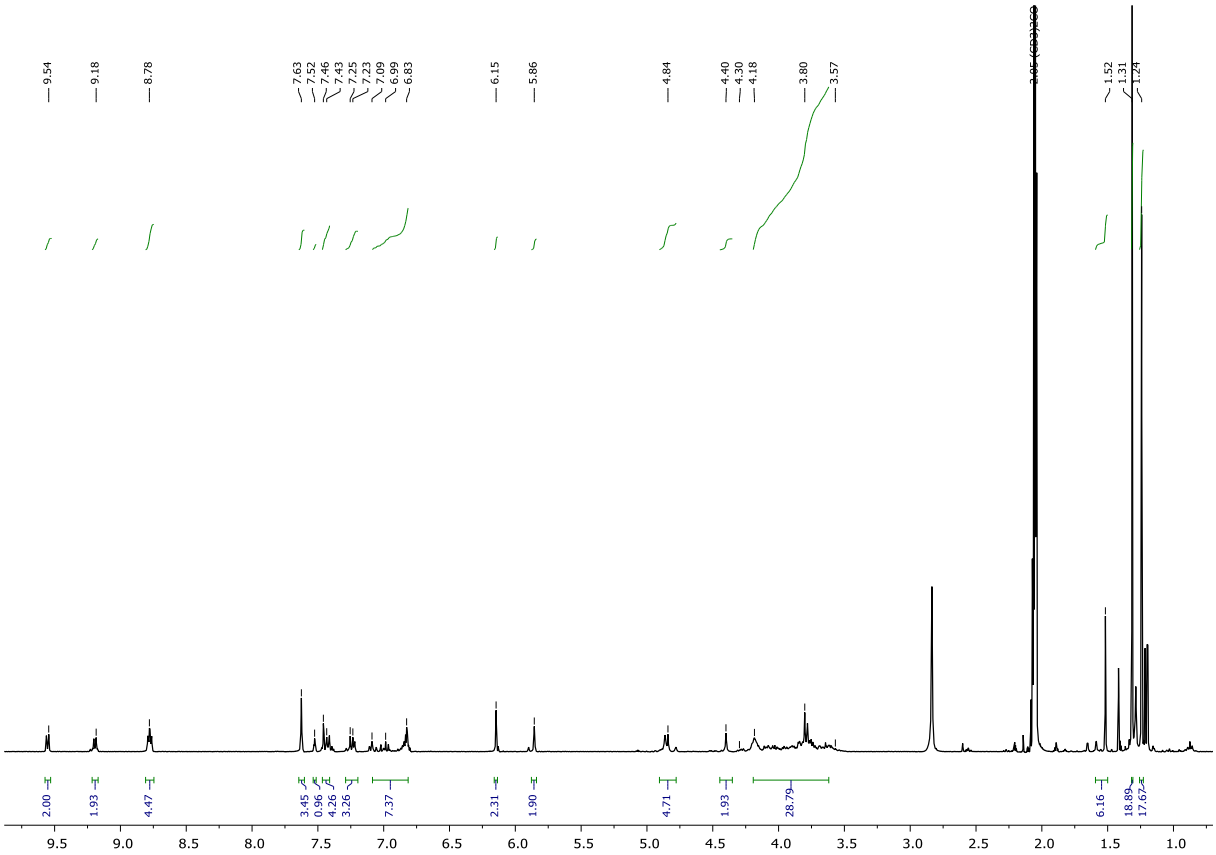

Figure 5.24 *^{1}H NMR of rotaxane* ***R4b^{3+}*** *in acetone-d_6.*

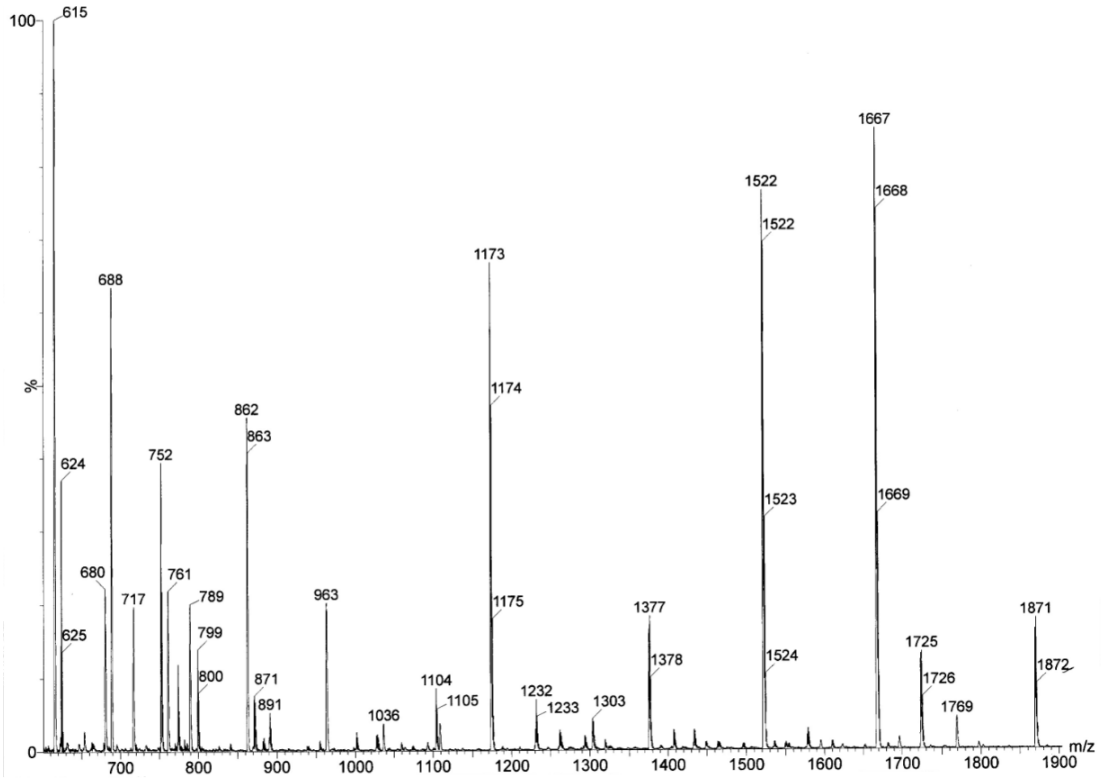

Figure 5.23 *ESI-MS spectrum of* ***R4b***$^{3+}$ *in methanol.*

5.4 Experimental section of chapter 4

3-bromo-5-*tert*-butyl-benzaldehyde,[4] 2,6-diethynylpyridine,[5] tosyl-azide[6] 2,3-bishydroxylamino-2,3-dimethylbutane (BHA),[7]and compound **18**[8] were synthesized according to literature procedures.
2,6-Diethynyl-benzene was purchased from Sigma-Aldrich, 3,5-dibromo-*tert*-butylbenzene was purchased from Fluorochem.

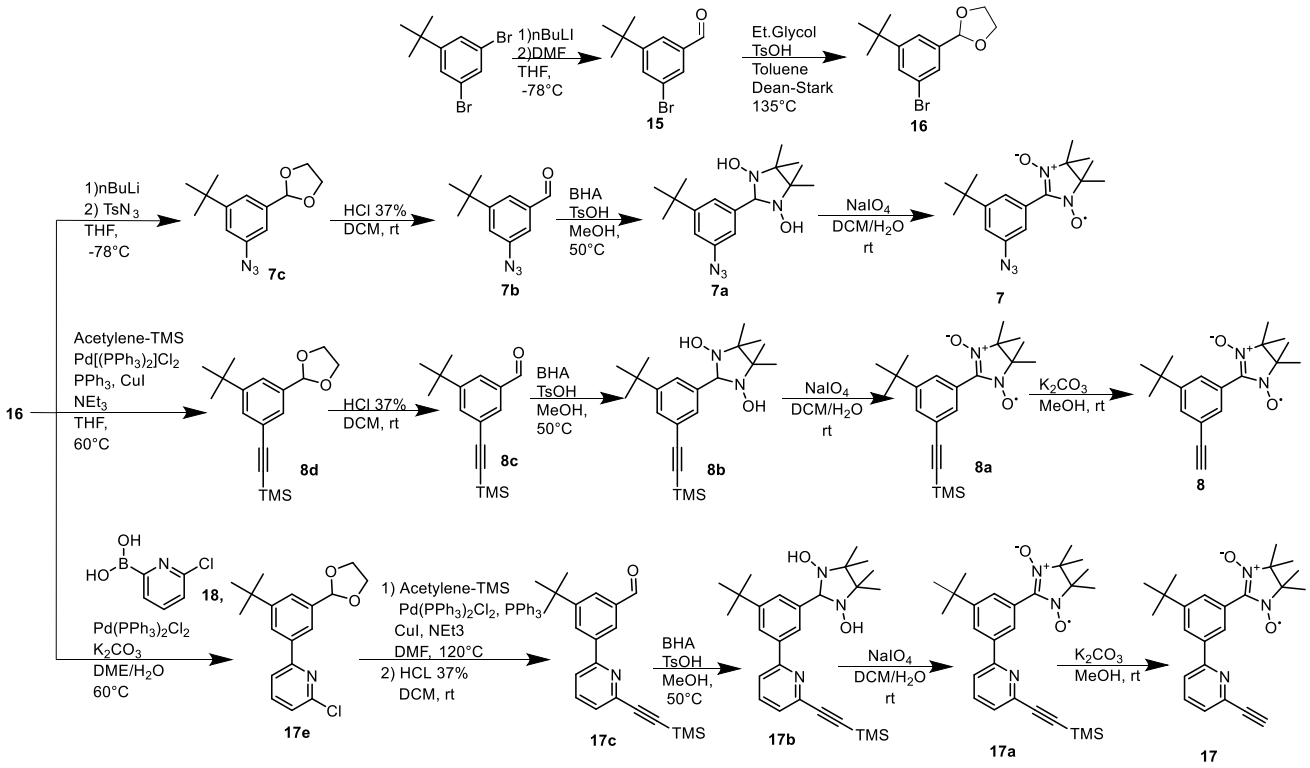

Scheme 5.1 *Synthesis of the NN labelled half threads.*

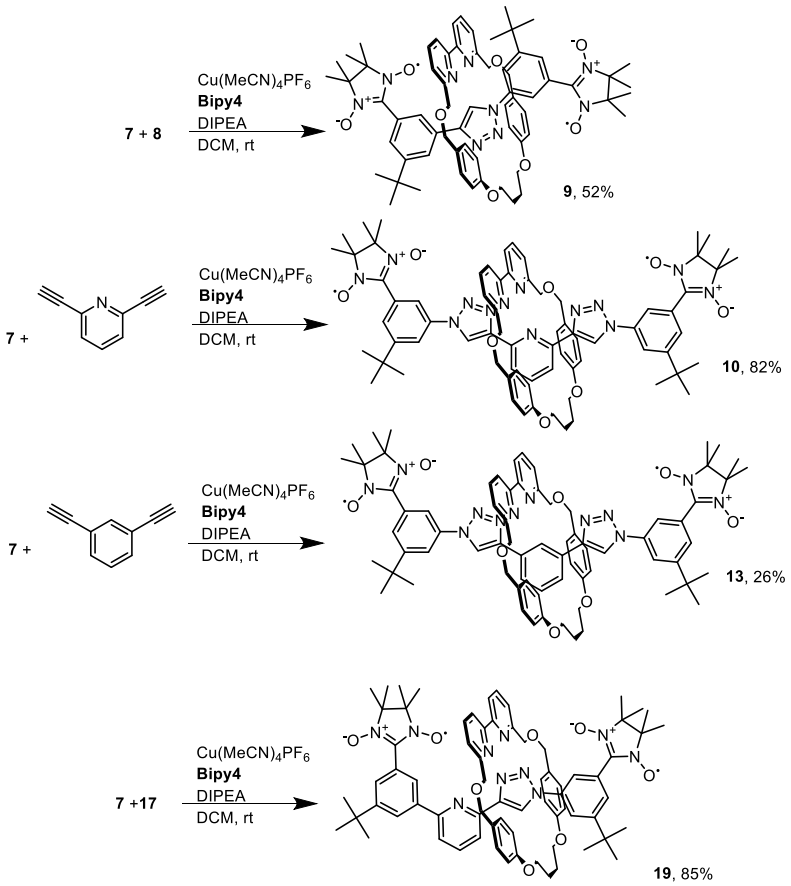

Scheme 5.2 *Synthesis of the NN labelled [2]rotaxanes.*

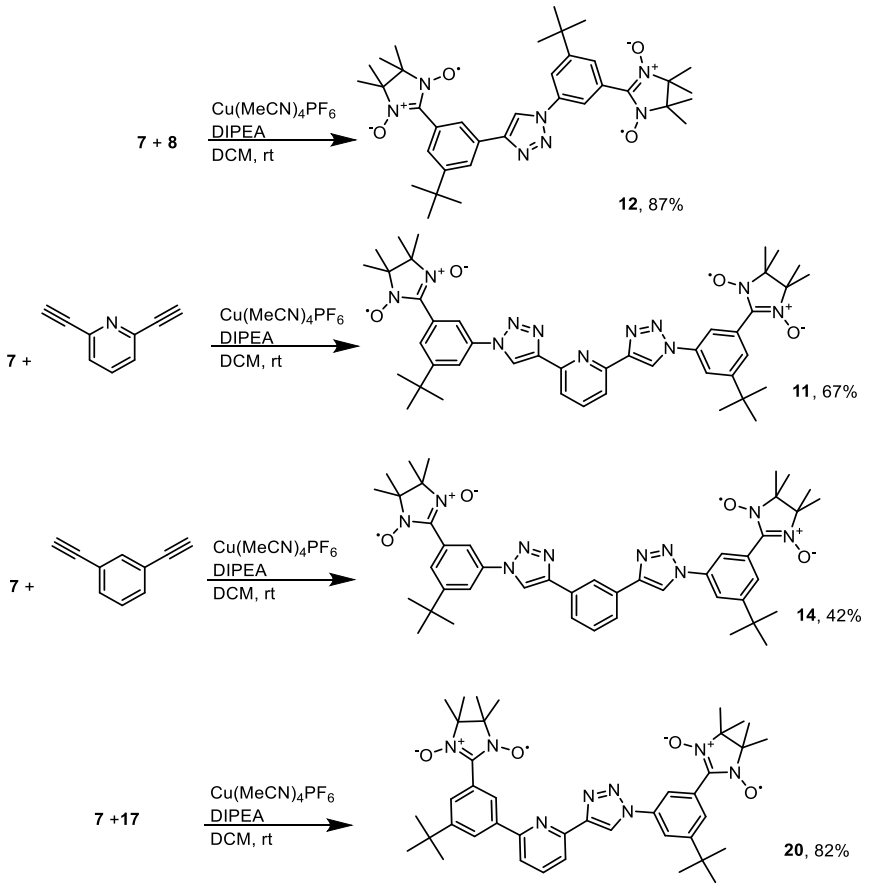

Scheme 5.3 *Synthesis of the NN labelled threads.*

Synthesis of 2-(3-bromo-5-(tert-butyl)-phenyl)-1,3-dioxolane (16):

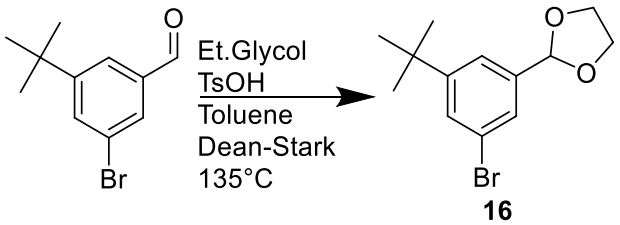

16

3-bromo-5-(tert-butyl)-benzaldehyde (4.37g, 18.15 mmol), ethylene glycol (5.06 mL, 90.78 mmol, 5 eq.), TsOH (311 mg, 10% mol) were placed in a round bottom flask and solubilized with toluene (125 mL). The solution was heated to reflux at 150°C for 20h in a Dean-Stark apparatus. the progression of the reaction was checked via TLC (Eluent P.Et/EtOAc 9:1). The reaction mixture was then cooled to RT and EtOAc. (125 mL) was added. the solution was then washed with saturated $NaHCO_3$ (250 mL) and brine (250 mL), dried on $MgSO_4$ and the solvent removed *in vacuo*. The crude mixture was purified via column chromatography (SiO_2, Eluent P.E./EtOAc 9:1) to yield compound **16** as a pale-yellow oil (4.85g, 93%). ^{1}H NMR (400 MHz, $CDCl_3$) δ = 7.50 (m, 1H), 7.46 (m, 1H), 7.40 (m, 1H), 5.76 (s, 1H), 4.13-3.03 (m, 4H), 1.31(s, 9H). ^{13}C NMR (101 MHz, $CDCl_3$) δ 153.79, 139.76, 129.62, 126.72, 122.52, 122.45, 103.22, 65.46, 35.08, 31.30. GC-MS (E.I., *m/z*, %): 284.9 [M-H$^+$, 95].

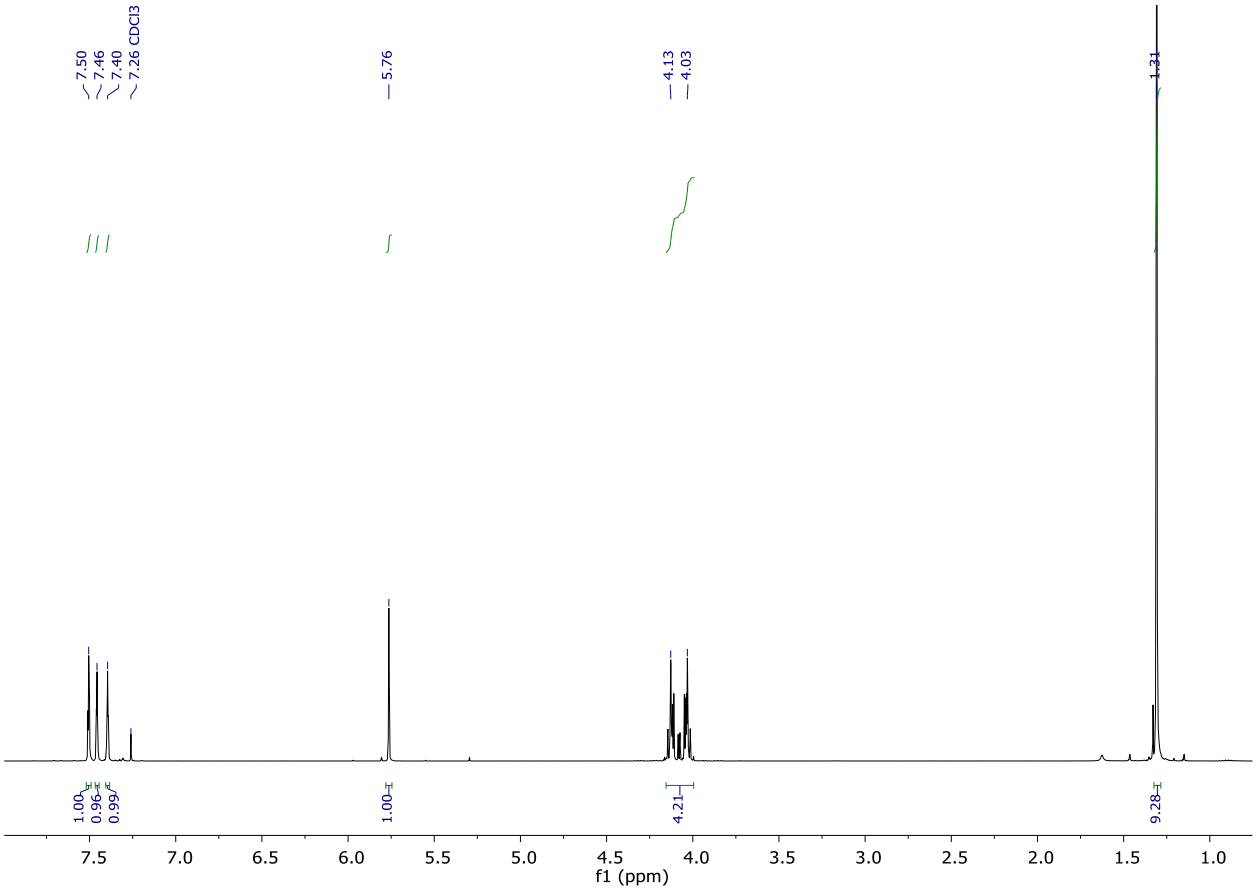

Figure 5.26 *^{1}H-NMR (400MHz) of **16** in $CDCl_3$ at 298K.*

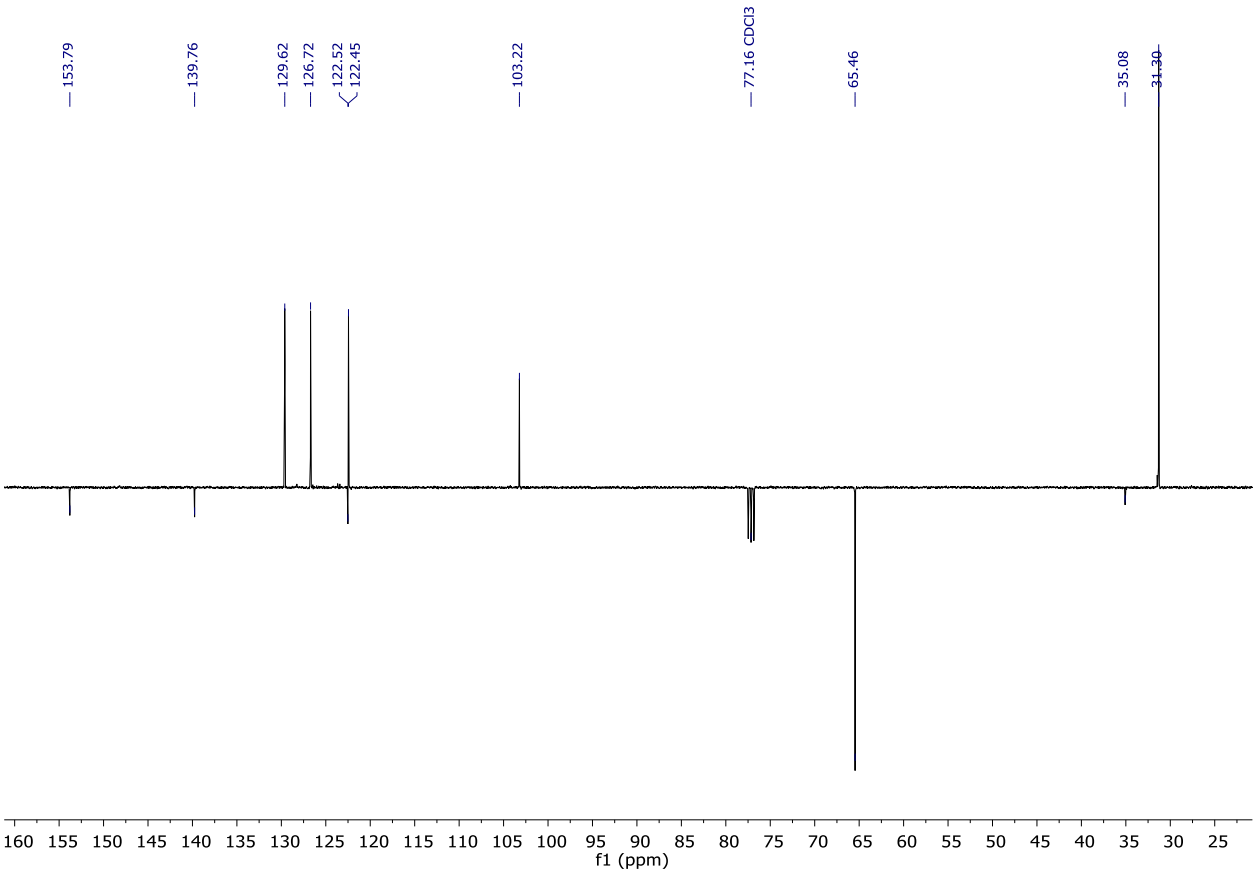

Figure 5.27 *J MOD NMR (101 MHz) of **16** in $CDCl_3$ at 298K.*

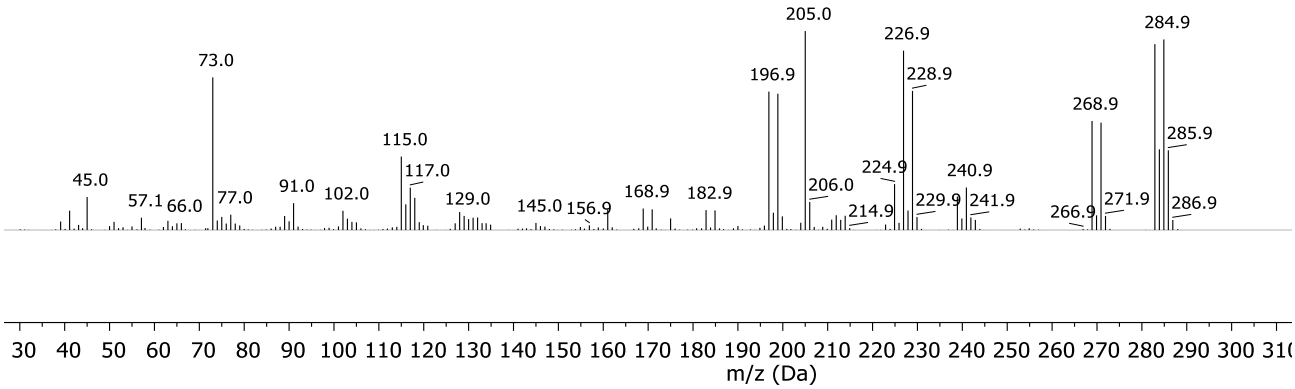

Figure 5.28 *GC-MS (EI) of compound* ***16.***

Synthesis of 3-Azido-5-(tert-butyl)benzaldehyde (7b):

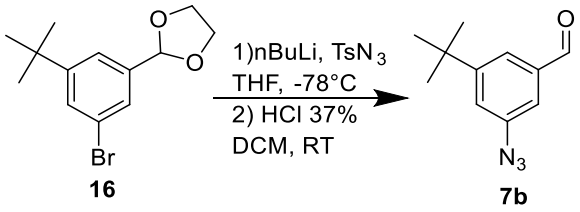

A solution of **2** (1.07g, 3.74 mmol) in dry THF (100 mL) under N_2 was cooled to -78°C and treated dropwise with a solution of n-BuLi 2.5M in hexane (1.72 mL, 4.30 mmol, 1.15 eq.) over 15 minutes. The solution was left to stir 30 minutes and then a solution of TsN_3 (1.10 g, 5.61 mmol, 1.5 eq.) in dry THF (14mL) was added dropwise. The deep red solution was stirred at -78°C for 30 minutes and then warmed to RT and stirred for 16h. The reaction was quenched with 100 mL of H_2O and the THF was removed *in vacuo*. The aqueous layer was then extracted with 3x100 mL Et_2O. The combined organic layer was the washed with water (300 ml) and then with brine (300 ml). The solution was dried on $MgSO_4$, filtered and concentrated in *vacuo* to yield **7c** as a yellowish oil. The crude mixture was used for the deprotection without further purification. (835 mg, 91%). ^{1}H NMR (400 MHz, Acetone-d_6) δ=7.42(m, 1H), 7.18 (m, 1H), 7.11 (m, 1H), 5.83 (s, 1H), 4.21-4.07 (m, 4H), 1.42 (s, 9H). The Crude dioxolane protected aldehyde (500 mg, 2.05mmol) was dissolved in DCM (25 mL) and treated with HCl 37% (111 µL, 2.05 mmol, 1 eq.). The mixture was stirred overnight at RT. The progress of the reaction

was monitored via TLC (Eluent P.Et/DCM 1:1). The mixture was neutralized with sat. $NaHCO_3$, the organic layer was then washed with H_2O (25 mL) and Brine (25 mL) and dried on $MgSO_4$. Compound **7b** was purified with column chromatography (SiO_2, Eluent: P.Et 100% to P.Et./ DCM 1:1) to yield title compound **7b** as a yellowish oil (337 mg, 80%). ^1H NMR (400 MHz, CD_3CN) δ = 9.96 (s, 1H) 7.75(m, 1H), 7.38 (m, 1H), 7.33 (m, 1H), 1.34 (s, 9H). ^{13}C NMR (101 MHz, CD_3CN) δ = 193.02, 155.51, 142.04, 138.92, 124.69, 123.07, 118.26, 117.13, 35.77, 31.19.

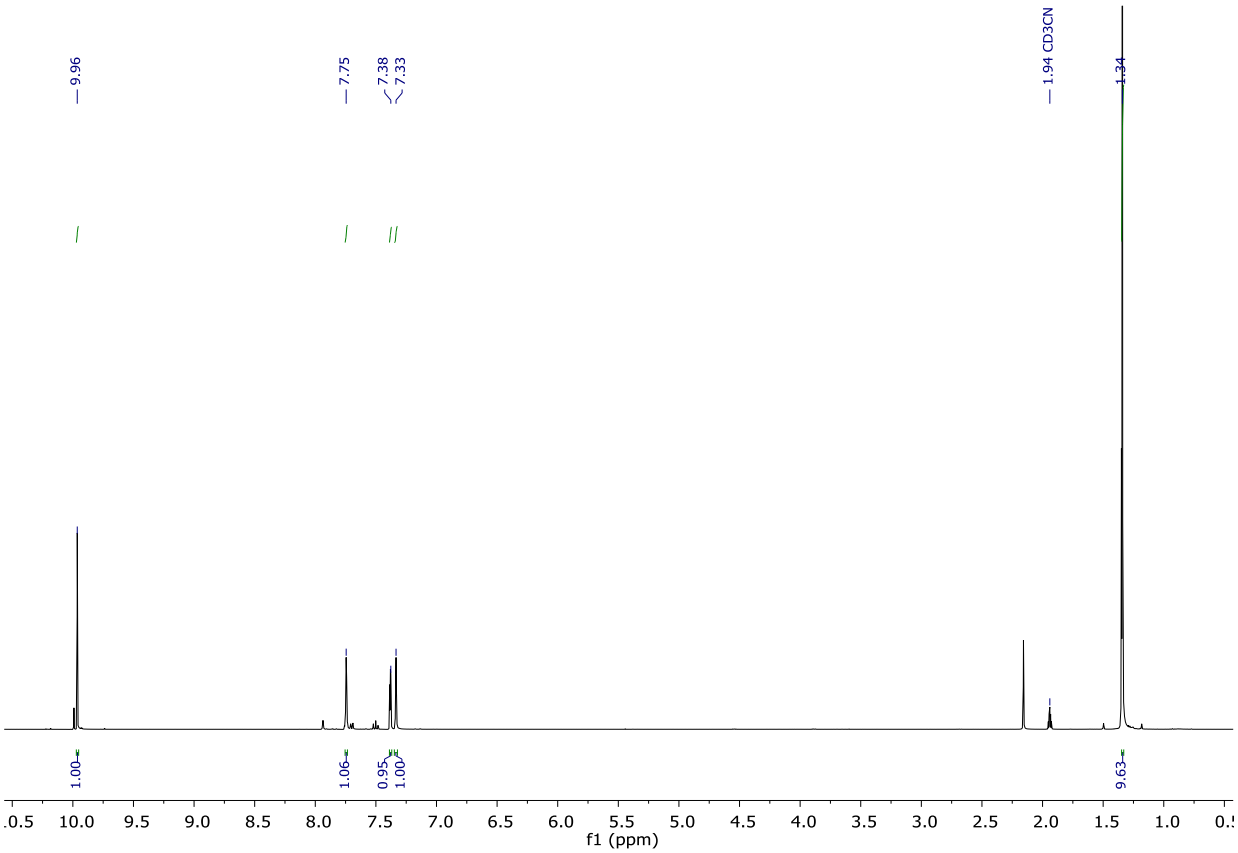

Figure 5.29 *^1H-NMR (400MHz) of **7b** in CD_3CN at 298K.*

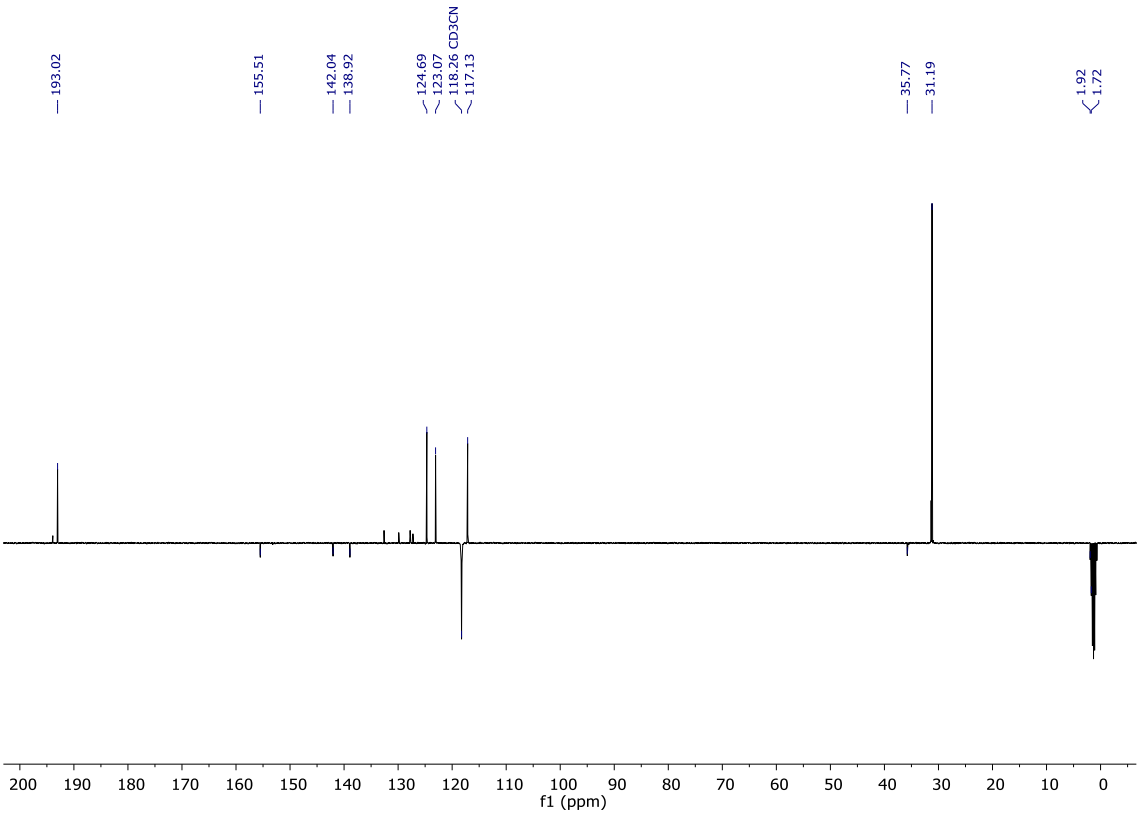

Figure 5.30 *J MOD NMR (101 MHz) of* ***7b*** *in CD_3CN at 298K.*

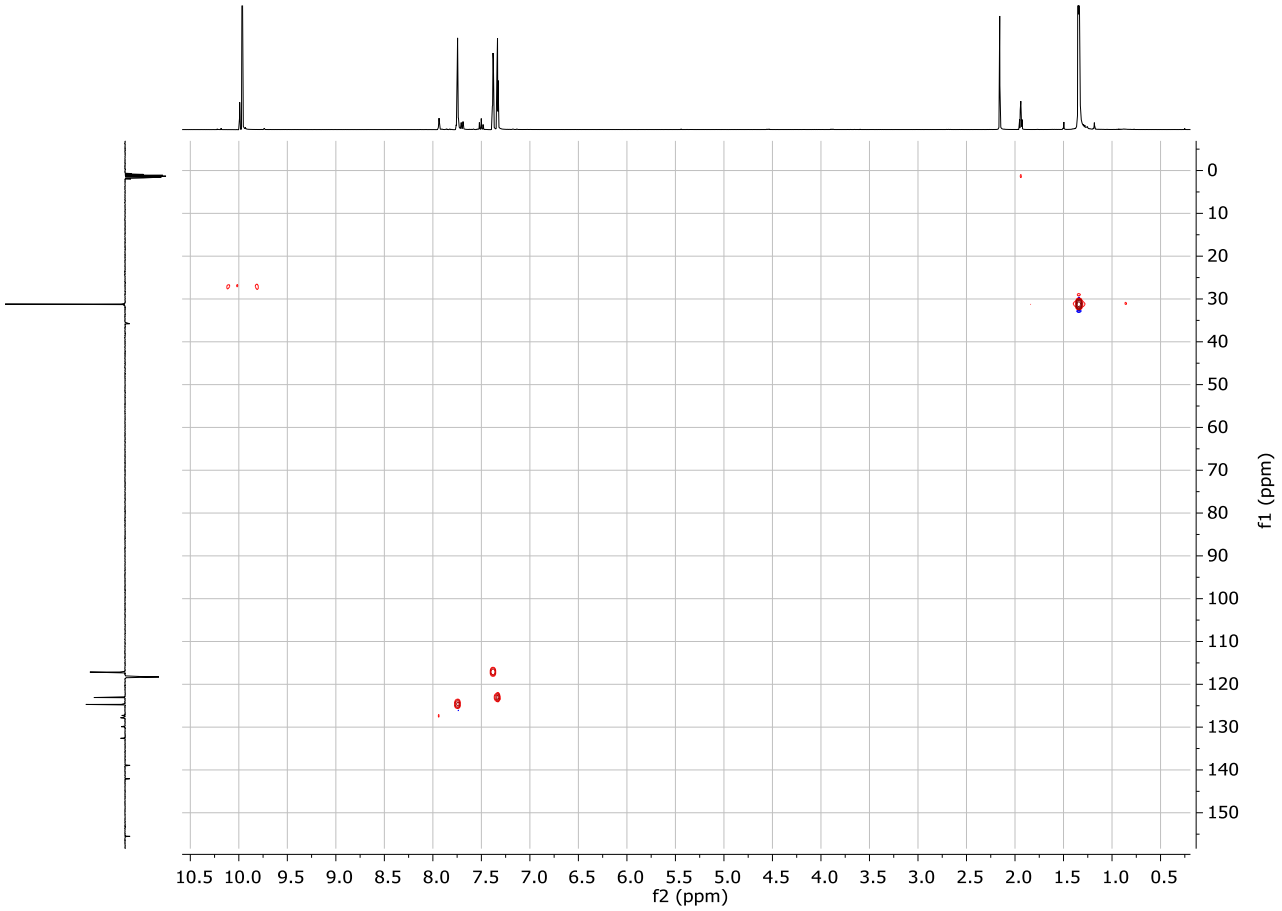

Figure 5.31 *HSQC NMR of* ***7b*** *in CD_3CN at 298K.*

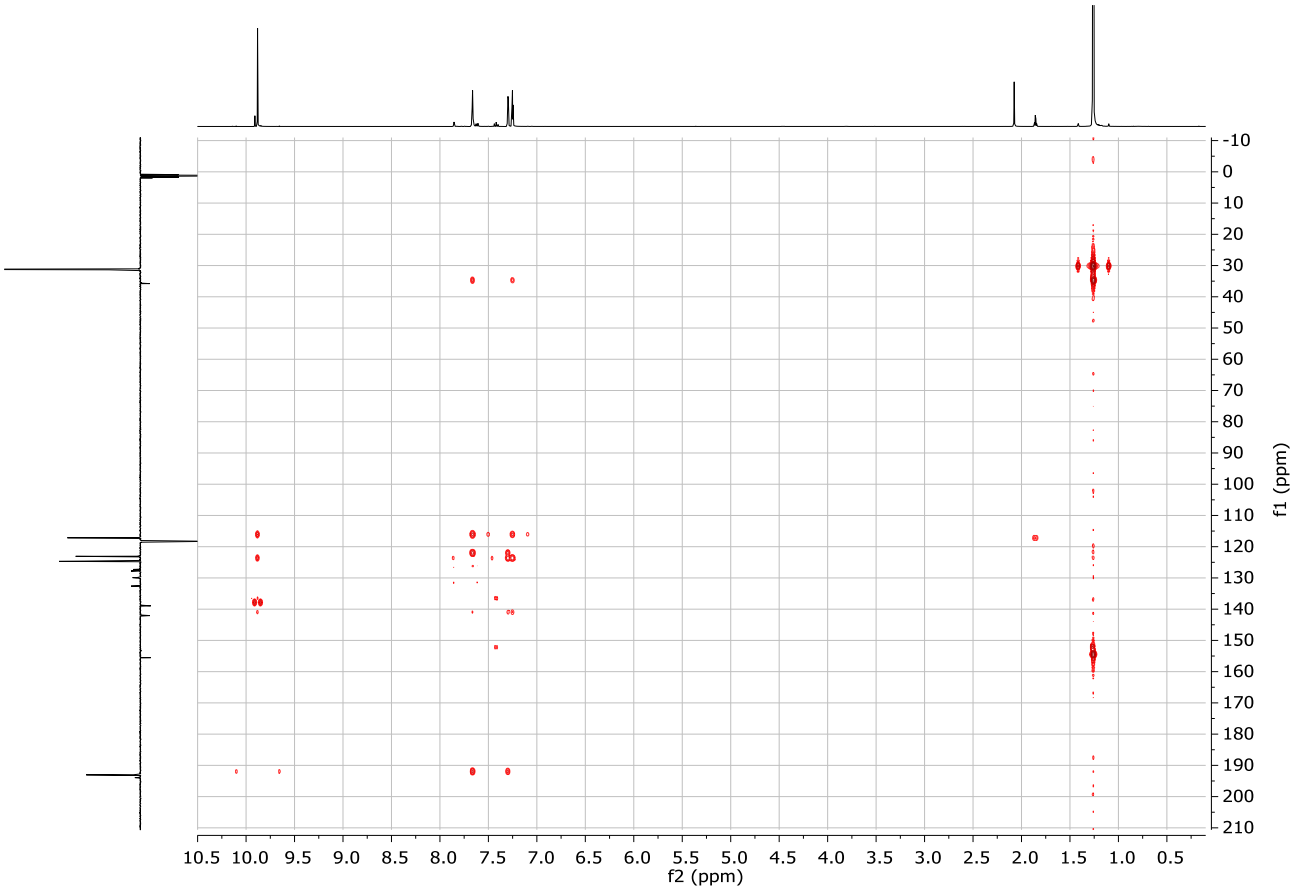

Figure 5.32 *HMBC NMR of* ***7b*** *in* CD_3CN.

Synthesis of 2-(3-azido-5-(tert-butyl)phenyl)-4,4,5,5-tetramethylimidazolidine-1,3-diol (7a):

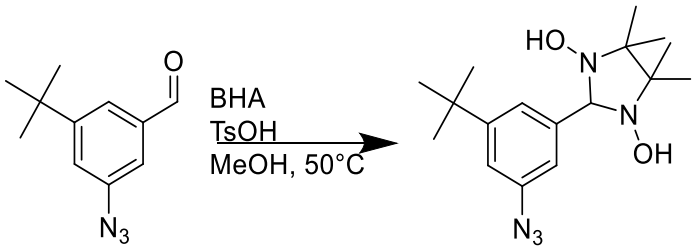

6

A degassed solution of aldehyde **7b** (337 mg, 1.65 mmol), BHA (244 mg, 1.65 mmol, 1 eq.), TsOH (15mg, 0.082 mmol, 5% mol.) in dry MeOH (7 mL) was stirred under N_2 at 50°C for 18h. The cloudy reaction mixture was then cooled to RT, concentrated *in vacuo* to a minimal volume and the product precipitated with pentane, filtered and washed again with pentane to yield **7a** as a white powder (346mg, 63%) that was used without further purification in the next step. ^{1}H-NMR (400 MHz, DMSO-d_6) δ = 7.84 (s, 2H, HO-N), 7.33 (m, 1H), 7.08 (m, 1H), 6.95 (m, 1H), 4.51 (s, 1 H), 1.28 (s, 9H), 1.08-1.05 (ds, 12H). ^{13}C NMR (101 MHz, DMSO-d_6) δ = 152.17, 143.88, 138.30, 122.63, 115.71, 115.11, 90.16, 66.23, 39.52, 34.58, 31.30, 31.05, 24.36, 17.17. ESI-MS (+, *m/z*, %): 334.5 [M+H$^+$, 100].

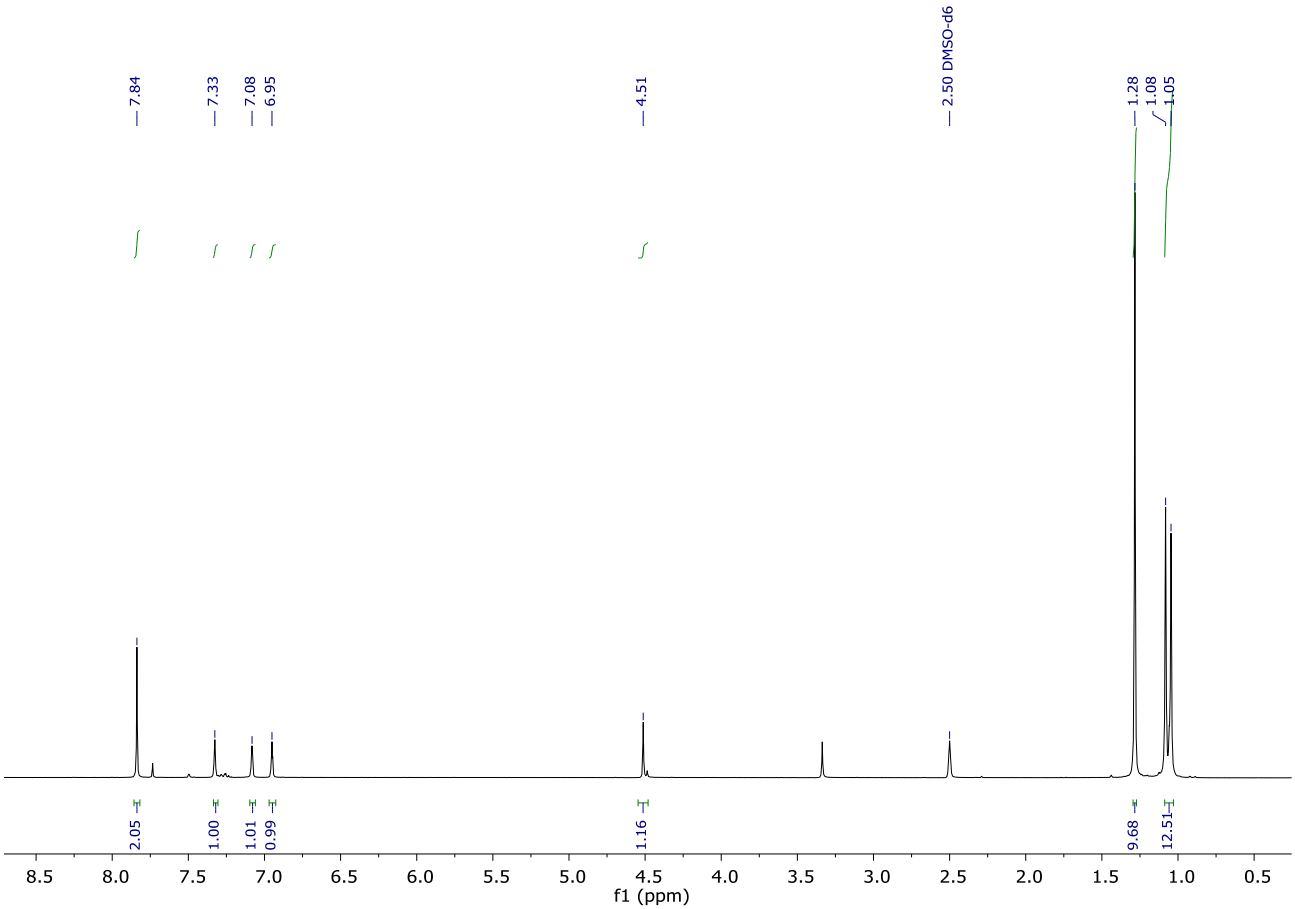

Figure 5.33 *^{1}H-NMR (400MHz) of **7a** in DMSO-d_6 at 298K.*

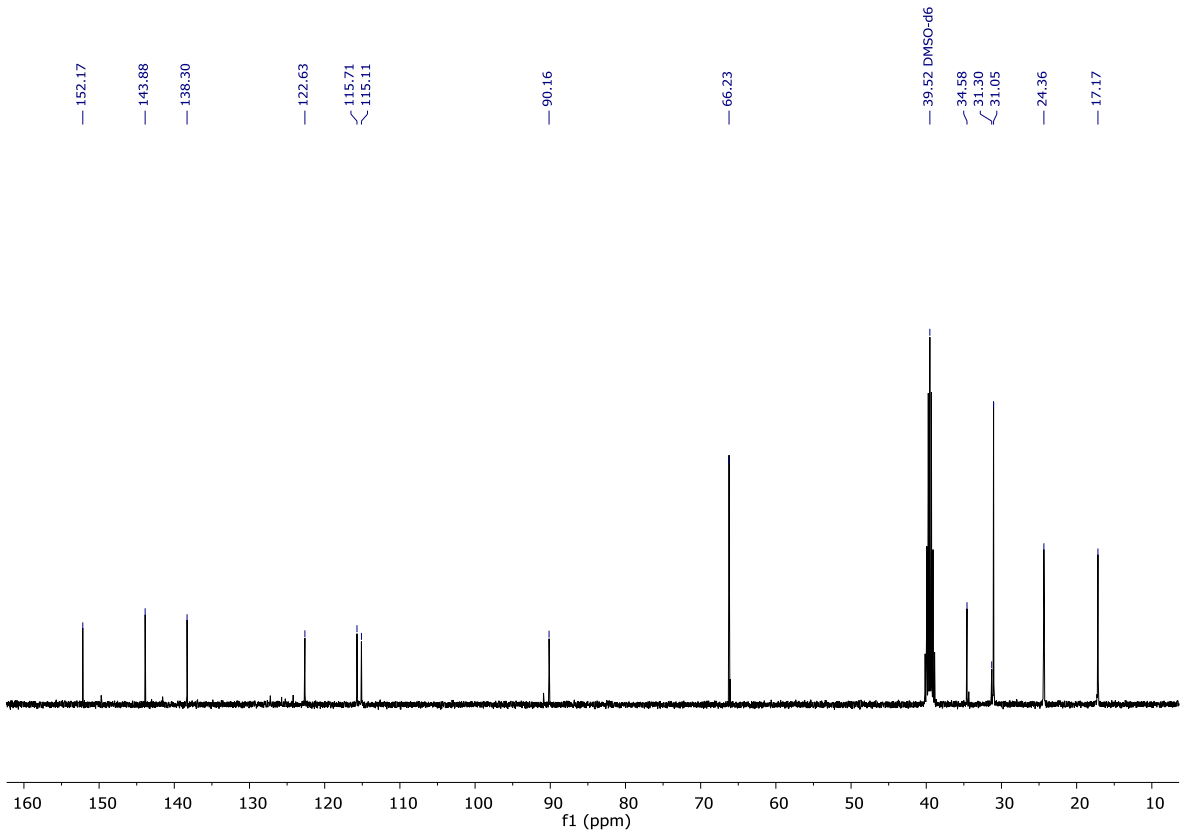

Figure 5.34 *^{13}C-NMR (101MHz) of **7a** in DMSO-d_6 at 298K.*

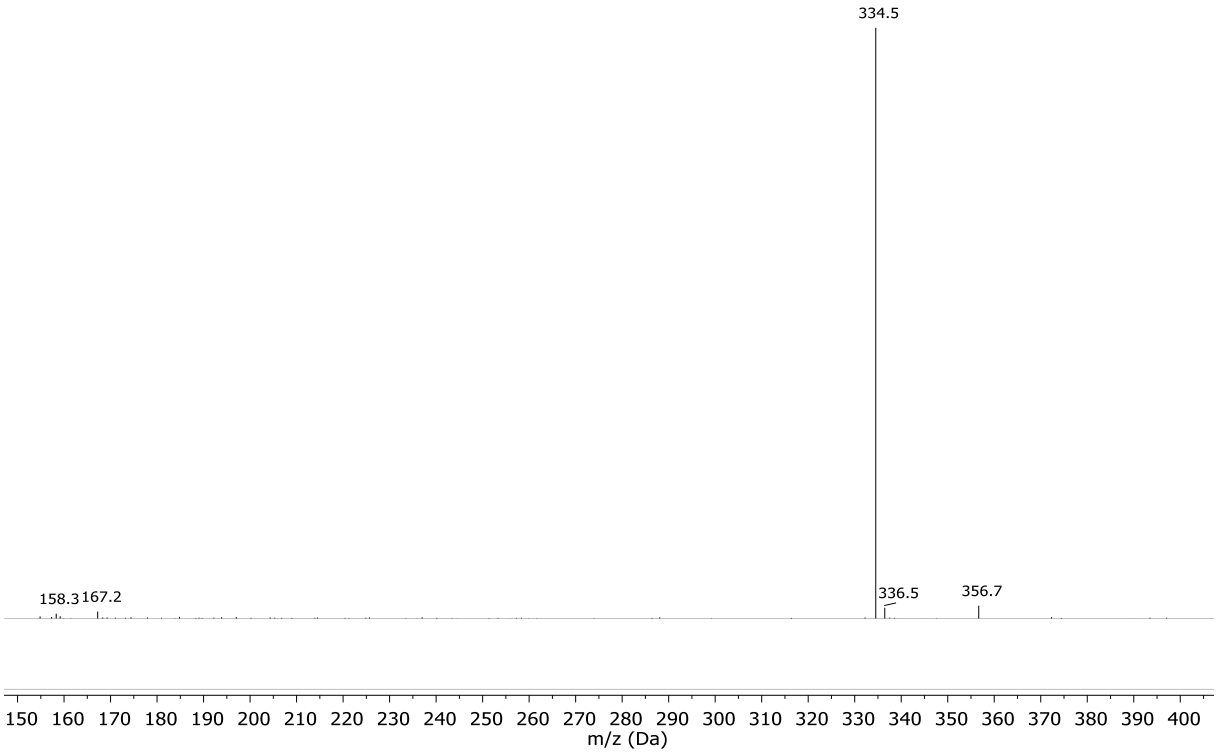

Figure 5.35** MS (ESI +) of compound **7a.

Synthesis of 1-(4,4,5,5-tetramethyl-1-oxyl-3-oxide- imidazoline-2-yl)-3azido-5-tertbuthylbenzene (7):

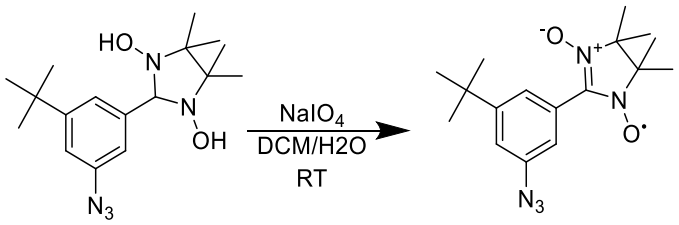

7

Compound **7a** (250 mg, 0.749 mmol) was dissolved in degassed DCM (50 mL) and a solution of $NaIO_4$ (200 mg, 0.973 mmol, 1.25 eq.) in degassed water (50 mL) was added dropwise over 25 min while vigorously stirring under N_2. The organic layer slowly turned deep blue and the mixture was left to stir for 1h. The progression of the reaction was monitored via TLC to monitor the disappearance of the starting material (eluent DCM). The reaction mixture was the diluted with 50 mL of DCM and the layers separated. The organic phase was then washed with distilled water (2x100 mL), brine (100 mL), dried over $MgSO_4$, filtered and the solvent removed *in vacuo*. The product was purified via column chromatography (SiO_2, Eluent P.Et/EtAc 9:1) to yield radical **7** as blue solid (197mg, 80%). ESI-MS (+, *m/z*, %): 331.5 [$M+H^+$,100], 353.4 [$M+Na^+$,1], 371.4 [$M+K^+$,3]; UV/Vis, λ/nm (ACN), (ε, $M^{-1}\times cm^{-1}$): 583 (222), 365 (8087).

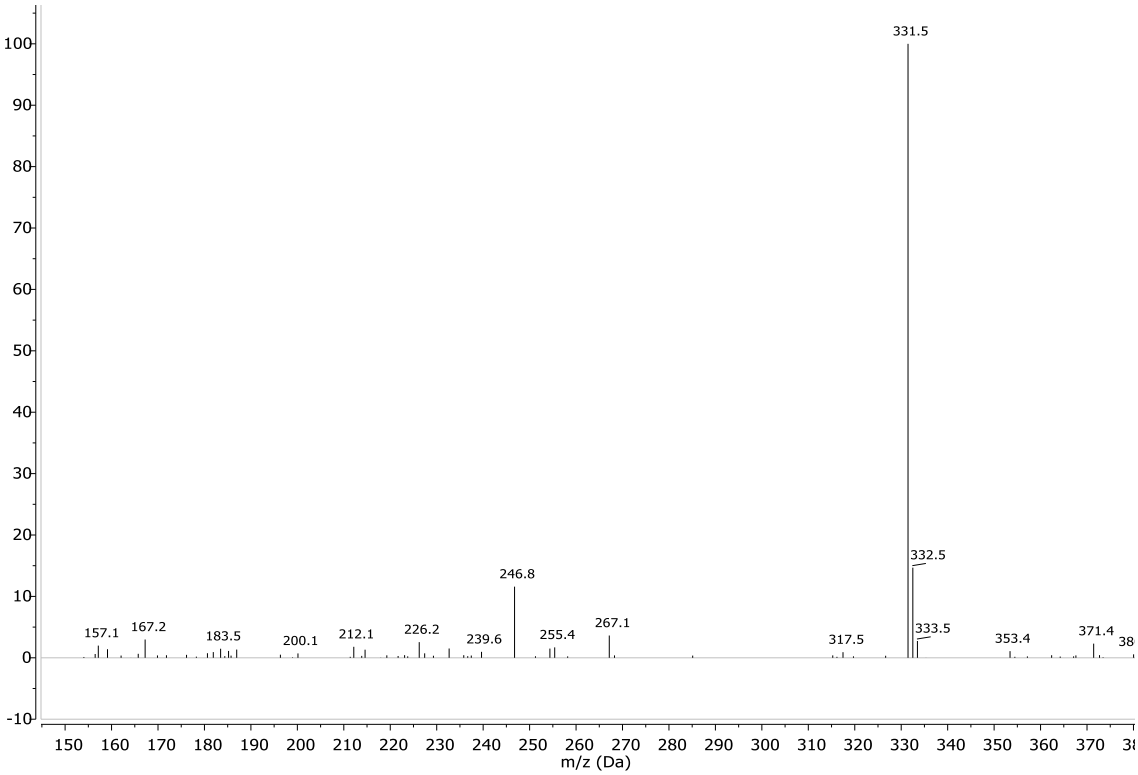

Figure 5.36 *MS (ESI +)* of compound **7**.

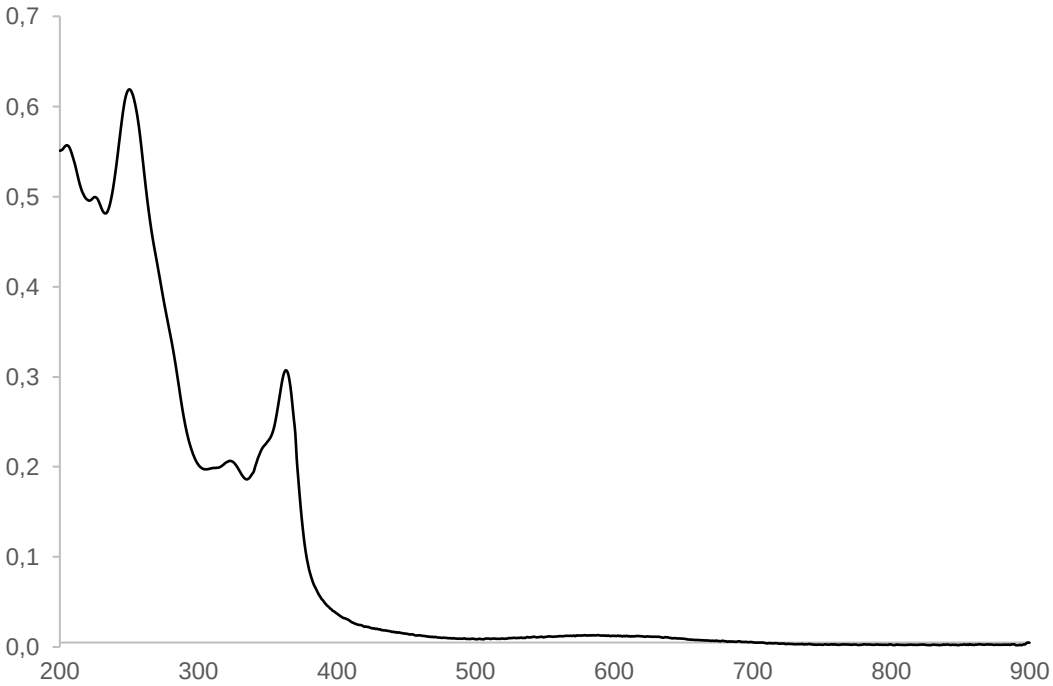

Figure 5.37 *UV-Vis spectra of compound **7** in ACN.*

Synthesis of ((3-(tert-butyl)-5-(1,3-dioxolan-2-yl)phenyl)ethynyl)trimethylsilane (8d):

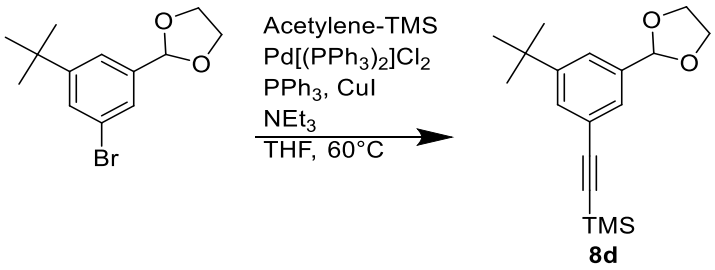

8d

Compound **16** (1.00g, 3.50 mmol), $Pd(PPh_3)_2Cl_2$ (61 mg, 2.5% mol.), PPh_3 (11 mg, 1.25% mol.), CuI (6.66 mg, 1% mol.) and triethylamine (0.97 mL, 2 eq.) were dissolved THF and the mixture degassed by N_2 bubbling. TMS-Acetylene (2.42 mL, 17.5 mmol, 5 eq.) was introduced in the reaction vessel and the mixture stirred at RT for 30' and then warmed to 60°C for 16h. The mixture was cooled to RT and filtered through a silica plug with Et_2O as eluent. The solvents were removed *in vacuo* to yield a brown oil. The crude mixture was purified via column chromatography (SiO_2 Eluent: P.Et/DCM 9:1) to yield **8d** as a yellowish oil (1.034 g, 98%). ^{1}H-NMR ($CDCl_3$, 400MHz) ^{1}H NMR (400 MHz, $CDCl_3$) δ = 7.48 (m, 1H), 7.43 (m, 2H), 5.77 (s, 1H), 4.13-4.03 (m, 4H), 1.31 (s, 9H), 0.25 (s, 9H). ^{13}C NMR (101 MHz, $CDCl_3$) ^{13}C NMR (101 MHz, $CDCl_3$) δ = 151.53, 137.86, 129.91, 127.46, 123.98, 122.96, 105.56, 103.66, 93.69, 77.16, 65.42, 34.88, 31.33, 0.15. GC-MS (EI, *m/z*, %): 302 [M^+, 54].

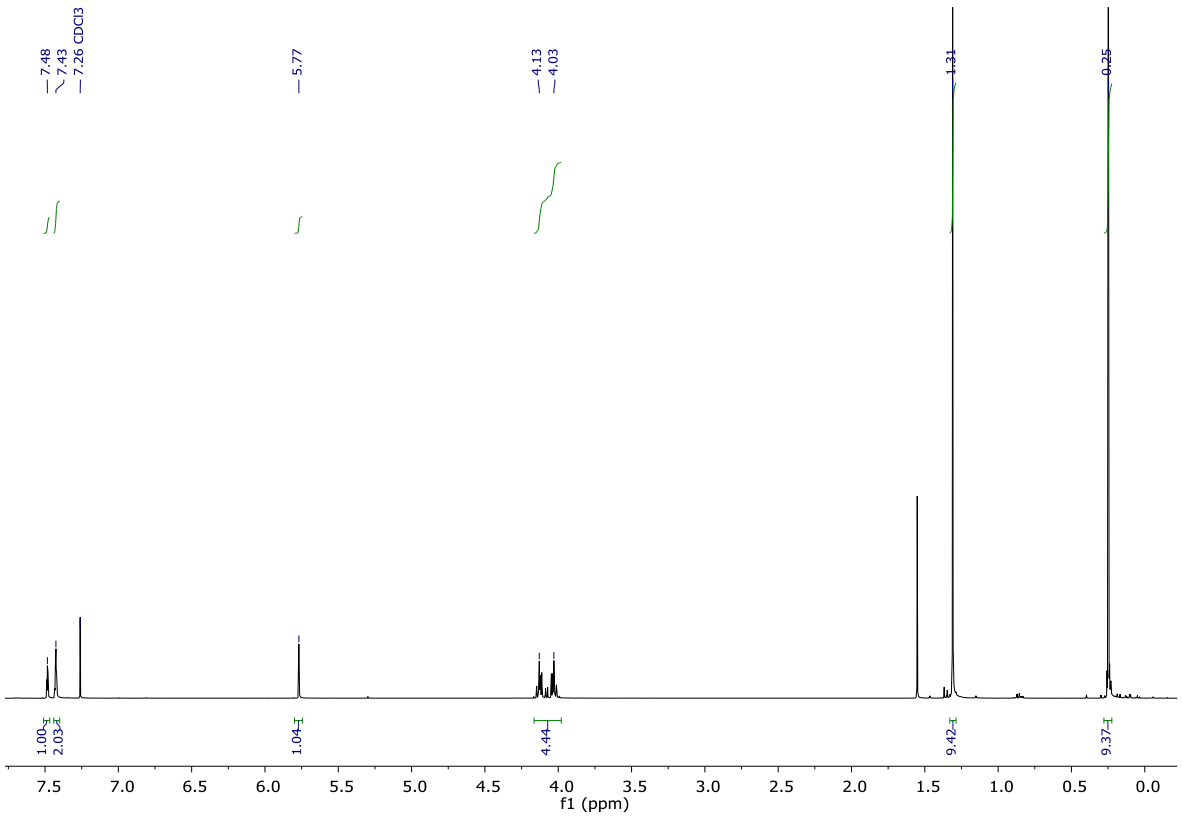

Figure 5.38 *^{1}H-NMR (400MHz) of **8d** in $CDCl_3$ at 298K.*

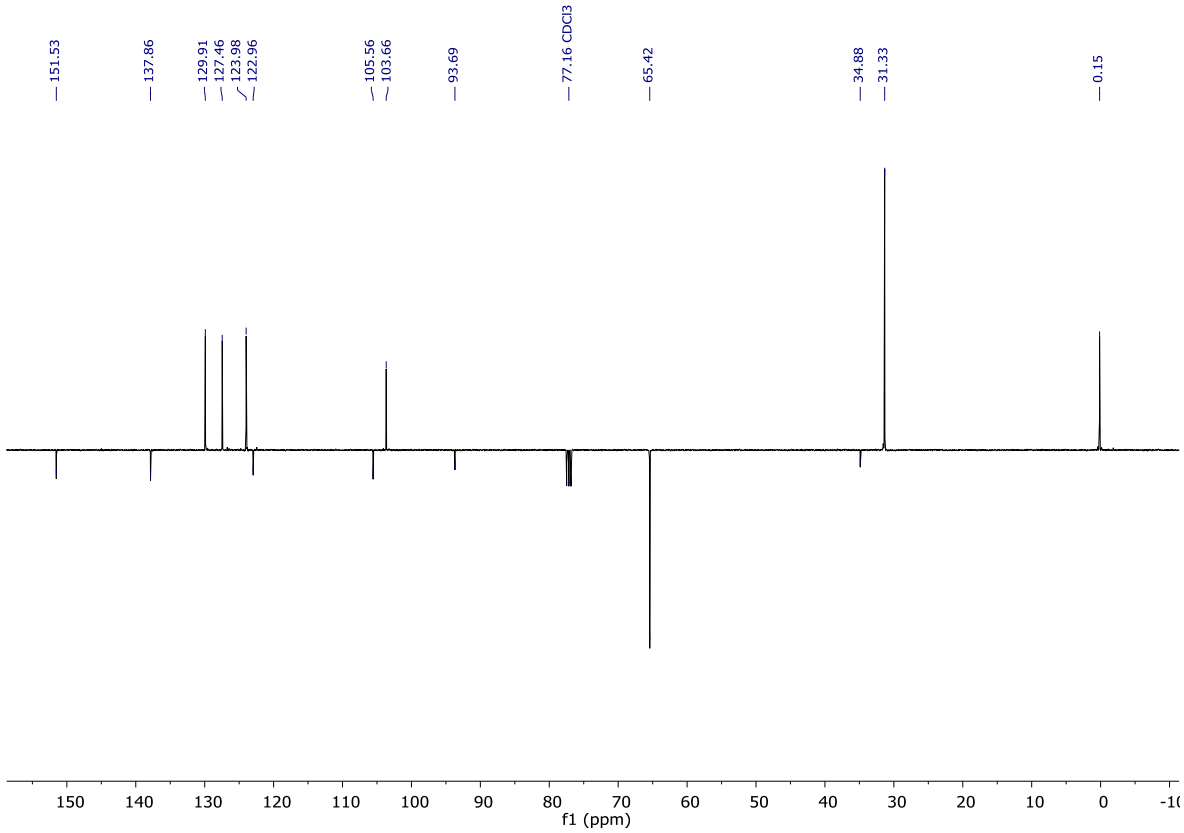

Figure 5.39 *J MOD NMR (101 MHz) of* ***8d*** *in* $CDCl_3$ *at 298K.*

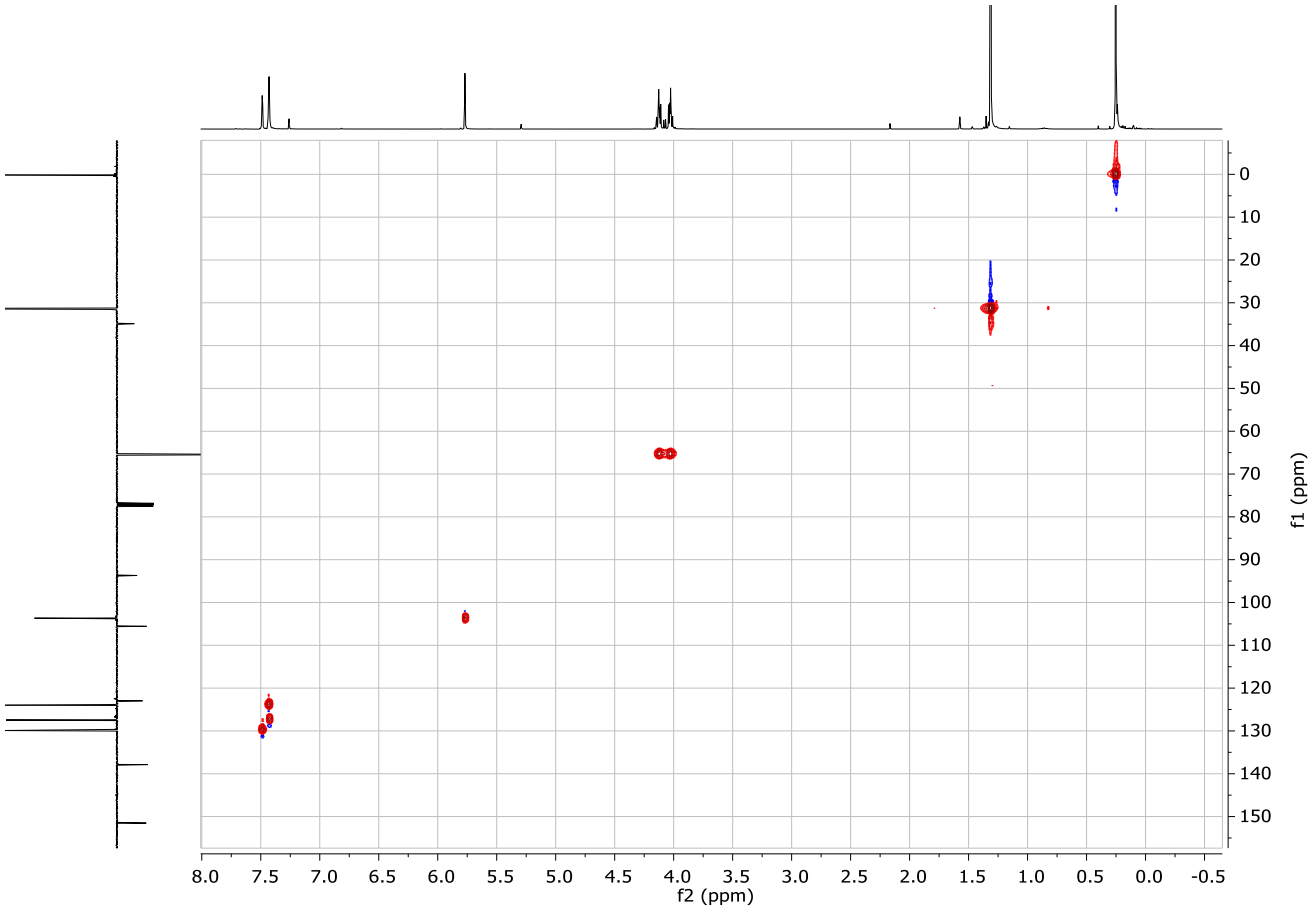

Figure 5.40 *HSQC NMR of* ***8d*** *in* $CDCl_3$.

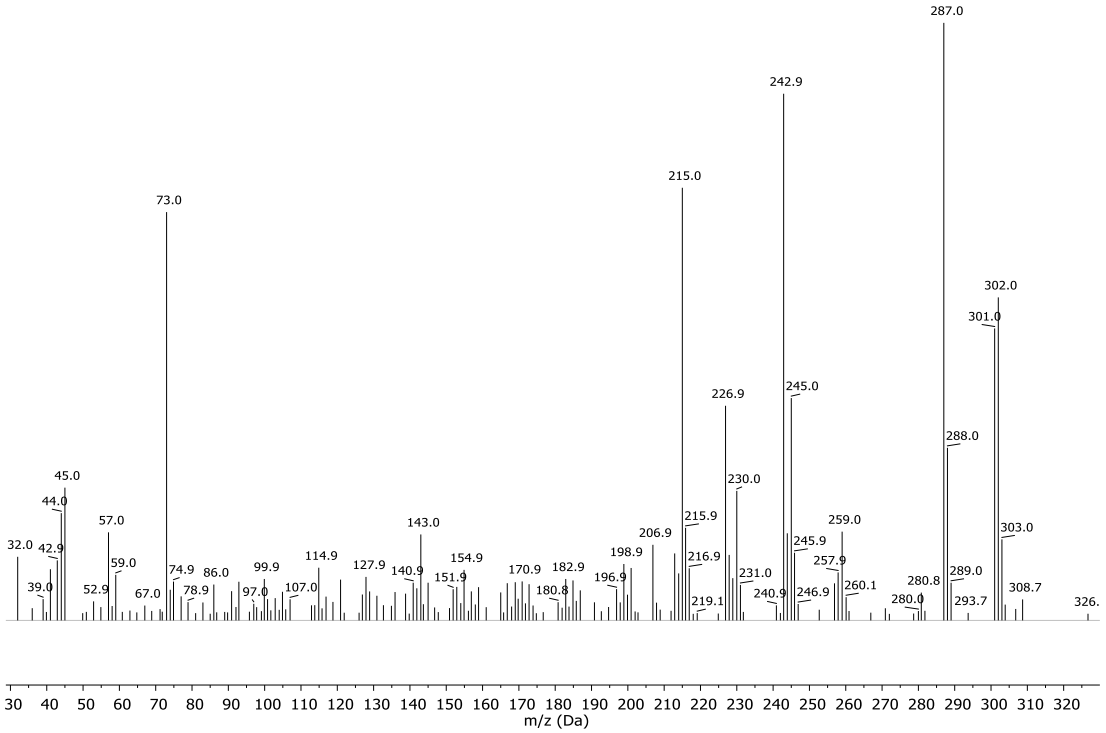

Figure 5.41 *Mass spectrum (EI) of compound* ***8d****.*

Synthesis of 3-(tert-butyl)-5-((trimethylsilyl)ethynyl)benzaldehyde (8c):

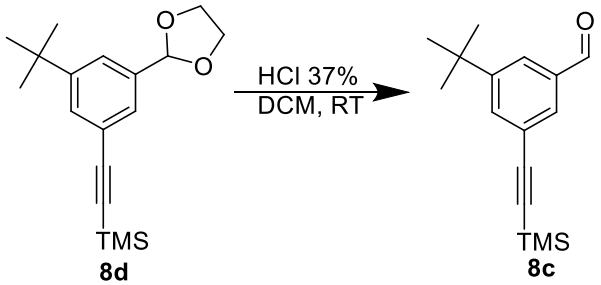

Compound **8d** (500 mg, 1.65 mmol) was dissolved in DCM (25 mL) and HCl 37% (139 µL, 1 eq.) was added. The mixture was stirred o.n. and then neutralized with sat. $NaHCO_3$, the organic layer was then washed with H_2O (25 mL) and Brine (25 mL) and dried on $MgSO_4$. The solvent was removed *in vacuo* to yield compound **8c** as a yellowish solid (426 mg, 99%) that was used without further purification in the next step. ^{1}H NMR (400 MHz, $CDCl_3$) δ 9.97 (s, 1H), 7.85(m, 1H), 7.78 (m, 1H), 7.73 (m, 1H), 1.35 (s, 9H), 0.27 (s, 9H). ^{13}C NMR (101 MHz, $CDCl_3$) δ = 192.04, 152.57, 136.45, 134.94, 131.33, 126.17, 124.06, 104.11, 95.49, 77.16, 35.03, 31.22, 0.04. GC-MS (EI, *m/z*, %): 258.2 [M^+, 30].

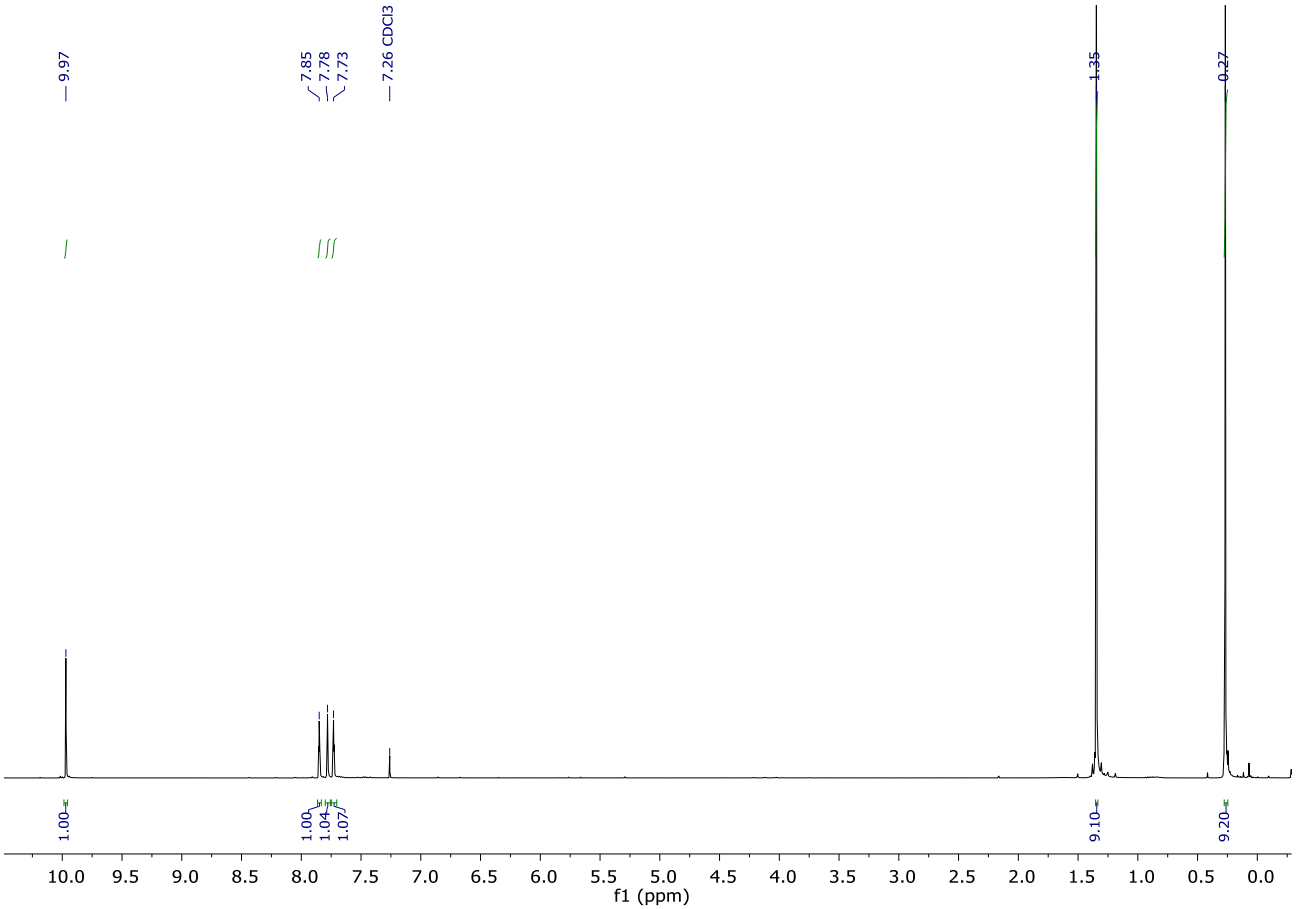

Figure 5.42 *^{1}**H-NMR** (400MHz) of **8c** in $CDCl_3$ at 298K.*

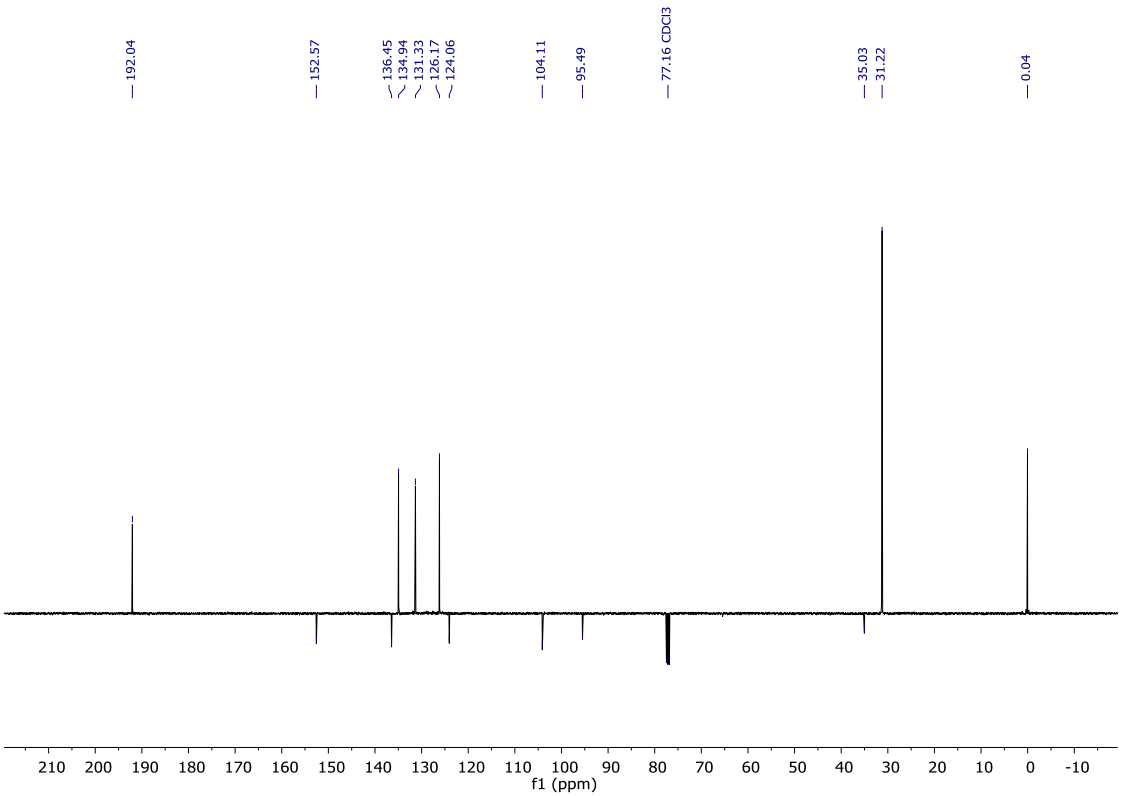

Figure 5.43 *J MOD NMR (101 MHz) of **8c** in $CDCl_3$ at 298K.*

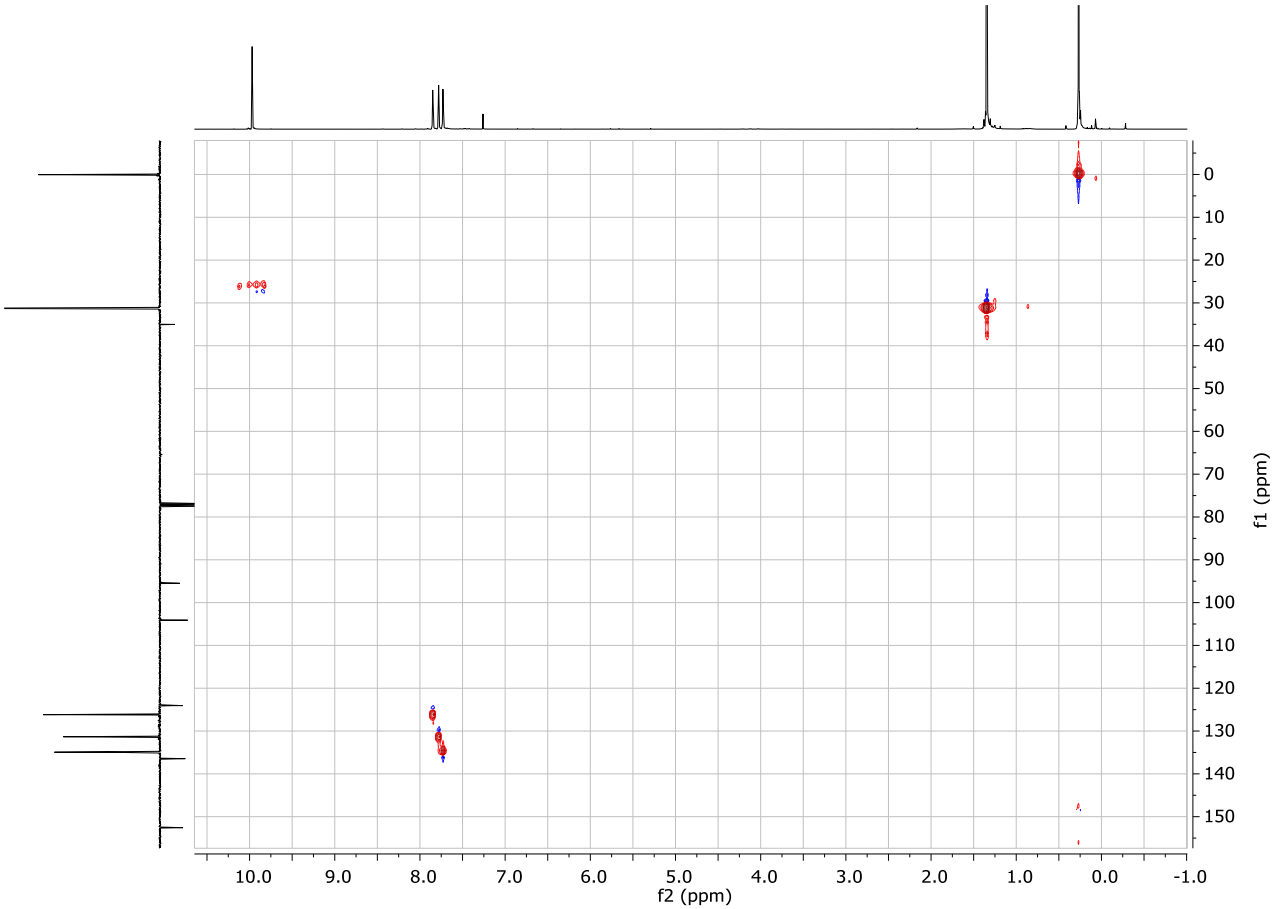

Figure 5.44 *HSQC NMR of* ***8c*** *in* $CDCl_3$ *at 298K.*

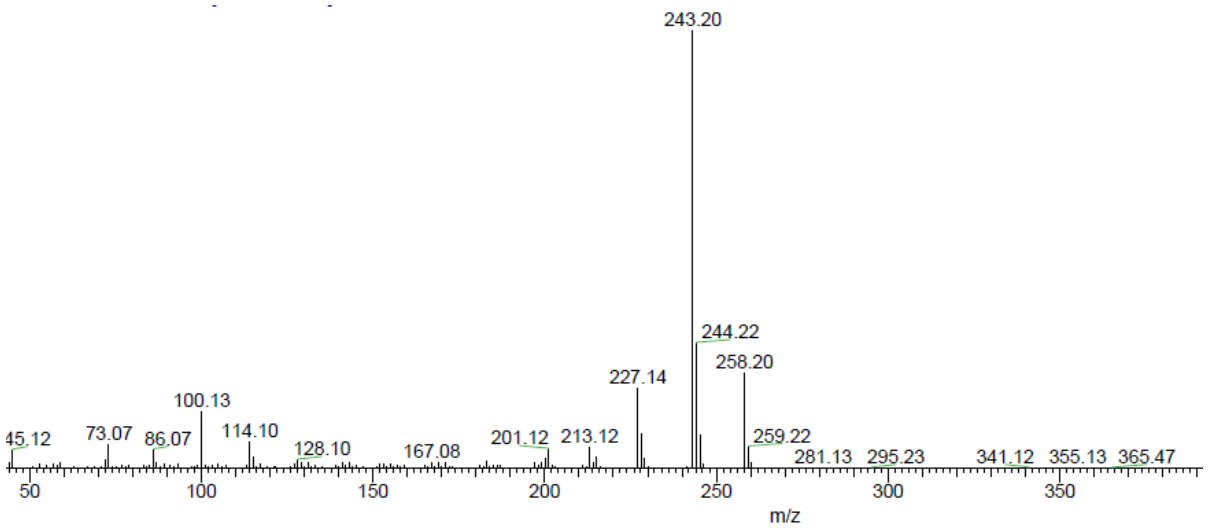

Figure 5.45 *Mass spectrum (EI) of compound* ***8c****.*

Synthesis of 2-(3-(tert-butyl)-5-((trimethylsilyl)ethynyl)phenyl)-4,4,5,5-tetramethylimidazolidine-1,3-diol (8b):

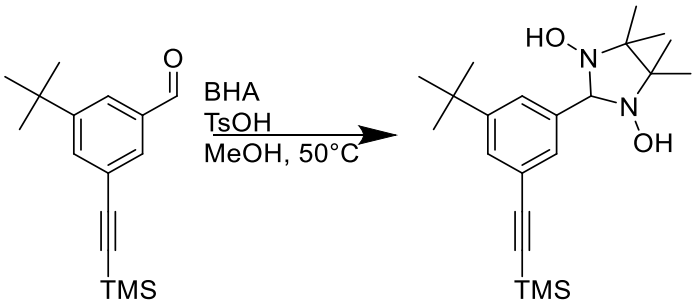

5

A degassed solution of aldehyde **3** (426 mg, 1.65 mmol), BHA (244 mg, 1.65 mmol, 1 eq.), TsOH (15mg, 0.082 mmol, 5% mol.) in dry MeOH (7 mL) was stirred under N_2 at 50°C for 18h. The cloudy reaction mixture was then cooled to RT, concentrated *in vacuo* to a minimal volume and the product precipitated with pentane, filtered and washed again with pentane to yield **5** as a white powder (337mg, 57%) that was used without further purification in the next step. ^{1}H NMR (400 MHz, DMSO-d_6) δ = 7.82(s, 2H, HO-N), 7.52 (m, 1H), 7.38 (m, 1H), 7.33 (m, 1H), 4.49(s, 1H), 4.74 (s, 1 H), 1.28 (s, 9H), 1.08-1.04(ds, 12H), 0.33 (s, 9 H). ^{13}C NMR (101 MHz, DMSO-d_6) δ = 150.36, 142.15, 128.63, 127.29, 126.38, 121.17, 106.23, 92.73, 90.02, 66.18, 39.52, 34.35, 31.03, 24.38, 17.16, 0.01. ESI-MS (+, *m/z*, %) 389.4 [M+H$^+$, 100].

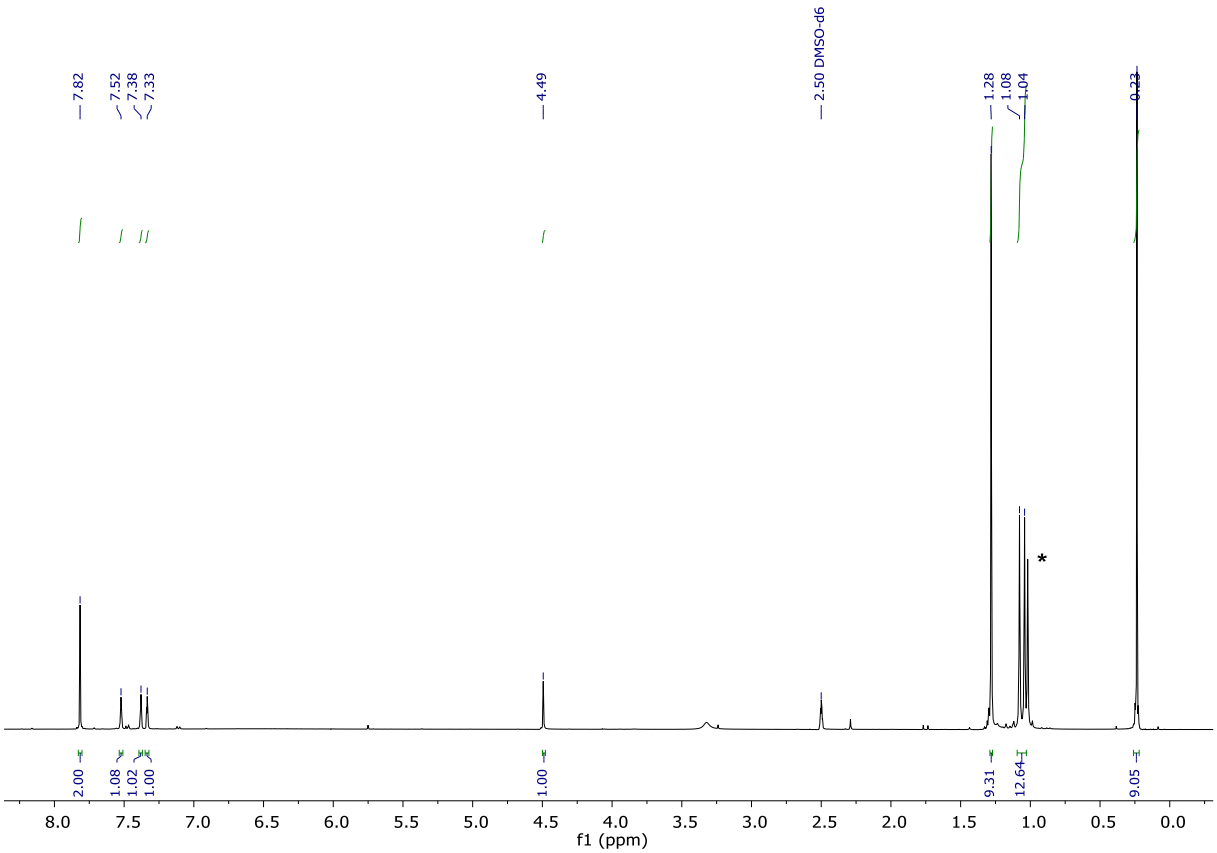

Figure 5.46 *^{1}H-NMR (400MHz) of **8b** in DMSO-d_6 at 298K. (*residual traces of BHA).*

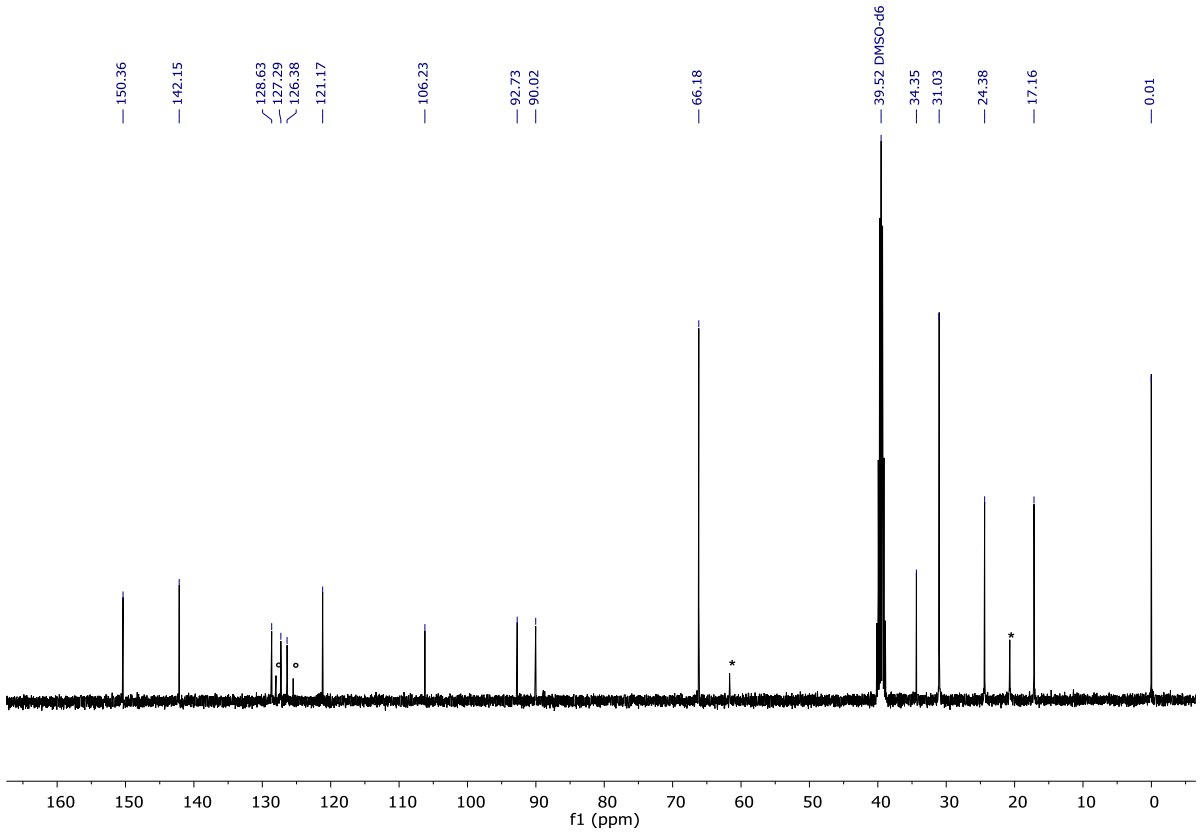

Figure 5.47 *^{13}C-NMR (101MHz) of* ***8b*** *in DMSO-d_6 at 298K. (*residual traces of BHA and* °unidentified impurities).

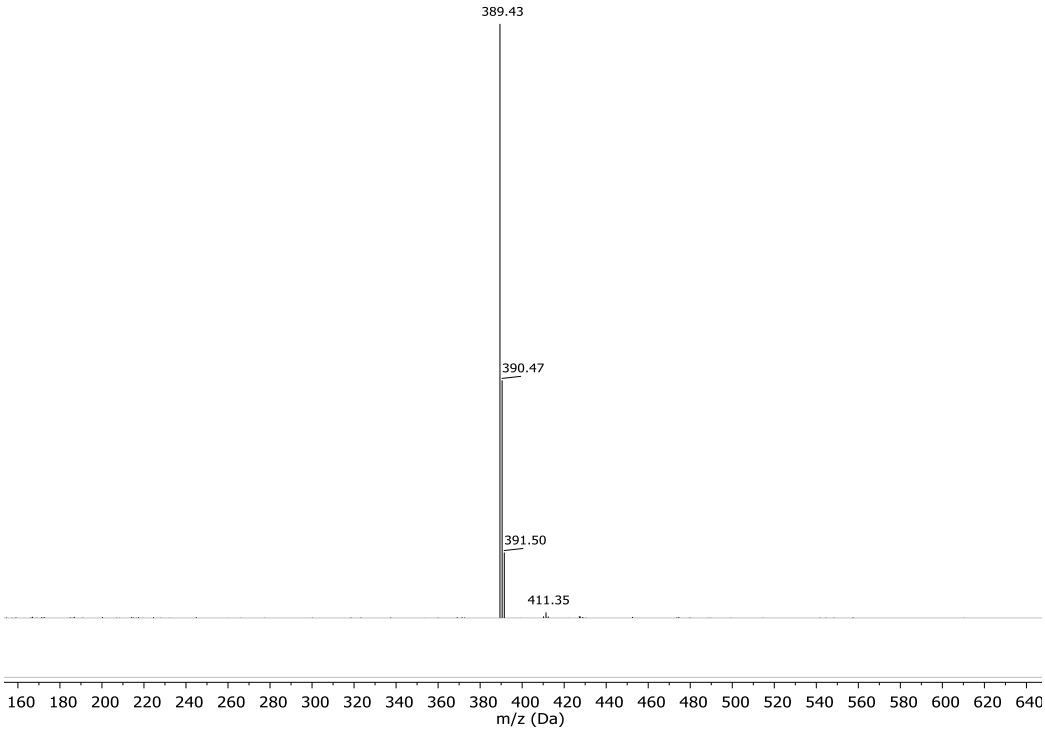

Figure 5.48 *Mass spectrum (ESI +) of compound* ***8b*** *in ACN.*

Synthesis of 1-(4,4,5,5-tetramethyl-1-oxyl-3-oxide- imidazoline-2-yl)-3[(trimethylsilyl)ethynyl]-5-tertbutylbenzene (8a):

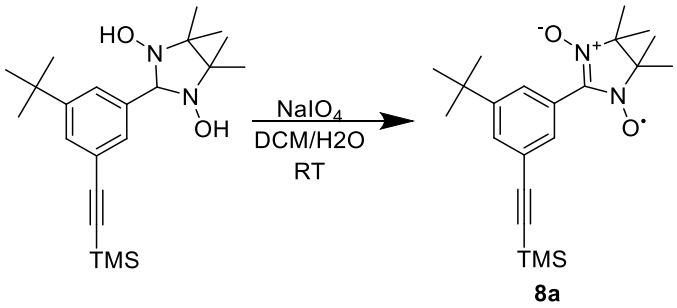

8a

Compound **8b** (250 mg, 0.643 mmol) was dissolved in degassed DCM (50 mL) and a solution of $NaIO_4$ (171 mg, 0.803 mmol, 1.25 eq.) in degassed water (50 mL) was added dropwise over 25 min while vigorously stirring under N_2. The organic layer slowly turned deep blue and the mixture was left to stir for 1h. The progression of the reaction was monitored via TLC to monitor the disappearance of the starting material (eluent DCM). The reaction mixture was the diluted with 50 mL of DCM and the layers separated. The organic phase was then washed with distilled water (2x100 mL), brine (100 mL), dried over $MgSO_4$, filtered and the solvent removed *in vacuo*. The product was purified via column chromatography (SiO_2, Eluent P.Et/EtAc 9:1, 8:2 then 7:3) to yield radical **8a** as blue solid (198 mg, 80%). ESI-MS (+, *m/z*, %) 386.5 [$M+H^+$, 100], 408 [$M+Na^+$, 5].

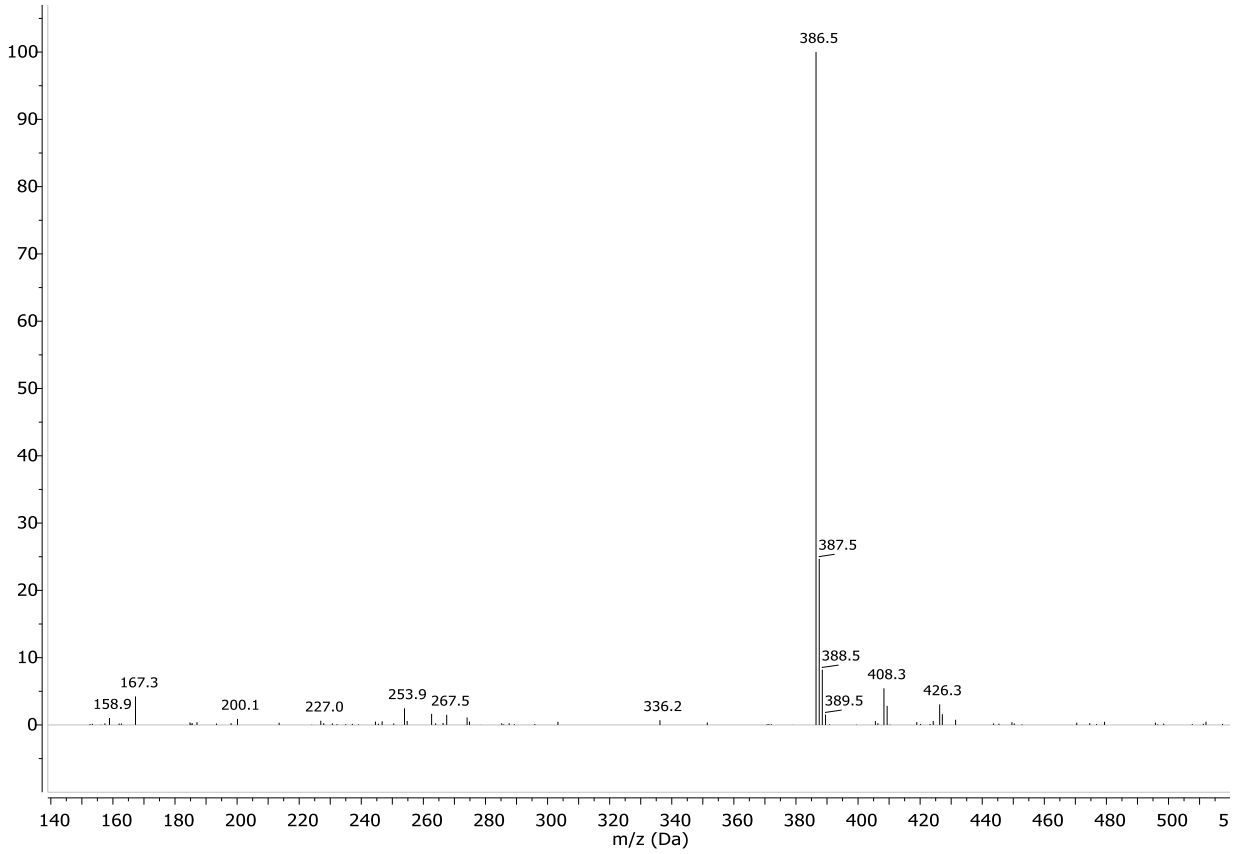

Figure 5.49 *Mass spectrum (ESI +) of compound* ***8a****.*

Synthesis of 1-(4,4,5,5-tetramethyl-1-oxyl-3-oxide- imidazoline-2-yl)-3(ethynyl)-5-tertbutylbenzene (8):

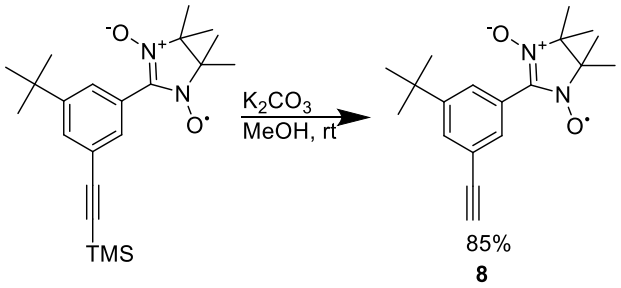

Radical **8a** (250 mg, 0.643 mmol) was dissolved in degassed MeOH (25 mL) and K_2CO_3 (266 mg, 1.92 mmol, 3 eq.) was added. The reaction mixture was stirred o.n. under nitrogen. After this time the suspension was filtered, MeOH removed *in vacuo* and re suspended in DCM (50 mL). The organic layer was washed with sat. $NaHCO_3$ (50mL), water (50 mL) and then brine (50 mL). the solution was dried on $MgSO_4$, filtered and the solvent removed *in vacuo*. Radical **8** was purified on silica gel (eluemt: DCM then DCM/Et.Ac 9:1) to yield radical **8** as a dark blue solid (141 mg, 70%). ESI-MS (+, *m/z*, %) 314.5 [$M+H^+$, 100], 336 [$M+Na^+$, 5], 354 [$M+K^+$, 10]. UV/Vis, λ/nm (ACN), (ε, $M^{-1}\times cm^{-1}$): 589 (371), 363 (11044).

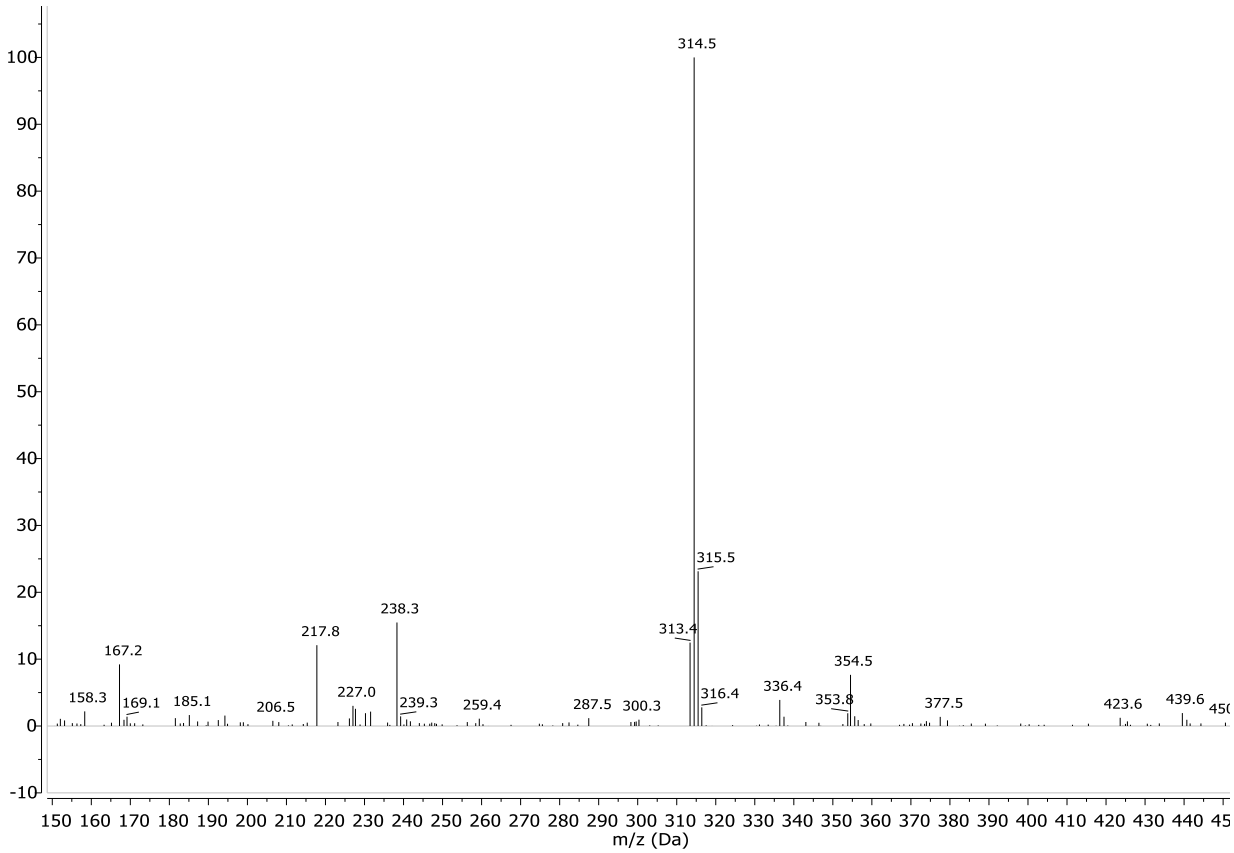

Figure 5.50 *Mass spectrum (ESI +) of compound* ***8****.*

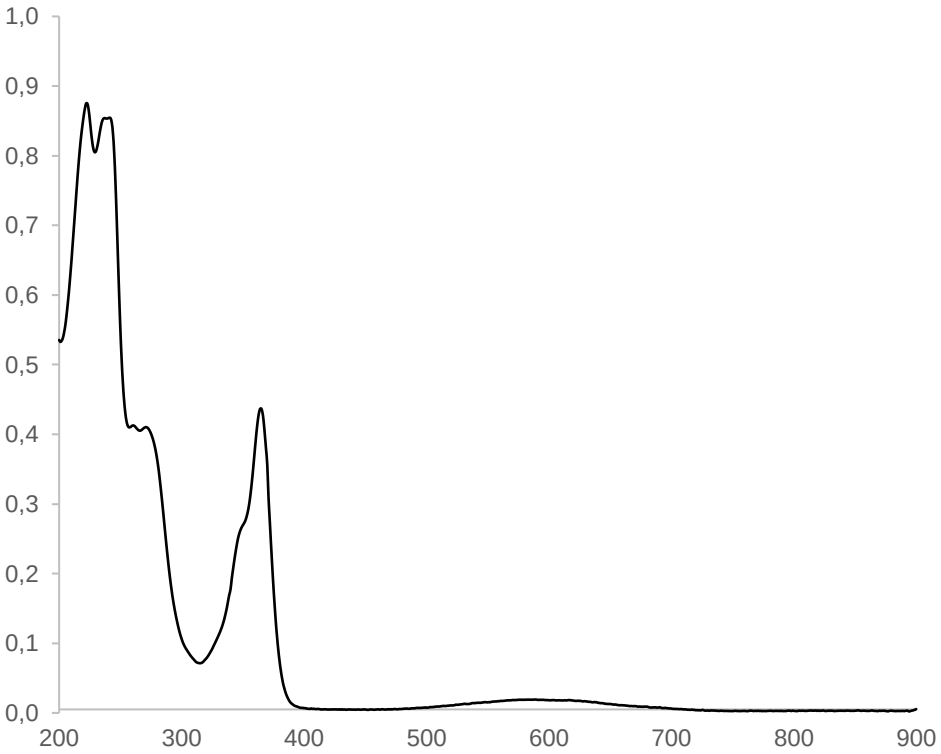

Figure 5.51 *UV-Vis spectra of compound* ***8*** *in ACN.*

Synthesis of 2-(3-(tert-butyl)-5-(1,3-dioxolan-2-yl)phenyl)-6-chloropyridine (17e):

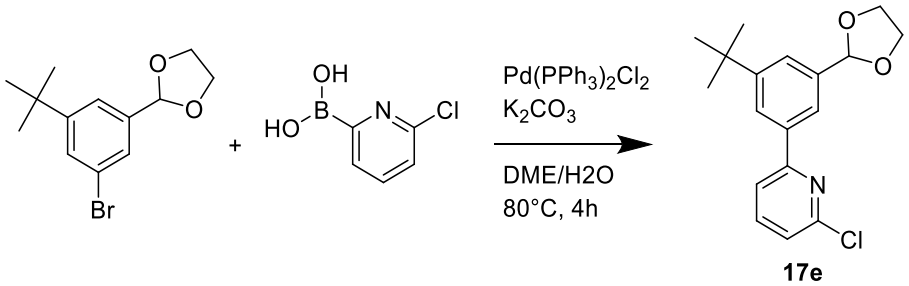

17e

A 10 ml RBF charged with compound **16** (244 mg, 0.86 mmol), (6-chloropyridin-2-yl)boronic acid **18** (136 mg, 0.86 mmol, 1 eq.), $Pd(PPh_3)_2Cl_2$ (12 mg, 0.017 mmol, 2% mol.) was flushed with Ar. Degassed DME (3 mL) was added and the suspension degassed again with Ar Bubbling. A degassed solution of K_2CO_3 (474 mg, 3.42 mmol, 4 eq.) was added and the solution slowly heated to 80°C. The mixture was stirred 4h at 80°C and the progress of the reaction checked via TLC (Eluent c-Hex/DM 9:1). The reaction mixture was then cooled to RT, diluted with water (15 mL) and extracted with Et_2O (3x15mL), washed with Brine (45 mL), dried on $MgSO_4$, filtered and the solvent removed *in vacuo* to yield a brown oil. The crude mixture was purified via column chromatography (SiO_2, Eluent C-Hex/EtAc 9:1) to yield compound **10** as a yellow solid (154 mg, 57%). ^{1}H NMR (400 MHz, CD_3CN) δ = 8.06 (m, 1H) 7.91(m, 1H), 7.87-7.80 (m, 2H), 7.60 (m, 1H), 7.36-7.34 (m, 1H), 5.80 (s, 1H), 4.13-4.01 (m, 4H), 1.37 (s, 9H). ^{13}C NMR (101 MHz, CD_3CN) δ = 275.56, 270.01, 268.69, 258.11, 256.93, 255.49, 242.97, 242.42,

237.23, 221.37, 183.14, 152.58, 148.47, 118.26. GC-MS (E.I., *m/z*, %): 315.8 [M-2H$^+$, 11], 280.9 [M-Cl-2H$^+$, 30].

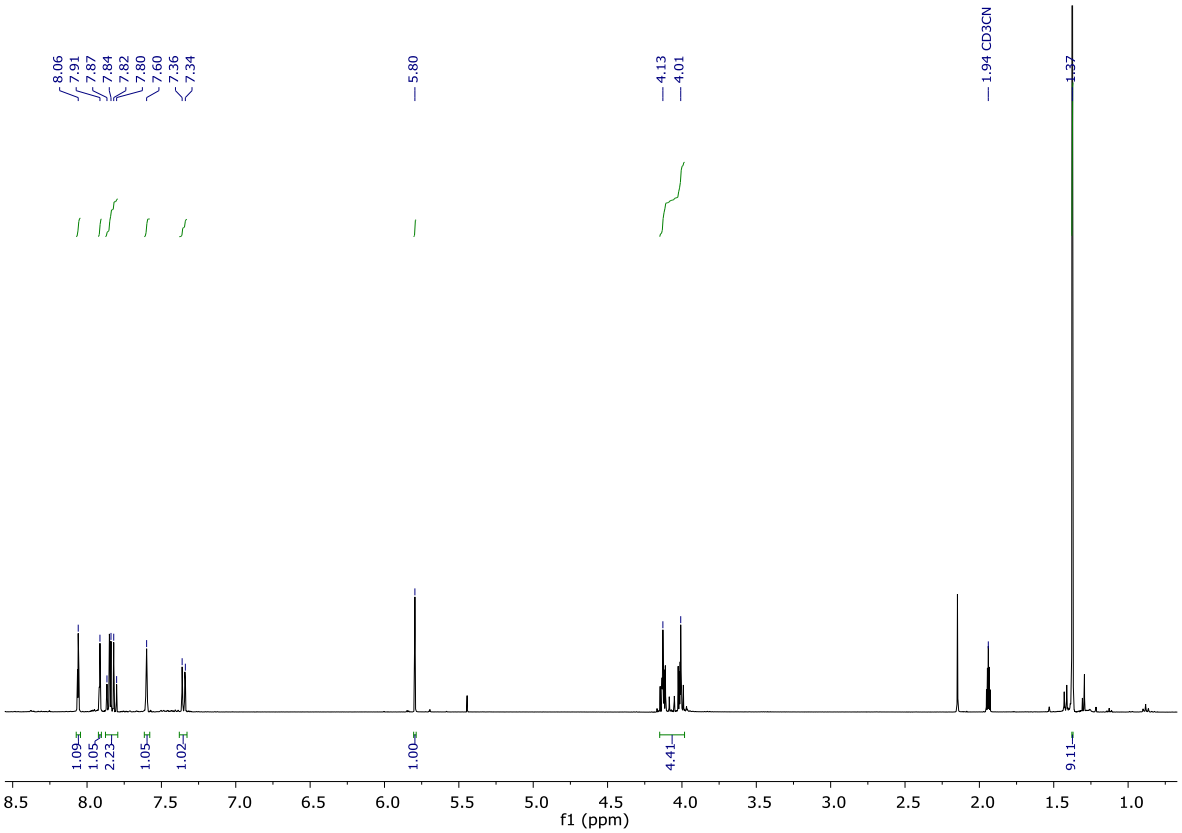

Figure 5.52 *^{1}H-NMR (400MHz) of **17e** in CD_3CN at 298K.*

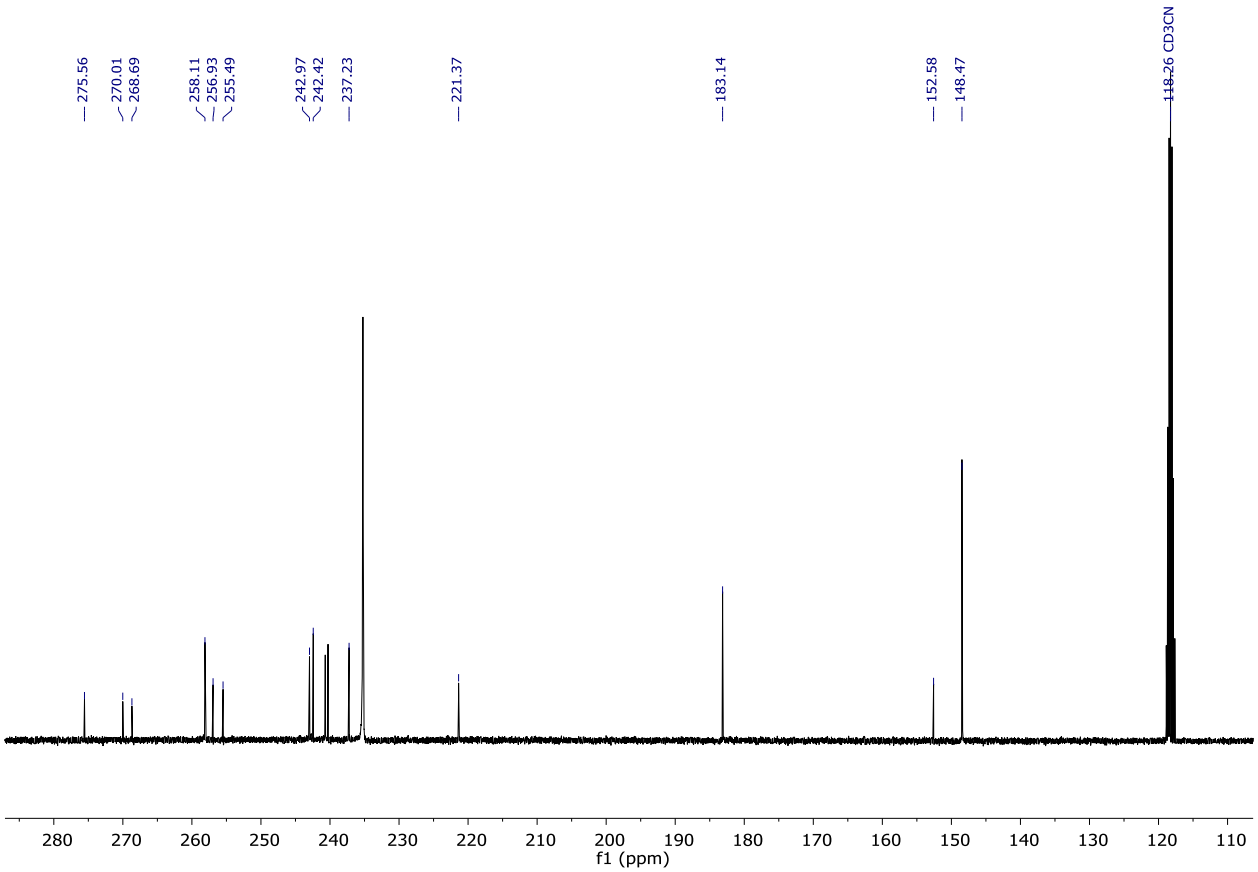

Figure 5.53 *^{13}C-NMR (101MHz) of **17e** in DMSO-d_6 at 298K.*

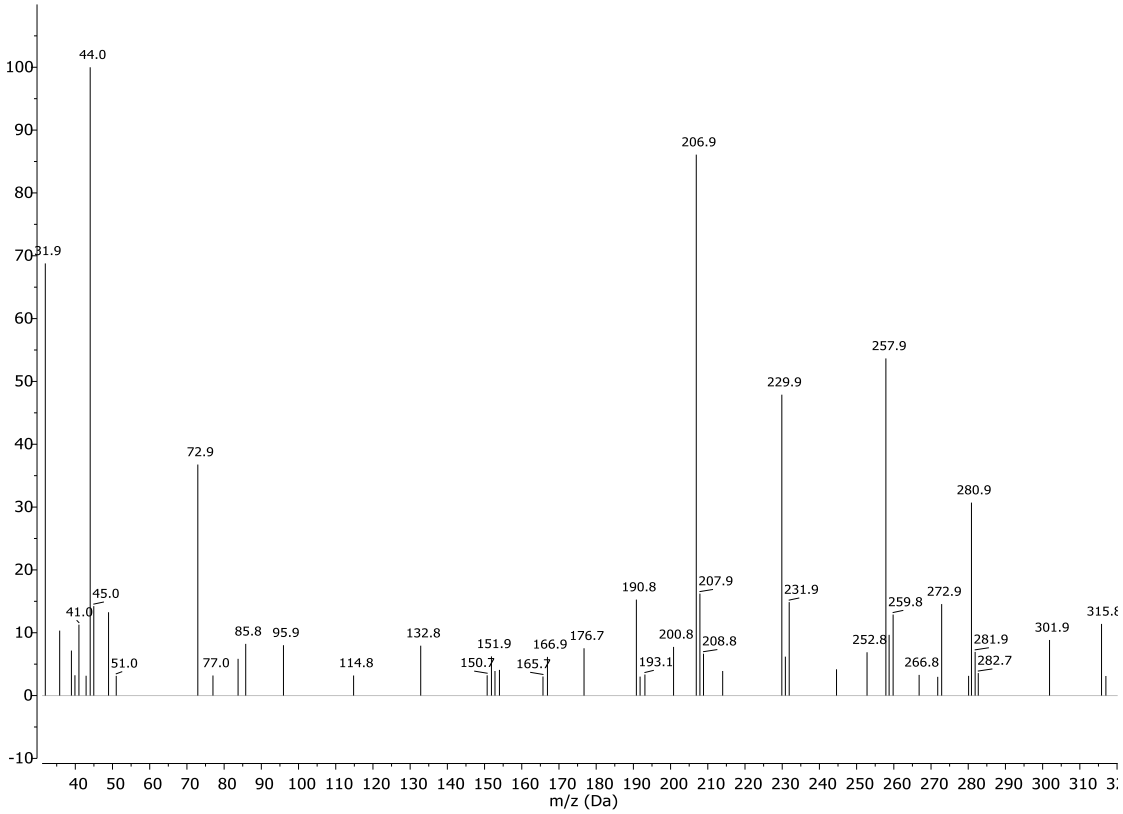

Figure 5.54 *Mass spectrum (EI) of compound **17e.***

Synthesis of 3-(tert-butyl)-5-(6-((trimethylsilyl)ethynyl)pyridin-2-yl)benzaldehyde (17c):

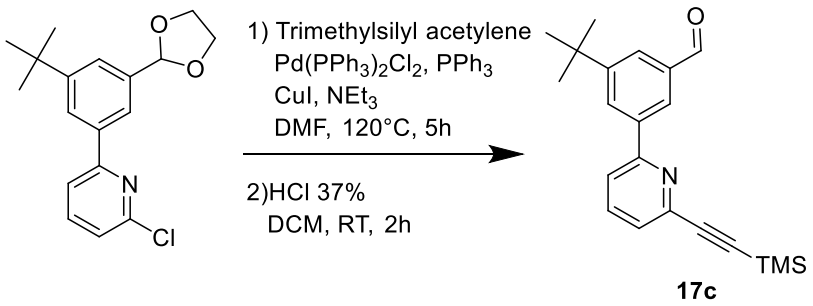

17c

Compound **17e** (250 mg, 0.786 mmol), $Pd(PPh_3)_2Cl_2$ (13.3 mg, 0.019 mmol, 2.5% mol.), PPh_3 (2.57 mg, 9.82 umol, 1.25%), CuI (1.49 mg, 7.86 umol, 1%) were added to a 10 ml RBF that was then flushed with Ar. Degassed dry DMF (4 mL) was added and the mixture degassed again with Ar bubbling. NEt_3 (220 µL, 1.57 mmol, 2 eq.) was added followed by TMS-Acetylene (544 µL, 3.93 mmol, 5 eq.). the mixture was stirred at RT for 1h and then heated to 120°C for 5h. the reaction was monitored via TLC (Eluent: c-Hex/EtAc 9:1). The reaction mixture was then cooled to RT and the DMF evaporated in vacuo to yield a brown oil that was filtered on silica (5cm, Eluent: Et_2O). The crude mixture was purified via column chromatography (SiO_2, Eluent c-Hex/EtAc 9:1) to yield the protected aldehyde **17d** as a brown oil (231 mg, 79%). ^1H NMR (400 MHz, CD_3CN) δ = 8.05 (m, 1H) 7.92(m, 1H), 7.88-7.79 (m, 2H), 7.59 (m, 1H), 7.45-7.43 (m, 1H), 5.80 (s, 1H), 4.15-3.99 (m, 4H), 1.38 (s, 9H), 0,29 (s, 9H). The protected aldehyde (231mg, 0.608 mmol) was dissolved in DCM (5mL) and HCl 37% (1eq.) was added. The mixture was stirred at RT for 2h. To the mixture was added $NaHCO_3$ (50 mL) and extracted with DCM (3 x 50 mL). The organic phase was washed twice with water and with brine, dried on $MgSO_4$ and the solvent removed in vacuo. the crude mixture was purified via column chromatography (SiO_2, Eluent c-Hex/EtAc 9:1) to yield compound **17c** as a yellowish solid (195 mg, 96%). ^1H NMR (400 MHz, CD_3CN) δ = 10.07(s, 1H), 8.30 (m, 2H), 8.00(m, 1H), 7.91-7.81 (m, 2H), 7.47 (m, 1H), 1.40 (s, 9H), 0,28 (s, 9H). ^{13}C NMR (101 MHz, CD_3CN) δ = 193.71, 157.28, 153.92, 143.55, 140.26, 138.63, 138.10, 130.51, 127.98, 127.50, 126.43, 121.58, 105.03, 95.13, 35.76, 31.42, 1.32, -0.28. GC-MS (E.I., *m/z*, %): 335 [M^+, 45], 320 [M^+-CH_3, 100].

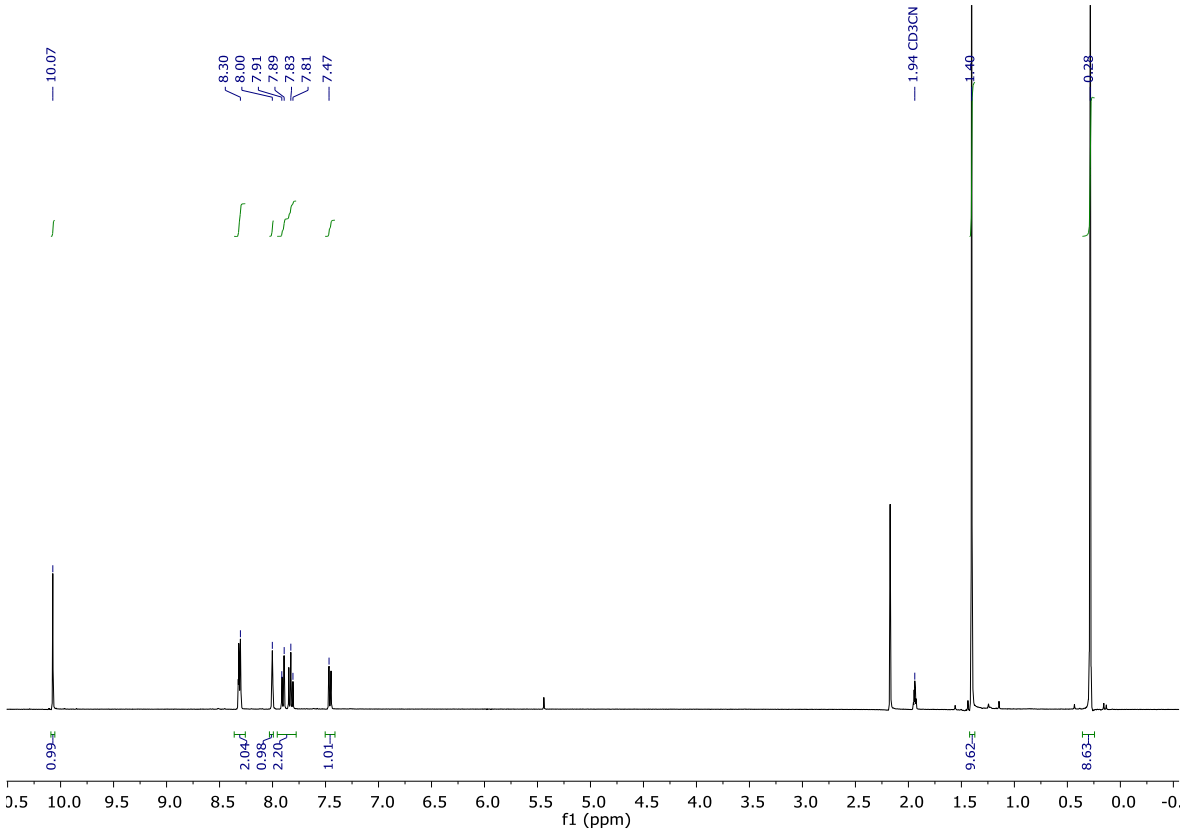

Figure 5.55 *^{1}H-NMR (400MHz) of **17c** in CD_3CN at 298K.*

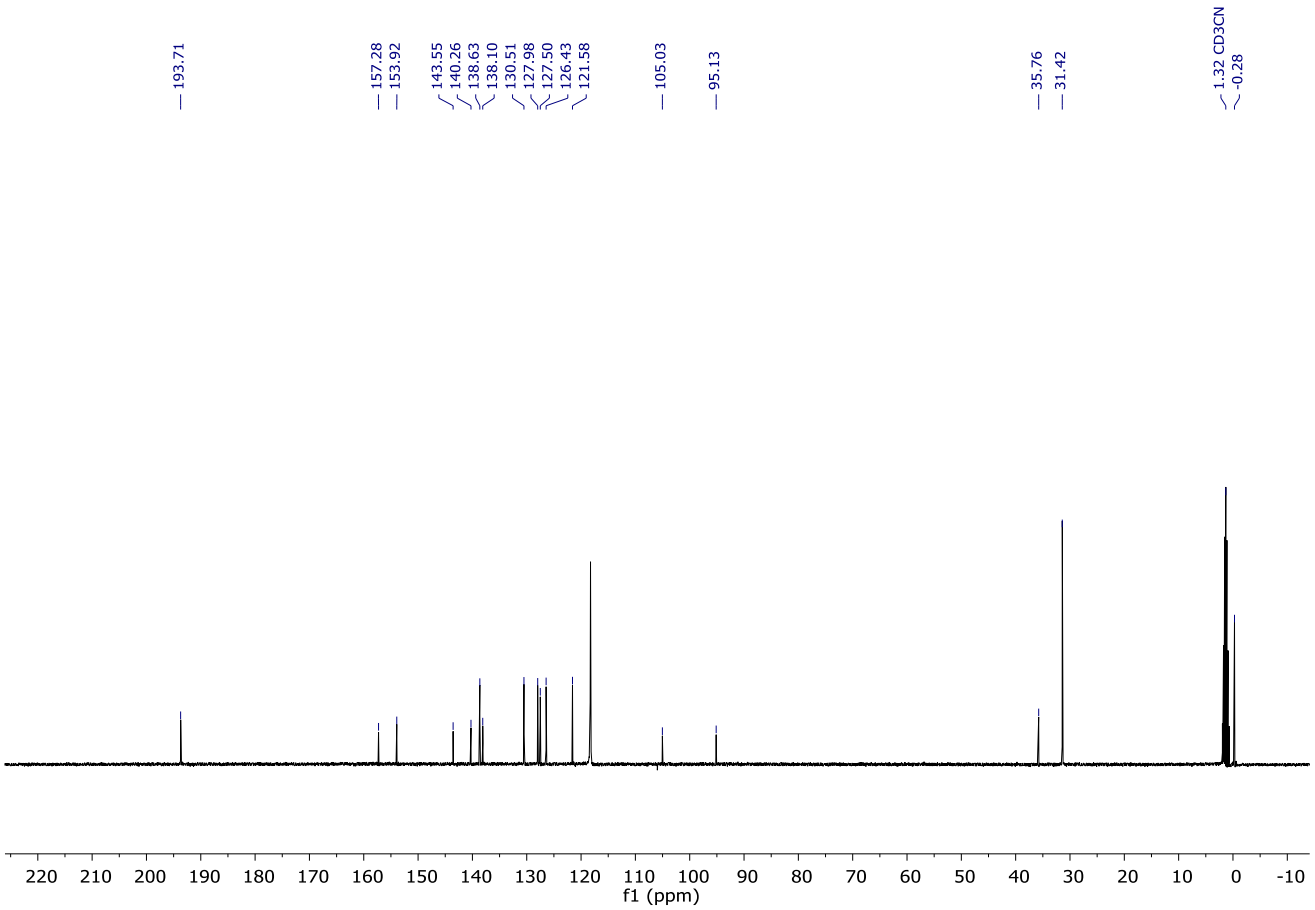

Figure 5.56 *^{13}C-NMR (101MHz) of **17c** in CD_3CN at 298K.*

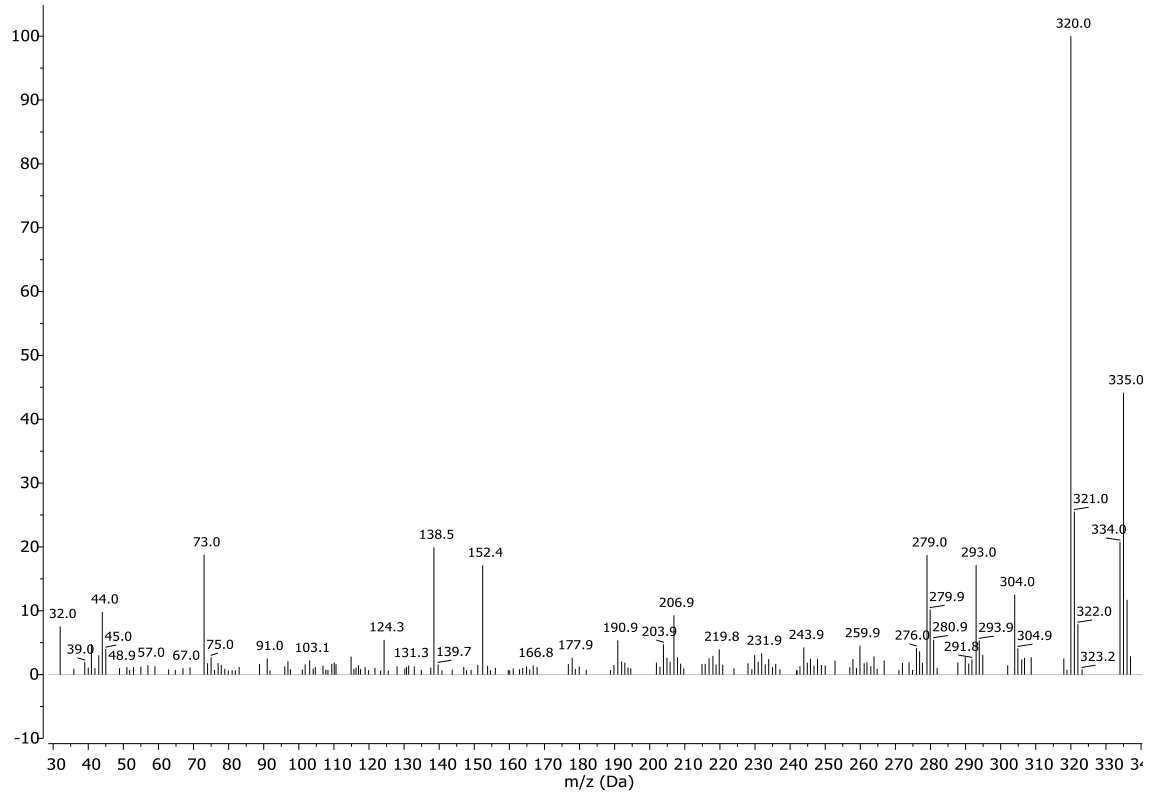

Figure 5.57 *Mass spectrum (EI) of compound* ***17c****.*

Synthesis of 2-(3-(tert-butyl)-5-(6-((trimethylsilyl)ethynyl)pyridin-2-yl)phenyl)-4,4,5,5-tetramethylimidazolidine-1,3-diol(17b):

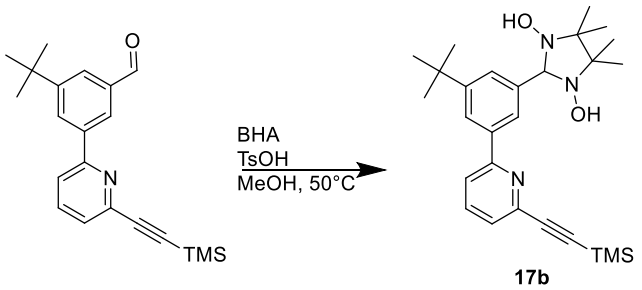

17b

A degassed solution of aldehyde **17c** (35 mg, 0.104 mmol), BHA (15.5 mg, 0.104 mmol, 1 eq.), TsOH (1 mg, 5.25 umol mmol, 5% mol.) in dry MeOH (1 mL) was stirred under N2 at 50°C for 18h. The cloudy reaction mixture was then cooled to RT, concentrated in vacuo to a minimal volume and the product precipitated with pentane, filtered and washed again with pentane to yield **17b** as a white powder (32mg, 65%) that was used without further purification in the next step. ^{1}H NMR (400 MHz, DMSO-d6) δ = 7.96-7.87(m, 4H),7,81 (s, 2H, HO-N), 7.63 (m, 1H), 7.51-7.49 (m, 1 H), 4.61 (s, 1 H), 1.36(s, 9H), 1.12-1.10 (ds, 12H), 0.29(s, 9H). 13C NMR (101 MHz, CDCl3) δ = 157.41, 150.44, 142.23, 141.72, 137.74, 137.13, 126.50, 125.97, 124.46, 122.58, 120.57, 104.73, 93.74, 90.70, 66.18, 39.52, 34.57, 31.29, 24.41, 17.15, -0.30. LC-MS (ESI +, *m/z*, %): 466.6 [M+H^{+}, 68], 488.6 [M+Na^{+}, 100], 504.6 [M+K^{+}, 10].

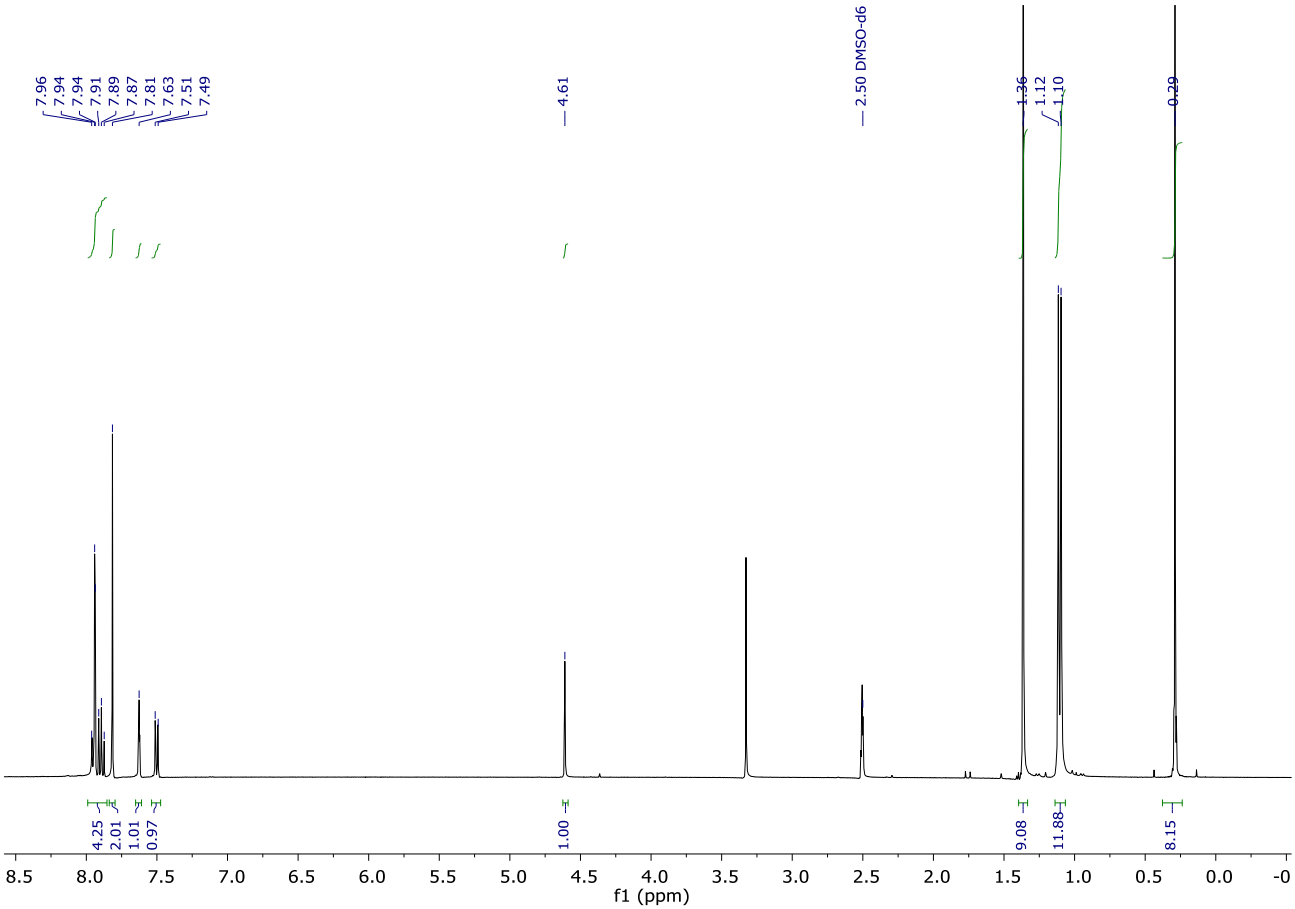

Figure 5.58 *^{1}H-NMR (400MHz) of **17b** in DMSO-d_6 at 298K.*

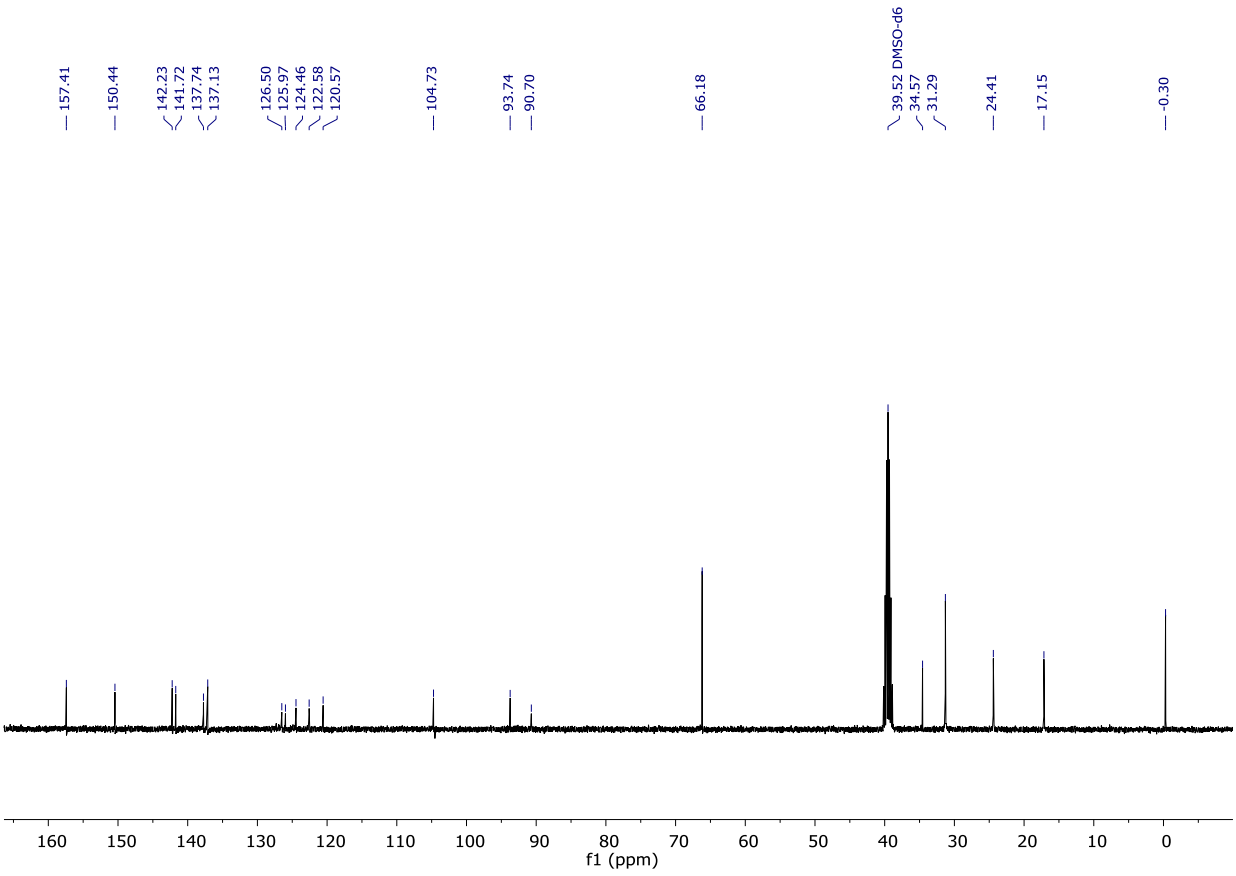

Figure 5.59 *^{13}C-NMR (101MHz) of **17b** in CD_3CN at 298K.*

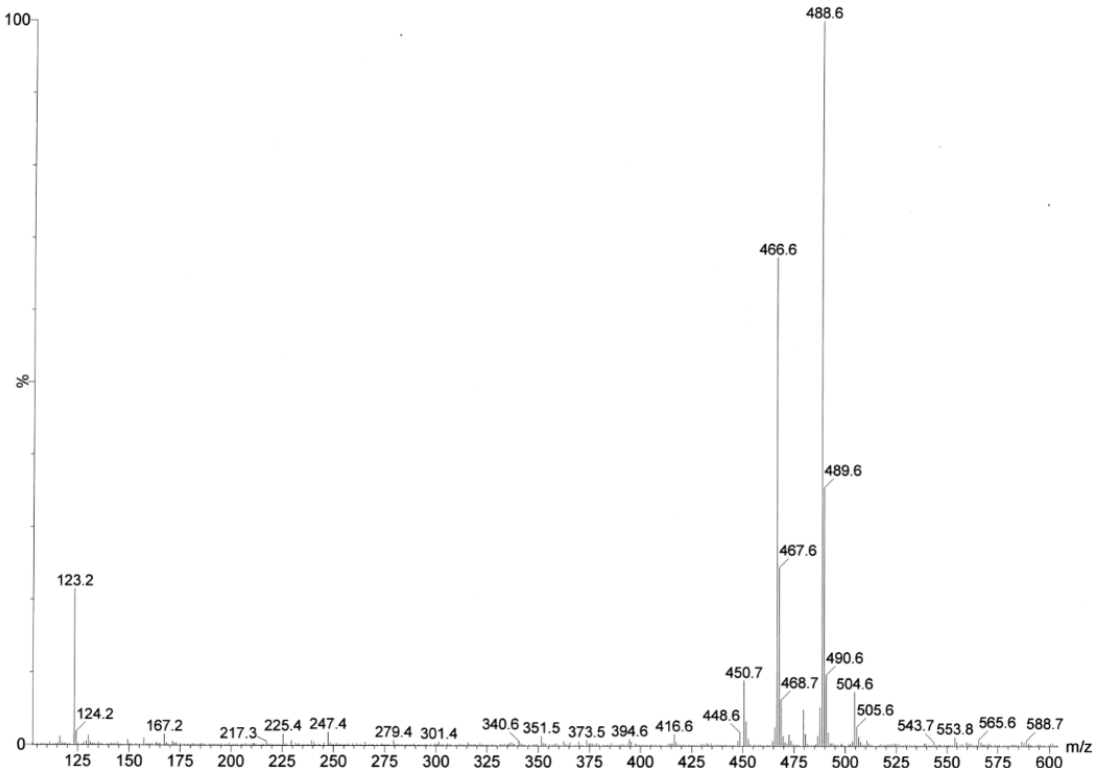

Figure 5.60 *Mass spectrum (ESI +) of* ***17b*** *in MeOH.*

Synthesis of 1-(4,4,5,5-tetramethyl-1-oxyl-3-oxide- imidazoline-2-yl) 3-(tert-butyl)-5-(6-((trimethynilsilyl)ethynyl)pyridin-2-yl)-benzene(17a):

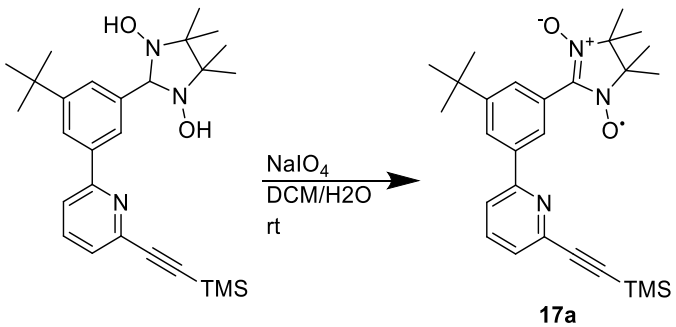

17a

Compound **17b** (32 mg, 0.0687 mmol) was dissolved in degassed DCM (5 mL) and then a solution of $NaIO_4$ (18.53 mg, 0.0859 mmol, 1.25 eq.) in degassed water (5 mL) was added dropwise over 25 min while vigorously stirring under N_2. The organic layer slowly turned deep blue and the mixture was left to stir for 1h. The progression of the reaction was monitored via TLC to monitor the disappearance of the starting material (Eluent: DCM/EtAc 98:2). The reaction mixture was the diluted with 15 mL of DCM and 15 mL of H_2O and the layers separated. The organic phase was then washed with distilled water (2x20 mL), brine (20 mL), dried over $MgSO_4$, filtered and the solvent removed *in vacuo*. The product was purified via column chromatography (SiO_2, Eluent DCM 100% then DCM/EtOAc 98:2) to yield radical **17a** as blue solid (21 mg, 66%). ESI-MS (+, *m/z*, %): 464 [$M+2H^+$, 100], 486 [$M+Na^+$, 90].

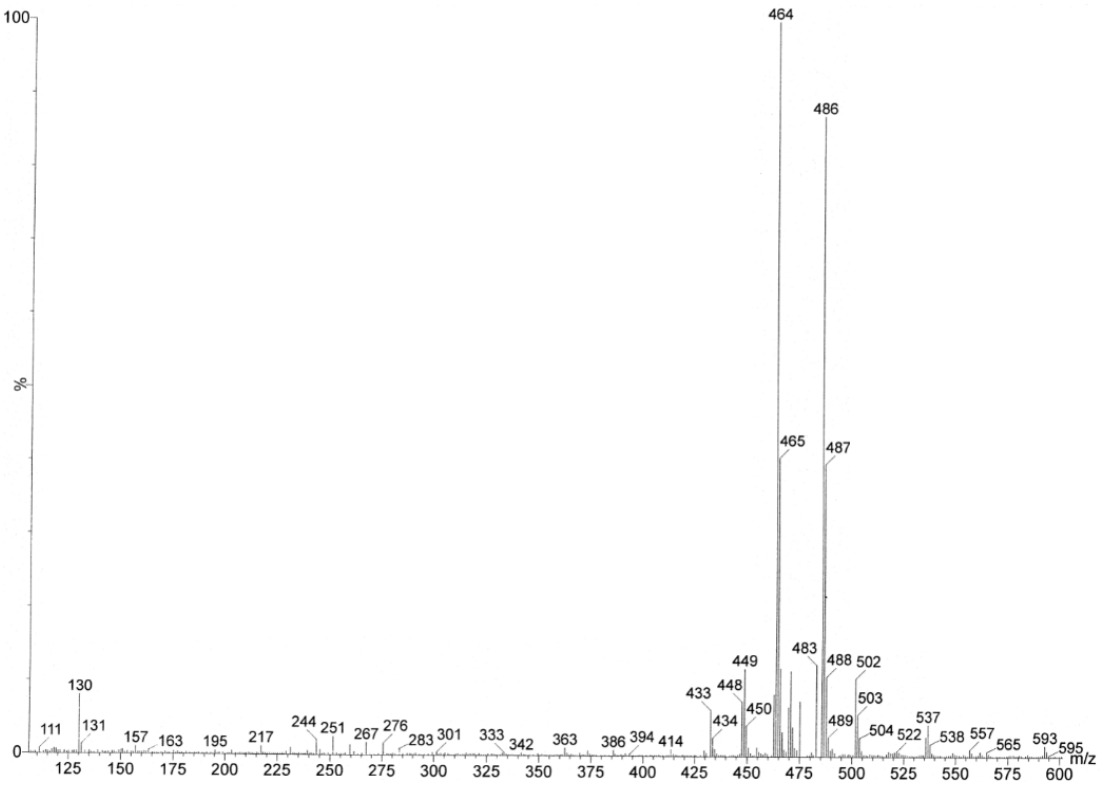

Figure 5.61 *Mass spectrum (ESI +) of compound* ***17a****.*

Synthesis of 1-(4,4,5,5-tetramethyl-1-oxyl-3-oxide- imidazoline-2-yl) 3-(tert-butyl)-5-(6-(ethynyl)pyridin-2-yl)-benzene(17):

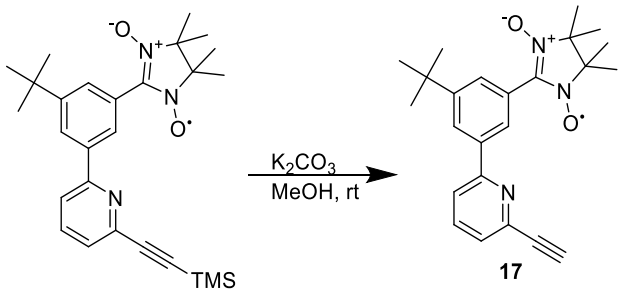

Radical **17a** (21 mg, 0.0454 mmol) was dissolved in degassed MeOH (1 mL) and K_2CO_3 (18 mg, 0.13 mmol, 3 eq.) was added. The reaction mixture was stirred overnight under nitrogen. After this time the suspension was filtered, MeOH removed *in vacuo* and re suspended in DCM (50 mL). The organic layer was washed with sat. $NaHCO_3$ (50mL), water (50 mL) and then brine (50 mL). the solution was dried on $MgSO_4$, filtered and the solvent removed *in vacuo*. Radical **14** was purified on silica gel chromatography (eluent: DCM then DCM/EtOAc 9:1) to yield radical **17** as a blue solid (17 mg, 98%). ESI-MS (+, *m/z*, %): 392 [$M+H^+$, 50], 414 [$M+Na^+$,100], 430 [$M+K^+$, 12].

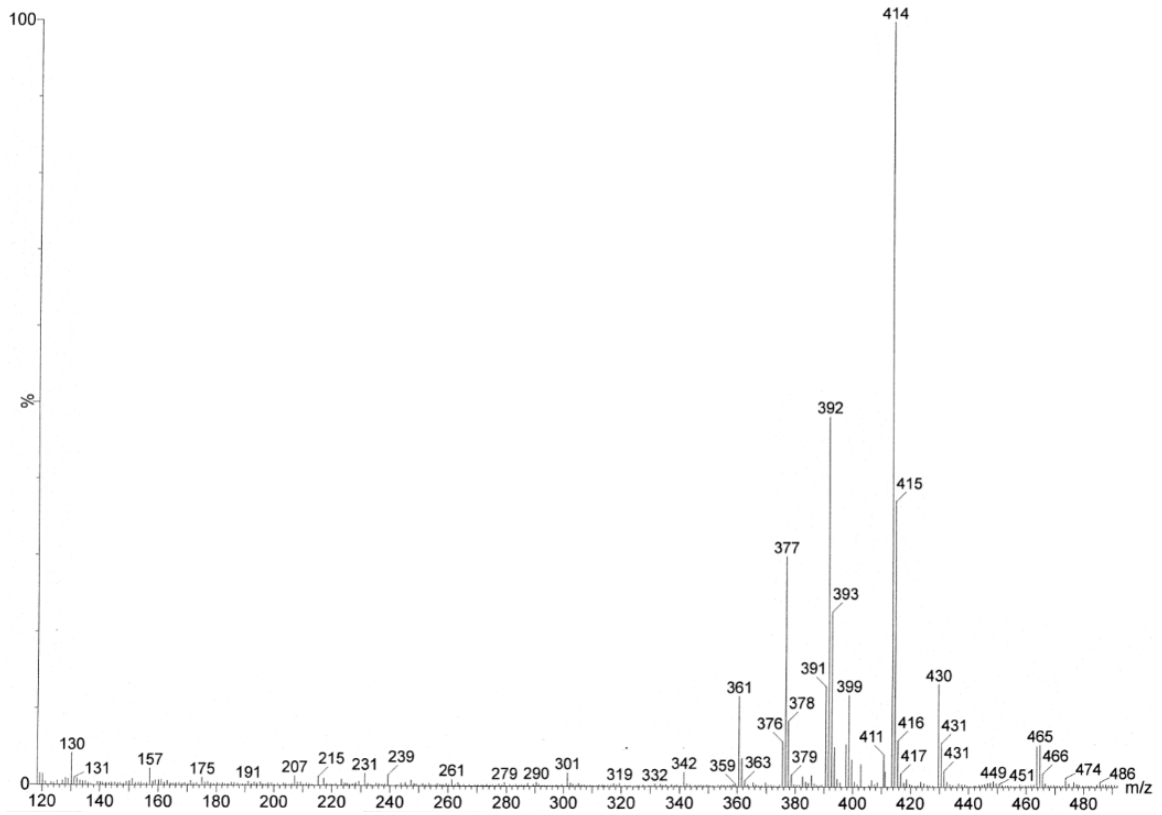

Figure 5.62 *Mass spectrum (ESI +) of compound* ***17****.*

Synthesis of rotaxane 9:

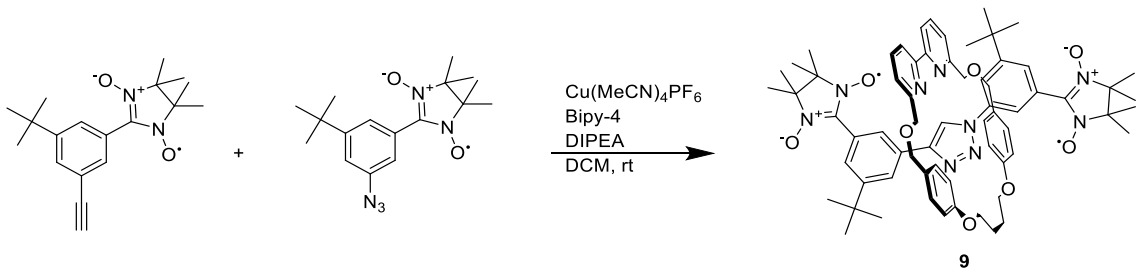

9

A solution of radicals **8** (21 mg, 0.0638 mmol) and **7** (20 mg, 0.0638 mmol, 1eq.) in degassed dry DCM (1mL) was transferred to a solution of $Cu(MeCN)_4PF_6$ (22.81mg, 0,0612 mmol, 0,96 eq.) and macrocycle **Bipy4** (30.80 mg, 0.0638 mmol, 1 eq.) in degassed dry DCM (1mL). DIPEA (22 µL, 0.127 mmol, 2 eq.) was added and the mixture stirred under N_2 for 18h. the progress of the reaction was monitored via TLC (Eluent DCM/EtOAc. 8:2). When the reaction was complete the mixture was diluted with 100 mL of DCM and Formic Acid (2 eq.) was added. The solution was stirred for 1h and then 100 mL of an $EDTA_{sat}/NH_3$ 17.5% solution was added. The bilayer mixture was stirred for an additional hour and then the layers were separated. The organic layer was washed with water (2x 100 mL), brine (100 mL) and dried over $MgSO_4$. Filtration and evaporation of the solvent led to a greenish solid that was purified via column chromatography (SiO_2, Eluent: DCM/EtOAc 9:1 then 8:2) to yield **9** as a blue solid (38 mg, 52%), ESI-MS (+, *m/z*, %): 1126.9 [$M+H^+$, 100], 1448.9 [$M+Na^+$, 5]. UV/Vis, λ/nm (ACN), (ε, $M^{-1}\times cm^{-1}$): 585 (852), 363 (17286).

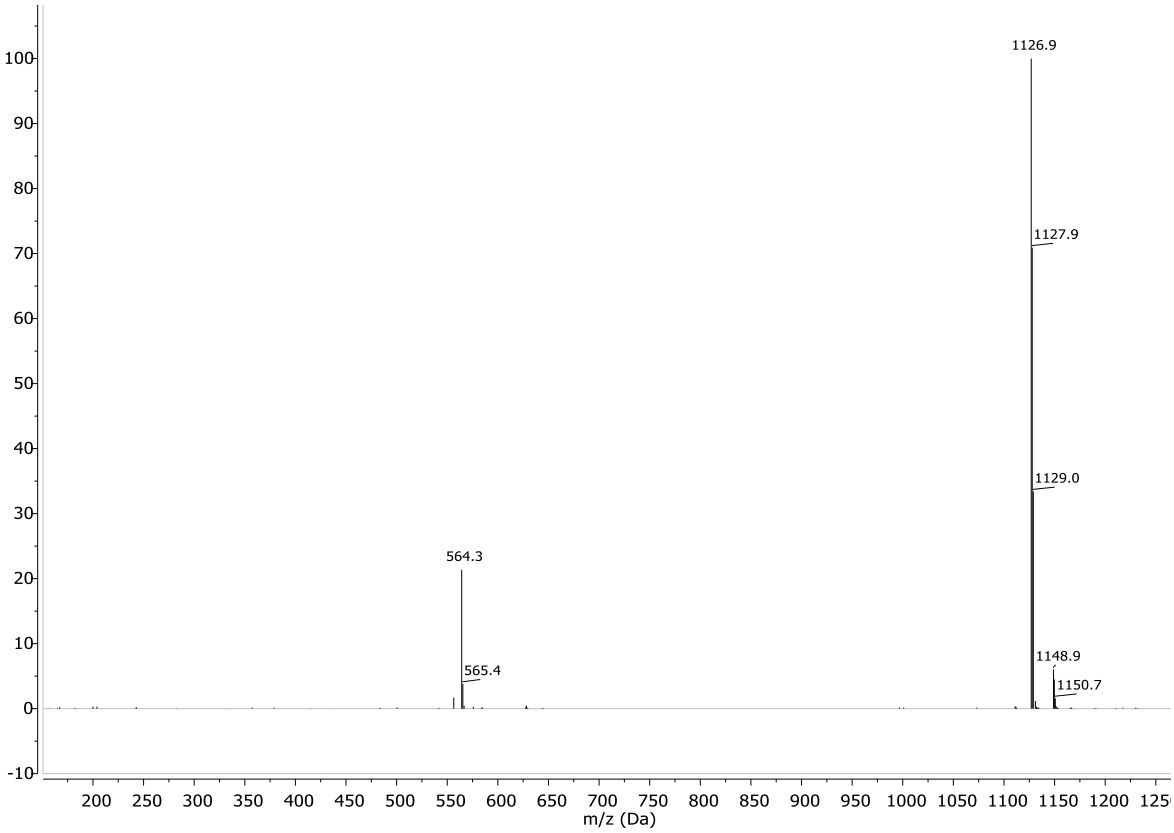

Figure 5.63 *Mass spectrum (ESI +) of Rotaxane* ***9*** *in MeOH.*

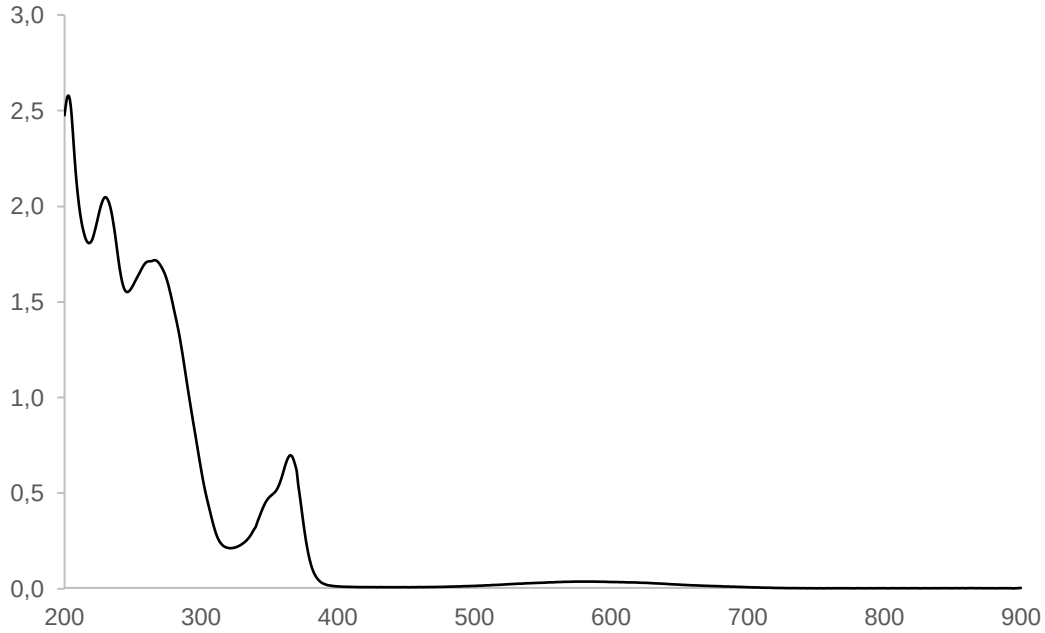

Figure 5.64 *UV-Vis spectra of rotaxane* ***9*** *in ACN.*

Synthesis of rotaxane 10:

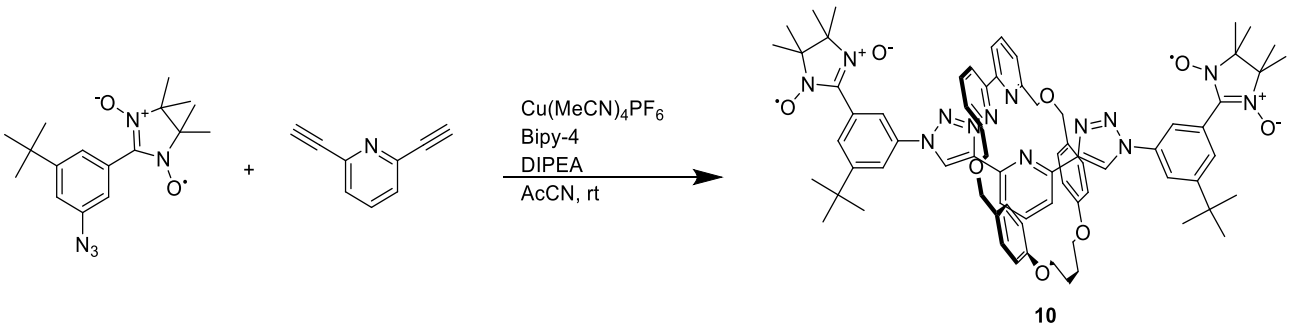

A solution of radical **7** (20 mg, 0.0605 mmol) and 2,6-diethynylpyridine (3.83 mg, 0.0302 mmol, 1eq.) in degassed dry AcCN (1mL) was transferred to a solution of $Cu(MeCN)_4PF_6$ (10.8 mg, 0.0290 mmol, 0.96 eq.) and macrocycle **Bipy4** (14.57 mg, 0.0302 mmol, 1 eq.) in degassed dry AcCN (1 mL). DIPEA (11 µL, 0.0605 mmol, 2 eq.) was added and the mixture stirred under N_2 for 18h. the progress of the reaction was monitored via TLC (Eluent DCM/EtOAc. 8:2). When the reaction was complete the mixture was diluted with 100 mL of DCM and 100 mL of an $EDTA_{sat}/NH_3$ 17,5% solution was added. The bilayer mixture was stirred for an additional hour and then the layers were separated. The organic layer was washed with water (2x 100 mL), brine (100 mL) and dried over $MgSO_4$. Filtration and evaporation of the solvent led to a greenish solid that was purified via column chromatography (SiO_2, Eluent: DCM/EtAc 9:1, 8:2 and 7:3) to yield **10** as a blue solid (32 mg, 82%). ESI-MS (+, *m/z*, %): 1272.1 [$M+2H^+$, 60], 1293.1 [$M+Na^+$, 8]. UV/Vis (ACN), λ/nm (ε, $M^{-1}\times cm^{-1}$): 815 (581), 366 (22137).

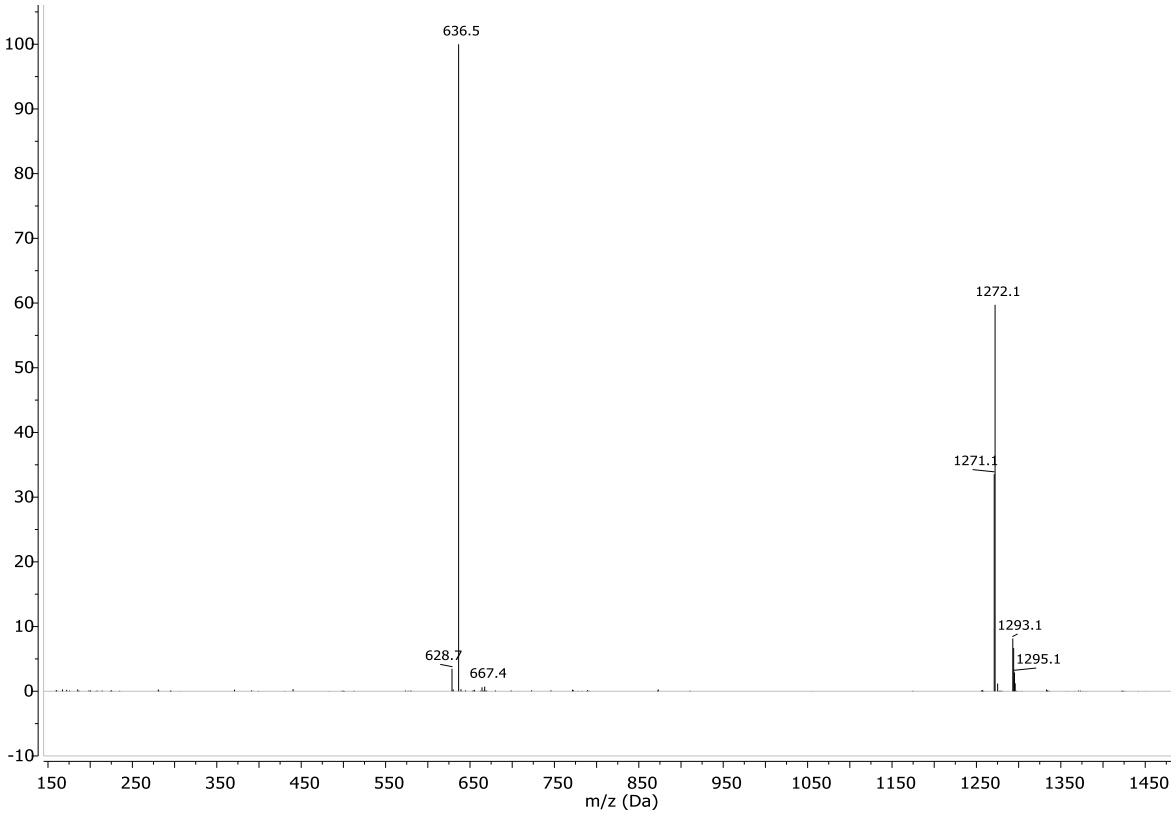

Figure 5.65 *Mass spectrum (ESI +) of Rotaxane* ***10.***

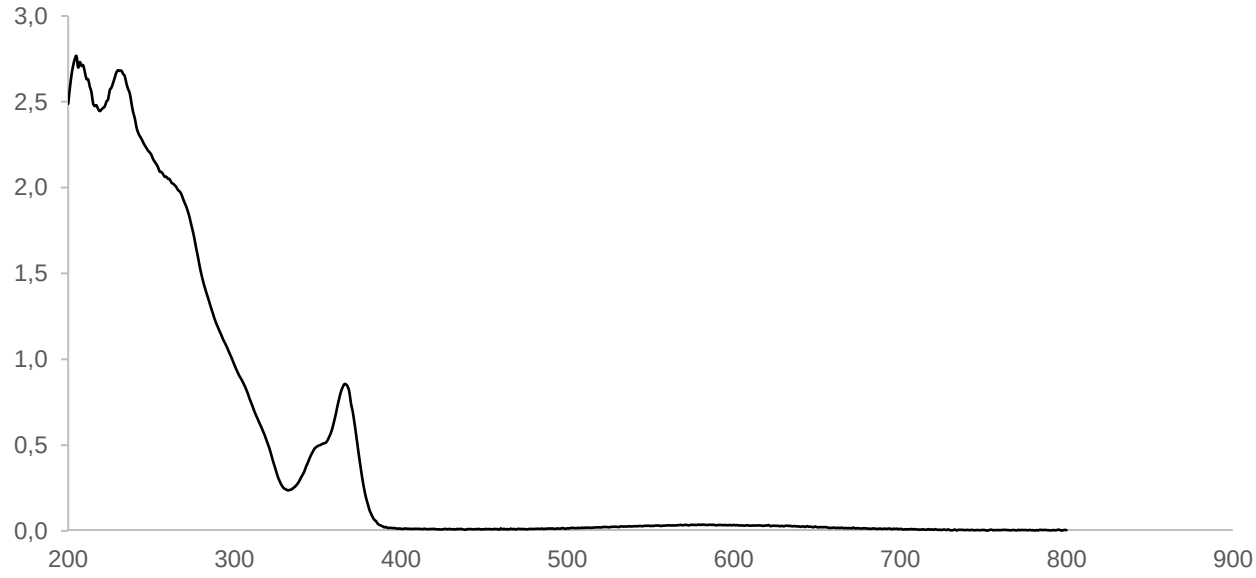

Figure 5.66 *UV-Vis spectra of rotaxane* ***10*** *in ACN.*

Synthesis of rotaxane 13:

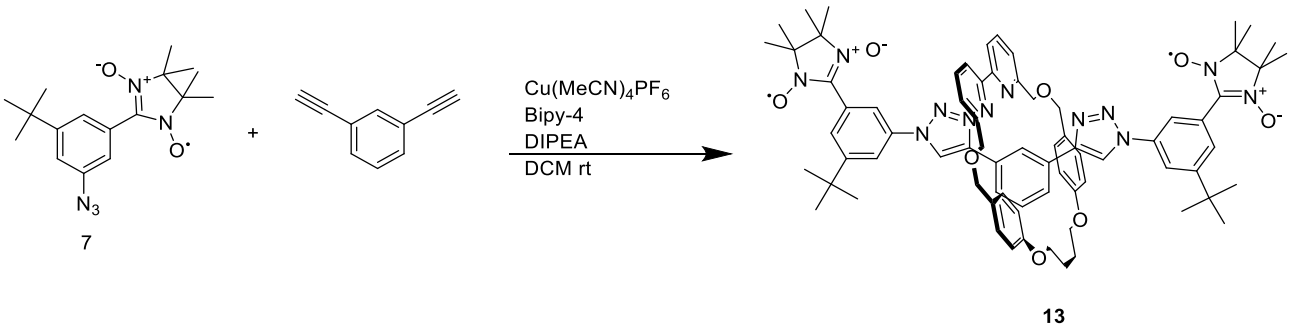

A solution of radical **7** (20 mg, 0,0605 mmol. 2 eq.) and 2,6-diethynylbenzene (3,81 mg, 0,0302 mmol, 1eq.) in degassed dry DCM (1mL) was transferred to a solution of $Cu(MeCN)_4PF_6$ (10,8 mg, 0,0290 mmol, 0,96 eq.) and macrocycle Bipy4 (14.57 mg, 0.0302 mmol, 1 eq.) in degassed dry DCM (1 mL). DIPEA (11 µL, 0.0605 mmol, 2 eq.) was added and the mixture stirred under N_2 for 72h. the progress of the reaction was monitored via TLC (Eluent DCM/EtOAc. 8:2). When the reaction was complete the mixture was diluted with 100 mL of DCM and 100 mL of an $EDTA_{sat}/NH_3$ 17,5% solution was added. The bilayer mixture was stirred for an additional hour and then the layers were separated. The organic layer was washed with water (2x 100 mL), brine (100 mL) and dried over $MgSO_4$. Filtration and evaporation of the solvent led to a greenish solid that was purified via column chromatography (SiO_2, Eluent: DCM/EtAc 9:1 and 7:3) to yield **13** as a blue solid (10 mg, 26%). ESI-MS (+, *m/z*, %): 1292 [$M+Na^+$, 100], UV/Vis (ACN), λ/nm (ε, $M^{-1}\times cm^{-1}$): 579 (680), 366 (18146).

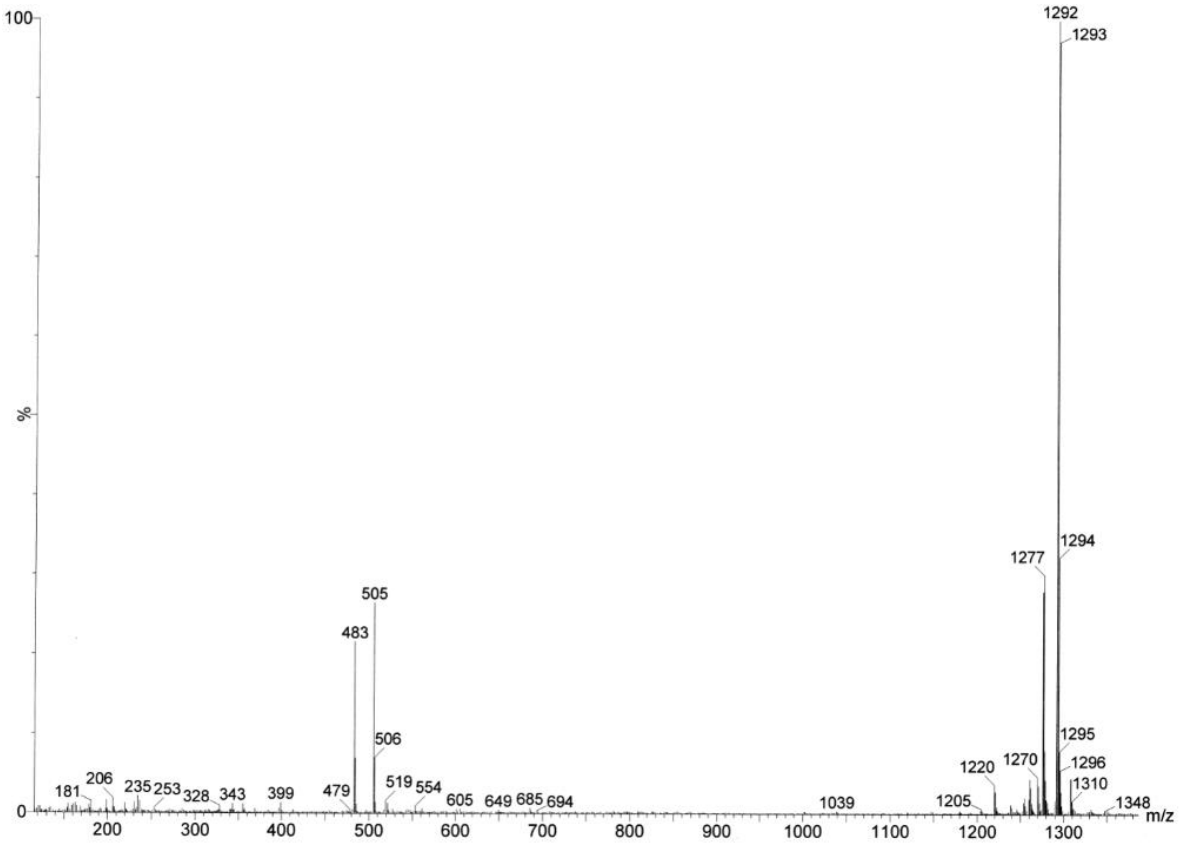

Figure 5.67 *Mass spectrum (ESI +) of rotaxane* ***13****.*

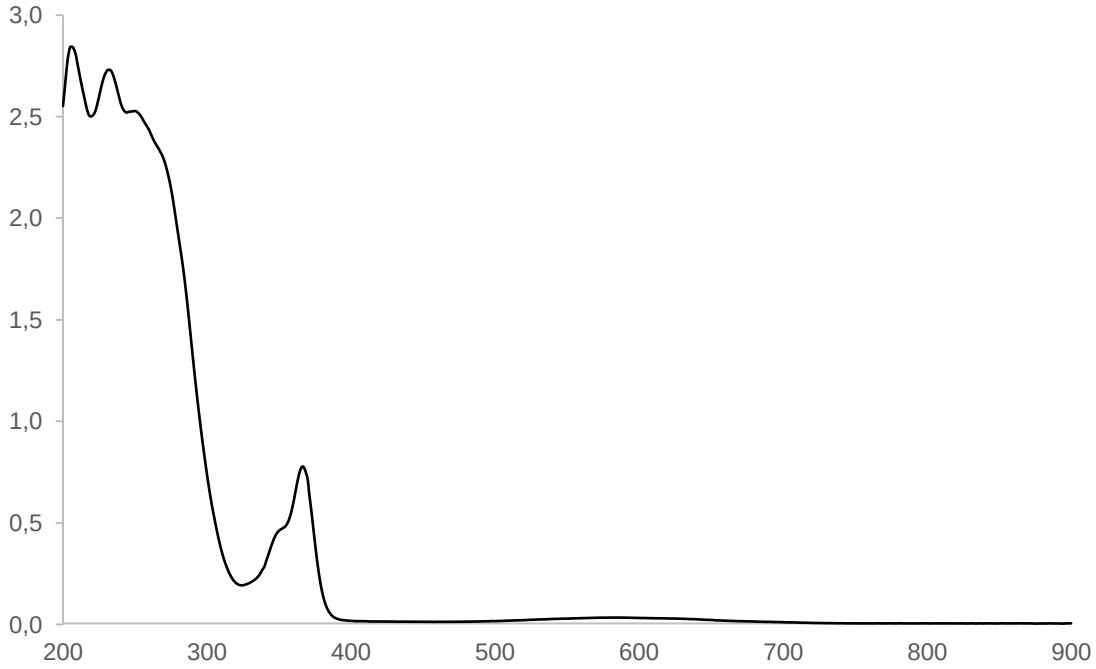

Figure 5.68 *UV-Vis spectra of rotaxane 13 in ACN.*

Synthesis of 19:

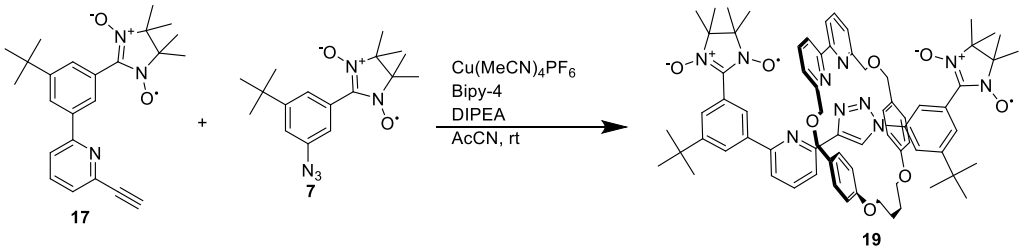

A solution of radical **17** (7 mg, 0,0179 mmol) and **7** (5.92 mg, 0,0179 mmol, 1eq.) in degassed dry ACN (0.5 mL) was transferred to a solution of $Cu(MeCN)_4PF_6$ (6.40 mg, 0.0172 mmol, 0,96 eq) and macrocycle Bipy4 (8.63mg, 0.0179 mmol, 1 eq) in degassed dry AcCN (0.5 mL). DIPEA (7 µL, 0.0358 mmol, 2 eq) was added and the mixture stirred under N_2 for 18h. the progress of the reaction was monitored via TLC (Eluent DCM/EtOAc. 9:1). When the reaction was complete the mixture was diluted with 25 mL of DCM and 25 mL of an $EDTA_{sat}/NH_3$ 17,5% solution was added. The bilayer mixture was stirred for an additional hour and then the layers were separated. The organic layer was washed with water (2x 25 mL), brine (25 mL) and dried over $MgSO_4$. Filtration and evaporation of the solvent led to a greenish solid that was purified via column chromatography (SiO_2, Eluent: DCM/EtAc 9:1 then 8:2) to yield **19** as a blue solid (18 mg, 85%). ESI-MS (+, *m/z*, %): 1204 [$M+H^+$, 65], 1226 [$M+Na^+$, 100]. UV/Vis, λ/nm (ACN), (ε, $M^{-1}\times cm^{-1}$): 589 (813), 365 (17383).

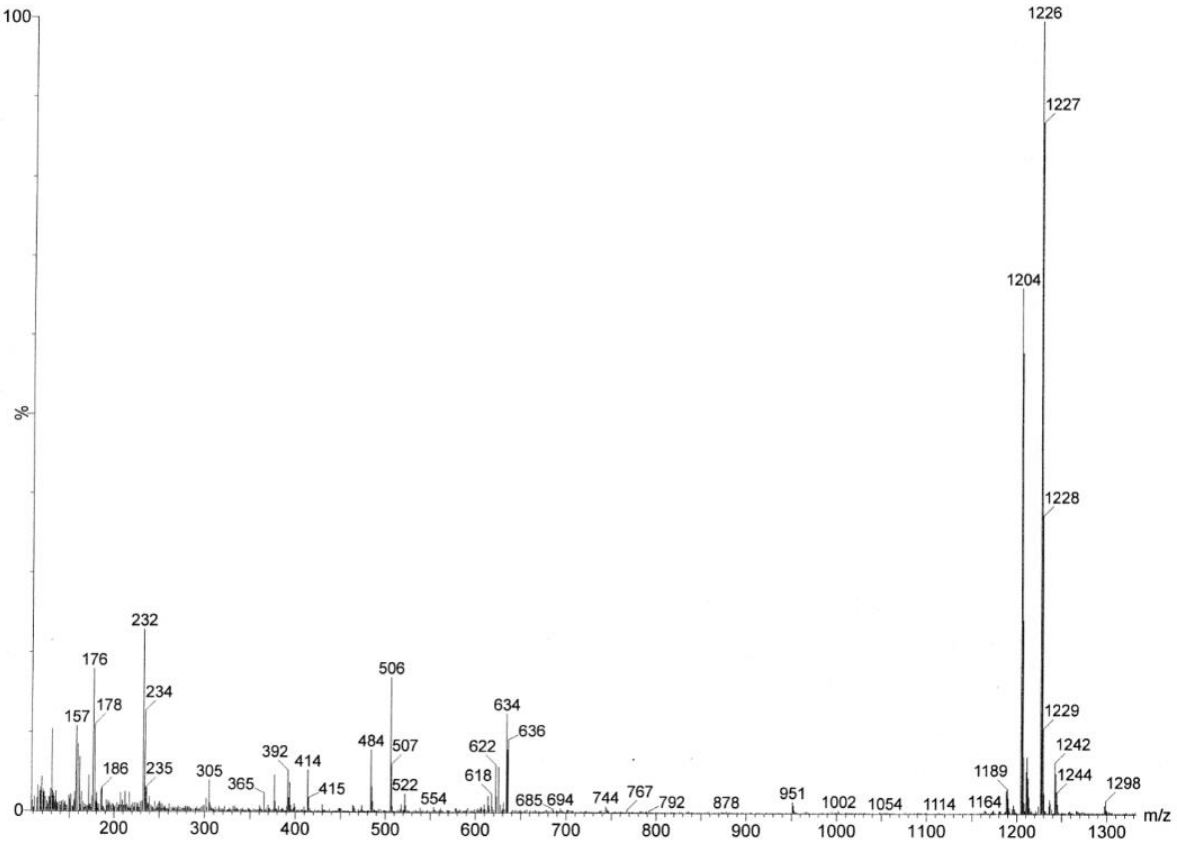

Figure 5.69 *Mass spectrum (ESI +) of rotaxane* ***19*** *recorded in MeOH.*

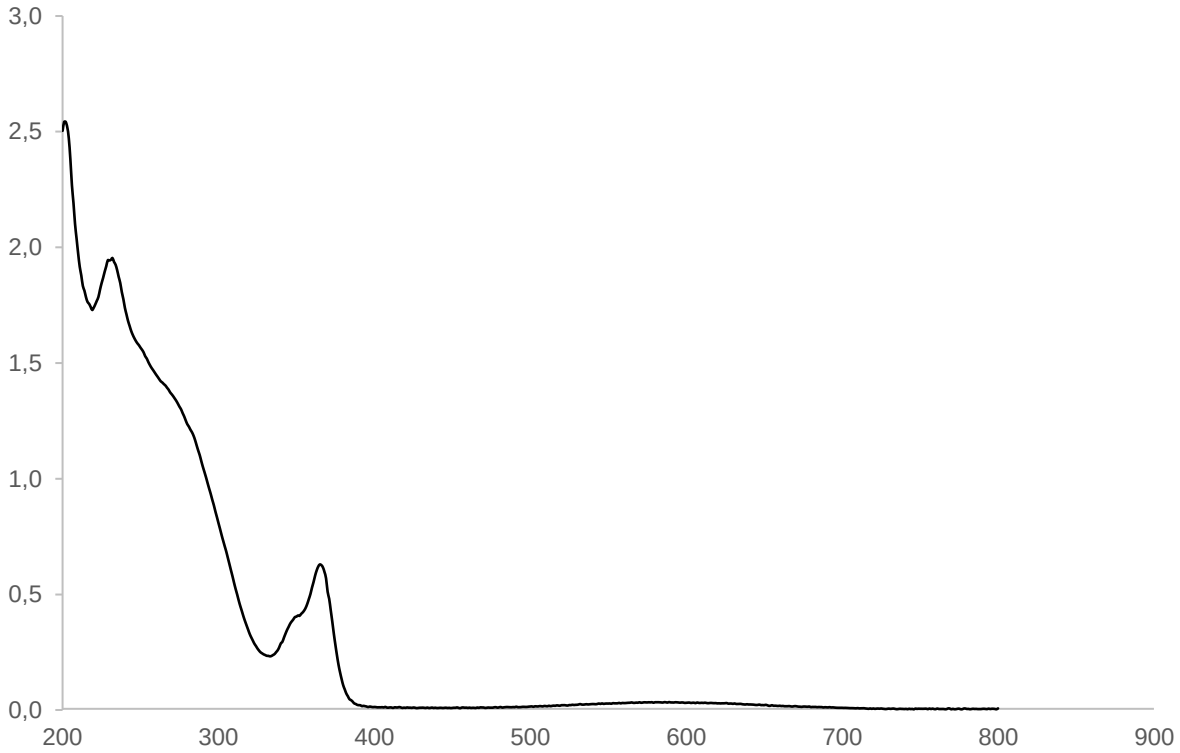

Figure 5.70 *UV-Vis spectra of rotaxane* ***19*** *in ACN.*

Synthesis of Thread 12:

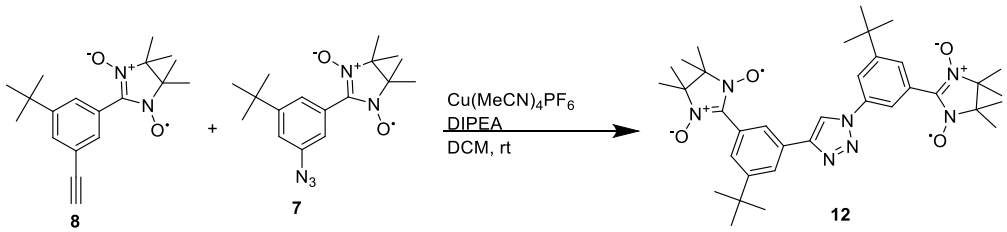

To a solution of radical **7** (10 mg, 0.0302 mmol) and radical **8** (9.48 mg, 0.0302 mmol, 1eq.) in degassed dry DCM (2mL) was added $Cu(MeCN)_4PF_6$ (10,80 mg, 0,0290 mmol, 1 eq.) and DIPEA (11 µL, 0.0605 mmol, 2 eq.). The mixture stirred under N_2 for 18h. The mixture was then diluted with 25mL of DCM and 25 mL of an $EDTA_{sat}/NH_3$ 17.5% solution was added. The bilayer mixture was stirred for an additional hour and then the layers were separated. The organic layer was washed with water (2x 25 mL), brine (25 mL) and dried over $MgSO_4$. Filtration and evaporation of the solvent led to a greenish solid that was purified via column chromatography (SiO_2, Eluent: DCM/EtOAc 7:3) to yield 12 as a blue solid (17 mg, 87%). ESI-MS (+, *m/z*, %): 644.7 [$M+H^+$, 100], 667,8 [$M+ Na^+$, 10]. UV/Vis, λ/nm (ACN), (ε, $M^{-1}\times cm^{-1}$): 581 (816), 266 (25737).

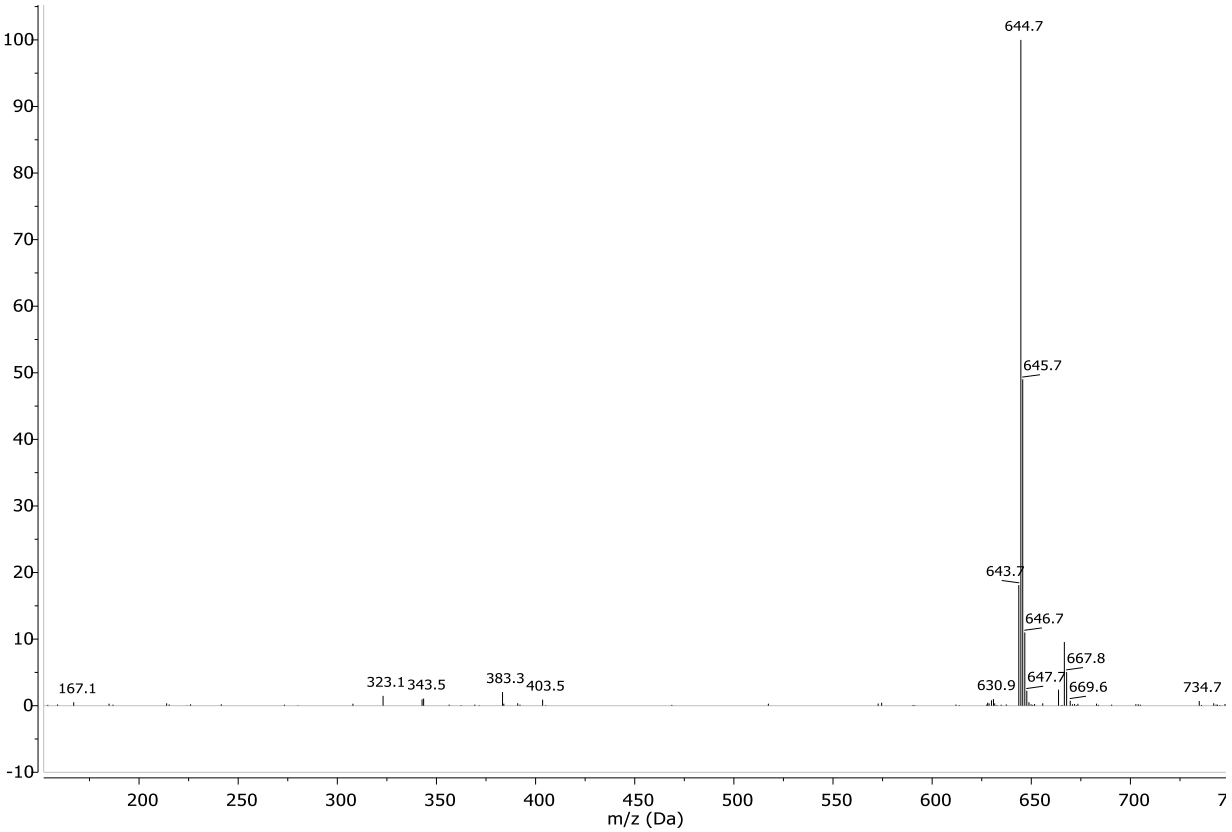

Figure 5.71 *Mass spectrum (ESI +) of thread* ***12*** *recorded in MeOH.*

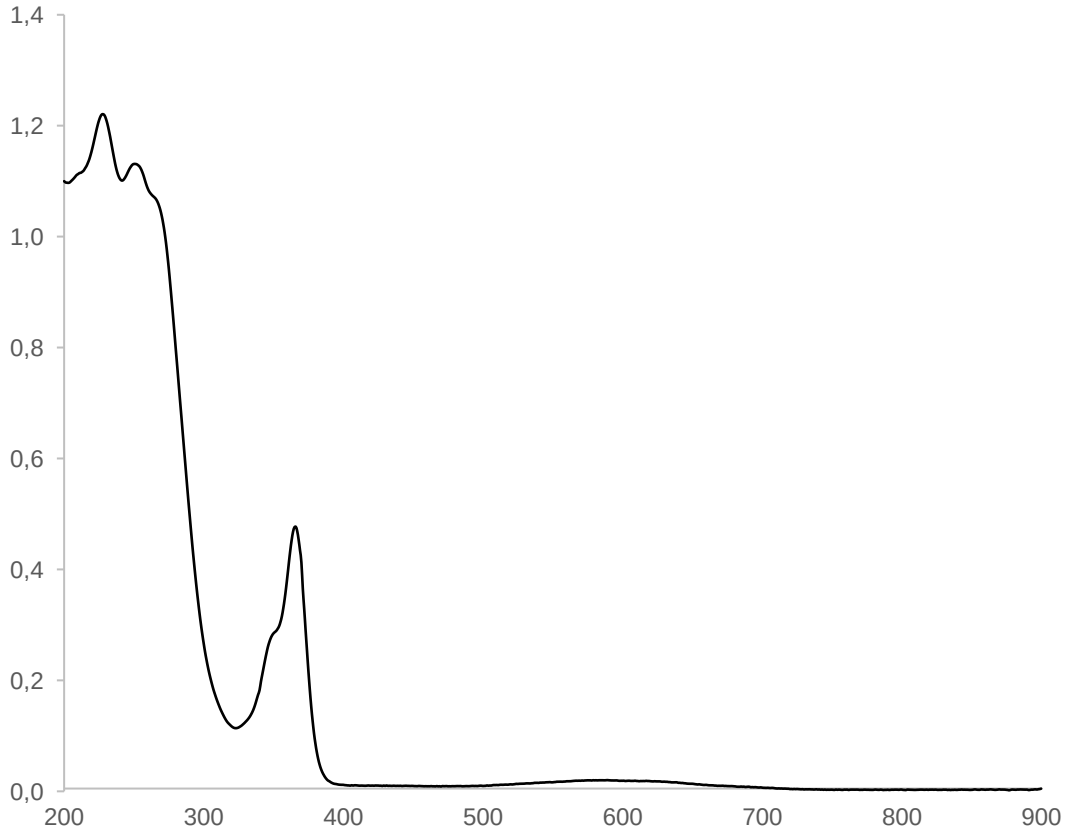

Figure 5.72 *UV-Vis spectra of thread* ***12*** *in ACN.*

Synthesis of Thread 11:

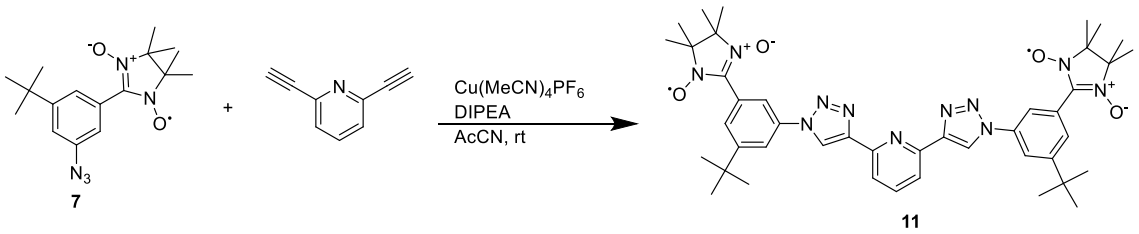

To a solution of radical **7** (20 mg, 0.0605 mmol) and 2,6-diethynylpyridine (3.84 mg, 0.0302 mmol, 1eq.) in degassed dry ACN (2mL) was added $Cu(MeCN)_4PF_6$ (11.27.8 mg, 0.03026 mmol, 1 eq) and DIPEA (11 µL, 0.0605 mmol, 2 eq). The mixture stirred under N_2 for 18h. The mixture was then diluted with 25mL of DCM and 25 mL of an $EDTA_{sat}/NH_3$ 17.5% solution was added. The bilayer mixture was stirred for an additional hour and then the layers were separated. The organic layer was washed with water (2x 25 mL), brine (25 mL) and dried over $MgSO_4$. Filtration and evaporation of the solvent led to a greenish solid that was purified via column chromatography (SiO_2, Eluent: DCM/EtOAc 7:3) to yield **11** as a blue solid (16 mg, 67%). ESI-MS (+, *m/z*, %): 788.7 [$M+H^+$, 100], 810.8 [$M+Na^+$, 25]. UV/Vis, λ/nm (ACN), (ε, $M^{-1}\times cm^{-1}$): 588 (579), 266 (17583).

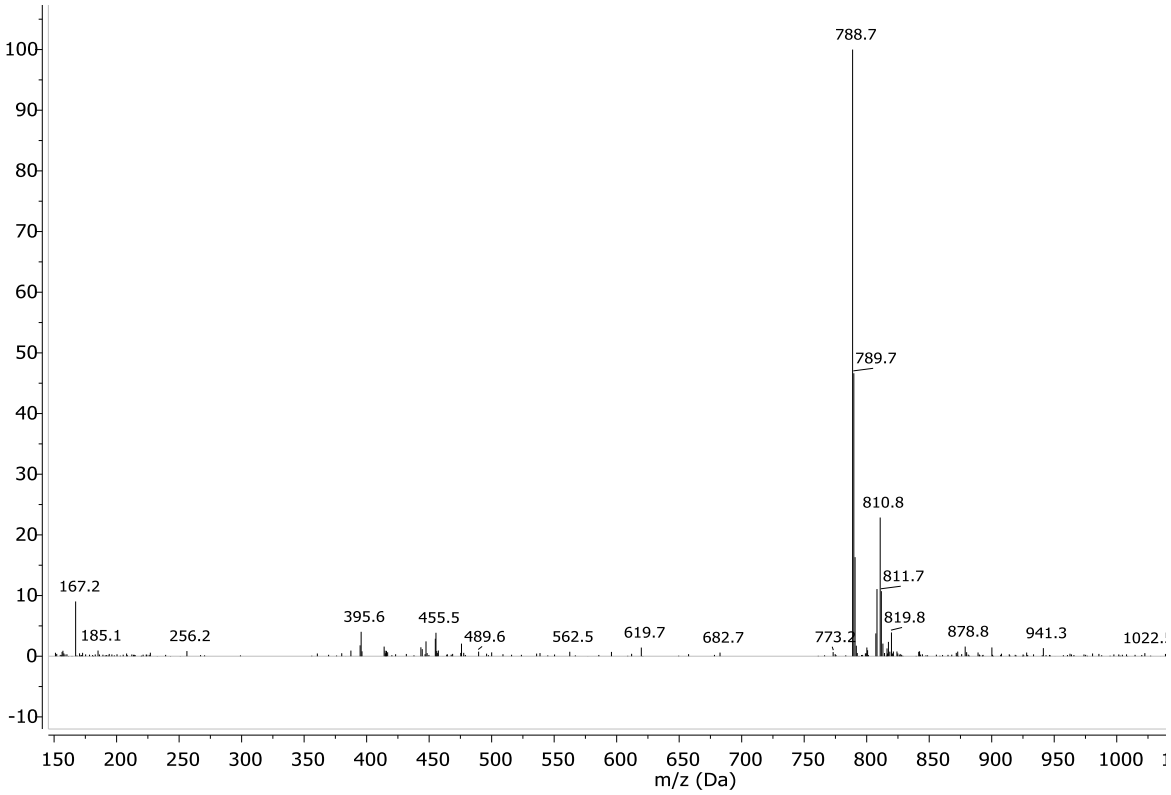

Figure 5.73 *Mass spectrum (ESI +) of thread* ***11*** *recorded in MeOH.*

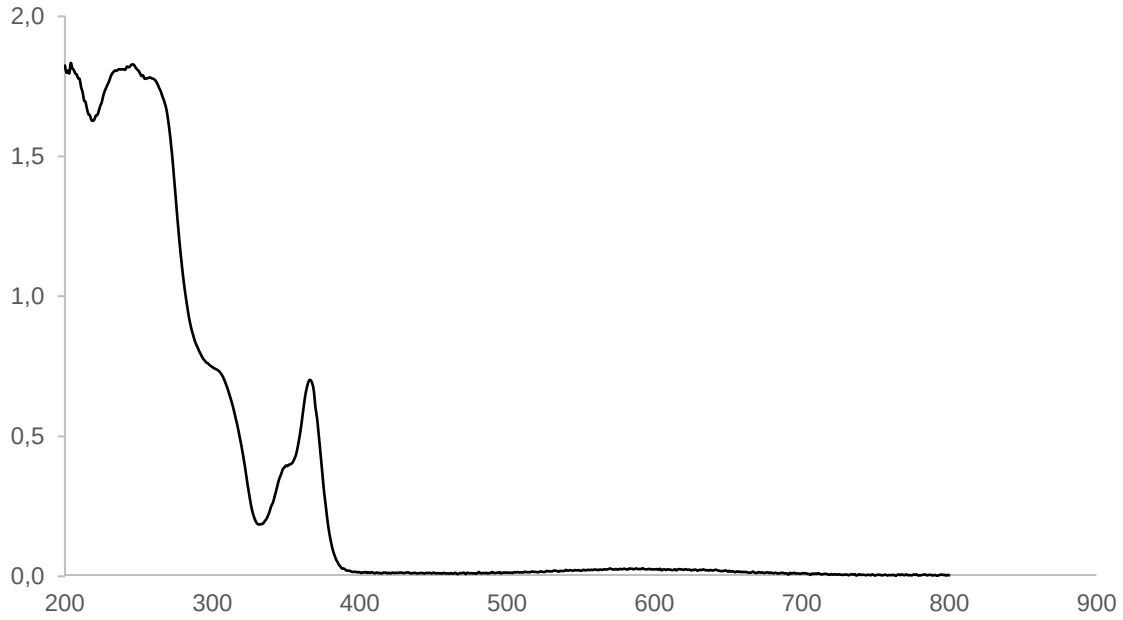

Figure 5.74 *UV-Vis spectra of thread* ***11*** *in ACN.*

Synthesis of Thread 14:

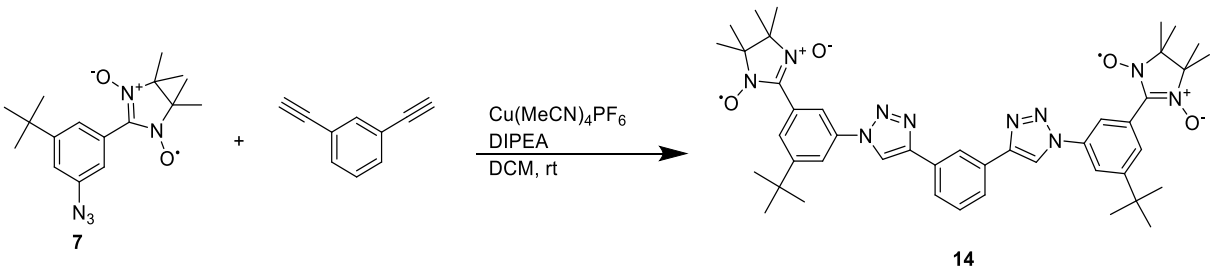

To a solution of radical **7** (20 mg, 0.0605 mmol) and 2,6-diethynylbenzene (3.81 mg, 0.0302 mmol, 1eq) in degassed dry DCM (2mL) was added $Cu(MeCN)_4PF_6$ (11.27 mg, 0.0302 mmol, 1 eq) and DIPEA (11 µL, 0.0605 mmol, 2 eq.). The mixture stirred under N_2 for 18h. The mixture was then diluted with 25mL of DCM and 25 mL of an $EDTA_{sat}/NH_3$ 17.5% solution was added. The bilayer mixture was stirred for an additional hour and then the layers were separated. The organic layer was washed with water (2x 25 mL), brine (25 mL) and dried over $MgSO_4$. Filtration and evaporation of the solvent led to a greenish solid that was purified via column chromatography (SiO_2, Eluent: DCM/EtOAc 8:2) to yield **14** as a blue solid (10 mg, 42%). ESI-MS (+, *m/z*, %): 810 [$M+Na^+$, 100]. UV/Vis, λ/nm (ACN), (ε, $M^{-1}\times cm^{-1}$): 586 (736), 366 (20739).

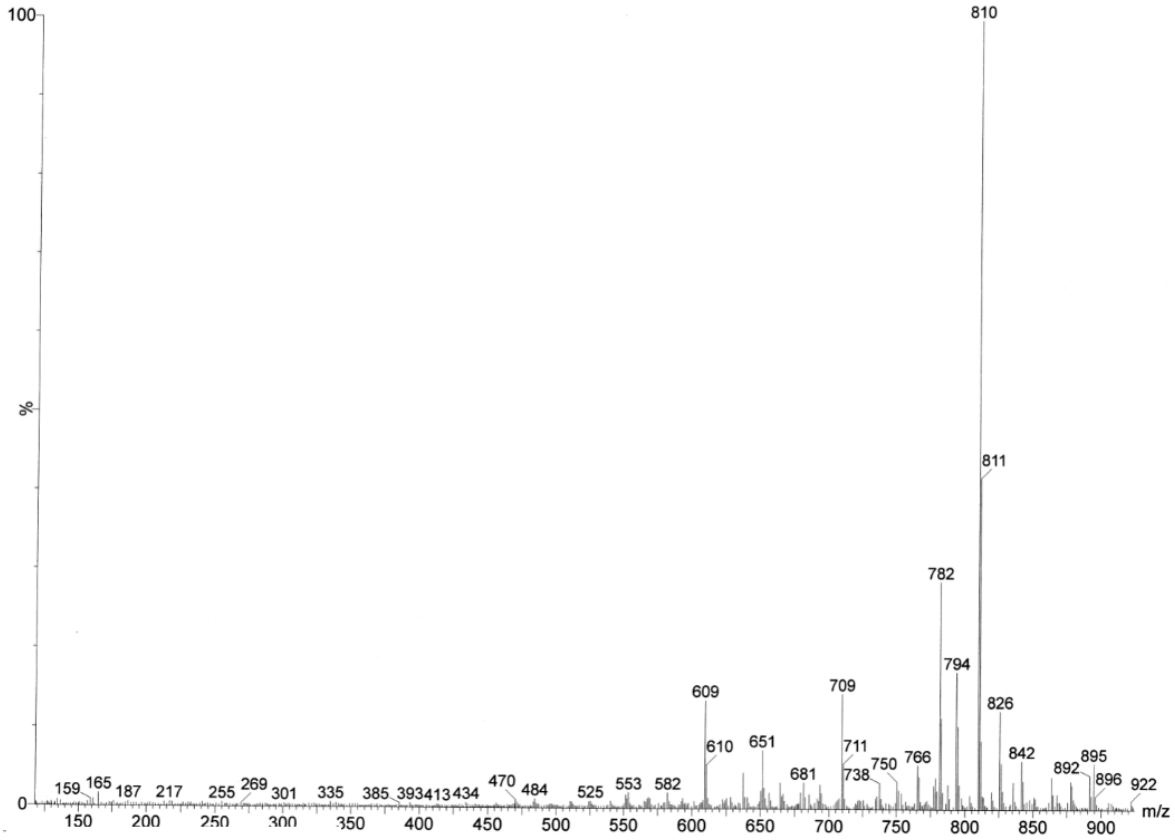

Figure 5.75 *Mass spectrum (ESI +) of thread* ***14*** *recorded in MeOH.*

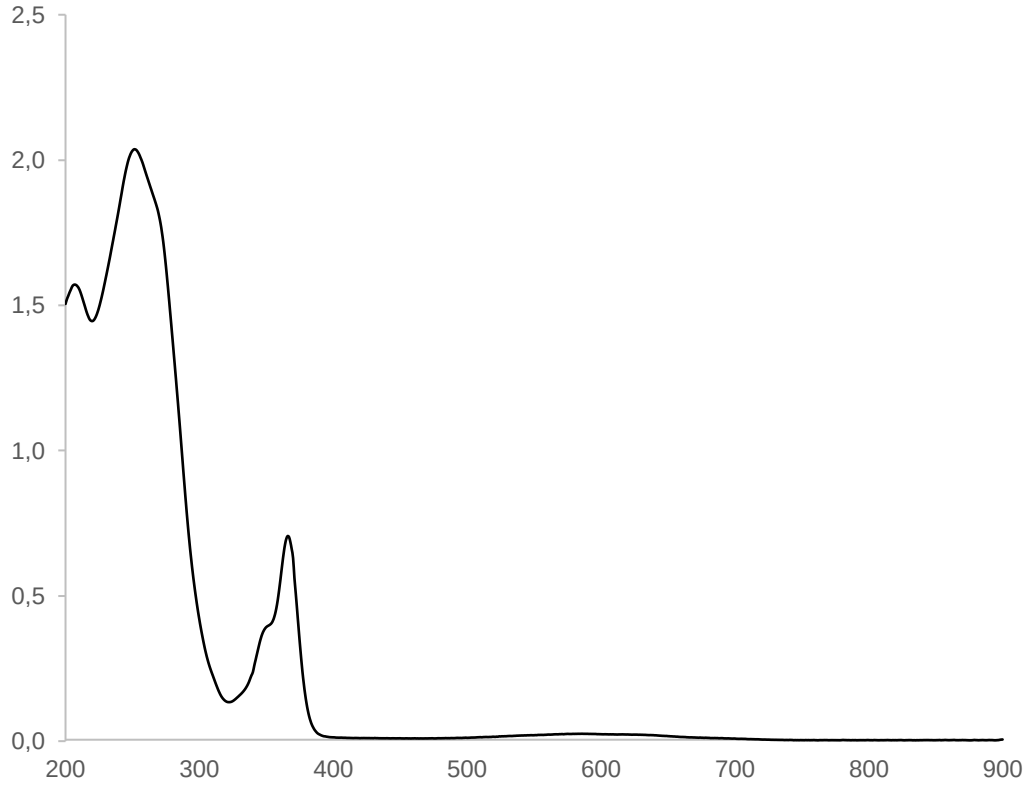

Figure 5.76 *UV-Vis spectra of thread* ***14*** *in ACN.*

Synthesis of 20:

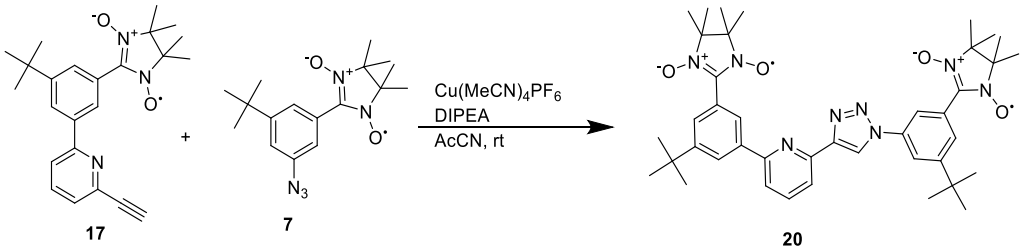

To a solution of radical **17** (7 mg, 0.0179 mmol) and **7** (5.92 mg, 0.0179 mmol, 1eq.) in degassed dry ACN (1 mL) was added $Cu(MeCN)_4PF_6$ (6.67 mg, 0.0179 mmol, 1 eq.) and DIPEA (7 µL, 0.0358 mmol, 2 eq.). The mixture stirred under N_2 for 18h. The mixture was then diluted with 25mL of DCM and 25 mL of an $EDTA_{sat}/NH_3$ 17.5% solution was added. The bilayer mixture was stirred for an additional hour and then the layers were separated. The organic layer was washed with water (2x 25 mL), brine (25 mL) and dried over $MgSO_4$. Filtration and evaporation of the solvent led to a greenish solid that was purified via column chromatography (SiO_2, Eluent: DCM/EtOAc 8:2) to yield **20** as a blue solid (10.4 mg, 80%). ESI-MS (+, *m/z*, %): 722 [$M+H^+$], 744 [$M+Na^+$, 100]. UV/Vis, λ/nm (ACN), (ε, $M^{-1}\times cm^{-1}$): 590 (845), 366 (18270).

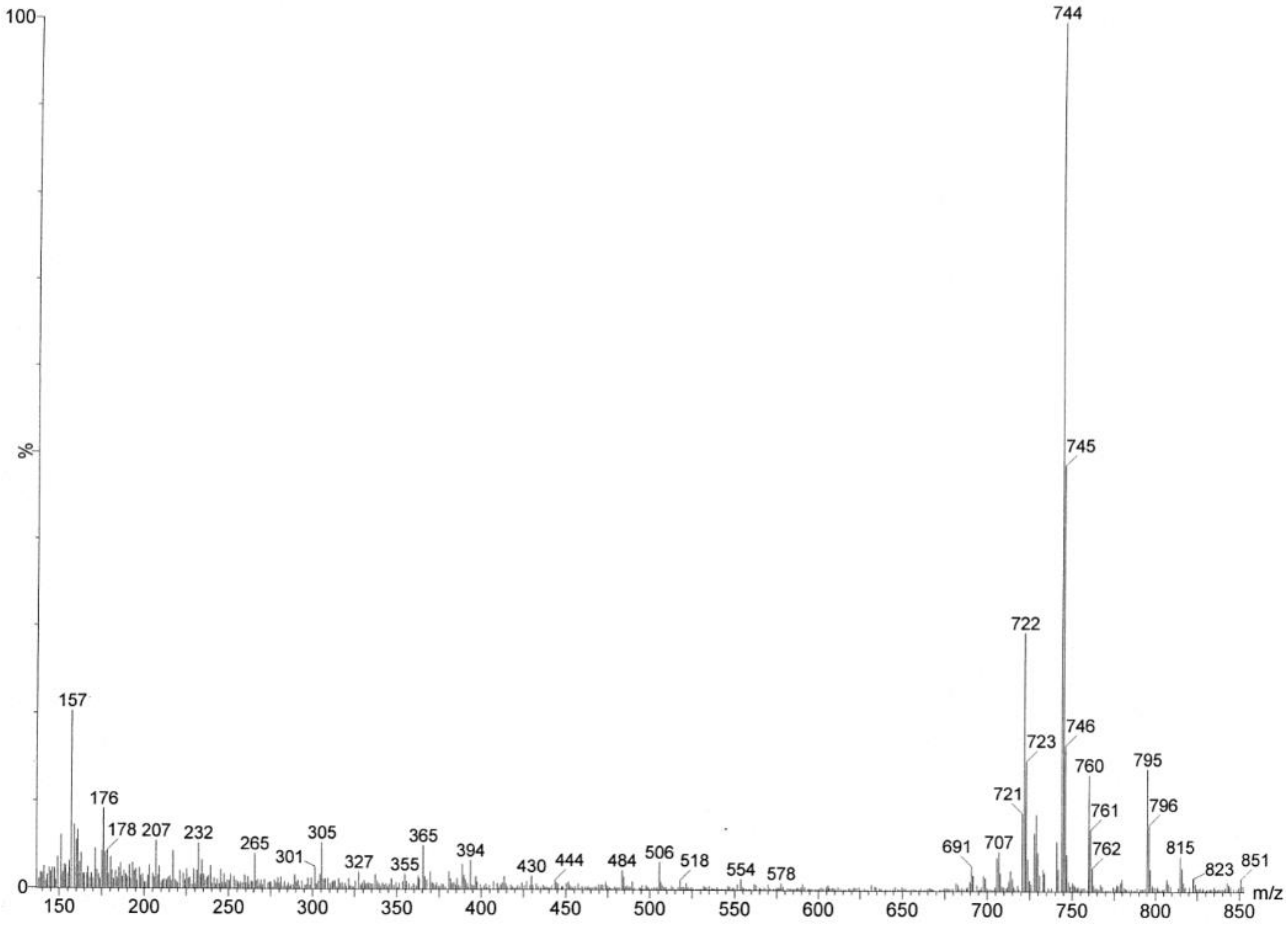

Figure 5.77 *Mass spectrum (ESI +) of thread* ***20*** *recorded in MeOH.*

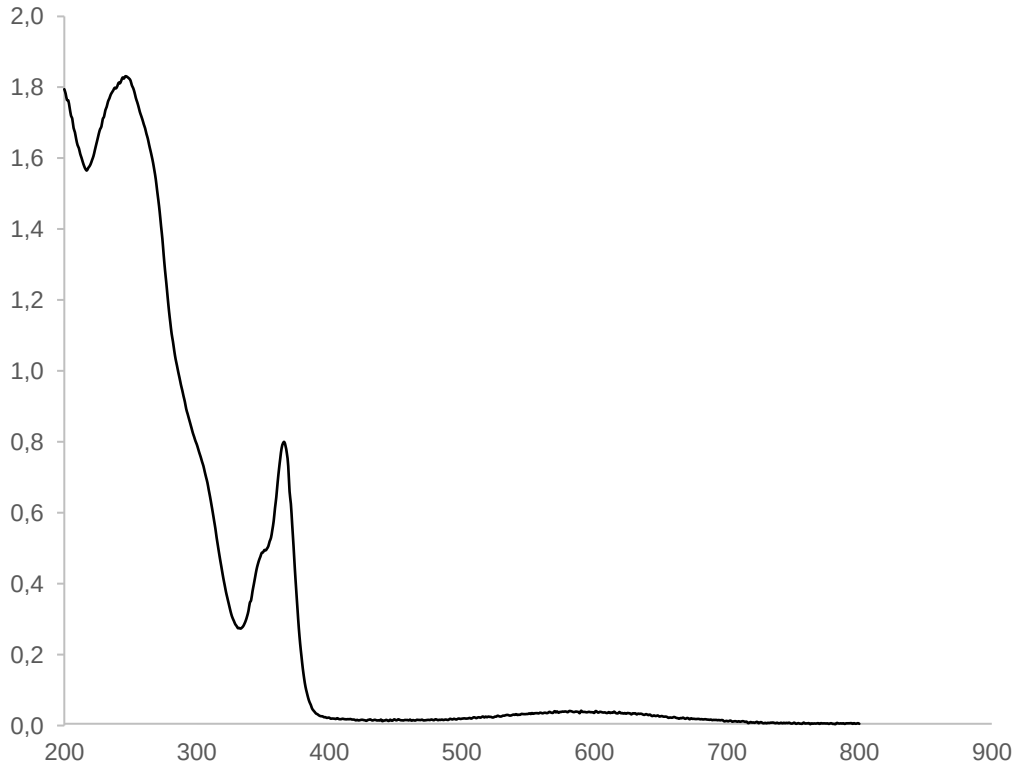

Figure 5.78 *UV-Vis spectra of thread* ***20*** *in ACN.*

5.5 References

1 O.Dumele, N. Trapp and F. Diederich, *Angew. Chem. Int. Ed.*, 2015, **54**: 12339-12344.

2 D. Liu, D. Wang, M. Wang, Y. Zheng, K. Koynov, G. K. Auernhammer, H-J. Butt and T. Ikeda, *Macromolecules*, 2013, **46**, 4617−4625.

3 P. R. Ashton, R. Ballardini, V. Balzani, I. Baxter, A. Credi, M. C. T. Fyfe, M. T. Gandolfi, M. Gomez-Lopez, M.-V. Martınez-Diaz, A. Piersanti, N. Spencer, J. F. Stoddart, M. Venturi, A. J. P. White and D. J. Williams, *J. Am. Chem. Soc.*, 1998, **120**, 11932 – 11942.

4 PHENEX PHARMACEUTICALS AG; C. Gege, C. Steeneck, O. Kinzel, G. Kleymann, T. Hoffmann, WO2013/178362, 2013, A1.

5 Q. Li, F. Huang, Y. Fan, Y. Wang, Li, Y. He, and H. Jiang, *Eur. J. Inorg. Chem*., 2014, **20**, 3235–3244.

6 F. De Simone, T. Saget, F. Benfatti, S Almeida, and J. Waser, *Chem. Eur. J.*, 2011,**17**, 14527-14538.

7 C. Hirel, K. E. Vostrikova, J. Pécaut, V. I. Ovcharenko and P. Rey, *Chem. Eur. J*., 2001, **7**, 2007-2014.

8 A. Bouillon, J.-C. Lancelot, J. Sopkova de Oliveira Santos, V.Collot, P. R. Bovyb and S. Rault, *Tetrahedron* 2003, **59**, 10043–10049.

Appendix

Covers

Volume 5 | Number 10 | 21 May 2018

ORGANIC CHEMISTRY

FRONTIERS

rsc.li/frontiers-organic